INVESTIGATION OF 3D ELECTRICAL IMPEDANCE MAMMOGRAPHY SYSTEMS FOR BREAST CANCER DETECTION

By

XIAOLIN ZHANG

Submitted For The Degree Of

Doctor Of Philosophy

BIOMEDICAL ENGINEERING

SCHOOL OF ENGINEERING AND INFORMATICS

UNIVERSITY OF SUSSEX

BRIGHTON

UK

June 2015

DEDICATION

To my parents Shihao Zhang and Jing Zhang for believing in my ability and encouraging me to overcome difficulties

To my fiance Huan Zhou for supporting my work in the last four years

INVESTIGATION OF 3D ELECTRICAL IMPEDANCE MAMMOGRAPHY SYSTEMS FOR BREAST CANCER DETECTION

SUMMARY

Breast cancer is a major disease in women worldwide with a high rate of mortality, second only to lung cancer. Hence, there is considerable interest in developing non-invasive breast cancer detection methods with the aim of identifying breast cancer at an early stage, when it is most treatable. Electrical impedance mammography (EIM) is a relatively new medical imaging method for breast cancer detection. It is a safe, painless, non-invasive, non-ionizing imaging modality, which visualizes the internal conductivity distribution of the breast under investigation. Currently some EIM systems are in clinical trials but not commercialized, as there are still many challenges with sensitivity, spatial resolution and detectability. The research in this thesis aims to enhance and optimize EIM systems in order to address the current challenges.

An enhanced image reconstruction algorithm using the duo-mesh method is developed. Both in simulations and real cases of phantoms and patients, the enhanced algorithm has proven more accurate and sensitive than the former algorithm and effective in improving vertical resolution for the EIM system with a planar electrode array. To evaluate the performance of the EIM system and the image reconstruction algorithms, an image processing based error analysis method is developed, which can provide an intuitive and accurate method to evaluate the reconstructed image and outline the shape of the object of interest.

Two novel EIM systems are studied, which aim to improve the spatial resolution and the detectability of a tumour deep in the breast volume. These are: rotary planar-electrode-array EIM (RPEIM) system and combined electrode array EIM (CEIM) system. The RPEIM system permits the planar electrode array to rotate in the horizontal plane, which can dramatically increase the number of independent measurements, hence improving the spatial resolution. To support the rotation of the planner electrode array, a synchronous mesh method is developed. The CEIM system has a planar electrode array and a ring electrode array operated independently or together. It has three operational modes. This design provides enhanced detectability of a tumour deep within the tissue, as required for a large volume breast. The studies of the RPEIM system and the CEIM system are based on close-to-realistic digital breast phantoms, which comprise of skin, nipple, ducts, acini, fat and tumour. This approach makes simulations very close to a clinical trial of the technology.

ACKNOWLEDGMENT

Studying in University of Sussex is an enjoyable experience for me. Many people played very important roles in my research work. The most important persons are Prof. Chris Chatwin and Prof. David Barber. Prof. Chris Chatwin gave me lots of support to help me to carry on my research. Prof. David Barber is not my formal supervisor, but he took me as his own student and gave me lots of suggestions in algorithms and system design. I really appreciate the suggestions and the help from Prof. Chris Chatwin and Prof. David Barber.

I must say thanks to Dr Wei Wang as he brought me to the EIT area and we had lots of discussion on system designs.

I would like to thank Weida Zhang. When I felt confused in hardware, I always sought help from him. His suggestions were very valuable.

I also want to express my gratitude to my friends Weifan Zhang and Tengfei Yin. They provided necessary backup for me and they made me feel that I was not alone in the UK.

The last one, who I am most thankful to is my fiance Huan Zhou. He gave me lots of support in the last 4 years when I was in the UK, both in life and in research.

PUBLICATIONS

1. **Xiaolin Zhang**, Wei Wang, Gerald Sze, David Barber, Chris Chatwin, "An Image Reconstruction Algorithm for 3-D Electrical Impedance Mammography," IEEE Transactions on Medical Imaging, vol. 33, 2223-2241, 2014.

2. **X. Zhang,** C. Chatwin, and D. C. Barber, "A feasibility study of a rotary planar electrode array for electrical impedance mammography using a digital breast phantom," Physiological Measurement, vol. 36, pp. 1311-35, 2015.

3. X. **Zhang,** C. R. Chatwin, and D. C. Barber. (2015, Effective electrode sampling strategies for 3D electrical impedance mammography. Electronics Letters 51(6), 449-450.
   Available: http://digital-library.theiet.org/content/journals/10.1049/el.2014.4454.

4. **Xiaolin Zhang**, Wei Wang, Chris Chatwin, The Data Acquisition Method of the Sussex MK4 EIM System, 15th International Conference on Biomedical Applications of Electrical Impedance Tomography (EIT), Gananoque, Ontario, Canada, 2014.

5. **Xiaolin Zhang**, Chris Chatwin, Wei Wang, A Comparison of Two Regularization Methods Based on the Sussex EIM MK4 System, 15th International Conference on Biomedical Applications of Electrical Impedance Tomography (EIT), Gananoque, Ontario, Canada, 2014.

6. **Xiaolin Zhang**, Tabassum Qureshi, Chris Chatwin, Wei Wang, Validity of Using the Sheffield Algorithm for the Sussex EIT MK4, 15th International Conference on Biomedical Applications of Electrical Impedance Tomography (EIT), Gananoque, Ontario, Canada, 2014.

7. Jinling Xing, Nan Li, Wang Wei, Mingqian Wang, Danyang Jiang, Hui Xu, **Xiaolin Zhang**, A High speed, high bandwidth Versatile DAS for breast cancer detection,

15th International Conference on Biomedical Applications of Electrical Impedance Tomography (EIT), Gananoque, Ontario, Canada, 2014.

8. Wei Wang, Gerald Sze, **Xiaolin Zhang**, David Barber, A feasibility study for High Resolution EIT imaging, 15th International Conference on Biomedical Applications of Electrical Impedance Tomography (EIT), Gananoque, Ontario, Canada, 2014.

9. Mingqian Wang, Nan Li, Jinling Xing, Wei Wang, Hui Xu, **Xiaolin Zhang**, The Channel Switch Method of the Cambridge MK4 EIT System, 15th International Conference on Biomedical Applications of Electrical Impedance Tomography (EIT), Gananoque, Ontario, Canada, 2014.

10. Fan Zheng, Guofeng Qiao, **Xiaolin Zhang**, C. Chatwin, Wei Wang, A comparison of two- and four-electrode bio-impedance measurements in electrolytes of different conductivity for measurement of cell suspension condition, 13th International Conference on Biomedical Applications of Electrical Impedance Tomography (EIT), Tianjin, China, 2012.

CONTENTS

LIST OF TABLES

LIST OF FIGURES

ACRONYMS

3D：	three-dimensional
DAS:	data acquisition system
DCIS:	ductal carcinoma in-situ
DYR:	dynamic range
EIM:	electrical impedance mammography
EIT:	electrical impedance tomography
EITS:	electrical impedance tomography spectroscopic
FEM:	finite element method
FSH:	follicle stimulating hormone
HPEA:	hexagonal planar electrode array
IDC:	invasive ductal carcinoma
ILC:	invasive lobular carcinoma
IM:	inner measurement
LCIS:	lobular carcinoma in-situ
LH:	luteinizing hormone
LCC:	craniocaudal view of the left breast
LMLO:	mediolateral oblique view of the left breast
MRI:	magnetic resonance imaging
OM:	outer measurement
PET:	positron emission tomography
PIF:	prolactin inhibiting factor
RCC:	craniocaudal view of the right breast
RLMO:	mediolateral oblique view of the right breast
RPEA:	rectangular planar electrode array
RPEIM:	rotary planar electrode array EIM
SNR:	signal to noise ratio
TEB:	terminal end bud

UOQ: outside of quadrant

MATHEMATICAL SYMBOLS

$\boldsymbol{B}$:	magnetic flux
$\boldsymbol{C}$:	contrast
C_{inj}:	injected current
$\boldsymbol{d}$:	detectable parameters
d:	diameter
D:	image distortion
$\boldsymbol{D}$:	fluxes-electric displacement
$\boldsymbol{\mathcal{D}}$, $\boldsymbol{\mathcal{M}}$:	domain
e:	electrode
$\boldsymbol{E}$:	electric field
$\boldsymbol{F}$:	sensitivity matrix for the logarithm image reconstruction algorithm
h:	*Planck's constant*
I, I_a, I_b:	X-ray intensity
I_{img}:	conductivity image
$\boldsymbol{I}$:	identity matrix
j:	boundary current density
$\boldsymbol{J}$:	electric current density
K:	number of mesh elements
l:	length
L:	number of image layers
m:	mass
$\boldsymbol{m}$:	model parameter
N:	number of mesh nodes
$\boldsymbol{n}$:	outward unit normal
$\boldsymbol{H}$:	magnetic field
p:	index of measurement position
P:	number of measurement positions
Q:	quantity of electricity
q:	charge
$\boldsymbol{S}$:	sensitivity matrix for the differential image reconstruction algorithm
$\boldsymbol{V}$:	voltage
V_e:	volume of mesh element
$\boldsymbol{Y}$:	forward solver
(x, y, z):	coordinate
μ, μ_a, μ_b :	attenuation coefficient
μ_0:	*nucleus's magnetic dipole strength*
ω_0:	*Larmor frequency in unit of radians per second*
v_0:	*Larmor frequency in unit of Hertz*
$\mathscr{h}$:	map function
ρ:	charge density
ε:	permittivity

μ':	permeability
$\sigma:$	conductivity
$\emptyset$:	potential
Ω:	3D field
$\partial\Omega$:	boundary of the 3D field
$\Delta Eng:$	difference of energy

1. Introduction

The overall aim of this research is to create technology that will greatly enhance the performance of Electrical Impedance Mammography in order to enable its development into a reliable breast cancer detection system.

The aims of this chapter are to provide a brief overview of breast anatomy, breast cancer and breast cancer risk factors to help females to understand and prevent breast cancer, introduce the current breast cancer detection methods to help people, especially patients, to understand the advantages and disadvantages of different diagnostic approaches, and introduce a relatively new but safe and valuable breast cancer detection method, named electrical impedance mammography (EIM) and the current EIM systems.

This chapter will firstly introduce breast anatomy and breast cancer to illustrate where, when and how breast cancer develops. Following this, breast cancer detection methods and their advantages and limitations will be introduced. Electrical impedance mammography is a relatively new breast cancer detection method, which is the research topic of the thesis. The main EIM research groups working on EIM systems will be introduced in this chapter. The challenges of the EIM systems will be presented. The research work of this thesis will focus on addressing these challenges.

1.1 Breast

Breast is a bilateral organ in the upper ventral region of the torso of a primate. Breasts of both men and women are developed from the same embryological tissues; however male breasts are undeveloped due to their suppression by testosterone. Female breasts have morphological changes at different development stages. A female breast appears at the first signs of sexual change at puberty and develops into a prominent mound with an

enlarged nipple and areole. During pregnancy and lactation, under a complex interplay of estrogen, progesterone and prolactin, the breast is fully developed and maximized in volume in order to produce milk. As a result, female breasts are vital organs to exhibit beauty and to nurse infant children (Russo and Russo, 2004, National Cancer Institute, 2012, Wikipedia, 2014a).

1.1.1 Breast Anatomy

A woman's breasts are attached to the pectoralis major muscles, by the deep fascia, which extends from the collarbone vertically down to the middle of the sternum, from the edge of the sternum horizontally out to the axilla (armpit). Anatomically, a healthy breast shows a corn shape with the base at the chest wall and the apex at the nipple at the center of the areola. For a young lady, the nipple is located between the 4th and 5th rib and is approximately 1 cm outward from the midclavicular line; however for a middle-aged lady, the nipple falls to the 6th rib and is 1 to 2 cm outward from the midclavicular line. Figure 1. 1 shows the anatomy of the breast. There is a space between the breast and the pectoralis major muscle called the pectoralis major muscle, which permits the movements of the breast. A mature breast is composed of the skin envelope, fibrous connective tissue, adipose tissue, glandular tissue and a significant number of vasculars and nerve, in which the first three components determine the shape and the volume of the breast (Mandal, 2013). The superficial fascia wraps the whole breast under the 0.5-2.5 cm of subcutaneous fat. It is mainly loose areolar connective tissue and adipose, which determines the shape of the breast. The suspensory Cooper's ligaments are connective tissue that sustain the breast by traversing and encompassing the adipose tissue and the gland tissue, from the deep fascia beneath the breast to the dermis (Maxwell and Gabriel, 2009, Wikipedia, 2014b). The skin envelope finally establishes and maintains the breast upon the chest wall. The adipose tissue occupies a large portion of the breast, which protects it from injury and forms its shape and volume. The functional component of the breast is the glandular

tissue, which produces milk to feed an infant child. An adule breast is made up of 12-20 irregular lactiferous lobes, which are seperated by the connective tissue and converge to the nipple (National Breast Cancer Foundation, 2012). Each lobe is made up from several lobules and each lobule is made up from several ducts and acinus. The number of lobes doesn't change in the whole life of a woman; however the number of lobules changes as the estrogan changes in particular stages, such as the menarche, pregnancy, lactation and menopause. Each lobe has one lactiferous duct with its openning in the nipple. Before lactation, the lactiferous ducts are locked by the keratin plugs to prevent bacterial infection. It was believed that there were lactiferous sinuses in the lactiferous ducts near the nipple, which accumulate milk between breastfeeding sessions; however in 2005, Ramsay and his collegues reported that the lactiferous sinuse didn't appear in their ultrasound images (Ramsay et al., 2005). The lactiferous ducts follow a tree pattern connecting the lobules of the breast. The functional units of the breast are the terminal duct lobular units, which produce milk for off-spring. Please refer to Figure 1. 2. The terminal duct lobular unit is composed of the lobules and the extralobular terminal ducts, in which the lobule is composed of the acinus and the intralobular terminal ducts. The milk is formed in the acinus and drained by the intralobular terminal ducts to the extralobular terminal ducts, then to the the lactiferous ducts, which lead to the nipple. All the milk ducts in the breast are surrounded immediately by the dense connective tissue, which acts as a support frame; however biochemically, the glandular tissue is supported by estrogen, thus the volume and the shape of the glandular tissue change as the estrogen level of the body changes.

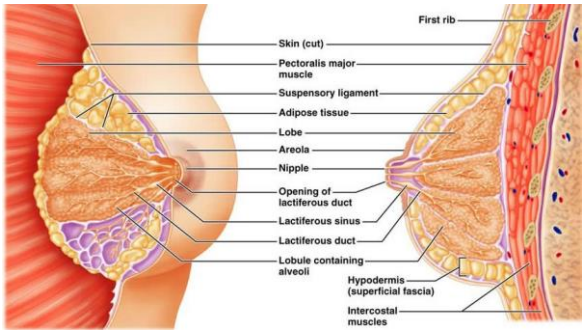

Figure 1. 1 The anatomy of the breast. (©Midlands Technical College)

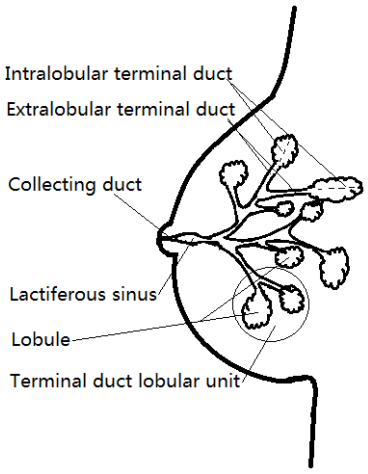

Figure 1. 2 The cross-section scheme of the mammary gland

The profuse blood vessels in the breast (shown in Figure 1. 3) play an important role in supplying nutrition and maintaining metabolism. 60% of the blood supply is from the medial mammary arteries, which start from the internal thoracic artery, run through the intercostal spaces near the sternum, penetrate the the pectoralis major and extend to the medial breast. 30% of the blood supply is from the lateral mammary arteries, which are derived from the lateral thoracic artery and reach to the lateral breast. In addition, the branches originally from the thoracic aorta provide blood to the deep and lower breast. Clinically, the veins of the breast are more significant than the artery, as it is related to breast cancer metastasis (Zhao, 2008). Breast veins exist in skin (superficial vein) and tissue (deep vein). The superficial vein is in the superfical layer of the superficial fascia. The blood in the superficial vein flows to the internal mammary vein and the anterior jugular vein. The deep veins include the medial mammary veins, which drain the blood of the medial breast to the internal thoracic vein, the lateral mammary veins, which drain the blood of the lateral breast to the subclavian vein and the intercostal veins, which lead the blood of the breast back to the azygos vein. The three deep veins run through the superior vena cava and finally reach to lung, thus breast cancer can be transfered to lung.

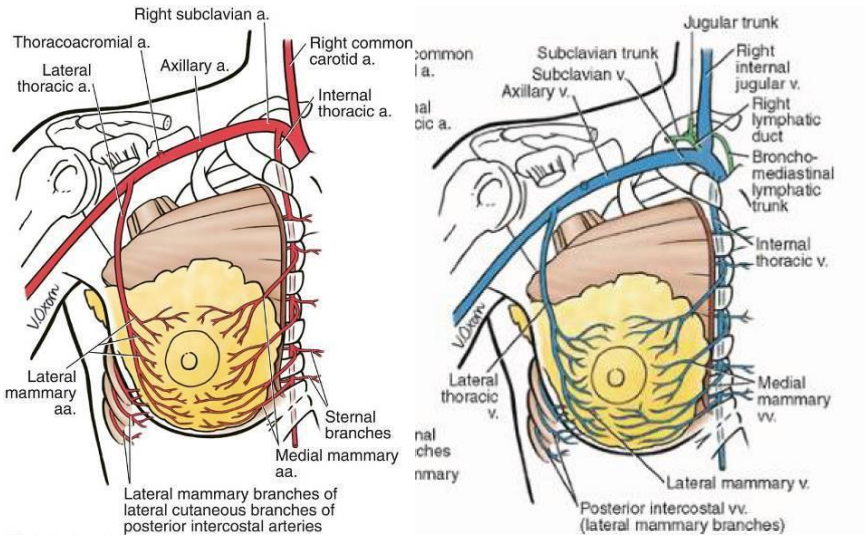

Figure 1. 3 The artery (left) and the vein (right) in the breast (©Study Blue)

Lymph system is a circulatory system which transports lymph around the body through a network of lymph vessels and lymph nodes. As a part of the immune system, it carries the disease-fighting cells and fluids, which can pick up bacteria and destroy them at lymph nodes. Lymphatic vessels permit the immune cells to enter and exit, therefore the metastatic cancer cells can easily enter and travel through lymph system until they get stuck in the narrow channels inside the nearby lymph node. As the circulation of lymph is slow, it is stressless for the cancer cells to develop to a secondary cancer (Cancerquest, 2014, National Breast Cancer Foundation, 2012). Breast has very concentrated lymph vessels, which distribute in skin, mammary lobulars and the interacinous spaces and connect with the lymphatic networks in the chest, neck, axilla and abdomen (shown in Figure 1. 4). The superficial lymph veins run along the milk ducts converging to the nipple and then go to the deep lymphatic network. The deep lymphatic network is in the horacic fascia, where lymph flows out through five paths:

1. axillary lymph nodes, where 75% of the lymph in breast flows out. Normaly, There are 20 to 30 lymph nodes in that region.

2. internal mammary lymph nodes, which are distributed around internal mammary

vessels. The lymph vessels pass through the intercostal muscles and reach to these nodes. The number of the lymph nodes in this region is about 6 to 10.

3. supraclavicular lymph nodes and infraclavicular lymph nodes, which spread near sternocleidomastoid muscle, jugular vein and subclavian vein, including approximatelly 10 lymph nodes.

4. abdominal lymph vessels, which lead to intra-abdominal lymph nodes and liver; thus metastatic cancer cells from breast can spread to the liver.

5. the subcutaneous lymphatic network of both breasts, where lymph flows from one side to the other, thus the breast cancer cells can spread from one side to the other.

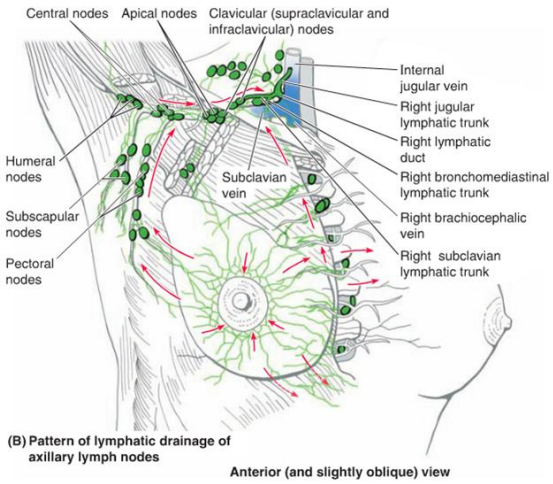

Figure 1. 4 The lymph system in breast (©Study Blue)

1.1.2 Breast Development

It is believed that the formation of breast cancer is related to breast development, therefore knowing the developmental process of the breast is helpful to understand the pathology of breast cancer. The development of a female breast lasts a lifetime, starting from the embryo. The breast varies in appearance, volume and position as a woman

experiences infancy, puberty, pregrancy, lactation and menopause.

The mammary gland is developed from a single epithelial ectodermal bud. At approximatly the 5th to 6th week after the formation of the embryo, the ectodermal primitive milk streak is developed and extends from axilla to the pelvis, which is also known as“galactic band”. At the 7th to 8th week, the galactic band gets atrophied and forms a mammary ridge in the region of the thorax. Following this, thickening of the mammary anlage (milk hill stage), invagination into the chest wall mesenchyme (disc stage) and tridimensional growth (globular stage) occur sequentially. Between the 12th and the 16th week of the fetal life, squamous cells from the surface start to intrude into the nipple bud; epithelial cells develop to mammary ducts (budding stage) and branch downward into 15 to 25 strips of epithelium (branching stage); mesenchymal cells differentiate into the smooth muscle of the nipple and areola. During the 16th to 24th week, the secondary mammary analage starts developing and differentiates to follicle, sebaceous gland and sweat gland elements; montgomery glands around the nipple are formed from special apocrine glands. From the 20th to the 32th week, placental sex hormones attend to fetal’s circulation and induce canalization of the branched epithelial tissues (canalization stage). In the last 2 months before parturition, lobuloalveolar structures are formed which are composed of a monolayer of epithelium and contain colostrum (end-vesicle stage). The newborn’s breast only has very primitive structures including ducts with small terminal branches lined by one or two layers of epithelium, where the epithelium has a finely vacuolated eosinophilic cytoplasm with typical apocrine secretion (Russo and Russo, 2004, American Medical Network, 2008).

The mammary gland keeps developing during childhood; however no siginificant changes can be observed from their appearance until the approach of puberty. The phenomenon of growth of the rudimentary mamma happens at the age of 10 to 12, which indicates the onset of the adolescent period. When children age to puberty, hypothalamus starts to produce gonadotropin release hormone. This promotes the release of follicle

stimulating hormone (FSH) and luteinizing hormone (LH) from the pituitary gland. As a result, the ovarian get mature and the estrogen starts to affect the development of female secondary sexual characteristics (Sabel, 2009). In puperty, the female breast swells progressively with the growth of the the glandular tissue and the surrounding stroma. The volume of the glandular tissue increases due to growth and division of the primary and secondary ducts, which are partly in dichotomous manner and partly in sympodial manner. The virginal ducts of newborn are terminated with club-shaped bulbous structures, which are named the terminal end buds (TEBs) and shown in Figure 1. 5. Each TEB is lined by two layers of cells: inner cells and basal cells. The inner cells have secretory properties, from which the milk is formed; whereas the basal cells have proliferous properties, from which the lengthening and branching of the virgin ducts originate. TEB cleaves into either two small ducts or alveolar buds (ABs). AB is a transitional structure, which is morphologocally more developped than TEBs, as they can develop into new branches or sprout into ductules, which are clusters of small terminal structures around the terminal duct (Russo and Russo, 2004). Figure 1. 6 shows the mammary gland before the onset of puberty with ABs and the structures developed from ABs. Usually one or two years later after menarche, lobule starts to formate in female breast, as shown in Figure 1. 7. When the ducts arborize and form a structural unite with ternimal ducts surrounding by 4 to 11 ductules, the terminal duct lobualr unit is established. These terminal duct lobualr units are virginal lobules. With the development of the breast, the number of lobules increases progressively. In this process, the surrounding vascularity and connective tissue increase to support the extension of the ducts in the breast. Ovarian hormones play a siginificant role in breast development; even after puberty, the resting breast still undergoes a menstrual development with the menstrual fluctuations of strogan and progesterone until approximately 35 years old. A non-pregnant adult woman has three types of lobules in her breast, which are differentiated by development level: Lob 1 has about 4 to 11 ductules around the terminal ducts, which is introduced before as virginal lobules; Lob 2 has an averge of 47 ductules per lobule; Lob 3 has at least a minumum of 80 ductules for one terminal duct.

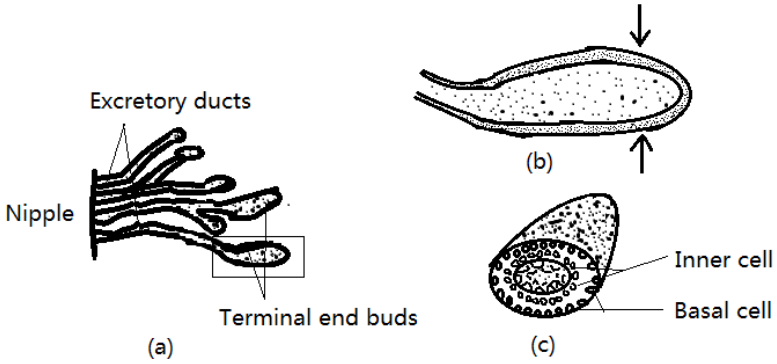

Figure 1. 5. The mammary gland at birth which are formed by several excretory ducts ending in terminal end buds.(a) the mammary gland at birth; (b) the terminal end bud; (c) the cross section of the terminal end bud at the level of the arrows in (b).

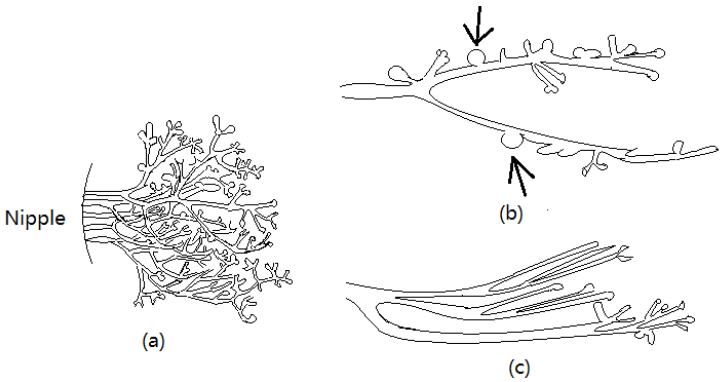

Figure 1. 6. The mammary gland before the onset of puberty, where the ducts grow and divide partly dichotomously and partly sympodially. (a) the mammary gland before puberty; (b) alveolar buds sprout from the duct; (c) the new branches and twigs developed from the alveolar buds.

Figure 1. 7. The mammary gland at puberty, where lobules are formed.(a) The mammary gland at puberty; (b) the virginal lobule or Lob 1

The mammary gland is fully developed during pregnancy. Once a woman conceives, estrogen and progesterone in her body increase suddenly and sharply, which stops the hypothalamus producing prolactin inhibiting factor (PIF). As a result, prolactin is realeased and increases gradually during pregnancy. In the early stage of pregnancy, under the influence of luteal and placental sex steroids and prolactin, the ducts elongate and ramify significantly. The rapid increase of ductals accelerates the formations of new lobules; as a result, the breast is dramatically enlarged and becomes tender, meanwhile the superfical veins dilate. In the second trimester of pregnancy, the ductals are progressed to secretory acini, which indiates the formation of the fully differentiated Lob 4. The breast in this stage continues enlarging, as the cells of each acinus of the newly formed lobules increase both in number and in volume, due to cell divisions and cytoplasmic enlargment. At this point, the acini contain colostrum but no lipid; prolactin continues to rise and will reach 3 to 5 times higher than the normal level. In the third trimester of pregnancy, the development of the breast focuses on the secretory activity. The formation of the acini increases apparently; however the proliferation of the newly formed acini diminishes to a minimum. The surrounding stroma of the lobules shrinks to make space for the acini, as the acini need to accumulate colostrum and lipids. Before delivery, the high levels of estrogen and progesterone restrain the prolactin receptor, hence prevent milk production; however after delivery, estrogen and progesterone decrease, as a resullt, milk is released. During lactation, there are no obvious morphological changes of the mammary gland. After lactation finishes, the acinar structures collapse; the tubules are narrowed; the breast returns to the previous size (Sabel, 2009, Russo and Russo, 2004).

Menopause occurs when 99% of the 400,000 follicles are exhausted. Normally a women enters menopause in between late 40’s and early 50’s. In this stage, estrogen and progesterone decline sharply; as a result, the breast begins to regress: the number of Lob 1 increases, meanwhile the number of Lob 2 and Lob 3 decreases. In the post-meno pause, Lob 1 is the dominating structure of the mammary gland; Lob 2 and Lob 3 almost disappear (Russo and Russo, 2004). From the appearance, the size of the breast is

shrunken; due to the absence of estrogen, the breast loses support and falls against the chestwall.

1.2 Breast cancer and its risk factors

1.2.1 Breast cancer

Cancer is a group of diseases, in which abnormal cells divide uncontrollably and have the potential to invade the nearby tissue and spread to other parts of the body. The cancer cells normally form a lump or mass of tissue, known as a malignant tumor. Breast cancer is cancer in breast tissue, which may be accompanied by some morphological changes of the breast, such as a mass in the breast, a shape change of the breast, skin dimpling, and nipple inversion. However these symptoms do not neccesarily indicate breast cancer, as most masses detected by mammography are benign and not life-threatening (American Cancer Society, 2014a). Normally, the cancerous cells are developed in milk ducts and lobules, which are known as ductal carcinomas and lobular carcinomas respectively. According to the spreading mechanism, cancer is classified as either in-situ or invasive. The in-situ or noninvasive breast cancer is the cancer that stays within the tissue, where it originates and does not invade normal tissue within or beyond the breast, including ductal carcinoma in-situ (DCIS), lobular carcinoma in-situ (LCIS) and other in-situ breast cancers having characteristics of both ductal and lobular carcinoma or having unknown origins. The invasive breast cancer is the cancer that breaks through the confines of the tissue where it forms and has the potential to invade the nearby or distant normal tissue, including invasive ductal carcinoma (IDC) and invasive lobular carcinoma (ILC). Figure 1. 8 shows the diagram of the above four main breast cancers.

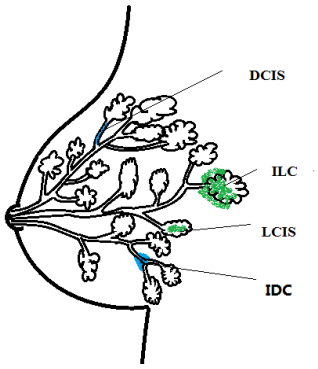

Figure 1. 8 In-situ and invasive ductal carcinomas and lobular carcinomas

Ductal carcinoma in-situ (DCIS), also known as intraductal carcinoma, is a noninvasive breast cancer, of which the uncontrolled cells grow in milk ducts and have not yet broken out from the original ducts. DCIS is believed to be the earliest stage of breast cancer that can be diagnosed. It is the majority of the nonivasive breast cancer, which accounts for 83% of the in-situ cases diagnosed during 2004-2010 (American Cancer Society, 2011, American Cancer Society, 2014a). DCIS doesn't usually form a sizeable lump; however it may cause breast pain or nipple discharge. Although DCIS is not fatal, it has the potential to progress to invasive cancers if left untreated. Studies suggest that 25% to 50% of the patients with DCIS will develop invasive breast cancer within 10 years.

Lobular carcinoma in-situ (LCIS), also known as lobular neoplasia, is not considered a true cancer, but results in an increased risk of developing invasive cancer, in which the proliferation of the abnormal cells are confined within the lobules. LCIS is less common than DCIS, which accounts for 11% to 12% of the invasive breast cancer during 2004-2010 (American Cancer Society, 2011, American Cancer Society, 2014a). There is no symptom for LCIS, therefore it can't be diagnosied clinically; most commonly it is found incidentally from biopsy, which is engaged for another reason (Foote and Stewart, 1941, Hajdu and Tang, 2009, Ratini, 2014). Even though the cancerous cells rarely escape from the original lobule, one-fifth of women will suffer from breast cancer metastasis over the next 15 years. LCIS can spread to either of the breasts, but most likely to the ipsilateral

(same-side) breast.

Invasive ductal carcinomas (IDC), also named infiltrating ductal carcinoma, is an invasive breast cancer that starts in a milk duct, penetrates throught the duct walls and begins to invade the surrounding normal tissue. IDC can either stay localized or enter the bloodstream or lymph system to spread to any part of the body. IDC is the most common type of breast cancer, which accounts for 80% of the invasive cases.

Invasive lobular carcinomas (ILC), also named infiltrating lobular carcinoma, is the cancer that originates in lobules, breaks out from the wall of the lobule and then begins to invade the surrounding tissure. ILC can spread within and beyond the breasts in the same way as IDC. Almost one third of women, who are diagnosed with ILC, will develop breast cancers in both breasts without proper treatment. ILC doesn’t present as a lump; instead it is characterized by a mass or a thickening in the breast, which usually occurs in the region between the nipple and armpit. ILC is the second most common invasive breast cancer following invasive ductal carcinoma, which accounts for 10% of the invasive cases.

There will be no obvious symptoms when the tumor is in the early stage. When developing to a size that can be felt, it always present as a painless lump. When cancer cells spread to the nearby lymph nodes, swellings or lumps may apprear there. A few cases involve breast pain and heaviness. The persistent changes of breast, such as swelling, thickening, redness of breast skin and nipple abnormality including spontaneous discharge, erosion, inversion and tenderness, may be indicators of breast cancer.

1.2.2 Breast cancer stages

Most breast cancers are invasive. The invasive breast cancers are stratified into different stages to help doctors undertand the prognosis and deliver treatment. TNM is

one of the staging systems for classifying the malignant tumours, where T, N and M are parameters discribing the tumor size, the nearly lymph nodes that are involved and the presence or absence of distant metastasis.

The letter T followed by a number from 0 to 4 indicates the size of the primary tumor and the extent of the tumor to the nearby tissue. A higher value indicates a larger size or a wider spread. The letter N followed by a number from 0 to 3 indicates the number of lymph nodes, in which cancer cells are found. The letter M followed by 0 or 1 indicates weather the cancer cells has transferred to distant organs. Detailed categories of T, N, and M, are tabulated in Table 1. 1. Breast cancer is staged to 5 levels from 0 to IV according to these parameters, which are shown in Table 1. 2 (American Cancer Society, 2014b, Breastcancer.org, 2015b).

Table 1. 1 TNM staging system

Primary tumor (T)		
TX	Tumor cannot be evaluated	
T0	No signs of tumor	
Tis	Carcinoma in-situ including DCIS, LCIS, or Paget disease of the nipple with no associated tumor mass	
T1	Tumor size smaller 2 cm	
T2	Tumor size greater than 2 cm and smaller than 5cm	
T3	Tumor size greater 5 cm	
T4	Tumor of any size infiltrating into the chest wall or skin. This includes inflammatory breast cancer.	
Lymph nodes involved (N)		
NX	Lymph nodes cannot be evaluated	
N0	Cancer cells haven't spread to the nearby lymph node	
	N0(i+)	Traces of cancer cells are found in the underarm lymph nodes by using routine or special stains. The invaded area has less than 200 cancer cells or is smaller than 0.2 mm.
	N0(mol+)	Cancer cells can't be seen in the underarm lymph nodes using special stains, but a tiny amounts of cancer cells can be detected using RT-PCR
N1	Cancer cells present in 1 to 3 axillary lymph nodes, or/and a tiny amounts of cancer cells are found in the internal mammary lymph nodes.	
	N1mi	Micrometastases in 1 to 3 lymph nodes under the arm. The invaded area is smaller than 2mm, containing at least 200 cancer cells.
	N1a	Micrometastases in 1 to 3 lymph nodes under the arm, at least one of which has a invaded area greater than 2 mm.
	N1b	Cancer cells enter internal mammary lymph nodes, but these cancer cells haven't resulted in an enlarged lymph node and could only be found by sentinel lymph node biopsy
	N1c	Phenomenon of both N1a and N1b
N2	Cancer cells are found in 4 to 9 axillary lymph nodes, or cancer has caused enlarged	

	internal mammary lymph nodes	
	N2a	Cancer cells have invaded to 4 to 9 axillary lymph nodes, in which at least one invaded area is greater than 2 mm.
	N2b	Cancer has spread to the lymph nodes under the clavicle and caused them to be enlarged.
N3	Cancer cells spread further or/and invade more lymph nodes	
	N3a	1) Cancer has spread to 10 or more axillary lymph nodes, in which at least one invaded area is greater than 2 mm. 2) Cancer has spread to the lymph nodes under the clavicle, in which at least one invaded area is greater than 2 mm.
	N3b	1) Cancer cells present in at least one axillary lymph node whose cancerous area is greater than 2 mm and cause enlargement of the internal mammary lymph. 2) Cancer cells present in 4 or more axillary lymph node, in which at least one invaded area is greater than 2 mm, and traces of cancer cells are found in internal mammary lymph nodes by sentinel lymph node biopsy.
	N3c	Cancer cells have transferred to the lymph nodes above the clavicle, in which at least one invaded area is greater than 2 mm,
Breast cancer metastasis (M)		
MX	Distant metastasis cannot be evaluated	
M0	No distant metastasis have been found by x-rays (or other imaging procedures) or by physical exam	
	cM0(i +)	Few cancer cells are found in blood or bone marrow or in distant lymph nodes with spreading area smaller than 0.2 mm.
M1	Cancer has spread to distant organs.	

Table 1. 2 Stages of breast cancer corresponding to TNM

Stage	TNM	Features
Stage 0	Tis, N0, M0	The cancer cells are confined within the tissue where it forms and haven't invaded the surrounding normal tissue; DCIS, LCIS, and Paget disease of the nipple are classified in Stage 0.
Stage IA	T1, N0, M0	The tumor is smaller than 2 cm and has not spread to the nearby lymph nodes and distant organs.
Stage IB	T0 or T1, N1mi, M0	The tumor is smaller than 2 cm and has a tiny spread to 1 to 3 lymph nodes. The cancer cells haven't reached distant sites.
Stage IIA	T0 or T1, N1 (but not N1mi), M0	The tumor is smaller than 2 cm and either: 1) cancer cells spread to 1 to 3 axillary lymph nodes with at least one invaded area greater than 2 mm, or 2) traces of cancer cells are found in internal mammary lymph nodes by sentinel lymph node biopsy, or 3) cancer cells invade both 1 to 3 axillary lymph nodes and internal mammary lymph nodes .
	T2, N0, M0	The tumor is larger than 2 cm and less than 5 cm, but doesn't spread to lymph nodes and distant sites

Stage IIB	T2, N1, M0	The tumor is larger than 2 cm and less than 5 cm. The cancer cells are found in 1 to 3 axillary lymph nodes or/and tiny amounts are found in in internal mammary lymph nodes but they haven't spread to distant sites.
	T3, N0, M0	The tumor is larger than 5 cm but doesn't reach skin and chest wall, and has not invaded lymph nodes and distant sites.
Stage IIIA	T0 to T2, N2, M0	The tumor is larger than 5 cm. Cancer cells have invaded 4 to 9 axillary lymph nodes or caused enlargements of the internal mammary lymph nodes, but haven't spread to distant sites.
	T3, N1 or N2, M0	The tumor is larger than 5 cm across but doesn't reach skin and chest wall. Cancer cells have invaded 1 to 9 axillary lymph nodes or internal mammary nodes but have not spread to distant sites.
Stage IIIB	T4, N0 to N2, M0	The tumor has infiltrated skin or chest wall and either: 1) cancer cells haven't spread to lymph nodes, or 2) cancer cells have spread to 1 to 3 axillary lymph nodes and/or tiny amounts are found in internal mammary lymph nodes, or 3) cancer cells are founded in 4 to 9 axillary lymph nodes, or cause the internal mammary lymph nodes to be enlarged
Stage IIIC	any T, N3, M0	The tumor is of any size and either 1) cancer cells are founded in more than 10 auxiliary lymph nodes, or 2) cancer cells have invaded the lymph nodes under the clavicle, or 3) cancer cells have invaded the lymph nodes above the clavicle, or 4) cancer cells are founded in more than 4 axillary lymph nodes and tiny amounts are found in internal mammary lymph nodes. Cancer cells have not spread to distant sites.
Stage IV	any T, any N, M1	The tumor is of any size. Cancer cells may or may not have spread to nearby lymph nodes but they are found in distant organs or lymph nodes. The most common invaded organs are the bone, liver, brain, or lung.

Another breast cancer staging system is the Surveillance, Epidemiology, and End Results (SEER) Summary Stage system, which is more simplified and commonly used for cancer registry and public health research (American Cancer Society, 2014a). It classifies the cancer as local stage, regional stage and distant stage. Local stage refers to the breast cancer that is confined within the breast corresponding to Stage I and partial Stage II in the TNM system. Regional stage refers to the breat cancer that has invaded the

surrounding tissue and the neaby lymph nodes, roughly corresponding to Stage II or Stage III in the TNM system. Distant stage referes to the breast cancer that has spread to the distant organs or lymph nodes, corresponding to Stage IIIc and Stage IV in the TNM system.

There are statistics for tumor size and five-year breast cancer survival in Table 1. 3 (Elkin et al., 2005). It shows that if the tumor can be detected when it is smaller than 2 cm, the patient will have at least a 90% survival rate. This could be referenced to make standards for breast cancer detection devices.

Table 1. 3 The statistics of tumour size and five-year breast cancer survival

Tumour size	Five-year relative breast cancer survival
Smaller than 1 cm	93%
1-1.9 cm	91%
2-2.9 cm	85%
3-3.9 cm	71%
4-4.9 cm	68%
Larger than 5	63%

1.2.3 Breast cancer metastasis

Cells are the fundamental units of life with specific functions. Healthy cells are developed in a controlled manner. They can reproduce themselves correctly and stop reproducing when enough cells are present. Healthy cells stick together in a specific place and become specialized for specific functions. If damaged, healthy cells will undergo self-destruction, and meanwhile new healhty cells will replace them to maintain their function. However cancer cells do not have these features and are developed in an uncontrollable manner. Cancer cells develop fast as they lose the gene that tells cells to stop reproducing or have the gene that keeps sending reproduction signals; as a result, cancer cells never stop doubling themselves. Cancer cells may or may not undergo apoptosis. However even though they may self destruct, the process is much slower than reproduction; eventually

billions of copies of the original cancer cell compose a tumor. Cancer cells also lose the adhesion molecules on their suface, which bond them to the neighboring cells and keep them in the right place; therefore cancer cells can escape from their originated positions and spread to the surrounding or/and distant tissue. Cancer cells are immature, thus they don’t have any fuctions; however they grow fast by depriving normal cells of nutrition, hence they affect the development of normal cells. When the immature cancer cells accumalate and the normal cells lose normal proliferation in an organ, the organ will malfuction and cause death.

Cancer is treatable if localized where it originates; however once cancer cells spread, it is very difficult to cure. The cancer that grows where it originally formed, is called the primary cancer. When cancer cells break away from their initial or primary sites, they may travel through the bloodstream and lymphatic system and stay to develop a cancer in another part of body. This cancer is called the secondary cancer. Cancer cells do not stick together, conversely they make a substance which stimulates them to move. Cancer spreads in three ways, which are: local spread, through the blood circulation and through the lymphatic system (Cancer Research UK, 2013b).

Local spread is when the cancer grows into the nearby normal tissue, which invloves the pressure from the growing tumour, a significant number of enzymes in the cancer cells, and the movements of the cancer cells through the tissue. As a tumor grows, it takes up more and more space, which will put pressure on the surrounding normal tissue. This will make the tumor grow through the normal tissue by choosing the easier path of least resistance. For example, tumors can grow easily into the adipose tissue rather than the large blood vessels, which have strong walls. In the growth path of the tumour, the small blood vessels are squeezed or blocked, which cuts the blood and oxygen supply to the surrounding normal cells; as a result the surrounding normal tissue die off, which makes the tumor extention easier. There are some enzymes existing in many normal blood cells, which have the function to break down the damaged cells and tissues as well as the

invading bacteria and viruses, so that the body can refresh itself. However studies suggest that many tumors contain a large amount of these enzymes, which likely make the tumors easier to grow through the normal tissue. Cancer cells are not boned together, conversely they can produce a substance to help them to move; therefore it is very easy for the cancer cells to directly move to the nearby tissue (Cancer Research UK, 2013a).

To spread through the blood circulation, cancer cells must get detached from the primary cancer and penetrate through the wall of a blood vessel to travel by the bloodstream. During the traveling, most cancer cells are killed by the white blood cells in our immune system or by battering around in the fast flowing blood. Only one out of many thousands of cancer cells can survive to form a secondary cancer, when they get stuck in a narrow path, usually a capillary. When the trapped cancer cell breaks through the wall of the capillary and enters an organ, it will develop a new cancer/tumor. Cancer cells may try to adhere to platelets to form clumps, which not only protect them from battering but also helps them to get lodged in capillaries.

Cancer spread through the lymphatic system is very similar to that through the bloodstream; however the flow of lymph is slow, thus it is much easier for cancer cells to spread via the lymphatic system. Cancer cells will stop travelling when they arrive at lymph nodes and then begin to develop a secondary cancer.

1.2.4 Breast cancer risk factors

Breast cancer is the second biggest killer of women following lung cancer, which has high incidence and mortality rates. It is a very common disease in most western countries and the societies, which are westernized or in the process of westernization. In the UK, there are approximately 49,900 women and 350 men diagnosed with breast cancer each year (Cancer Research UK, 2014). In United States, it is reported in 2014 that

1 in 8 women will develop invasive breast cancer in their life (Breastcancer.org, 2015c). There are many factors that are considered relavant to breast cancer, including family and personal historty, life-style, personal factors such as early menarche and late menopause, enviromental factors such as radiation and pollution.

Women, who have a family history of breast cancer, especially for the first-degree relative, have an increased risk of developing breast cancer. The risk for the woman having a first-degree relative (sister, mother, daughter) diagnosed with breast cancer is 1.8 times higher than the woman having no family history. If more than one first-degree relative has had this desease, the risk will be higher. The risk of breast cancer is nearly 3 times higher for the woman who has two infected first-degree relatives and nearly 4 times higher for the woman who has three and more infected first-degree relatives. A woman, whose father or brother is diagnosed with breast cancer, also has a higher risk than average; however how much higher is not known presently. A family history of ovarian cancer also associates with an increased risk of breast cancer for both men and women. Women whose immediate family or either parent's extended family has a history of breast or ovarian cancer, may have a genetic predisposition to cancer. About 5% to 10% of breast cancer is due to the mutant genes inherited from parents, in which BRCA1 and BRCA2 account for 15% to 20% of the familial cases. BRCA1 and BRCA2 present in less than 1% of the general population, but most commonly in certain ethnic groups such as Ashkenazi. By the age of 70, 44% to 78% of women with BRCA1 mutations and 31% to 56% of women with BRCA2 mutations will develop breast cancer. Women with a history of breast cancer have a high risk of recurrence, especially for the ones who are diagnosed at a younger age. Women who are diagnosed with breast cancer at less than 40 years old, have about 4.5 fold risk to get a second breast cancer, in which genetic predisposition may play an important role (Schwartz et al., 2008, Turnbull and Rahman, 2008, American Cancer Society, 2014a, Breastcancer.org, 2015a).

Studies suggest that a dense breast has a 4 to 6 fold increased risk to develop breast

cancer, compared to a fatty breast (Tamimi et al., 2007, Boyd et al., 2007, Cummings et al., 2009). Breast density is a measure to compare the area of the mammary gland and the connective tissue with the area of fat seen on a mammogram. There are many factors affecting breast density such as gene, age, pregnancy, menopause, and drugs. Basically, breast density is influenced by genes; however with the increase of age, breast density decreases, especially after pregnancy and menopause. Some drugs including tamosfen or combined menopausal hormone have the effect of decreasing or increasing breast density. The risk of breast cancer is associated with the increase of breast density. Researchers point out that the breast cancer patients under age 50 tend to have a higher breast density than the healthy women of the same age level (Preidt, 2013).

Endogenous hormone levels are important fators in developing breast cancer. Studies suggest that early menarche (before age 12) leads to a higher risk of breast cancer (Kelsey et al., 1993). Each 2 years delay of menarche will decrease the breast cancer risk by 10% (Hsieh et al., 1990); women who experience menarch at or after the age of 15 will reduce the breast cancer risk by 23% compared to those at or before age 12 (Brinton et al., 1988). Women who expirence a late menopause (after age 55) also have an increased risk of breast cancer. Each five years delay of menopause will cause a 17% increase of breast cancer risk (Hsieh et al., 1990). It seems that women who have more menstrual cycles due to early menarche and late menopause have a slightly higher risk of breast cancer. This may result from the longer lifetime exposure to the reproductive hormone.

Breast cancer also has relationships with later first full-term pregnancy (after 30) and nulliparity. If a woman gave birth before 24 years old, she will have a marked reduction of breast cancer risk, however if her first full-term pregnancy occurred after 35 years old, she will have a very high risk to get breast cancer, espetical during the time following delivery (MacMahon et al., 1970, Russo and Russo, 2004). Breastfeeding, lasting for one year or more, will slightly lower the risk of breast cancer; every 1 year of

breastfeeding will decrease the risk by 4.3% (American Cancer Society, 2014a). One explanation for this is that breastfeeding reduces a woman's total number of lifetime menstrual cycles.

Lifestyles such as using menopause hormones, smoking, drinking alcohol, and physical activity are considered relevant with breast cancer risk. Taking menopause hormones with combined estrogen and progestin will inrease the risk of developing and dying from breast cancer, especially for the women who have a long term use. The risk is higher for the women who start hormone therapy immediately after the onset of menopause than those who start to use later. The risk reduces after 5 years of discontinuation. There is limited evidence that breast cancer is associated with tabacco smoking. Researchers from the American Cancer Society found that smokers have a 12% higher risk of breast cancer than non-smokers (Gaudet et al., 2013). Some studies also indicate that the women, who start smoking before their first childbirth, may incurr a higher risk (Luo et al., 2011, DeRoo et al., 2011). The use of smokeless tobacco was reported significantly raising the risk of breast cancer for the women under age 55 (Spangler et al., 2001). Alcohol consumption is demonstrated as having an association with breast cancer. A woman who drinks alcohol of about 10g per day will have 7% to 12% increased risk of developing breast cancer (Hamajima et al., 2002, Chen et al., 2011, Allen et al., 2009). Any history of alcohol intake increases the risk 1.2 fold compared with that of those who never drink (95% confidence interval 0.7-1.8). Women who drink more heavily than their lifetime average ingestions and last for half a year or more will increase the relative risk of breast cancer to 2.6 (95% confidence interval 1.1–5.8). Alcohol consumption increases hormonal levels, which may be the mechanism of increased breast cancer risk. More and more evidence shows that regular physical activities will reduce the risk of breast cancer by 10%-20%. This benefit is more obvious for the postmenopause than the premenopause (Peters et al., 2009, Eliassen et al., 2010). Physical activity may prevent breast cancer by regulating body mass, hormones and energy balance (Neilson et al., 2009).

Radiation is desmonstrated a trigger for breast cancer, in the studies of the survivors in the atomic bombs in Hiroshima and Nagasaki in Japan (McGregor et al., 1977) and the chest X-ray fluoroscopy (Boice et al., 1991). According to statistics, only the women who experienced the bombs in Japan at the age younger than 29 developed breast cancer; those who were older developed benign breast disease (McGregor et al., 1977). The repeated X-ray fluoroscopy also has a carcinogenic effect on breast cancer. There is convincing evidence that exposure to radiation at younger ages will increase the risk of breast cancer (Boice et al., 1991, Preston et al., 2002). According to the studies in Europe and USA, women, who are treated successfully with radiation for early-stage Hodgkin's disease, have an increased risk of developping breast caner. Those irradiated between puberty and 30 are of the highest risk. Women who are treated with radiation at a median age of 21 to 24, subsequently develop breast cancer after a median interval of 15 years. Most radiation-induced breast cancers are unfavorable, in which the infiltrating ductal carcinoma with a great number of aggressive cancer cells is the predominant type. Women with these cancers have significantly lower overall survival than those threatened by sporadic breast cancer (Hancock et al., 1993, Cutuli et al., 2001, Gaffney et al., 2001, Janov et al., 2001).

1.3 Breast cancer detection

Currently, various breast cancer screening techniques are developed, aiming to detect the breast cancer at early stages, when it is most treatable. These include mammography, magnetic resonance imaging (MRI), breast ultrasound, positron emission tomography (PET), and electrical impedance mammography (EIM).

1.3.1 Mammography

Mammography is a diagnostic and screening tool using a low-dose X-ray to visualize the internal structures of the breast. It is the oldest and the most frequently used method and considered a gold standard for breast cancer detection. Mammography is based on the theory of X-ray absorption. For mono-energetic radiation, when a beam of X-ray passes through matter, it will be attenuated exponentially due to the absorption ability of the matter. The relationship between the transmitted intensity and the original intensity is given by

$$I = I_0 e^{-\mu L} \quad (1.1)$$

where: I indicates the transmitted intensity, I_0 indicate the original intensity, μ denotes the attenuation coefficient of the matter. If the X-ray beam goes along Path A in Figure 1. 9, through the Matter A with an attenuation coefficient of μ_a, the transmitted intensity can be writen as

$$I_a = I_0 e^{-\mu_a Z} \quad (1.2)$$

where Z denotes the thickness of Matter A. However if the X-ray beam goes along Path B, passing through the object of interest Matter B having a attenuation coefficient of μ_b, the transmitted intensity is given by

$$I_b = I_0 e^{-\mu_a (Z - Z_b) - \mu_b Z_b} \quad (1.3)$$

where Z_b is the thickness of Matter B. The difference of the transmitted X-ray intensity caused by the presence of Matter B is:

$$\Delta I = I_a - I_b = I_0 e^{-\mu_a z}\left(1 - e^{(\mu_a - \mu_b) z_b}\right) \quad (1.4)$$

If the radiation contrast is defined as:

$$C = \frac{I_a - I_b}{I_a + I_b} \quad (1.5)$$

Substituting (1.2) and (1.3) into (1.5), we get

$$C = \frac{1 - e^{(\mu_a - \mu_b) z_b}}{1 + e^{(\mu_a - \mu_b) z_b}} \quad (1.6)$$

Equation (1.6) demonstrates that the contrast of the X-ray image is relative to the thickness of the object of interest and the difference of the attenuation coefficient between the object and its surrounding matter (Yaffe, 2010, Brown, 1999).

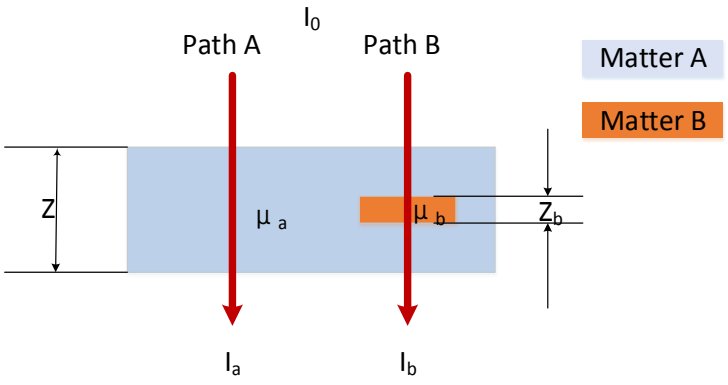

Figure 1. 9 X-ray detection

In examination of mammography, a breast is tightly squeezed by a pair of parallel plates attached to the mammography machine, as shown in Figure 1. 10, so that it can produce a sharp image with less X-ray exposure. The top plate is adjustable and made of plastic; the bottom plate is fixed for holding the X-ray film or the digital detector that records the image. Differrent tissues of the breast have different attenuation coefficients,

for example the attenuation coefficients of adipose, fabrous and cancerous tissue at 15 keV are approximately 0.797, 1.659, and 1.608 (cm^{-1}); thus when the X-ray beam goes through these tissues, it will have different levels of attenuation, as a result, it will produce a gray scale mammogram (X-ray image) that can distiguish the cancerous tissue from the normal tissue.

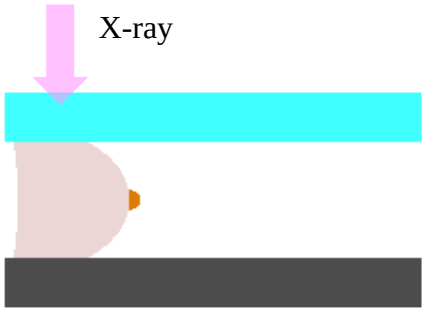

Figure 1. 10 Mammography

There are two kinds of mammography: screening mammography and diagnostic mammography. Screening mammography is used to find the previous breast abnormalities, which have not formed symptoms or signs that can be felt by women and their doctors. It aims to find the breast cancer at an early stage, possibly before it has spread. The American Cancer Society recommends women to start annual mammography when they are 40 years old. Normally, each breast is imaged in two directions, these are: head-to-foot (craniocaudal, CC) direction and angled side (mediolateral oblique, MLO) direction; however more directions may be needed for the breasts with implants or of large volumes. Diagnostic mammography is performed when a breast problem is found by physical examination or routine screening mammography. The precedure of diagnostic mammography takes longer than that of screening mammography, as it needs more pictures of the concerned area to evaluate the abnormality. The advantage of mammography is that it can detect breast cancers too small to be felt, hence it reduces the risk of dying from breast cancer; however it is not 100% effective. False negtives occur often and account for 20%. It is more often among younger women than among older women, as younger women always have more areas of fibrous and glandular tissue, which

make the small tumor hard to see. Thus mammographgy is not recommended for the women who are under the age 40 and have an average risk of breast cancer. Mammographgy requires exposing the breast to X-ray, which leads to concerns that the repeated low dose x-ray may increase the risk of breast cancer. Many studies suggest that the dose of radiation from mammography is small and the harm from mammography is minimal; the harm of mammography is out weighted by the benefits for the women who are 40 years old or more. However there is significant evidence that medical X-rays, including mammography, fluoroscopy and computed tomography (CT) scans, exert carcinogentic effects on the breast, especially for those exposed to ionizing radiation during childhood and adolescence (Ma et al., 2008, Gofman, 1999). Some researchers believe that the low energy X-ray provided by mammography causes greater damage to DNA than was predicted and the risk of breast cancer resulting from mammography was underestimated (Millikan et al., 2005, Heyes et al., 2009, Breast Cancer Fund, 2015).

1.3.2 Magnetic resonance imaging (MRI)

Breast MRI has developed rapidly in the last few decades and has become very important in breast cancer detection. It is considered more sensitive and accurate than the other breast cancer detection methods such as mammography, ultrasound, PET; however in practice, breast MRI acts as an adjunct to mammography rather than a replacement of mammography, as MRI has relatively higher false positives than mammography, which may lead to unneeded bioposies and other tests. Breast MRI requires injection of a contrast material, which contains a metal called gadolinium, into the vein in the arm during examination. Breast MRI is used in 2 situations: 1) if breast cancer is found by mammography or other methods, breast MRI is used to determine the location and the size of the tumor and look for any other tumors in either of the breasts; 2) For certain women with high risk of breast cancer, Breast MRI is used along with mammography as a routine examination (American Cancer Society, 2014c).

Breast MRI is based on the magnetic resonance phenomena, which is shown in Figure 1. 11. When the human body is placed in the MRI system, tissue magnetization is formed from the hydrogen nuclei with a single proton. Like a spinning top, the proton possesses spin about its axis, which makes it have two important intrinsic properties: rotating mass and magnetic moment. The spinning proton behaves like a small magnet, which has a north and a south magnetic pole, also known as a dipole. Normally, protons spin in a random way with different orientations of rotational axis (Figure 1. 11 a); however when an external magnetic field or electromagnetic wave is applied, they will arrange in a regular way: either with (up) or against (down) the external magnetic field (Figure 1. 11 b). When the field becomes stable, the difference of the energy of the two states depends on the strength of the applied magnetic field B_0 and the nucleus's magnetic dipole strength μ_0 (Hashemi et al., 2003, Hendrick, 2008, Weishaupt et al., 2003)

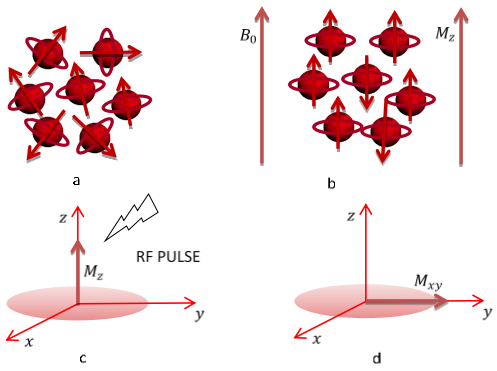

Figure 1. 11 Schematics of MRI

$$\Delta Eng = \mu_0 B_0 \qquad (1.7)$$

where ΔEng is the energy difference. The magnetic dipole strength of a proton is proportional to its charge q and spin $h/4\pi$ (h is Planck's constant, $h = 6.626 \times 10^{-34}$), and is inversely proportional to its mass m

$$\mu_0 = \frac{qh}{4\pi m} \quad (1.8)$$

Using an electromagnetic wave to supply energy, which is exactly equal to the energy difference, will cause the magnetic dipole moment of the nucleus to flip from its lower energy state to it higher energy state (Figure 1. 11 c). The frequency of the electromagnetic wave, which achieves this transition is the Larmor frequency and can be computed from the following equation:

$$\Delta Eng = h\nu_0 = h\frac{\omega_0}{2\pi} = \mu_0 B_0 \quad (1.9)$$

where ν_0 is the Larmor frequency in units of Hertz, ω_0 is the Larmor frequency in units of radians per second, $\omega_0 = 2\pi\nu_0$. Hence, the Larmor frequency can be written as

$$\omega_0 = \gamma B_0 \quad (1.10)$$

or

$$\nu_0 = \gamma B_0 / 2\pi \quad (1.11)$$

where $\gamma = 2\pi\mu_0/h$. Once the precise electromagnetic wave invades the stable field, the tissue magnetization will rotate out of the direction of the static magnetic field (also known as longitudinal direction) and into the plane perpendicular to B_0 (also known as the transverse plane), where is can be measured (Figure 1. 11 d).

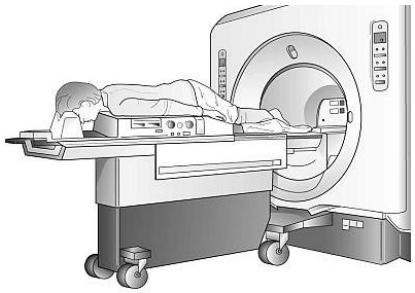

Figure 1. 12 Breast MRI (MedicalLook, 2015)

Figure 1. 12 shows the sketch of breast MRI examination. Compared with mammography, MRI is safer as it is radiation free. Breast MRI provides a high-contrast 3D image, which has a good performance on dense breast and can accurately present and locate the tumour. Breast MRI is valuable in detecting and staging breast cancer, especial when the other methods, such as mammography and ultrasound, failed to provide adequate information. However the process of generating an MRI scan is relatively long and often lasts for an hour. Before examination, patients will be required to remove anything made of metal, as metal object will interfere with the magnetic field of the MRI unit. If patients have metal parts in their body such as cochlear implant, cardiac defibrillators and pacemakers, they are not allowed to enter the MRI scanning area, as the magnetic field may cause movements of the metal object. During examination, patient needs to lie in a prone position inside a narrow tube, as shown in Figure 1. 12; thus claustrophobics are not suitable for breast MRI. The risk of MRI may be from the injected contrast material, which may cause an allergic reaction in some patients. Mothers who used the contrast medium should not breastfeed their babies for 48 hours (Radiological Society of North America Inc., 2015). Breast MRI is not used alone to diagnose breast cancer, as it has a relatively high ratio of false positives. A dedicated breast MRI is very expensive, so it is not available in most hospitals.

1.3.3 Breast ultrasound

Ultrasound is sound with its frequency beyond the detection ability of the human ear, which is above 20 kHz. However, the frequency of diagnosis ultrasound is far above this and in a range between 1 to 10 MHz. Ultrasound applied to medical imaging is divided to two main fields: one is to visualize the inner structure of human body by detecting the pulse-echo; the other is to determine the blood velocity by measuring the Doppler shift within a single-frequency ultrasound beam. Presently, these methods tend to be combined (Brown et al., 1999).

The pulse-echo technique is achieved in the following way. A pulse of ultrasonic energy is emitted from a transmitter and goes through human body. If the wave reaches the interface of different tissues, reflection, refraction and absorption will happen at the interface and the echo will be produced and detected by the receiver, therefore the distance, intensity and attenuation information can be obtained to analyse the tissues. The ultrasound frequency will be altered by reflection from a moving object. It obeys the Doppler Effect. This effect has been used to detect blood velocity by using a continuous transmitted beam of ultrasound.

Breast ultrasound is safe and painless. During examination, a gel is put on the skin of the breast and a small transducer (probe) is pressed against the breast and scans in a meandering and over lapping path. Breast ultrasound is not for routine examination and is not used alone, as it may miss the tumours, which can be found by mammography. It is less sensitive than MRI, but it is very valuable to use along with mammography. Some studies suggested that using ultrasound as an adjunct to mammography may be helpful to diagnose the cancer in dense breasts (American Cancer Society, 2014c, Berg et al., 2012). Breast ultrasound is considered valuable, as it can take a close look at some masses to judge if the mass is a cyst or a tumour.

1.3.4 Positron Emission Tomography (PET)

Positron Emission Tomography (PET) is a nuclear medical imaging technique, which visualizes the internal structures of the body as a 3D image. It is based on the decay of some short-lived substance. Certain isotopes emit positrons spontaneously. Subsequently, the positrons will combine with electrons to produce two photons at 511 keV in opposite directions. This radiation energy is captured by sensors to produce the image of internal structures of the human body. If one photon propagated a shorter

distance, the opposite one will propagate a longer distance, therefore the average signal level is the same, regardless of patients' attenuation and point of origin (Siedband, 2010). The isotopes decay, as an orbital electron is drawn to the nucleus and annihilated with a positive charge; alternatively, a positive charge escapes from the nucleus and after short travel, it combines with an external electron. The combination of negative and positive particles annihilate the charges and masses of each; simultaneously energy and momentum are generated in the form of two opposite-travelling 511 keV gamma rays (Brown, 1999), which is the source of image.

To conduct the scan, a kind of necessary biologically active molecule, such as glucose, protein, nucleic acids, fatty acids, with short-lived radioactive tracer isotope (usually it is F15 or C11) is injected into the living body, usually into the blood circulation. After a waiting period, during which the biologically active molecules accumulate in the tissue of interest, the patient can go to the imaging scanner. Normally, malignant tumour cells take features of more frequent glucose transportation and nucleotide expression, which leads to an increase of glucose transport. The glucose incorporated by the tracer isotope can go through the cell membrane freely. In the process of glycolysis, it will be phosphorylated, hence cannot go out of cells. If glycolysis increases in tumour cells, the tracer isotope marked glucose will concentrate in it, which indicates more nutrition absorption of tumour cell. PET will produce a reliable glucose metabolism image, from which the shape and location of a tumour can be clearly identified.

PET can distinguish a malignant tumour by characterizing the high metabolism of molecules in the cancer cells; however it is not accurate enough to be helpful (American Cancer Society, 2014c). PET is only used after the breast cancer is diagnosed for the purpose of determining whether the cancer has spread or weather the cancer has returned after treatment. The whole process of PET takes about 90 minutes. The radiation from PET is about the same amount as mammography; therefore people who are pregnant, breastfeeding or have claustrophobia or allergies to the injected dye are not suggested to

use PET (MedlinePlus, 2015). Breast PET scans are only available in a few centres, as they are very expensive and only can only be performed by specialists.

1.3.5 Electrical impedance mammography (EIM)

Electrical impedance mammography (EIM) is an under-developed, non-invasive medical imaging method for investigating the internal impedance (conductivity or/and permittivity) distribution of the breast. It is an application of electrical impedance tomography (EIT) technology in breast cancer detection. As biological tissues have distinguishable electrical properties, the impedance image of the internal breast will show weather a tumor is present or not. Normally the malignant tumor has much higher conductivity or/and permittivity than its surrounding tissue (Surowiec et al., 1988, Jossinet, 1996, Guofeng et al., 2012); thus an abnormally high conductivity or/and permittivity area in the resulting image may be an indicator of breast cancer.

During examination, a small amplitude current/voltage is applied to the surface of the breast, via a pair or several pairs of selected electrodes; simultaneously voltage/current measurements are collected on the skin surface, via the same or other electrodes. Subsequently, the measurements are sent to a computer to reconstruct the internal conductivity or/and permittivity of the breast. Clinically, before symptoms develop, cytological and histological changes have already occurred in cancerous tissue. These involve: changes in the cellular and extracellular contents, electrolyte balances, and cellular membrane properties, which produce significant electrical differences when compared with normal tissue. The changes of dielectric properties precede the appearance of a sizeable tumour, which enables EIM to detect breast cancer at an early and most treatable stage. EIM is non-invasive, painless, harmless, and relatively low-cost, which attracts more and more researchers to study its performance, but significant challenges remain and EIM needs to be fully tested in clinical trials.

1.4 Historical Reviews of EIM systems

1.4.1 T-scan ™

T-scan ™, also known as TransScan TS2000, is the earliest EIM system developed by an Israeli group in 1990 (Piperno et al., 1990). It is the only commercially available EIM system for breast cancer detection. TS2000 is a live time system, which comprises a metallic cylindrical electrode, a scan probe and a computer. The scan probe contains a planar electrode array, which has three different types, these are 1) small probe having an 8 by 8 pad array with a total footprint of 32 mm by 32mm, 2) big probe having a 16 by 16 pad array with a total footprint of 72 mm by 72mm, and 3) small probe having a 16 by 16 pad array with a total footprint of 32 mm by 32mm (Ammari et al., 2004). During examination, the patient lies on a bed with one hand holding the cylindrical electrode, through which a voltage of 1 to 2.5 V is applied. When the scanning probe with the ground potential is applied to the breast, current flows due to the voltage difference between the hand and the breast skin and flows out from the electrodes of the probe. Current is measured from the electrodes and sent to the computer to extract conductance and capacitance information of the breast. The computer displays two gray level images for each breast, in real time, which are conductance image and capacitance image. White spots in the images indicate the suspicious malignancy. In clinical trials, TS2000 demonstrated that it is sensitive and has the ability to detect a breast cancer minimum size of 3 mm in diameter; however it has limited abilities to detect the lesion near the nipple or deep in the breast (Melloul et al., 1999, Scholz and Anderson, 2000, Malich et al., 2001b, Malich et al., 2001a).

1.4.2 MEIK and MEM

MEIK is a 3D EIM system developed by a Moscow research group. It received an EC certificate in 2006 and had been approved for clinical usage in Russia. The MEIK

system is composed of two remote electrodes, a hand-held scan probe and a computer. The scan probe comprises a planar electrode array with 256 electrodes arranged in a round base with a square pattern. The diameter of the electrode plane is 12 cm. It is believed that compared with the rectangular arrangement, the round arrangement avoids the corner areas and increases the density of electrodes, which is helpful to improve the resolution (Cherepenin et al., 2002). MEIK is a signal frequency system. During examination, the two remote electrodes are attached to the arm of the patient, in which one electrode is connected with a safe alternating current source and the other one is connected with a potential difference detector. The scan probe is pressed against the breast, flattening it toward the chest to reduce the thickness of the breast and make sure that all the electrodes have good contact with the body (Cherepenin et al., 2001). A 0.5 mA current at 50 kHz is injected into the breast from each of the 256 electrodes, subsequently potential differences are measured by the other 255 electrodes; hence there are 32640 ($256 \times 255/2$) independent measurements in total. The 3D impedance of the breast is reconstructed from the 32640 measurements by using proper image reconstruction algorithms and visualized by several gray scale cross-sectional images at different depths. It is reported that the MEIK system can detect early breast cancer with a size of 3 to 5 mm; however it has difficulties to detect tumors close to the nipple (MACKAY LIFE SCIENCES, 2014, Ng et al., 2008, Hassan and El-Shenawee, 2011).

MEM, whose full name is Multi-frequency Electrical Impedance Mammograph, is the updated version of the single-frequency MEIK system. The operating frequency is from 10 kHz to 50 kHz. It retains the electrode arrangement and the examination method. According to the relative reports, comparing with the single frequency MEIK system, MEM can differentiate a cystic mastopathy from an acystic one and is effective in diagnostics of benign and malignant tumours of breast (Trokhanova et al., 2008, Impedance Medical Technologies Company, 2011).

1.4.3 Adaptive Current Tomography 4 (ACT4)

ACT4 was developed by the Rensselaer Polytechnic Institute research group for breast cancer detection. The ACT4 system is similar to mammography, which has two planar electrode arrays placed parallel to each other. During examination, the breast is pressed and flattened in between the electrode plates. The ACT4 system can support up to 72 electrodes, but in practice, it uses 30 electrodes in each planar electrode array, deployed in a rectangular 5×6 manner. Each electrode has an independent current source and voltage source connecting with a voltmeter and ammeter. The operating frequencies of the ACT4 system are from 300 Hz to 1MHz. The ACT4 system applies voltage sources of orthogonal patterns and measures both the applied voltages and the resulting currents through the electrodes (Kim et al., 2007, Saulnier et al., 2006). With these measurements, the conductivity and permittivity inside the breast are reconstructed. Then they use electrical impedance spectroscopy (EIS) plots and linear correlation measure (LCM) images to analyze the reconstructed result, in which EIS plots are curves with angular frequency times the reconstructed permittivity on the vertical axis versus the reconstructed conductivities on the horizontal axis at different frequencies. According to their report, the EIS plots of malignant tissue are highly correlated with straight lines; therefore they use gray scale LCM images to present the internal structure of the breast, in which a higher gray value indicates a higher correlation with a line, hence it is more likely a tumour. According to their studies, the ACT4 system can roughly localize tumours and clearly distinguish malignant tumours from normal tissues and benign lesions (Kao et al., 2008). However, as in mammography, pressing the breast during examination will cause pain or discomfort to patients. Also this system is not sensitive to the region in the middle of the electrode plates.

1.4.4 Electrical Impedance Tomography Spectroscopic (EITS)

The first generation Electrical Impedance Tomography Spectroscopic (EITS) system was developed by the Dartmouth group in 2000. It comprises a bed and a ring electrode array with 16 Ag/AgCl electrodes adjustable radially and vertically. There are 10 operating frequencies spanning from 10 kHz to 1MHz. During examination, a patient lies on the bed in a prone position, with a breast hanging in the circular electrode array. After the electrodes are well attached to the skin of the breast, current or voltage excitations, at selected frequencies, are simultaneously applied to the electrodes; subsequently the corresponding voltage or current measurements are obtained from the same electrodes. These measurements are used to reconstruct the 2D conductivity image and the permittivity image at the electrode plane. As the circular electrode array is moveable in the vertical (chest-to-nipple) direction, it can scan the breast at different depths to find the tumour (Hartov et al., 2000, Osterman et al., 2000). According to Kerner's report, 5 out of 6 patients with high suspicion of lesions are identified by EITS; the permittivity image provides more information than the conductivity image; using multi-frequency EIM is helpful to determine malignant tumours (Kerner et al., 2002).

The second generation EITS is a 3D EIM system, which has 64 electrodes fixed at four levels (each level has 16 electrodes arranged in a circle). The multiple rings of the electrodes are helpful to confirm the geometry of the breast, hence benefiting the accuracy of the boundary conditions (including the location of the electrodes and the shape of the breast). The new system extends the operating frequency up to 10 MHz in clinical trials. According to the report from the Dartmouth group, the performance of the updated system is significantly improved in accuracy, bandwidth and speed; the signal to noise ratio (SNR) is better than 80 dB at high frequencies, compared with the former system of 60-70 dB. 96 patients were studied base on this system. They concluded that the impedance spectra of the 96 women obtained from the 3D images are close to the reports in their literature. Further statistical analysis of these patients based on this system is still underway (Halter

et al., 2008). According to the clinical trials in Kerner and Halter's reports, the EITS system is sensitive to the tumour close to skin but less sensitive the tumour in the centre of the breast or off the electrode plane.

1.4.5 3D EIT system from Duke University

The Duke University research group developed a 3D EIM system using a funnel shape electrode array. 128 stainless steel electrodes are arranged at 7 levels on the internal surface of the funnel-shaped applicator with a height of 11.7 cm, a top diameter of 19.1 cm and a bottom diameter of 3.7 cm. During examinations, the funnel-shaped applicator is filled with a conductive fluid with a conductivity close to that of breast tissue; then the breast is immersed in the conductive fluid to get detection. Current excitations and voltage measurements are adopted in the system, with an operating frequency of 10 kHz. There are 128 driving events; for each excitation, there are 125 voltages measurements; therefore there are 16,000 voltage measurements in total (Gang et al., 2008). These measurements are used to reconstruct the 3D conductivity distribution of the field in the funnel-shaped applicator. Currently there is no clinical data available from the Duke University research group; however according to their experimental result, this system can detect 1) a conductive, cylindrical target with a diameter of 11 mm and a height of 50 mm, and 2) a resistive, spherical target with a diameter of 27 mm (Gang et al., 2006).

1.5 Challenges of EIM

The clinical trials of the EIM systems mentioned above demonstrate that using electrical impedance tomography technology to diagnose breast cancer is realizable; however most of the EIM systems are in the research and development stages and not yet commercialized as medical equipment for breast cancer detection. The challenges hindering the development of EIM include: detectability, repeatability, reliability,

accuracy and spatial resolution.

According to the results from clinical trials, many tumours are missed in the impedance (conductivity or/and permittivity) maps. This may be caused by the limited detectability of the EIM systems. The detectability of the EIM systems is determined by the numbers of electrodes, electrode arrangement, drive and measuring method, and the distance between the object of interest and the electrode array. Generally, a small number of electrodes will lead to a weak detectability of the system, as the information obtained from the surface of the field under investigation are via electrodes; conversely increasing the number of electrodes will provide more information of the field. The electrode geometric arrangement also affects the detectability, for example, the detectability of the ring electrode array and the planar electrode array is different: the ring electrode array is sensitive to the tumours in the periphery of the breast but less sensitive to those in the centre of the breast or/and off the electrode plane; however a planar electrode array is sensitive to the tumours in the front of the breast but less sensitive to those close to the chest wall. It is a common problem for all EIM systems that when the tumour is far from electrodes, it is hardly detected. Thus usually researchers will use a method to confine the breast in a relative sensitive region, which is close to the electrodes. Simulation studies are necessary to determine the electrode configuration including the electrode arrangement and the driving and measuring method.

The impedance (conductivity or/and) permittivity maps from a patient may not be repeatable in several examinations, which is directly related to the system noise and the ill-posed nature of the EIT inverse problem. For EIM systems, an arbitrary small perturbation of the measurements will lead to an arbitrary larger perturbation of the reconstructed impedance distribution. Normally EIM systems require a signal to noise ratio (SNR) better than 60 dB. The contact between the electrodes and the breast skin also introduces noise to measurements, which need be considered in system design or image reconstruction. Physiologically, the breast undergoes changes with menstrual cycles

under the influence of hormones. This will cause changes to the breast conductivity, which is another reason for lack of repeatability.

The reliability of EIM examinations is also relevant to noise. Noise in the measurements may cause abnormally high or low impedance (conductivity or/and permittivity) values in the reconstructed result. In the visualized impedance (conductivity or/and permittivity) maps, these present as isolated, abnormally light or dark spots. These artefacts are false positives which may lead to mistaken diagnosis.

The accuracy of the reconstructed impedance distribution of the breast depends on both hardware and software (the image reconstruction algorithms), but fundamentally, it is limited by the non-local property of impedance imaging. The non-local impedance imaging is the opposite of the local X-ray imaging. An X-ray beam travels in a straight line when passing through an object, so in the detection plane, the target object only affects the measurements locally in its projection. However current will spread when it enters into a conductive medium; a change of conductivity, caused by the target object, will have an effect on any surface measurement. So in practice, the reconstructed image of the object of interest is not exactly located at its real position and is not exactly the same as its real shape, instead it has projections and extensions. Although the non-local property limits the accuracy of the reconstructed image, a carefully designed EIM system with good image reconstruction algorithms will enhance the image accuracy and distinguish tumours from the surrounding normal tissue.

Most impedance (conductivity or/and permittivity) maps have poor resolution. The spatial resolution of EIM systems is determined by the electrode density, the distance away from the electrodes and the mesh used in image reconstruction. For a planer electrode array, the spatial resolution at the electrode plane is more or less equal to the distance between the adjacent electrodes (Hartov et al., 2005a); while the spatial resolution reduces as the distance from the electrode array increases. The size of the mesh

elements applied to the image reconstruction algorithm is a direct factor which influences the spatial resolution. A coarse mesh will reduce the spatial resolution; while a fine mesh is helpful to improve the spatial resolution; however a significantly fine mesh, whose elements are far smaller than the size that the system can distinguish, will result in greater ill-conditioning. There are some applications using small elements in the region near the electrodes and big elements in the region remote from the electrodes. For example, for the ring electrode array, it is very common to use the mesh with small elements on the periphery and big elements in the centre. This will lead to a non-uniform spatial resolution.

To modify EIM systems, the challenges described above need to be considered.

1.6 Methodology

This research investigates three EIM systems, which are: the Sussex MK4 system, the rotary planar electrode array EIM (RPEIM) system and the combined electrode array EIM (CEIM) system and the algorithms to solve the EIT (EIM) problem. The MK4 system was in a clinical trial, so the studies of the MK4 system are based on both simulations and real experiments. The RPEIM system and the CEIM system are newly designed systems, so the studies of both of the systems are based on simulations using close-to-realistic digital breast phantoms. All the three systems are 3D image reconstruction systems and use the operational method of current excitation and voltage measurement. The software of the systems are written in Matlab.

The EIT problem includes the EIT forward problem and the EIT inverse problem. The EIT forward problem is knowing the conductivity distribution of the field and the position of the surface current excitations to determine the surface voltage measurements; the EIT inverse problem is knowing the surface current excitations and the corresponding surface voltage measurements to determine the conductivity distribution of the field under

investigation. Both the EIT forward problem and the EIT inverse problem are solved by the finite element method (FEM), which means using a collection of a finite number of simplexes (tetrahedral elements) to approximate the 3D field. For the forward problem, the value of the simplexes/elements, which represent the conductivity at the local positions are known; for the inverse problem, the value of the simplexes/elements are chosen as the underdetermined parameters. The EIT inverse problem is very ill-conditioned, which means a small change of the voltage measurements will cause a big change of the solutions (the reconstructed conductivities), or the change of the surface measurements, which caused by a big change of the conductivity in the field, may not be detected at the required precision. To solve the ill-posed problem, Tikhonov regularization is employed.

The MK4 system is studied based on simulations, phantoms and clinical trials. Simulations are made to make analysis of the efficiency of the system configurations, which include the electrode arrangement and the data acquisition method (drive and measurement method) and study the accuracy, the sensitivity, and the detectability of the MK4 system. Phantoms are controllable and have known features, for example, the size, the position and the conductivity of the target object can be determined and changed during experiment, so they are very important for testing the MK4 system in real applications. Clinical trial is the last step to analyse the performance of the MK4 system. In clinical trials, the position and the boundary of the breast should be determined firstly from the reconstructed conductivity map, then the position of the tumour could be determined.

The RPEIM system and the CEIM system are under design and manufacture. Experimental data are currently unavailable. To make the study of the two systems close to clinical trials, close-to-realistic digital phantoms are used. These breast phantoms are composed of a skin envelope, a nipple, fat, ducts, acini, a gland area and a tumour, which are created using analytic geometry. Different components of the breast phantom are

assigned different conductivity values to differentiate different tissues. A 3D mesh is used to discretize the breast phantom. The values of the mesh elements are equal to the conductivity at their centres. The algorithm of the EIT forward problem is used to determine the surface voltage measurement. These measurements are simulated measurements for image reconstruction. Using the algorithm for the inverse problem, the reconstructed conductivity maps of the breast phantom can be obtained. Comparing the reconstructed results with the digital phantoms, we can analyse the performance of the RPEIM system and the CEIM system.

1.7 Research objectives and achievements

The purpose of this thesis is to propose solutions to tackle the challenges outlined in section 1.5.

Achievements include:

1) A comparison of two regularization methods (two image reconstruction algorithms: differential algorithm and logarithm algorithm).
2) A comparison of two planar electrode array: rectangular planar electrode array and hexagonal planar electrode array.
3) A new image reconstruction algorithm, which has a better accuracy and sensitivity than the former one and is proven valuable in clinical trials.
4) A design of a rotary planar electrode array EIM system, which gives a better performance in image accuracy, spatial resolution and noise tolerance (reliability) than the former MK4 system.
5) A design of a combined electrode array EIM system, which has a better detectability than the former MK4 system.
6) An image processing based error analysis method to assess EIM systems.
7) A method to build digital breast phantoms for simulated clinical trials

1.8 Thesis arrangement

Chapter 2 introduces the mathematical and physical basis of the EIT problems. It includes introductions to EIT theory, the EIT forward and the EIT inverse problem, the mathematical formulas of the EIT forward and inverse problem, introduction to the ill-posed problem and the solutions to the ill-posed problem.

In Chapter 3, the Sussex MK4 system, which is a dedicated 3D EIM system for breast cancer detection, is introduced. This chapter focuses on the novel hexagonal planar electrode array, the hexagonal data acquisition method and the image reconstruction algorithm of the MK4 system.

Chapter 4 introduces an enhanced image reconstruction algorithm, applied to the MK4 system. A comparison between the new algorithm and the former algorithm is made based on simulations, phantoms and real patients.

Chapter 5 presents a method to program close-to-realistic digital breast phantoms and provides a method to apply the digital breast phantoms to EIM systems.

Chapter 6 proposes a rotary planar electrode array EIM (RPEIM) system and demonstrates the improvements of the RPEIM system in image accuracy, spatial resolution and noise tolerance.

Chapter 7 introduces a combined electrode array EIM (CEIM) system including the operational modes and the advantage it provides in detecting a tumour deep in a big volume breast.

Chapter 8 discusses this thesis and concludes the contribution of this work.

Chapter 9 gives some suggestions for future work.

2. Mathematical and Physical Basis of EIT

This chapter introduces the mathematical and physical basis of the EIT problem. The EIT problem is based on the assumptions of a quasi stationary electromagnetic field and a passive field. The algorithms of the EIT forward problem and the EIT inverse problem are introduced in this chapter. The ill-posed nature of the EIT inverse problem is analysed. The EIT inverse problem is a non-linear problem. If the change of the conductivity is small, the EIT inverse problem can be solved using a linear approach. However in medical applications, the change of the conductivity is always large. To solve this problem, we need to use the iteration method, which is to repeat the process of computing the sensitivity matrix (Jacobin matrix) and solving the regular linear approximation. This chapter gives solutions to the EIT problems.

2.1 EIT Theory

Using mathematics, all the internal structures of an object can be characterized by model parameters. In this thesis, model parameters indicate the variables which are used to identify the matters of the object. For the EIT/EIM problem, the model parameter is conductivity. Normally, the model parameters are invisible; different values of the model parameter indicate different matters or substances. For example, water and air have different density values, so density can be used to distinguish water and air. The model parameters are difficult to measure directly; therefore in practice, people chose to measure the detectable parameters, which have some relationships with the model parameters, to infer the model parameters. For example, water density is an undetectable model parameter; nevertheless it can be obtained by measuring the mass and the volume of the water. In most cases, the relationship between the model parameters and detectable parameters is not linear, which can be written as:

$$\boldsymbol{d} = \hbar(\boldsymbol{m}) \qquad (2.1)$$

where $\boldsymbol{m}$ indicates the model parameters belonging to $\boldsymbol{\mathcal{M}}$ domain, $\boldsymbol{d}$ indicates the detectable parameter belonging to $\boldsymbol{\mathcal{D}}$ domain, $\hbar$ is the forward model which maps $\boldsymbol{\mathcal{M}}$ domain to $\boldsymbol{\mathcal{D}}$ domain. In a linear case

$$\boldsymbol{d} = \boldsymbol{Y}\boldsymbol{m} \qquad (2.2)$$

where $\boldsymbol{Y}$ is the forward solver. Given the model parameters $\boldsymbol{m}$ and the mapping relationship $\hbar$ to compute the detectable parameter $\boldsymbol{d}$ is the forward problem; given the detectable parameter $\boldsymbol{d}$ and the mapping relationship $\hbar$ to compute model parameters $\boldsymbol{m}$ is the inverse problem. In practice, because of the errors in measurements and modelling, it is nearly impossible to get an accurate solution of the inverse problem, which means it is very challenging to get an accurate solution of the following equation:

$$\hbar(\boldsymbol{m}) - \boldsymbol{d} = \boldsymbol{0} \qquad (2.3)$$

Therefore approximated solutions for inverse problems are generally acceptable. The EIT inverse problem is based on the mathematical theory above. The solution of the EIT inverse problem is an approximated estimation of the distribution of the conductivity distribution of the field under investigation. Practically, EIT systems inject currents into a human's body and measure the voltages on its surface to reconstruct the impedance (conductivity or/and permittivity) distribution, which is finally visualized by several cross-sectional images for people to read. The EIT problem is based on Maxwell's equations.

$$\begin{cases} \boldsymbol{\nabla} \times \boldsymbol{H} = \dfrac{\boldsymbol{\partial D}}{\boldsymbol{\partial t}} + \boldsymbol{J} \\ \boldsymbol{\nabla} \times \boldsymbol{E} = \dfrac{\boldsymbol{\partial B}}{\boldsymbol{\partial t}} \\ \boldsymbol{\nabla} \cdot \boldsymbol{D} = \rho \\ \boldsymbol{\nabla} \cdot \boldsymbol{B} = 0 \end{cases} \quad (2.4)$$

where $\boldsymbol{H}$ and $\boldsymbol{E}$ denote the magnetic field and the electric field respectively, $\boldsymbol{D}$ and $\boldsymbol{B}$ denote the fluxes-electric displacement and the magnetic flux respectively, $\boldsymbol{J}$ is the electric current density, ρ is the charge density. $\boldsymbol{\partial D/\partial t}$ is known as displacement current. Bold symbols indicate vectors. If the permittivity and permeability of the field are ε and μ',

$$\boldsymbol{B} = \mu' \boldsymbol{H} \quad (2.5)$$

$$\boldsymbol{D} = \varepsilon \boldsymbol{E} \quad (2.6)$$

The mathematic model of EIT is based on two assumptions: the assumption of a quasi stationary electromagnetic field, in which the displacement current is negligible; and the assumption of a passive field, which means there is no current source points and merged points in the field under investigation, therefore the divergence of the fluxes-electric displacement in this field is 0. Therefore Maxwell's equations can be written as:

$$\begin{cases} \boldsymbol{\nabla} \times \boldsymbol{H} = \boldsymbol{J} \\ \boldsymbol{\nabla} \times \boldsymbol{E} = \dfrac{\boldsymbol{\partial B}}{\boldsymbol{\partial t}} \\ \boldsymbol{\nabla} \cdot \boldsymbol{D} = 0 \\ \boldsymbol{\nabla} \cdot \boldsymbol{B} = 0 \end{cases} \quad (2.7)$$

It is known that

$$\boldsymbol{\nabla} \cdot \boldsymbol{\nabla} \times \boldsymbol{H} \equiv \boldsymbol{0} \quad (2.8)$$

therefore we have the following equation

$$\boldsymbol{\nabla} \cdot \boldsymbol{\nabla} \times \boldsymbol{H} = \boldsymbol{\nabla} \cdot \boldsymbol{J} = \mathbf{0} \quad (2.9)$$

In a conductive medium, according to Ohm's law,

$$\boldsymbol{J} = \sigma \boldsymbol{E} \quad (2.10)$$

where σ denotes the conductivity of the medium. The electric field $\boldsymbol{E}$ and the scalar potential $\emptyset$ satisfy the following relationship:

$$\boldsymbol{E} = -\nabla \emptyset \quad (2.11)$$

Substituting (2.10) and (2.11) into (2.9), we can get

$$\nabla \cdot \sigma \nabla \emptyset = 0 \quad (2.12)$$

Assume that the surface of the field is $\partial \Omega$; the current density on the surface/boundary is j, then we have

$$j = -\boldsymbol{J}\boldsymbol{n} = \sigma \nabla \emptyset \boldsymbol{n} \quad (2.13)$$

where $\boldsymbol{n}$ is the outward unit normal to $\partial\Omega$. Equation (2.12) and (2.13) express the relationship of the current density, conductivity distribution and potential distribution in the field.

2.2 EIT Forward Problem

For a closed 3D quasi-static field Ω with a smooth boundary $\partial\Omega$, given the conductivity distribution $\sigma(x,y,z)$, which is a function of the space coordinates, and the applied current on the boundary, to compute the surface voltage measurements is the EIT forward problem. If the scalar potential is $\emptyset(x,y,z)$, we have the following equations:

$$\begin{cases} \nabla\cdot\big(\sigma(x,y,z)\nabla\emptyset(x,y,z)\big)=0 & (x,y,z)\in\Omega \\ \sigma(x,y,z)\nabla\emptyset(x,y,z)\cdot\boldsymbol{n}=j(x,y,z) & (x,y,z)\in\partial\Omega \end{cases} \quad (2.14)$$

where $j(x,y,z)$ indicates the current density on the boundary

$$j(x,y,z)=\begin{cases} Q_l/|e_l| & (x,y,z)\in e_l, l=1,2,\cdots,L \\ 0 & (x,y,z)\in\partial\Omega,(x,y,z)\notin\bigcup_{l=1}^{L}e_l \end{cases} \quad (2.15)$$

where e_l denotes the *l*th electrode, $|e_l|$ denotes the area of e_l, Q_l denotes the current applied from e_l, L denotes the number of electrodes. A method generally used for solving the partial differential equations above is the variational approach, which constructs a functional and minimizes the functional to make it stationary. In an electric field, the functional is the energy equation

$$\mathcal{F}(\emptyset)=\frac{1}{2}\int_{\Omega}\sigma\nabla\emptyset^2 d\Omega+\int_{\partial\Omega}j\emptyset d\partial\Omega \quad (2.16)$$

To obtain $\emptyset$, which minimizes $\mathcal{F}(\emptyset)$, the finite element method (FEM) is adopted. Assuming that the field Ω is approximated by a collection of *K* simplex tetrahedral elements with *N* vertices, $\mathcal{F}(\emptyset)$ can be written as follows:

$$\mathcal{F}(\emptyset) = \sum_{k=1}^{K} \frac{1}{2} \int_{\Omega_k} \sigma^k \nabla \emptyset^2 d\Omega + \int_{\partial\Omega} j\emptyset d\partial\Omega \qquad (2.17)$$

where Ω_k denotes the field of the *k*th element, σ^k denotes the conductivity value of the *k*th element. Minimizing $\mathcal{F}(\emptyset)$, we can obtain the following equation:

$$\boldsymbol{Y}\emptyset = \boldsymbol{Q} \quad or \quad \emptyset = \boldsymbol{Y^{-1}Q} \qquad (2.18)$$

where $\boldsymbol{Y}$ is a sparse $N \times N$ matrix, which is determined by the vertex coordinates of the mesh and the conductivity values of the elements. In each element, the conductivity is taken to be constant. $\emptyset$ is the $N \times 1$ vector of the unknown nodal scalar potentials, $\boldsymbol{Q}$ is the $N \times 1$ vector of the known nodal current. For detailed method to get (2.18), please refer to Appendix I. For the point electrode model (PEM), if the current is applied through the electrode pair e_m and e_h,

$$Q_i = \begin{cases} C_{inj} & i = N_{e_m} \\ -C_{inj} & i = N_{e_h} \\ 0 & otherwise \end{cases} \qquad (2.19)$$

where Q_i is the *n*th element of $\boldsymbol{Q}$. N_{e_m} and N_{e_h} indicate the mesh node under e_m and e_h. C_{inj} is a scalar equal to the current amplitude. The voltage measurement between the *f*th electrode e_f and the *g*th electrode e_g is

$$V_{e_f e_g}^{e_m e_h} = \emptyset_{e_g}^{e_m e_h} - \emptyset_{e_f}^{e_m e_h} \qquad (2.20)$$

where $V_{e_f e_g}^{e_m e_h}$ indicates the voltage measurement between e_f and e_g with excitation applied between e_m and e_h, $\emptyset_{e_g}^{e_m e_h}$ and $\emptyset_{e_f}^{e_m e_h}$ indicate the potential at e_f and e_g under the current excitation from e_m and e_h. The reference potential is at N_{e_m} with 0

potential, $\emptyset_{e_m}^{e_m e_h} = \emptyset_{N_{e_m}}^{e_m e_h} = 0$.

2.3 EIT Inverse problem

The EIT inverse problem is an ill-posed problem, which requires solution/reconstruction of the conductivity distribution of the field under investigation, by using a modest number of surface measurements. According to Gauss's theorem, given a field Ω with a smooth boundary $\partial\Omega$, if $\boldsymbol{G}$ is a continuously differentiable vector field defined on a neighbourhood of Ω, then we have

$$\int_{\partial\Omega} \boldsymbol{G}\, d\partial\Omega = \int_{\Omega} \nabla \cdot \boldsymbol{G}\, d\Omega \qquad (2.21)$$

Let two arbitrary scalar functions $\emptyset$ and Ψ satisfy $\boldsymbol{G} = \emptyset\nabla\Psi$ and multiply σ on both sides of equation (2.21), we get the following equation:

$$\begin{aligned}\int_{\partial\Omega} \sigma\emptyset\nabla\Psi\, d\partial\Omega &= \int_{\Omega} \sigma\nabla\cdot(\emptyset\nabla\Psi)\, d\Omega = \int_{\Omega} \sigma(\nabla\emptyset.\nabla\Psi + \emptyset\nabla.\nabla\Psi)\, d\Omega \\ &= \int_{\Omega} \sigma\nabla\emptyset.\nabla\Psi\, d\Omega + \int_{\Omega} \emptyset\nabla\cdot(\sigma\nabla\Psi)\, d\Omega\end{aligned} \qquad (2.22)$$

Let Ψ be a solution of equation (2.12), so $\nabla\cdot(\sigma\nabla\Psi) = 0$, then we have the following equation:

$$\int_{\partial\Omega} \sigma\emptyset\nabla\Psi\, d\partial\Omega = \int_{\Omega} \sigma\nabla\emptyset\cdot\nabla\Psi\, d\Omega \qquad (2.23)$$

See Figure 2. 1. If there is a current I_Ψ applied to the field from electrode *a* and *b*, there

will be a potential formed on the boundary. $\sigma\nabla\Psi$ in (2.23) is current density; however except the current excitation electrodes, the current density on the boundary is 0; therefore equation (2.23) can be written as

$$\int_{\partial\Omega} \sigma\emptyset\nabla\Psi \, d\partial\Omega = I_\Psi(\emptyset_a - \emptyset_b) = I_\Psi\emptyset_{ab} \qquad (2.24)$$

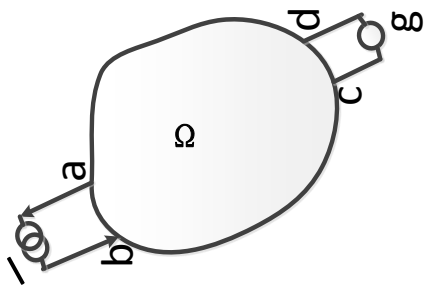

Figure 2. 1 Current injection and voltage measurement

Similarly, if current $I_\emptyset$ is applied from electrode *c,d*, and let $\emptyset$ be a solution of equation (2.12), then we have

$$\int_{\partial\Omega} \sigma\emptyset\nabla\Psi \, d\partial\Omega = I_\emptyset(\Psi_c - \Psi_d) = I_\emptyset\Psi_{cd} \qquad (2.25)$$

Assume $I_\emptyset = I_\Psi = 1$, then

$$V = \emptyset_{ab} = \Psi_{cd} = \int_\Omega \sigma\nabla\emptyset \cdot \nabla\Psi \, d\Omega \qquad (2.26)$$

According to the reciprocity theorem, if the voltage measurement V_{ab} is measured through electrode a and b with current excitation through electrode c and d and the

voltage measurement V_{cd} is measured through electrode c and d with current excitation through electrode a and b, then we have

$$V_{ab} = V_{cd} \tag{2.27}$$

Provided that the conductivity of the uniform field is σ_u and there is a small perturbation σ_p to the uniform field, the conductivity distribution becomes

$$\sigma = \sigma_u + \sigma_p \tag{2.28}$$

Similarly, the voltage measurements can be written as

$$V = V_u + V_p \tag{2.29}$$

where V_u are the voltage measurements of the uniform field, V_p are the change of the voltage measurements, when a perturbation is introduced into the uniform field. Let it be:

$$\begin{cases} \nabla\emptyset = \nabla\emptyset_u + \nabla\emptyset_p \\ \nabla\Psi = \nabla\Psi_u + \nabla\Psi_p \end{cases} \tag{2.30}$$

where u indicates the uniform field, p indicates the perturbation. Submitting (2.28) and (2.30) into (2.26), we obtain the following equation:

$$\begin{aligned} V = \int_{\Omega} \sigma\nabla\emptyset \cdot \nabla\Psi \, d\Omega &= \int_{\Omega} \left(\sigma_u + \sigma_p\right)\left(\nabla\emptyset_u + \nabla\emptyset_p\right)\left(\nabla\Psi_u + \nabla\Psi_p\right) d\Omega \\ &= \int_{\Omega} \sigma\nabla\emptyset_u \cdot \nabla\Psi_u \, d\Omega + \int_{\Omega} \sigma\nabla\emptyset_p \cdot \nabla\Psi_u \, d\Omega \\ &+ \int_{\Omega} \sigma\nabla\emptyset_u \cdot \nabla\Psi_p \, d\Omega + \int_{\Omega} \sigma\nabla\emptyset_p \cdot \nabla\Psi_p \, d\Omega \end{aligned} \tag{2.31}$$

where

$$\int_{\Omega} \sigma \nabla \emptyset_u \cdot \nabla \Psi_p \, d\Omega = -\int_{\Omega} \sigma_p \nabla \emptyset_u \cdot \nabla \Psi_u d\Omega \quad (2.32)$$

$$\int_{\Omega} \sigma \nabla \emptyset_p \cdot \nabla \Psi_u \, d\Omega = -\int_{\Omega} \sigma_p \nabla \emptyset_u \cdot \nabla \Psi_u d\Omega \quad (2.33)$$

$$\int_{\Omega} \sigma \nabla \emptyset_p \cdot \nabla \Psi_p \, d\Omega = -\int_{\Omega} \sigma_p \nabla \emptyset_u \cdot \nabla \Psi_p d\Omega \quad (2.34)$$

For details on (2.32)~(2.34), please refer to Appendix II. Substituting equation (2.32)~(2.34) to equation (2.31), we get the following equation:

$$\begin{aligned} V &= \int_{\Omega} \sigma \nabla \emptyset_u \cdot \nabla \Psi_u \, d\Omega - 2\int_{\Omega} \sigma_p \nabla \emptyset_u \cdot \nabla \Psi_u d\Omega - \int_{\Omega} \sigma_p \nabla \emptyset_u \cdot \nabla \Psi_p d\Omega \\ &= \int_{\Omega} \sigma_u \nabla \emptyset_u \cdot \nabla \Psi_u \, d\Omega - \int_{\Omega} \sigma_p \nabla \emptyset_u \cdot \nabla \left(\Psi_u + \Psi_p\right) d\Omega \end{aligned} \quad (2.35)$$

According to (2.26), $V_u = \int_{\Omega} \sigma_u \nabla \emptyset_u \cdot \nabla \Psi_u \, d\Omega$; therefore (2.35) becomes:

$$V_p = -\int_{\Omega} \sigma_p \nabla \emptyset_u \cdot \nabla \left(\Psi_u + \Psi_p\right) d\Omega \quad (2.36)$$

If the conductivity perturbation σ_p is small, so that $\Psi_p \ll \Psi_u$, the equation (2.36) can be written as:

$$V_p = -\int_{\Omega} \sigma_p \nabla \emptyset_u \cdot \nabla \Psi_u d\Omega \quad (2.37)$$

If the field is approximated by a finite number of elements and the conductivity of each element is a constant, equation (2.37) can be written as

$$V_p = S\sigma_p \quad or \quad \Delta V = S\Delta\sigma \tag{2.38}$$

where V_p and ΔV indicate the change of voltage measurements, σ_p and $\Delta\sigma$ indicate the change of conductivity distribution, S is the $M \times K$ sensitivity matrix, M is the number of the voltage measurements, K is the number of the elements of the mesh. The element of S in the *i*th row and the *j*th column is:

$$S^{ij} = \int_{jth\ element} \nabla\emptyset_u \cdot \nabla\Psi_u d\Omega \tag{2.39}$$

Submitting equation (I. 15) to (2.39), we get

$$S^{ij} = [\emptyset_{\boldsymbol{u}}]_j^T [\boldsymbol{B}]_{\boldsymbol{j}}^{\boldsymbol{T}} [\boldsymbol{B}]_{\boldsymbol{j}} [\Psi_{\boldsymbol{u}}]_{\boldsymbol{j}} \tag{2.40}$$

where $[\emptyset_{\boldsymbol{u}}]_{\boldsymbol{j}}$ and $[\Psi_{\boldsymbol{u}}]_{\boldsymbol{j}}$ indicate the nodal potential of the jth element under the excitation from $I_\emptyset$ and I_Ψ. The drive and measuring pattern will affect the sensitivity matrix and the reconstructed image. Equation (2.38) is only valid for the assumption that the conductivity perturbation σ_p (or the change of conductivity $\Delta\sigma$) is small, so that the change of the potential caused by the conductivity perturbation σ_p is ignored ($\Psi_p \ll \Psi_u$).

2.4 Ill-posed problem

Ill-posed problem, also known as ill-conditioned problem, is a problem that is not well-posed. The well-posed problem has the following properties: 1) a solution exists; 2) the solution is unique; 3) the solution's behaviour changes continuously with the initial

conditions. Most inverse problems are ill posed.

As mentioned in Section 2.1, due to the errors in measurements and modelling, it is nearly impossible to get an accurate solution for the inverse problem; therefore it is generally accepted to get approximate solutions using the least square method,

$$\boldsymbol{m_{ls}} = argmin_m \|h(\boldsymbol{m}) - \boldsymbol{d}\|^2 \qquad (2.41)$$

where $\boldsymbol{m}$ is the model parameter ($\boldsymbol{m} \in \boldsymbol{R}^{\mathcal{M}\times 1}$), $\boldsymbol{d}$ is the detectable parameter ($\boldsymbol{d} \in \boldsymbol{R}^{\mathcal{D}\times 1}$), $\arg min_m$ indicates the argument $\boldsymbol{m}$, which minimizes what follows, $\| \ \|^2$ indicates 2-norm, $\boldsymbol{m_{ls}}$ is the least square solution.

2.4.1 Linear problem

For a linear inverse problem, equation (2.41) can be written as

$$\boldsymbol{m_{ls}} = argmin_m \|\boldsymbol{Y}\boldsymbol{m} - \boldsymbol{d}\|^2 \qquad (2.42)$$

where $\boldsymbol{Y}$ is the forward solver, which maps the model parameter domain $\mathcal{M}$ to detectable parameter domain $\mathcal{D}$ ($\boldsymbol{Y}: \mathcal{M} \to \mathcal{D}$, $\boldsymbol{Y} \in \boldsymbol{R}^{\mathcal{D}\times\mathcal{M}}$). To get the solution, we need to use singular value decomposition (SVD). The SVD of $\boldsymbol{Y}$ is

$$\boldsymbol{Y} = \boldsymbol{U}\boldsymbol{\Sigma}\boldsymbol{W}^T = \sum_{i=1}^{q} \boldsymbol{u}_i \lambda_i \boldsymbol{w}_i^T \qquad (2.43)$$

where $\boldsymbol{U} = (\boldsymbol{u}_1, \boldsymbol{u}_2, \cdots, \boldsymbol{u}_D) \in \boldsymbol{R}^{\mathcal{D}\times\mathcal{D}}$, $\boldsymbol{W} = (\boldsymbol{w}_1, \boldsymbol{w}_2, \cdots, \boldsymbol{w}_M) \in \boldsymbol{R}^{\mathcal{M}\times\mathcal{M}}$ are orthogonal matrices, which are composed of singular vectors，vector $\boldsymbol{u}_i$ and $\boldsymbol{v}_i$ are left and right singular vectors,

$$\Sigma = \begin{cases} \begin{bmatrix} \lambda_1 & & & \\ & \lambda_2 & & \\ & & \ddots & \\ & & & \lambda_q \end{bmatrix} & \mathcal{M} = \mathcal{D} \\ \begin{bmatrix} \lambda_1 & & & \cdots & 0 \\ & \lambda_2 & & \cdots & 0 \\ & & \ddots & \cdots & 0 \\ & & \lambda_q & \cdots & 0 \end{bmatrix} & \mathcal{M} > \mathcal{D} \\ \begin{bmatrix} \lambda_1 & & & \\ & \lambda_2 & & \\ & & \ddots & \\ & & & \lambda_q \\ \vdots & \vdots & \vdots & \vdots \\ 0 & 0 & 0 & 0 \end{bmatrix} & \mathcal{M} < \mathcal{D} \end{cases} \quad (2.44)$$

Where $\Sigma \in \boldsymbol{R}^{\mathcal{D}\times\mathcal{M}}$, $q = \min(\mathcal{M}, \mathcal{D})$; $\{\lambda_1 \geq \lambda_2 \geq \cdots \geq \lambda_q \geq 0\}$, λ_i are singular values. The rank of the matrix $\boldsymbol{Y}$ is r. If $r < q$, the singular values $\{\lambda_{r+1}, \lambda_{r+2}, \cdots, \lambda_q\}$ are equal to 0 and the relative singular vectors $\{\boldsymbol{w}_{r+1}, \boldsymbol{w}_{r+2}, \cdots, \boldsymbol{w}_q\}$ belong to null space of $\mathcal{M}$. Given the SVD of $\boldsymbol{Y}$, the model parameters and the detectable parameters can be written as:

$$\boldsymbol{m} = \sum_{i=1}^{r} (\boldsymbol{w}_i^T \boldsymbol{m})\, \boldsymbol{w}_i \quad (2.45)$$

$$\boldsymbol{d} = \sum_{i=1}^{r} \lambda_i (\boldsymbol{w}_i^T \boldsymbol{m})\, \boldsymbol{u}_i \quad (2.46)$$

Equation (2.46) indicates that the high order singular values $\lambda_i \to 0$, will dampen $\boldsymbol{d}$ by reducing the contribution of $\boldsymbol{m}$ corresponding to the high order of singular vectors $\boldsymbol{v}_i$; therefore $\boldsymbol{d}$ contributed by the high order components of $\boldsymbol{m}$ is not reliable. Conversely in the inverse problem, the small singular values will lead to great errors in the reconstructed result, which may cover the valuable information from the low order

singular values, hence resulting in an unstable solution. In the inverse problem, the ill-condition is evaluated by the condition number in the following equation:

$$cond(\boldsymbol{Y}) = \frac{\lambda_1}{\lambda_q} \qquad (2.47)$$

The condition number is used to evaluate the sensitivity of a function to changes or errors in the input. For $\boldsymbol{Ym} = \boldsymbol{d}$, if the condition number $cond(\boldsymbol{Y})$ is large, even a small error in $\boldsymbol{d}$ will result in a large error in $\boldsymbol{m}$; however if the condition number is small, the error in $\boldsymbol{m}$ won't be much greater than the error in $\boldsymbol{d}$.

For a linear problem, if $\boldsymbol{Y}$ is full rank and $\mathcal{M} < \mathcal{D}$, $\boldsymbol{Ym} = \boldsymbol{d}$ has a unique least square solution, which is

$$\boldsymbol{m}_{LS} = \boldsymbol{Y}^{+}\boldsymbol{d} \qquad (2.48)$$

where $Y^{+} = (Y^{T}Y)^{-1}Y^{T}$ is the Moore-Penrose pseudoinverse of H,. Submitting (2.43) to (2.48), we have:

$$\boldsymbol{m}_{LS} = \sum_{i=1}^{r} \frac{\boldsymbol{u}_i^{T}\boldsymbol{d}}{\lambda_i}\boldsymbol{w}_i \qquad (2.49)$$

For the high order singular values, λ_i are very small, in other words, $1/\lambda_i$ are very large, therefore any noise in $\boldsymbol{d}$ will be greatly amplified and accumulate on $\boldsymbol{m}_{LS}$, thus the solution is very unstable.

2.4.2 Non-linear problem

For the nonlinear inverse problem, iteration is used to obtain the solution of (2.41). For the following function:

$$\mathcal{G}(\boldsymbol{m}) = \|h(\boldsymbol{m}) - \boldsymbol{d}\|^2 \qquad (2.50)$$

if m_n is the result of the *n*th iteration, $\mathcal{G}(m)$ can be approximated by the Taylor series at $\boldsymbol{m}_n$

$$\mathcal{G}(\boldsymbol{m}) = \mathcal{G}(\boldsymbol{m}_n) + \frac{\partial \mathcal{G}(\boldsymbol{m}_n)}{\partial \boldsymbol{m}}^T (\boldsymbol{m} - \boldsymbol{m}_n) + \frac{1}{2}(\boldsymbol{m} - \boldsymbol{m}_n)^T \frac{\partial^2 \mathcal{G}(\boldsymbol{m}_n)}{\partial^2 \boldsymbol{m}} (\boldsymbol{m} - \boldsymbol{m}_n) \qquad (2.51)$$

To obtain the solution $\boldsymbol{m}_{n+1}$, which minimizes $\mathcal{G}(\boldsymbol{m})$, it requires $\partial \mathcal{G}(\boldsymbol{m})/\partial \boldsymbol{m} = 0$; therefore we have the following equation:

$$\frac{\partial \mathcal{G}(\boldsymbol{m}_{n+1})}{\partial \boldsymbol{m}} = \left(\frac{\partial \mathcal{G}(\boldsymbol{m}_n)}{\partial \boldsymbol{m}}\right) + \frac{\partial^2 \mathcal{G}(\boldsymbol{m}_n)}{\partial^2 \boldsymbol{m}} (\boldsymbol{m}_{n+1} - \boldsymbol{m}_n) = 0 \qquad (2.52)$$

If $\frac{\partial^2 \mathcal{G}(\boldsymbol{m}_n)}{\partial^2 \boldsymbol{m}}$ is invertible,

$$\boldsymbol{m}_{n+1} = \boldsymbol{m}_n - \left(\frac{\partial^2 \mathcal{G}(\boldsymbol{m}_n)}{\partial^2 \boldsymbol{m}}\right)^{-1} \frac{\partial \mathcal{G}(\boldsymbol{m}_n)}{\partial \boldsymbol{m}} \qquad (2.53)$$

$\frac{\partial \mathcal{G}(\boldsymbol{m}_n)}{\partial \boldsymbol{m}}$ can be written as:

$$\frac{\partial \mathcal{G}(\boldsymbol{m}_n)}{\partial \boldsymbol{m}} = 2\left(\frac{\partial\big(h(\boldsymbol{m}_n)\big)}{\partial \boldsymbol{m}}\right)^T (h(\boldsymbol{m}_n) - \boldsymbol{d}) \tag{2.54}$$

$\frac{\partial^2 \mathcal{G}(\boldsymbol{m}_n)}{\partial^2 \boldsymbol{m}}$ can be written as

$$\frac{\partial^2 \mathcal{G}(\boldsymbol{m}_n)}{\partial^2 \boldsymbol{m}} = 2\left(\frac{\partial h(\boldsymbol{m}_n)}{\partial \boldsymbol{m}}\right)^T \left(\frac{\partial h(\boldsymbol{m}_n)}{\partial \boldsymbol{m}}\right) + 2\frac{\partial\left(\left(\frac{\partial h(\boldsymbol{m}_n)}{\partial \boldsymbol{m}}\right)^T\right)}{\partial \boldsymbol{m}}(h(\boldsymbol{m}_n) - \boldsymbol{d}) \tag{2.55}$$

where $\frac{\partial h(\boldsymbol{m}_n)}{\partial \boldsymbol{m}}$ is the Jacobian matrix. If the Jacobian matrix is denoted by $\boldsymbol{J}_n$ and we ignore the second order item in (2.55), (2.54) and (2.55) can be written as:

$$\frac{\partial \mathcal{G}(\boldsymbol{m}_n)}{\partial \boldsymbol{m}} = 2\boldsymbol{J}_n^T(h(\boldsymbol{m}_n) - \boldsymbol{d}) \tag{2.56}$$

$$\frac{\partial^2 \mathcal{G}(\boldsymbol{m}_n)}{\partial^2 \boldsymbol{m}} = 2\boldsymbol{J}_n^T\boldsymbol{J}_n \tag{2.57}$$

Substituting (2.56) and (2.57) into (2.53), we can get the Newton iteration formula:

$$\boldsymbol{m}_{n+1} = \boldsymbol{m}_n - (\boldsymbol{J}_n^T\boldsymbol{J}_n)^{-1}\boldsymbol{J}_n^T(h(\boldsymbol{m}_n) - \boldsymbol{d}) \tag{2.58}$$

or

$$\boldsymbol{m}_{n+1} = \boldsymbol{m}_n - \boldsymbol{J}_n^+(h(\boldsymbol{m}_n) - \boldsymbol{d}) \tag{2.59}$$

where $\boldsymbol{J}_n = \partial h(\boldsymbol{m}_n)/\partial \boldsymbol{m}$, $\boldsymbol{J}_n^+ = (\boldsymbol{J}_n^T\boldsymbol{J}_n)^{-1}\boldsymbol{J}_n^T$.

2.5 Regularizing EIT

Provided that the field under investigation is approximated by a collection of K simplex elements with N vertices, if the EIT inverse problem is simplified as a linear problem, according to (2.38) and (2.48), the change of conductivity distribution and the change of the voltage measurement satisfy the following equation:

$$\Delta\boldsymbol{\sigma} = \boldsymbol{S}^{+}\Delta\boldsymbol{V} \tag{2.60}$$

where: $\boldsymbol{S}^{+} = (\boldsymbol{S}^{T}\boldsymbol{S})^{-1}\boldsymbol{S}^{T}$, $\boldsymbol{S}$ is the $M \times K$ sensitivity matrix, M is the number of the voltage measurements, $\Delta\boldsymbol{\sigma}$ is the $K \times 1$ vector denoting the change of the conductivity distribution, $\Delta\boldsymbol{V}$ is the $M \times 1$ vector denoting the change of the voltage measurements. If the SVD of the sensitivity matrix is written as:

$$\boldsymbol{S} = \boldsymbol{U}\boldsymbol{\Sigma}\boldsymbol{W}^{T} = \sum_{i=1}^{q} \boldsymbol{u}_i \lambda_i \boldsymbol{w}_i^{T} \tag{2.61}$$

Equation (2.60) can be written as:

$$\Delta\boldsymbol{\sigma} = \boldsymbol{S}^{+}\Delta\boldsymbol{V} = \sum_{i=1}^{r} \frac{\boldsymbol{u}_i^{T}\Delta\boldsymbol{V}}{\lambda_i}\boldsymbol{w}_i \tag{2.62}$$

For the high order singular values $\lambda_i \to 0$, $1/\lambda_i \to \infty$; therefore even a small error in $\Delta\boldsymbol{V}$ will cause a very large error in $\Delta\boldsymbol{\sigma}$, which is very ill-conditioned. To solve the ill-posed problem, an additional constraint is needed to penalize the highly oscillatory conductivity.

Assume that the conductivity of the field under investigation $\boldsymbol{\sigma}$ and the computed surface measurements $\boldsymbol{V}'$ have the following relationship

$$\boldsymbol{V}' = h(\boldsymbol{\sigma}) \tag{2.63}$$

Then we need to seek the $\boldsymbol{\sigma}$ which satisfies the following equation

$$\boldsymbol{\sigma} = argmin_{\sigma}\|\boldsymbol{V} - h(\boldsymbol{\sigma})\|^2 + \alpha^2\left\|\boldsymbol{\sigma} - \boldsymbol{\sigma}_{ref}\right\|^2 \tag{2.64}$$

where $\boldsymbol{V}$ is the real measurement, $\boldsymbol{\sigma}_{ref}$ is the reference conductivity (for example, including some known features). The first item in the right hand side of equation (2.64) is the same as (2.41), which minimize the voltage error; the second item on the right hand side of equation (2.64) is a penalty for great changes of conductivities. Equation (2.64) is a trade-off between the accuracy of fitting voltage and the changes of conductivity. α is the regularization parameter, which controls the trade-off. Hence:

$$\mathcal{F}(\boldsymbol{\sigma}) = \mathcal{G}(\boldsymbol{\sigma}) + \alpha^2\left\|\boldsymbol{\sigma} - \boldsymbol{\sigma}_{ref}\right\|^2 = \|\boldsymbol{V} - h(\boldsymbol{\sigma})\|^2 + \alpha^2\left\|\boldsymbol{\sigma} - \boldsymbol{\sigma}_{ref}\right\|^2 \tag{2.65}$$

To obtain $\boldsymbol{\sigma}$ which minimizes $\mathcal{F}(\boldsymbol{\sigma})$, we need $\partial\mathcal{F}(\boldsymbol{\sigma})/\partial\boldsymbol{\sigma} = 0$. Provided that $\boldsymbol{\sigma}_0$ is an initial estimated conductivity ($\boldsymbol{\sigma}_0$ is not necessarily the same with $\boldsymbol{\sigma}_{ref}$), $\mathcal{G}(\boldsymbol{\sigma})$ can be approximate by the Taylor series at $\boldsymbol{\sigma}_0$

$$\begin{aligned}\mathcal{G}(\boldsymbol{\sigma}) = \mathcal{G}(\boldsymbol{\sigma}_0) + \frac{\partial\mathcal{G}(\boldsymbol{\sigma}_0)^T}{\partial\boldsymbol{\sigma}}(\boldsymbol{\sigma} - \boldsymbol{\sigma}_0) \\ + \frac{1}{2}(\boldsymbol{\sigma} - \boldsymbol{\sigma}_0)^T\frac{\partial^2\mathcal{G}(\boldsymbol{\sigma}_0)}{\partial^2\boldsymbol{\sigma}}(\boldsymbol{\sigma} - \boldsymbol{\sigma}_0)\end{aligned} \tag{2.66}$$

Therefore $\partial\mathcal{F}(\boldsymbol{\sigma})/\partial\boldsymbol{\sigma}$ can be written as follows:

$$\frac{\partial \mathbb{f}(\boldsymbol{\sigma})}{\partial \boldsymbol{\sigma}} = \frac{\partial \mathcal{G}(\boldsymbol{\sigma})}{\partial \boldsymbol{\sigma}} + 2\alpha^2 \boldsymbol{I}\left(\boldsymbol{\sigma} - \boldsymbol{\sigma}_{ref}\right)$$
$$= \left(\frac{\partial \mathcal{G}(\boldsymbol{\sigma}_0)}{\partial \boldsymbol{\sigma}}\right) + \frac{\partial^2 \mathcal{G}(\boldsymbol{\sigma}_0)}{\partial^2 \boldsymbol{\sigma}}(\boldsymbol{\sigma} - \boldsymbol{\sigma}_0)$$
$$+ 2\alpha^2 \boldsymbol{I}\left(\boldsymbol{\sigma} - \boldsymbol{\sigma}_{ref}\right) \quad (2.67)$$

where $\boldsymbol{I}$ is identity matrix. According to equation (2.56) and (2.57), equation (2.67) can be written as:

$$\frac{\partial \mathbb{f}(\boldsymbol{\sigma})}{\partial \boldsymbol{\sigma}} = -2\boldsymbol{J}^{\boldsymbol{T}}\left(\boldsymbol{V} - h(\boldsymbol{\sigma})\right) + 2\boldsymbol{J}^T\boldsymbol{J}(\boldsymbol{\sigma} - \boldsymbol{\sigma}_0) + 2\alpha^2\boldsymbol{I}\left(\boldsymbol{\sigma} - \boldsymbol{\sigma}_{ref}\right)$$
$$= -2\boldsymbol{J}^{\boldsymbol{T}}\left(\boldsymbol{V} - h(\boldsymbol{\sigma})\right) + 2\boldsymbol{J}^T\boldsymbol{J}(\boldsymbol{\sigma} - \boldsymbol{\sigma}_0)$$
$$+ 2\alpha^2\boldsymbol{I}\left(\boldsymbol{\sigma} - \boldsymbol{\sigma}_0 + \boldsymbol{\sigma}_0 - \boldsymbol{\sigma}_{ref}\right)$$
$$= -2\boldsymbol{J}^{\boldsymbol{T}}\left(\boldsymbol{V} - h(\boldsymbol{\sigma})\right) + 2(\boldsymbol{J}^T\boldsymbol{J} + \alpha^2\boldsymbol{I})(\boldsymbol{\sigma} - \boldsymbol{\sigma}_0)$$
$$+ 2\alpha^2\boldsymbol{I}\left(\boldsymbol{\sigma}_0 - \boldsymbol{\sigma}_{ref}\right) = 0 \quad (2.68)$$

If we let $\Delta\boldsymbol{V} = \boldsymbol{V} - h(\boldsymbol{\sigma})$, $\Delta\boldsymbol{\sigma} = \boldsymbol{\sigma} - \boldsymbol{\sigma}_0$, equation (2.68) can be written as follows

$$(\boldsymbol{J}^T\boldsymbol{J} + \alpha^2\boldsymbol{I})\Delta\boldsymbol{\sigma} = \boldsymbol{J}^T\Delta\boldsymbol{V} - \alpha^2\boldsymbol{I}\left(\boldsymbol{\sigma}_0 - \boldsymbol{\sigma}_{ref}\right) \quad (2.69)$$

Actually the Jacobian matrix is the sensitivity matrix of the EIT inverse problem $\boldsymbol{J} = \boldsymbol{S}$, therefore we have the following solution:

$$\begin{cases} \Delta\boldsymbol{\sigma} = (\boldsymbol{S}^T\boldsymbol{S} + \alpha^2\boldsymbol{I})^{-1}\left(\boldsymbol{S}^T\Delta\boldsymbol{V} - \alpha^2\boldsymbol{I}\left(\boldsymbol{\sigma}_0 - \boldsymbol{\sigma}_{ref}\right)\right) \\ \boldsymbol{\sigma} = \boldsymbol{\sigma}_0 + \Delta\boldsymbol{\sigma} \end{cases} \quad (2.70)$$

Substituting (2.61) into (2.70), we have

$$\Delta\boldsymbol{\sigma} = \sum_{i=1}^{r} \frac{\lambda_i^2}{\lambda_i^2 + \alpha^2} \frac{\boldsymbol{u}_i^T \Delta \boldsymbol{V}}{\lambda_i} \boldsymbol{w}_i - \sum_{i=1}^{r} \frac{\alpha^2}{\lambda_i^2 + \alpha^2} \boldsymbol{w}_i^T \left(\boldsymbol{\sigma}_0 - \boldsymbol{\sigma}_{ref}\right) \boldsymbol{w}_i \qquad (2.71)$$

There are two constraints in (2.71). The first item on the right hand side of the equation shows that if $\lambda_i \ll \alpha$, the item $\lambda_i^2/\lambda_i^2 + \alpha^2$ will converge to 0, thus compared with (2.62), there is a damping action of the high order singular values, which prevents the huge amplification of noise, and therefore guarantees the stability of the solutions. While if $\lambda_i \gg \alpha$, the item $\lambda_i^2/\lambda_i^2 + \alpha^2$ will converge to 1, which ensures that the information from low orders can be fully collected. The function of this item is to keep the solutions stable by reducing the influence from noise but it knows nothing about the conductivity. The second item on the RHS of (2.71) contains the conductivity information and it guarantees stable solutions by penalizing the changes, which makes the conductivity difference too large. Both of the items help to achieve stable solutions.

The linear approximation of the EIT problem is only valid for small deviations from the reference conductivity; however in medical applications, the differences between the real conductivity and the reference conductivity can be very large; therefore the non-linear problem needs to be solved by iteration, which repeats calculating the sensitivity matrix and the approximated conductivity. Assume that $\boldsymbol{\sigma}_n$ is the *n*th approximation of the conductivity distribution, then $\mathcal{G}(\boldsymbol{\sigma})$ can be approximated by the Taylor series at $\boldsymbol{\sigma}_n$:

$$\mathcal{G}(\boldsymbol{\sigma}) = \mathcal{G}(\boldsymbol{\sigma}_n) + \frac{\partial \mathcal{G}(\boldsymbol{\sigma}_n)}{\partial \boldsymbol{\sigma}} (\boldsymbol{\sigma} - \boldsymbol{\sigma}_n) + \frac{1}{2} (\boldsymbol{\sigma} - \boldsymbol{\sigma}_n)^T \frac{\partial^2 \mathcal{G}(\boldsymbol{\sigma}_0)}{\partial^2 \boldsymbol{\sigma}} (\boldsymbol{\sigma} - \boldsymbol{\sigma}_n) \qquad (2.72)$$

Therefore we have:

$$\frac{\partial \mathcal{F}(\boldsymbol{\sigma})}{\partial \boldsymbol{\sigma}} = \left(\frac{\partial \mathcal{G}(\boldsymbol{\sigma}_n)}{\partial \boldsymbol{\sigma}}\right)^T + (\boldsymbol{\sigma} - \boldsymbol{\sigma}_n)^T \frac{\partial^2 \mathcal{G}(\boldsymbol{\sigma}_n)}{\partial^2 \boldsymbol{\sigma}} + 2\alpha^2 \left(\boldsymbol{\sigma} - \boldsymbol{\sigma}_{ref}\right)^T \boldsymbol{I} \qquad (2.73)$$

Let $\boldsymbol{J}_n = \partial h(\boldsymbol{\sigma}_n)/\partial \boldsymbol{\sigma}$. If $\boldsymbol{\sigma_{n+1}}$ is the (*n+1*)th approximation which makes $\frac{\partial f(\boldsymbol{\sigma})}{\partial \boldsymbol{\sigma}} = 0$, then we have

$$(h(\boldsymbol{\sigma}_n) - \boldsymbol{V})^T \boldsymbol{J}_n + (\boldsymbol{\sigma}_{n+1} - \boldsymbol{\sigma}_n)^T \boldsymbol{J}_n^T \boldsymbol{J}_n + \alpha^2 \left(\boldsymbol{\sigma}_{n+1} - \boldsymbol{\sigma}_{ref}\right)^T \boldsymbol{I} = \boldsymbol{0} \qquad (2.74)$$

where $\boldsymbol{\sigma}_{n+1} - \boldsymbol{\sigma}_{ref}$ can be written as $\boldsymbol{\sigma}_{n+1} - \boldsymbol{\sigma}_n + \boldsymbol{\sigma}_n - \boldsymbol{\sigma}_{ref}$, $\boldsymbol{J}_n = \boldsymbol{S}_n$. If let $\Delta \boldsymbol{V} = \boldsymbol{V} - h(\boldsymbol{\sigma}_n)$, $\Delta \boldsymbol{\sigma} = \boldsymbol{\sigma}_{n+1} - \boldsymbol{\sigma}_n$, we can get the following solution:

$$\begin{cases} \Delta \boldsymbol{\sigma} = (\boldsymbol{S}_n^T \boldsymbol{S}_n + \alpha^2 \boldsymbol{I})^{-1} \left(\boldsymbol{S}_n^T \Delta \boldsymbol{V} - \alpha^2 \boldsymbol{I}\left(\boldsymbol{\sigma}_n - \boldsymbol{\sigma}_{ref}\right)\right) \\ \boldsymbol{\sigma_{n+1}} = \boldsymbol{\sigma}_n + \Delta \boldsymbol{\sigma} \end{cases} \qquad (2.75)$$

Equation (2.75) is the Newton-Raphson iteration formula.

2.6 L-curve method

The regularization parameter α controls the trade-off between fitting the data exactly and not making the derivatives of $\boldsymbol{\sigma}$ too large. Practically, if the value of α is too big, it will cause loss of the detailed information in the reconstructed result; however if the value of α is too small, it will lead to a noisy result; therefore α is a parameter, which needs to be optimized. For the EIT problem, we have equation: $\boldsymbol{S}\Delta \boldsymbol{\sigma} = \Delta \boldsymbol{V}$. Using Tikhonov regularization, we have the solution:

$$\Delta \boldsymbol{\sigma} = argmin\{\|\boldsymbol{S}\Delta \boldsymbol{\sigma} - \Delta \boldsymbol{V}\|^2 + \alpha^2 \|\Delta \boldsymbol{\sigma}\|^2\} \qquad (2.76)$$

According to (2.71), if the original guess $\boldsymbol{\sigma}_0$ is equal to the reference $\boldsymbol{\sigma}_{ref}$, we have

$$\begin{cases} \|\Delta\boldsymbol{\sigma}\|^2 = \sum_{i=1}^{r}\left(\frac{\lambda_i^2}{\lambda_i^2+\alpha^2}\frac{\boldsymbol{u}_i^T\Delta\boldsymbol{V}}{\lambda_i}\right)^2 \\ \|\boldsymbol{S}\Delta\boldsymbol{\sigma}-\Delta\boldsymbol{V}\|^2 = \sum_{i=1}^{r}\left(\frac{\alpha^2}{\lambda_i^2+\alpha^2}\boldsymbol{u}_i^T\Delta\boldsymbol{V}\right)^2 \end{cases} \quad (2.77)$$

where λ_i are singular values of the sensitivity matrix, α is the regularization parameter. We can find that $\|\Delta\boldsymbol{\sigma}\|^2$ and $\|\boldsymbol{S}\Delta\boldsymbol{\sigma}-\Delta\boldsymbol{V}\|^2$ are functions of α. L-curve is the log-log plot of $\|\Delta\boldsymbol{\sigma}\|^2$ and $\|\boldsymbol{S}\Delta\boldsymbol{\sigma}-\Delta\boldsymbol{V}\|^2$ at different α. The shape of the curve is like the letter 'L'; the optimized α could be chosen at the corner of the curve.

2.7 Conclusion

This chapter has introduced the mathematical basis of the EIT forward problem and the inverse problem. The forward problem is knowing the conductivity distribution of the field and the current excitations applied to its surface to compute the surface voltage measurements. The EIT inverse problem is knowing the applied current excitation and the corresponding voltage measurements to estimate the conductivity distribution of the filed under investigation. Both the forward problem and the inverse problem are based on the finite element method, which is discretizing the field under investigation by a collection of a finite number of elements and the values of the elements are constants denoting the conductivities at the corresponding positions. For the forward problem, the values of the elements are known; for the inverse problem, the values of the elements are the parameters, which need to be determined. The EIT inverse problem is very ill-posed, which means even a small error in the measurements will cause a big error in solution. For the ill-posed problem, only constricting the residual between the fitting result and the real measurements will result in unstable solutions. Therefore the Tikhonov regularization method is used to constrict both the residual of the fitting result and the norm of the solutions. It is a trade-off between fitting the data exactly and not making the derivatives

of the conductivity too large. The trade-off is controlled by the regularization parameter. For a small change of conductivity in the field, the EIT inverse problem can be taken as a linear problem; however in most medical cases, the difference between the real conductivity and the reference conductivity is large, therefore iterations are needed to make the estimated result approach the real field.

3. The Sussex MK4 System

The Sussex MK4 system is a dedicated 3D EIM system for breast cancer detection. It was started in 2010 and developed by the Sussex Biomedical Engineering Research Group. The clinical trials were performed in 'Oxford University Hospitals NHS Trust – John Radcliffe Cancer Centre'.

3.1 The development history of the Sussex MK4 system

The first, second, and third generation Mark (MK) systems, including MK1, MK2, MK3a and MK3b, were developed by the research group of De Montfort University, Leicester. The MK4 system is the fourth generation MK system, based on continuous research of more than 15 years.

The original EIM system MK1 was designed to detect breast cancer in vitro. It has a specialized impedance chamber with two pairs of electrodes, where freshly excised tissue are placed in the filled body-temperature saline. Current excitations are applied from a pair of electrodes with 31 different frequencies ranging from 1 kHz to 4 MHz. Complex impedance signals corresponding to these operating frequencies are obtained by using software (Tunstall et al., 1997, Brien, 2011). Tunstall and his colleagues reported 100 breast samples in 1997 based on the MK1 system. They found that the mean values of the conductivity in fat and the other tissue are 8 mV/mm and 1.5 mV/mm respectively. They also concluded that electrical impedance mammography could be further developed for 2D and 3D imaging.

In 1998, the second generation EIM system MK2 was built, which was designed as an electronic bra. It was the first attempt, in which the De Montfort group used EIM to detect breast cancer in vivo. The MK2 system has a ring electrode array with 32 electrodes

embedded in a cloth brassiere. During examination, the patient needed to wear the bra as a normal bra would be worn. Multiple frequencies with a range from 1 kHz to 1 MHz were used in the MK2 system, so that it gave the conductivity distributions of the breast at different operational frequencies (Wang et al., 1998, Brien, 2011). Due to the limitation of the ring electrode array, the MK2 system can only generate a 2D cross-sectional image in the electrode plane. The image reconstruction algorithm used in the MK2 system was a modified back-projection algorithm (Avis and Barber, 1995). The design of the MK2 system was novel and made the examination convenient, fast, and comfortable; however it failed to get any valuable results. The limitations of the MK2 systems are: 1) different breast volumes require different sizes of bra; 2) the electrodes could not be well attached to the skin of the breast, hence introducing a significant number of errors to the measurements (SZE, 2012).

The third generation EIM system MK3 started in 2006, in which the De Montfort group firstly employed a tank and a bed in examination. During examination, the patient could lie on the bed with a breast in the saline filled tank. This design could accommodate different breast volumes and solve the contact problem, which existed in the former MK2 system. The scanner head of the MK3a system presents a ‘bowl’ shape with electrodes arranged at 3 levels. The MK3b system replaced the bowl-shape scanner by an adjustable planar electrode array with electrodes slightly recessed from the surface. The MK3b system is the prototype of the MK4 system; however it failed to enter clinical trials as it didn’t meet the safety standards required for medical instruments.

3.2 Overview of the Sussex MK4 System

The MK4 system is the latest MK system, which is developed in the University of Sussex, in 2010. The appearance of the MK4 system is a bed with a tank in the appropriate position to contain the breast, which is shown is Figure 3. 1. In the bed, it has a saline

pumping system, a saline warming system, an electrode adjustment system, a data acquisition system, a safety and emergency system, a cleaning system, and two power systems. The MK4 system is a multiple-frequency system with operating frequencies at 10 kHz, 20 kHz, 50 kHz, 100 kHz, 200 kHz, 500 kHz, 1 MHz, 2 MHz, 5 MHz.

Figure 3. 1 The Sussex MK4 system (left) and the data acquisition tank (right)

To perform an examination, a patient will lie on the bed with a breast in the tank. The saline pumping system will work first to pump the fresh saline into the tank. When the saline overflows, the overflow sensor will trigger the command to stop the pumping system. As the conductivity of the saline changes, as the temperature changes, a warming system is necessary to keep the saline at the body temperature to make the patient comfortable and maintain the conductivity of the saline. The temperature of the saline is monitored by a temperature sensor and fed back to the warming system to achieve a constant temperature environment. The conductivity of the saline in use is about 0.05 S/m, which is close to the conductivity of the breast adipose tissue (Jossinet and Schmitt, 1999). At the bottom of the tank, there is a planar electrode array, through which current excitations are applied and voltage measurements are collected, as shown in Figure 3. 1 (right). The cylindrical tank is 18 cm in diameter and has a maximum depth of 5 cm; therefore it can accommodate breasts up to 1250 ml in volume, covering 90% of female breasts. Under the control of the electrode adjustment system, the planar electrode array moves in the vertical direction to adapt to different sizes of breast. During examination, the breast is gently pressed by the planar electrode array into the chest wall to reduce its

thickness, so that the whole breast can be within a relatively sensitive area of the planar electrode array. The safety and emergency system will work once disorder occurs. For example, the safety system will cut the power supply if a short circuit happens; the emergency system will permit manual operation, when the saline pumping system or the electrode adjustment system stops working. After examination, the cleaning system will empty, disinfectant, and rinse the tank, and dispose of the waste saline. The MK4 system is powered by two systems: one power supply is from a battery and serves for the data acquisition system to provide a stable, less-noisy source, the other one is from an external supply and serves the other systems, such as the saline systems and the electrode adjustment system.

3.3 The data acquisition system of the Sussex MK4 system

The data acquisition system (DAS) is the core of the MK4 system, which obtains information from the patients. The sensor or scanner head of the data acquisition system is the planar electrode array. The planar electrode array is made up by 85 stainless steel electrodes organized in a hexagonal pattern. They are 2.5 mm in diameter and spaced at intervals of 17 mm. The electrodes are not in the same plane as the base plate, but are a little recessed to a depth of approximately 2 mm. The recessed electrodes and the saline form a conductive interface between the electrodes and the breast skin, which provides a stable contact surface and reduces the contact impedance. It is known that the saline-electrode polarization impedance is only approximately 1/500 of the skin-electrode impedance at low frequency (Grimnes, 1983, Ragheb and Geddes, 1991), this approach will minimize the error caused by the contact impedance.

An important innovative characteristic of this clinical instrument is the hexagonal planar electrode design and data acquisition method. In data acquisition, electrodes are selected in hexagonal sub-patterns, which is shown in Figure 3. 2. At angles of 0°, 120°

and 240°, there are five electrodes in each direction in each sub-pattern, together these define a hexagonal measurement area. In each hexagonal measurement area, there are a maximum of three current excitation events and each current excitation is applied from the two opposite electrodes on the boundary of the hexagon; the voltage measurements are collected between adjacent electrodes in a rapid pair-wise sequence, parallel to the electric field, within the hexagon. Please refer to Figure 3. 2.

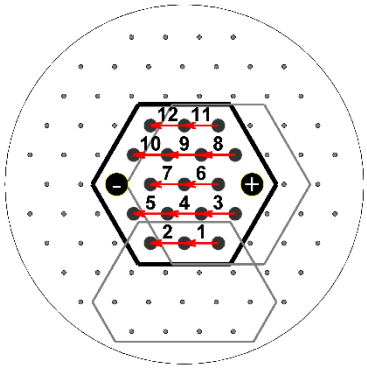

Figure 3. 2. Electrode drive and receive hexagon. The big dots with '+' and '-' indicate the drive pair. The middle sized dots connected by arrows indicate that measuring pair. The other small dots indicate the electrodes, which do not participate in measurement. The regions surrounded by a bold line and fine lines indicate 3 different measurement areas

In a complete hexagonal measurement area, there are three current excitations in the 0°, 120°, and 240° directions respectively and each current excitation corresponds to 12 voltage measurement pairs, therefore there are 3×12 = 36 independent measurements in total, in each complete hexagonal measurement area, which is shown in Figure 3. 2 and Figure 3. 3. However, in an asymmetric hexagonal measurement area, the number of current excitations and voltage measurements are less than the values above. For example, in Figure 3. 4, there is only one current excitation in the 0° direction, which corresponds to 9 independent measurements, thus there are only 9 independent measurements in total, in this asymmetric hexagon. According to the design, there are 123 drive pairs corresponding to 1416 independent measurements in total. In this data acquisition method, small hexagonal measurement areas scan the whole field and only the strongest

measurements in the corresponding hexagonal measurement areas are collected, these will guarantee a high SNR for the MK4 system.

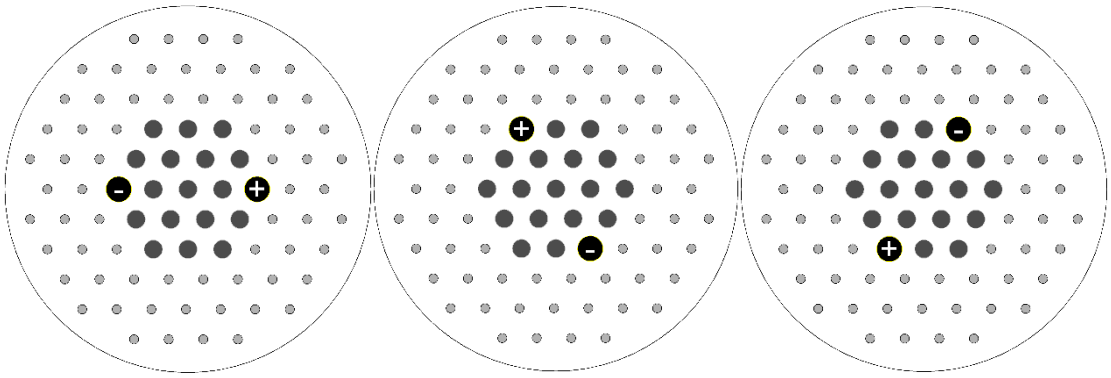

Figure 3. 3 Three current excitations in a complete hexagon measurement area. The big dots with '+' and '-' indicate the drive pairs. The middle sized dots indicate the measuring electrodes. The small dots indicate the electrodes, which do not participate in measurement.

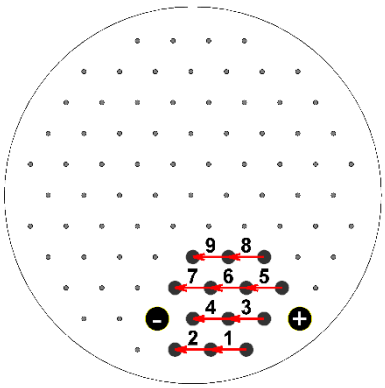

Figure 3. 4 An asymmetric hexagonal measurement area

The advantage of this data acquisition method is gaining the strongest measurements for each excitation to guarantee a much smaller dynamic range (DYR) between the maximum and the minimum measurements in each excitation. Compared with the traditional large-DYR DAS system in EIT, which collects voltage measurements from all the electrodes, it has achieved a much better overall SNR. A simulation is made to investigate the relationship between the number of measurements for each excitation and the SNR based on the MK4 system. Please see Figure 3. 5. We name the 12 measurements within the hexagonal measurement area as the inner measurements (IMs) (Figure 3. 5 left)

and the 14 additional measurements outside the hexagonal measurement area as the outer measurements (OMs) (Figure 3. 5 right). Figure 3. 6 displays the total 26 measurements shown in Figure 3. 5, which are simulated for a 4.5 cm height of saline with a conductivity of 0.05 S/m in the tank. It shows that the DYR of the IMs is about 10 times smaller than that of all the 26 measurements including both the IMs and the OMs. Therefore for a 60dB SNR DAS system, the IMs based MK4 data acquisition method has successfully avoided the additional 20dB SNR lost compared with the IMs and OMs based data acquisition method, for a fixed system.

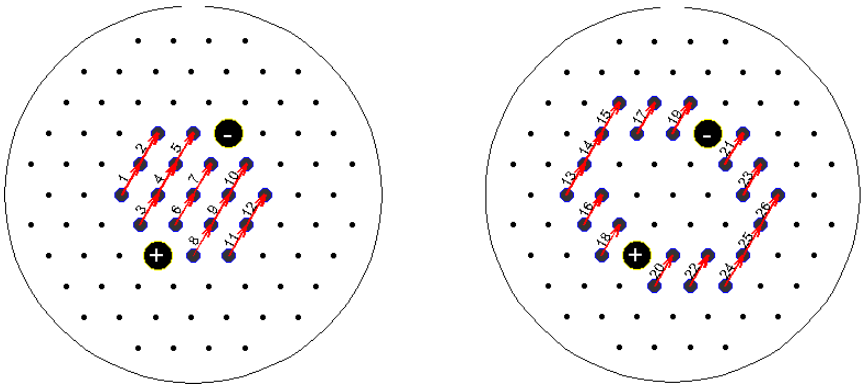

Figure 3. 5. Measurement pairs: the left diagram shows the measurements within the hexagonal measurement (IMs) area, the right diagram shows the measurements outside the hexagonal measurement (OMs) area.

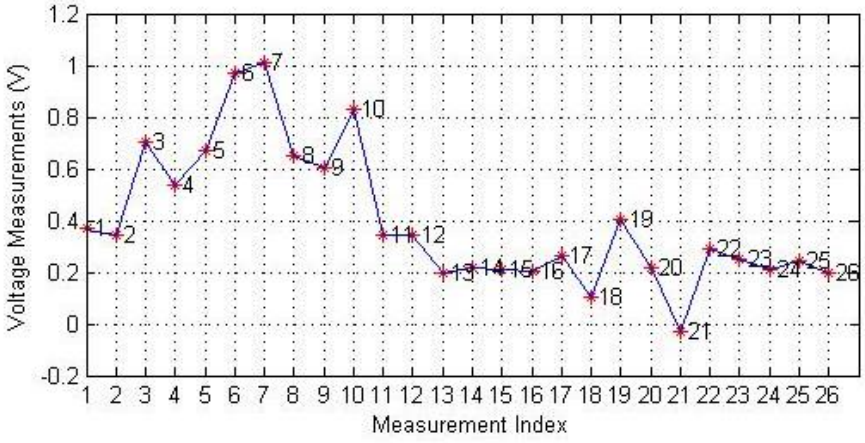

Figure 3. 6 The voltage measurements corresponding to Figure 3. 5

In this design, each current excitation corresponds to a hexagonal measurement area.

The hexagonal measurement areas overlap with each other therefore avoiding blind regions in the measurements. This hexagonal electrode arrangement and novel data acquisition method maximizes the number of independent measurements with good SNR. The spatial resolution is related to the electrode density and the distance away from the electrode plane. The spatial resolution in the electrodes contact plane is equal to the distance between the adjacent electrodes (Hartov et al., 2005b); while the spatial resolution reduces as the plane moves away from the electrode plane. In the Sussex MK4 system, the electrode distance is 17mm. In practice, an object of 10 mm to 17 mm in length can be detected and an object greater than 34 mm can be imaged well.

3.4 The forward problem of the Sussex MK4 system

For the EIT forward problem, given the conductivity distribution, the 3D mesh and the amplitude and the coordinates of the current excitation, the 3D nodal potentials can be computed using (2.18). Thereupon the surface voltage measurements $\boldsymbol{V}$ (using (2.20)) and the 3D electric field E ($E = -\nabla\emptyset$) can be obtained. These are helpful to analyse the sensitivity of the planar electrode array. For the MK4 system, an object placed at different depths in the tank will result in significant differences in the voltage measurements and electric fields. Define parameters as follows: V_{Bg} and E_{Bg} denote the simulated voltage measurements and electric field of the background field, which is usually a uniform field; V_{Obj} and E_{Obj} denote the simulated voltage measurements and electric field with an object placed in the background field; $\Delta V = V_{Obj} - V_{Bg}$ and $\Delta E = E_{Obj} - E_{Bg}$ denote the difference before and after placing the object in the background field.

Figure 3. 7 presents the models with an object placed in the bottom and the top of the tank respectively. The object is a rectangular parallelepiped in the centre of the cylindrical tank with length equal to 2.55 cm, width equal to 1.47 cm, height equal to 0.9

cm, and conductivity equal to 0.03 S/m. A current excitation is applied from (3.4, 0, 0) (cm) and (-0.34, 0, 0), the dots in Figure 3. 7. The height of the tank is 4.5 cm. The background conductivity is 0.05 S/m. The simulated measurement differences ΔV corresponding to the two models are displayed in Figure 3. 8. As mentioned before, the MK4 system has 123 current excitation events corresponding to 1416 measurements. Figure 3. 8 displays the changes of the 1416 voltage measurements made by the object at the bottom and the top position. The scale of ΔV in the left diagram is about 40 times larger than that in the right diagram, which indicates that the MK4 system is more sensitive to the object closer to the planar electrode array. Figure 3. 9 and Figure 3. 10 show the changes of the electric field ΔE, when the object is placed in the bottom and the top of the tank. Please note that ΔE is a 3D matrix corresponding to the current excitation (only one excitation) shown in Figure 3. 7. The difference of the electric field at the detection plane in Figure 3. 10(c) is much weaker than that in Figure 3. 9(c), which also illustrates the limitation of the planar electrodes in detecting remote objects.

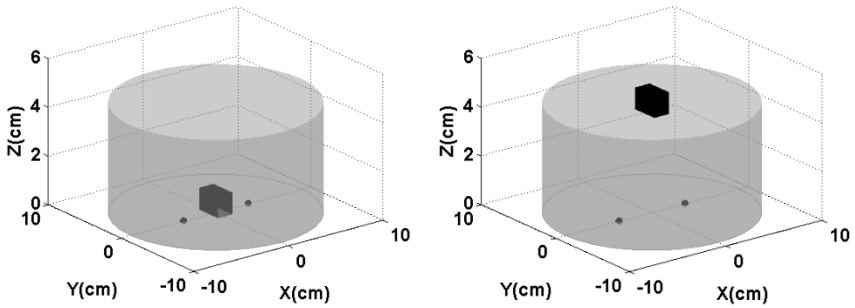

Figure 3. 7 Model 1: a rectangular parallelepiped object in the bottom (left) and the top (right) of the tank. The two dots indicate the drive pair.

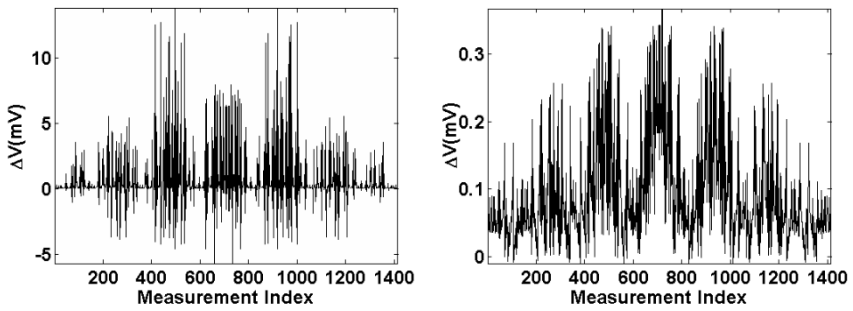

Figure 3. 8 The measurement differences of the uniform field and the field with an object. The left diagram

corresponds to the left model in Figure 3. 7; the right diagram corresponds to the right model in Figure 3. 7.

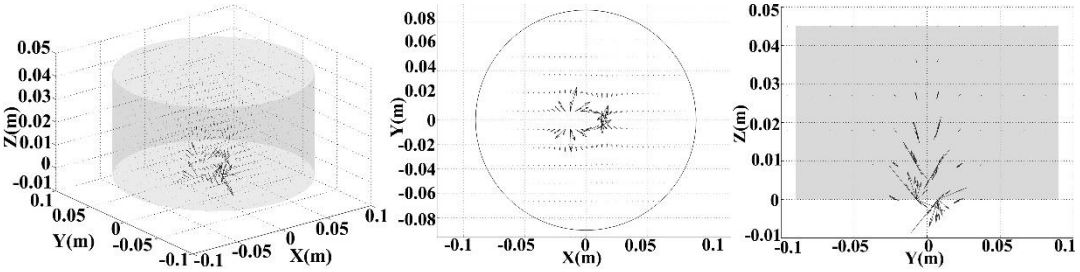

Figure 3. 9. Difference of the electric field intensity of the left model in Figure 3. 7. (a) is the 3D view. (b) is the XY view. (c) is the XZ view

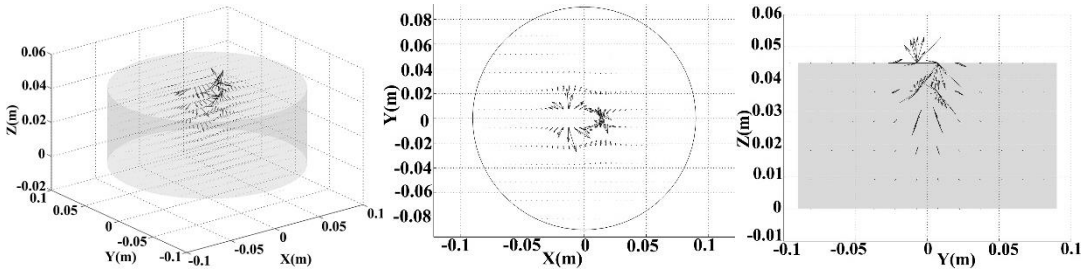

(a) (b) (c)

Figure 3. 10. Difference of the electric field intensity of the right model in Figure 3. 7. (a) is the 3D view. (b) is the XY view. (c) is the XZ view

3.5 The image reconstruction algorithm of the Sussex MK4 system

The image reconstruction algorithm of the Sussex MK4 system inherits the idea from the Sheffield group, using the logarithm of the voltage ratio instead of the differences to reconstruct the conductivity distribution in the tank. The relationship between the conductivity distribution and the voltage measurements are as follows

$$\begin{cases} \Delta \ln \boldsymbol{V} = \ln \boldsymbol{V} - \ln \boldsymbol{V}_0 = \boldsymbol{F}(\ln \boldsymbol{\sigma} - \ln \boldsymbol{\sigma}_0) = \boldsymbol{F}\,\Delta \ln \boldsymbol{\sigma} \\ \boldsymbol{\sigma} = \boldsymbol{\sigma_0} e^{\Delta \ln \boldsymbol{\sigma}} \end{cases} \quad (3.1)$$

where $\boldsymbol{\sigma}_0$ is $K \times 1$ vector indicating the initial conductivity estimate, $\boldsymbol{V}_0 = h(\boldsymbol{\sigma}_0)$, $\Delta \ln \boldsymbol{V}$ is the $M \times 1$ vector indicating the logarithm of the voltage ratios between the real measurements $\boldsymbol{V}$ and the predicted measurements $\boldsymbol{V}_0$. If the *i*th elements of $\boldsymbol{V}$ and $\boldsymbol{V}_0$ are

V^i and V_0^i, the *i*th element of $\Delta \boldsymbol{ln}\boldsymbol{V}$ is $\Delta\ln V^i = \ln\left(V^i/V_{ref}^i\right)$. Similarly $\Delta\ln\boldsymbol{\sigma}$ is the $K \times 1$ vector indicating the logarithm of the conductivity ratios between the real conductivity values and the estimated conductivity values, $\Delta\ln\sigma^i = \ln\left(\sigma^i/\sigma_0^i\right)$. $\boldsymbol{F}$ is the $\mathrm{M} \times K$ sensitivity matrix for the Sheffield algorithm. The element of $\boldsymbol{F}$ can be written as:

$$F^{ij} = \frac{\partial \ln V^j}{\partial \ln \sigma^i} = \frac{\partial \ln V^j}{\partial V^j}\frac{\partial V^j}{\partial \sigma^i}\frac{\partial \sigma^i}{\partial \ln \sigma^i} = \frac{1}{V^j}S^{ij}\sigma^i \qquad (3.2)$$

where S^{ij} is the element of the sensitivity matrix *S* for the delta algorithm (2.38) and can be computed by (2.40). V^j indicates the *j*th voltage measurement. σ^i indicates the conductivity value of the *i*th mesh element. $\boldsymbol{F}$ is a function of $\boldsymbol{\sigma}$**.** If $\boldsymbol{\sigma}$ changes, $\boldsymbol{F}$ changes; therefore equation (3.1) is valid for the assumption that the changes of the conductivity are small, so that the changes of $\boldsymbol{F}$ caused by the changes of the conductivity can be ignored.

Using Tikhonov Regularisation, we obtain the solution of (3.1) as:

$$\begin{cases} \Delta \ln \boldsymbol{\sigma} = (\boldsymbol{F}^T\boldsymbol{F} + \alpha^2\boldsymbol{I})^{-1}\left(\boldsymbol{F}^T\Delta\ln\boldsymbol{V} - \alpha^2\boldsymbol{I}\left(\ln \boldsymbol{\sigma}_0 - \ln \boldsymbol{\sigma}_{ref}\right)\right) \\ \boldsymbol{\sigma} = \boldsymbol{\sigma}_0 e^{\Delta \ln \boldsymbol{\sigma}} \end{cases} \qquad (3.3)$$

where $\Delta\ln\boldsymbol{V} = \ln\boldsymbol{V} - \ln\boldsymbol{V}_0$, $\boldsymbol{\sigma}_0$ the initial conductivity estimate, $\boldsymbol{\sigma}_{ref}$ is the reference conductivity, which may include some known features of the field, $\boldsymbol{\sigma}_0$ and $\boldsymbol{\sigma}_{ref}$ are not necessarily the same,**.** If $\boldsymbol{\sigma}_0 = \boldsymbol{\sigma}_{ref}$, Equation (3.3) can be written as:

$$\begin{cases} \Delta \ln \boldsymbol{\sigma} = (\boldsymbol{F}^T\boldsymbol{F} + \alpha^2\boldsymbol{I})^{-1}\boldsymbol{F}^T\Delta\ln\boldsymbol{V} \\ \boldsymbol{\sigma} = \boldsymbol{\sigma}_0 e^{\Delta \ln \boldsymbol{\sigma}} \end{cases} \qquad (3.4)$$

For iteration formula, we have:

$$\begin{cases} \Delta \ln \boldsymbol{\sigma} = (\boldsymbol{F}_n^T \boldsymbol{F}_n + \alpha^2 \boldsymbol{I})^{-1} \left(\boldsymbol{F_n} \Delta \ln \boldsymbol{V} - \alpha^2 \boldsymbol{I} \left(\ln \boldsymbol{\sigma}_n - \ln \boldsymbol{\sigma}_{ref} \right) \right) \\ \boldsymbol{\sigma}_{n+1} = \boldsymbol{\sigma}_{\mathrm{n}} e^{\Delta \ln \boldsymbol{\sigma}} \end{cases} \quad (3.5)$$

where $\boldsymbol{\sigma}_n$ is the *n*th estimated conductivity matrix, $\boldsymbol{F_n}$ is the updated sensitivity matrix corresponding to $\boldsymbol{\sigma}_n$, $\Delta \ln \boldsymbol{V} = \ln \boldsymbol{V} - \ln \boldsymbol{V}_n$, $\boldsymbol{V}_n = h(\boldsymbol{\sigma}_n)$. If the SVD of $\boldsymbol{F}_n$ is:

$$\boldsymbol{F}_n = \boldsymbol{U} \boldsymbol{\Sigma} \boldsymbol{W}^T = \sum_{i=1}^{q} \boldsymbol{u}_i \lambda_i \boldsymbol{w}_i^T \quad (3.6)$$

$\Delta \ln \boldsymbol{\sigma}$ can be written as:

$$\Delta \ln \boldsymbol{\sigma} = \sum_{i=1}^{r} \frac{\lambda_i^2}{\lambda_i^2 + \alpha^2} \frac{\boldsymbol{u}_i^T \Delta \ln \boldsymbol{V}}{\lambda_i} \boldsymbol{w}_i - \sum_{i=1}^{r} \frac{\alpha^2}{\lambda_i^2 + \alpha^2} \boldsymbol{w}_i^T \left(\boldsymbol{\sigma}_n - \boldsymbol{\sigma}_{ref} \right) \boldsymbol{w}_i \quad (3.7)$$

3.6 A comparison of two regularization methods base on the MK4 system

To distinguish the algorithms, the algorithm using voltage differences to reconstruct the conductivity values is named as the differential algorithm, and the algorithm using the logarithm of the voltage ratios to reconstruct the conductivity values is named as the logarithm algorithm.

According to the studies of the Sheffield group, the errors caused by the spacing and the shape of the electrodes and any small (random) variations in spacing will be greater than the noise. Considering that the EIT inverse problem is very ill-posed and the magnitude of $V - V_{ref}$ will depend on the exact physical spacing of the electrodes, any differences between this and the presumed spacing will result in reconstruction errors. However using $\ln(V./V_{ref})$ will remove the uncertainties caused by the spacing of the electrodes, where './ ' denotes element-by-element division (Barber, 2005). In the MK4

system, the planar electrode array has 85 electrodes. Due to the manufacture errors, some electrodes may be higher than the standard. See Figure 3. 11. E3 is the standard; E1 and E2 are higher than the standard. In detection, the wall of the electrodes will contact with the saline in the tank; therefore it is very challenging to accurately measure the spacing between the 85 electrodes and the saline. In this situation, using ratios of the voltage measurements is very critical.

Figure 3. 11. The electrode manufacture error

The Sheffield algorithm provides a positive constraint to the EIT inverse problem. The EIT inverse problem is a very ill-posed problem, especially when the independent measurements are not sufficient enough. No matter what current patterns are applied, there are many significantly different conductivity distributions which can generate similar measurements, thus the reconstructed conductivity could be significantly different from the real one. Therefore some reasonable constraints are needed to exclude the impossible solutions. Equation (3.4) and (3.5) provide a positive constraint that ensures the reconstructed conductivity cannot be zero or negative, but Equation (2.70) and (2.75) don't. For example, for the image reconstruction algorithm based on Equation (2.70), it is possible that some elements of $\Delta\sigma$ are negative values and the absolute values of these elements are greater than the initial conductivity estimate, which means $\sigma_0^i < |\Delta\sigma^i|, \Delta\sigma^i < 0$. As a result, some elements of the reconstructed conductivity σ will be negative $\sigma^i = \sigma_0^i + \Delta\sigma^i < 0$. Obviously negative conductivity values are wrong; however in the practice of the MK4 system, the differential algorithms (2.70) and (2.75) do give negative conductivity values, but the logarithm algorithms (3.4) and (3.5) never do.

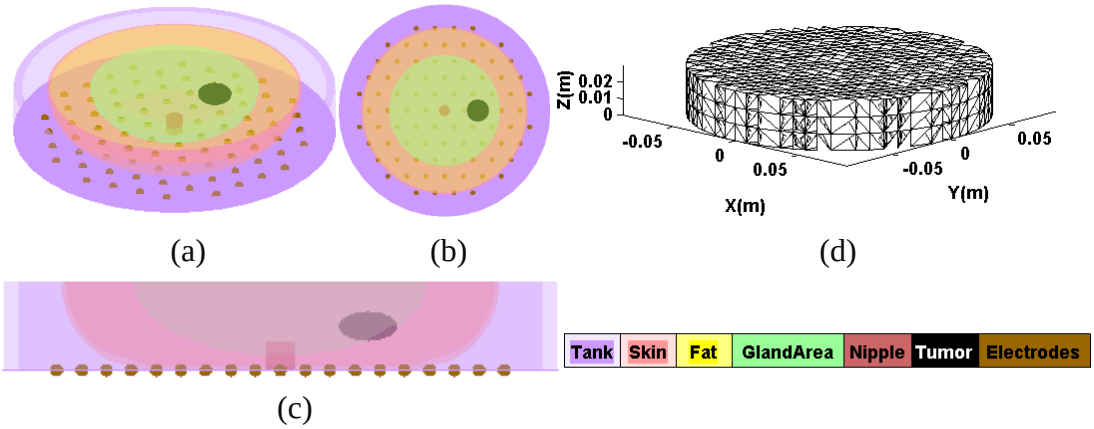

Figure 3. 12 Simple breast model

Despite the limitations of the differential algorithm, it is still available in the MK4 system. A comparison between the differential algorithm and the logarithm algorithm is made based on a simple breast model, which is shown in Figure 3. 12. The simple breast model is composed of skin, fat, a gland area, a nipple and a tumor. The breast is pressed by the electrode array into the chest with a contact diameter of 9cm. The maximum diameter of the breast is 15cm. The height of the tank is 3cm. The thickness of the skin is 0.155cm (Sutradhar and Miller, 2013); the conductivity of the skin is 0.456 S/m (De Lucia et al., 2007). The maximum diameter of the gland area is 10cm; the conductivity of the gland area is 0.2S/m. The nipple is 1 cm in diameter and 1cm in height; the conductivity of the nipple is 0.3S/m. The tumor is located at (3,0,1.5) with a diameter of 2 cm. The conductivity of the tumor is 0.7 S/m. Fat is in between the skin and the gland area with conductivity of 0.05 S/m. In this simulation, a SNR of 60 dB while Gaussian additive noise and 0.5% random multiplicative noise are added. The ADC quantization is considered. The mesh used for image reconstruction is shown in Figure 3. 12 (d). It has 3 layers, 7020 elements and 1684 vertices.

To make the comparison of the two algorithms fair, the L-curve method is employed to determine the optimized α, which is shown in Figure 3. 13 and Figure 3. 14. The images in the L-curve diagrams indicate the conductivity distribution in the middle of the tank, which are also the reconstructed results of the middle layer of the 3D mesh. A small

α will make the result to noisy, so that the information from the breast will be submerged in noise, as shown in the images in the front of the L-curves in Figure 3. 13 and Figure 3. 14. A big α will filter the measurements of high orders, which will cause a loss of the detailed information of the breast, as shown in the images in the terminal of the L-curves in Figure 3. 13 and Figure 3. 14. The optimized α for the differential and the logarithm algorithms are at the corner of the L-curves, which are $\alpha^2 = 0.04$ and $\alpha^2 = 0.004$ for the differential and the logarithm algorithms respectively. The reconstructed results at the optimized α are shown in Figure 3. 15 and Figure 3. 16. The images from left to right indicate the conductivity distributions in the bottom, middle and top of the tank. In the first cross-sectional images of Figure 3. 15 and Figure 3. 16, the red circular area in the centre is caused by the highly conductive skin, which contacts with the electrode plane. The region near the electrodes is more sensitive than the other regions, so it is noisier in the first cross-sectional image. In the second cross-sectional images of Figure 3. 15 and Figure 3. 16, the black elements at 3 o'clock indicate the presence of the tumour. The red circular area in the centre indicates the gland area. The red ring surrounding the gland area is caused by the skin. The yellow area in between the gland area and the skin indicates fat. In the third cross-sectional images of Figure 3. 15 and Figure 3. 16, the black elements at 3 o'clock are projections of the tumour. As this layer is relatively far away from the electrodes, it is less sensitive than the other layers; therefore the skin of the breast is not well imaged. Comparing Figure 3. 15 and Figure 3. 16, we can find that the result from the logarithm algorithm is less noisy than that from the differential algorithm; thus the logarithm algorithm is more robust to noise.

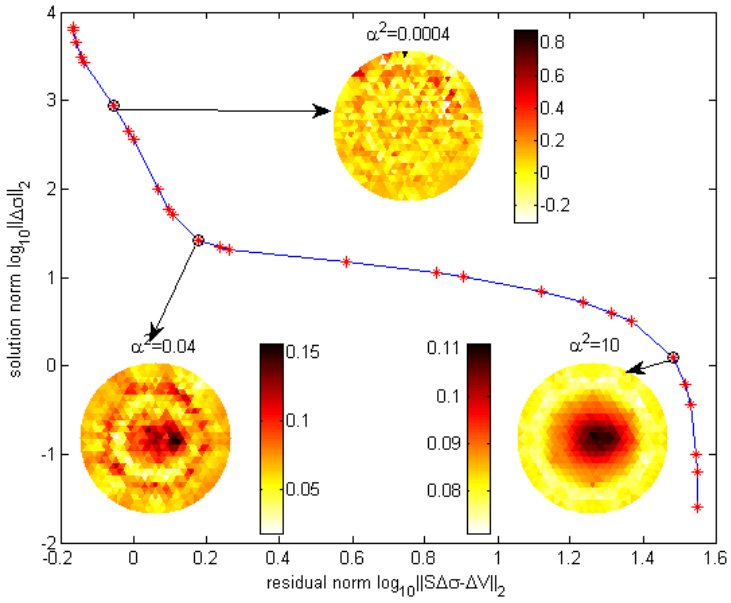

Figure 3. 13. The L-curve of the differential algorithm

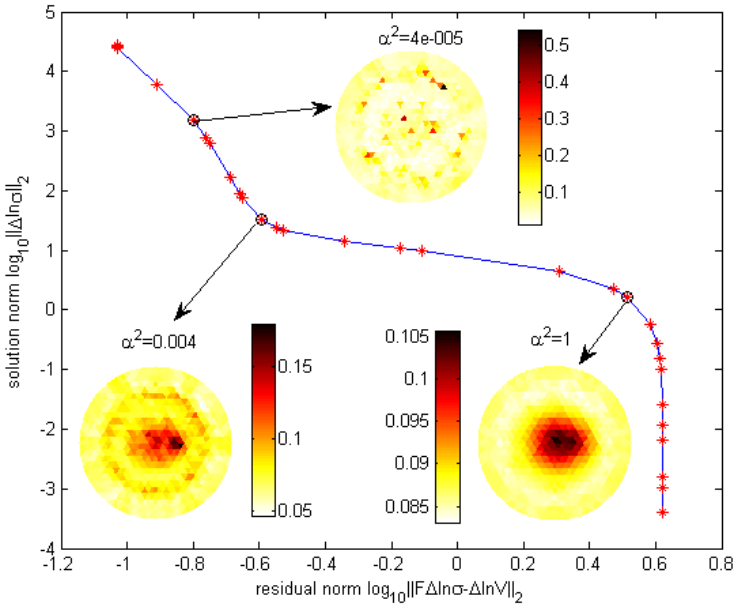

Figure 3. 14 the L-curve of the logarithm algorithm

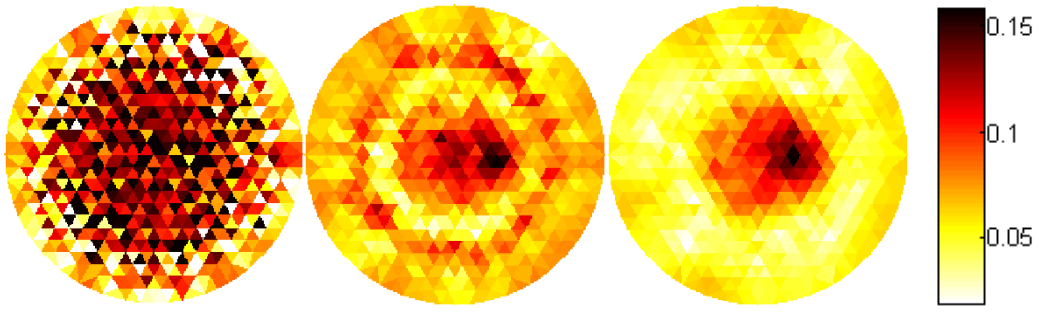

Figure 3. 15. The reconstructed result from the differential algorithm at the optimized α, $\alpha^2 = 0.04$. The images from left to right indicate the conductivity distribution in the bottom, middle, and top of the tank.

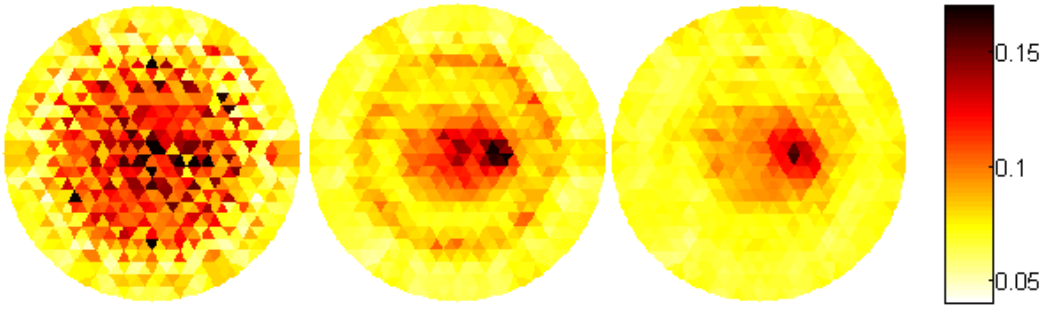

Figure 3. 16. The reconstructed result from the logarithm algorithm at the optimized α, $\alpha^2 = 0.004$. The images from left to right indicate the conductivity distribution in the bottom, middle, and top of the tank.

3.7 A comparison of two planar electrode arrays for the MK4 system

Most planar electrode array EIM systems deploy the electrodes in a rectangular pattern. As mentioned before, the novel part of the MK4 system is the hexagonal planar electrode array; however actually the MK4 system has a rectangular planar electrode array as well but this electrode array is not usually used. This section will give a comparison of the rectangular planar electrode array (RPEA) and the hexagonal planar electrode array (HPEA) for the MK4 system, based on computer simulations.

The electrode deployments of the RPEA and the HPEA are shown in Figure 3. 17. The HPEA was introduced in section 3.3. The RPEA has 89 electrodes in total with the adjacent electrode distance in the X-axis and Y-axis equal to 15mm. The data acquisition method of the HPEA is similar to that of the RPEA, which uses small rectangular measurement areas to scan the tank to obtain the strongest voltage measurements. Every nine adjacent electrodes make up a rectangular measurement area, shown as Figure 3. 18 (a) and (b). The current is applied from the electrode pairs with an interval of three electrodes; the voltage measurements are collected from the adjacent electrode pairs within the rectangular measurement area and parallel to the drive pair. The data acquisition method is shown in Figure 3. 18. The dots within the black circle indicate the electrodes. The red squares indicate the measurement areas. The yellow dots with '+' and '-' indicate the drive pairs. The blue dots indicate the measuring electrodes. The red

arrows in between the adjacent measuring electrodes indicate the voltage measuring pairs. In a complete measurement area, there are 2 current excitation events; each current excitation corresponds to 14 voltage measurements (see Figure 3. 18 (a) and (b)). In an asymmetric measurement area, there might be only one excitation event and the voltage measurements are less than that of a complete measurement area (see Figure 3. 18 (c)). According to this design, there are 94 current excitation events corresponding to 1380 independent measurements.

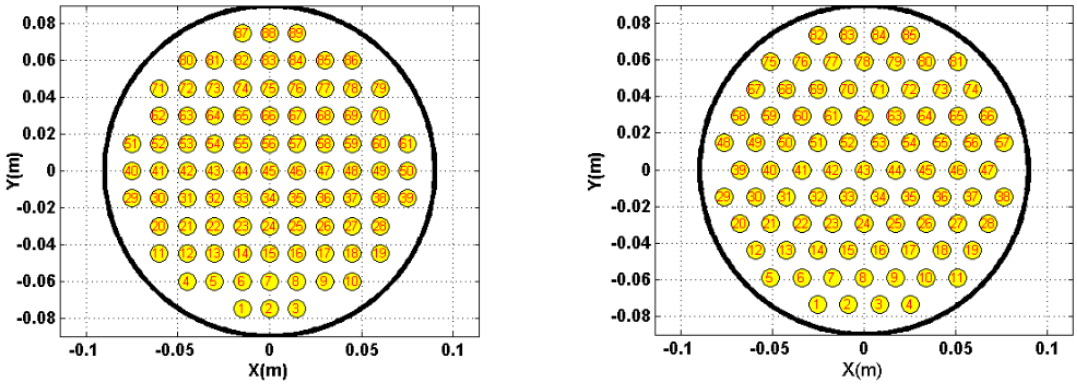

Figure 3. 17. The rectangular electrode array (left) and the hexagonal electrode array (right)

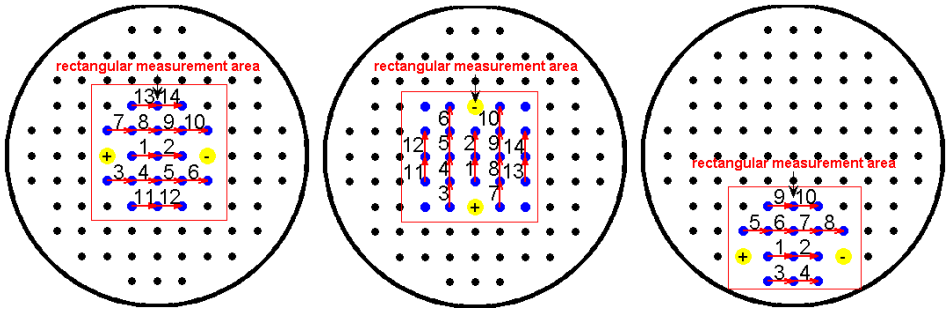

(a) (b) (c)

Figure 3. 18. The data acquisition method of RPEA (a) the current excitation is applied along the X-axis direction. (b) the current excitation is applied along the Y-axis direction

Similar to the data acquisition method of HPEA, the reason for this data acquisition method is to achieve a smaller dynamic range and a good SNR by only collecting the strongest measurements for each excitation. For a uniform field, the dynamic range of the 1380 measurements is 8.05. If we apply the current from the yellow dots in Figure 3. 18

(a), the voltage measurements are plotted in Figure 3. 19. These measurements almost have the same scale with the IMs in Figure 3. 6 (the first 12 measurements in Figure 3. 6 corresponding to the left diagram in Figure 3. 5).

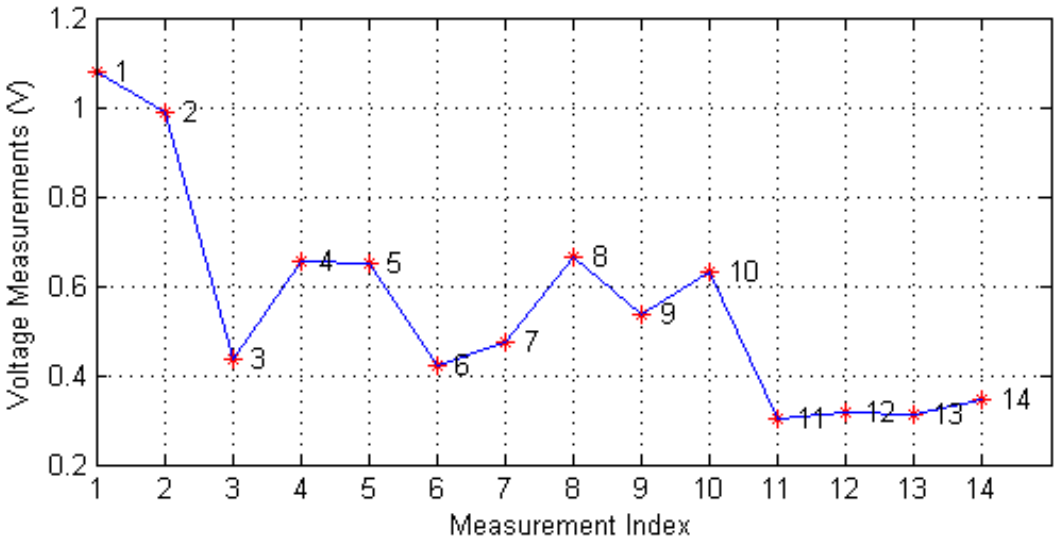

Figure 3. 19. The voltage measurements corresponding to Figure 3. 8 (a)

The configurations of the two planar electrode array are tabulated in Table 3. 1. There are 85 electrodes in the HPEA deployed in a hexagonal pattern. The adjacent distance of the neighboring electrodes is 17 mm. The RPEA has 89 electrodes deployed in a rectangular pattern with an adjacent distance of 15 mm along the X axis and Y axis and an adjacent distance of 21.2 cm in the 45° and 135° directions (the directions along y=x and y=-x). For a planar electrode array, the spatial resolution at the contact plane is approximately equal to the distance of the adjacent electrodes, therefore theoretically the spatial resolution of HPEA is 17 mm; the spatial resolution of RPEA is 15 mm along the X-axis and Y-axis directions and 21.2 mm in the 45° and 135° directions. There are 1416 independent measurements corresponding to 123 excitation events of the HPEA, compared with 1380 measurements and 94 excitations of the RPEA. The HPEA has a smaller dynamic range than the RPEA. In EIT systems, a big dynamic range is undesirable for image reconstruction.

Table 3. 1 The configurations of the planar electrode arrays

Configuration	HPEA	RPEA
The number of electrodes	85	89
The adjacent electrode distance	17mm	15mm and 21.2mm
The spatial resolution	≥17mm	≥15mm along the X-axis and Y-axis directions; ≥21.2mm along the directions of y=x and y=-x
The number of excitations	123	94
The number of measurements	1416	1380
Dynamic range	3.20	8.05

The simple breast model in Figure 3. 12 is used to compare the reconstructed results from the two planar electrode arrays. In the forward problem, the SNR of 60 dB while Gaussian additive noise and 0.5% random multiplicative noise are added to the simulated measurements. In the inverse problem, to make the comparison fair, the L-cure method is used to determine the optimized regularization parameter α. Figure 3. 20 and Figure 3. 21 show the L-curves of the differential and logarithm algorithms respectively, using the RPEA. The optimized α for the two algorithms are $\alpha^2 = 0.04$ and $\alpha^2 = 0.004$ which are the same with those of the HPEA. This is because that the noise added to the RPEA measurements and the HPEA measurements are the same. Figure 3. 22 and Figure 3. 23 present the reconstructed results from the differential and the logarithm algorithms respectively. Comparing Figure 3. 22 and Figure 3. 23 with Figure 3. 15 and Figure 3. 16, we can see that the HPEA produces a better result than the RPEA, as the images of the tumor in Figure 3. 22 and Figure 3. 23 spread to a big range. That may be due to the non-uniform spatial resolution (or the non-equal adjacent electrode distance) and the big dynamic range of the measurements.

Although the number of electrodes in the RPEA is greater than that of the HPEA, the number of independent measurements of the RPEA is smaller. As we know, more independent measurements means more constraints to the EIT inverse problem, which produces a more stable and reliable solution; therefore from this point, the hexagonal array is superior to the rectangular array. The dynamic range of the measurements of the RPEA is big, which is a disadvantage for EIT image reconstruction. The spatial resolution

of the RPEA is not uniform as the adjacent electrode distance along X axis and Y axis is different from that in the directions of y=x, and y=-x. The spatial resolution in the later directions is poor. Generally, the RPEA does not perform as well as the HPEA; therefore the HPEA is preferred in the MK4 system.

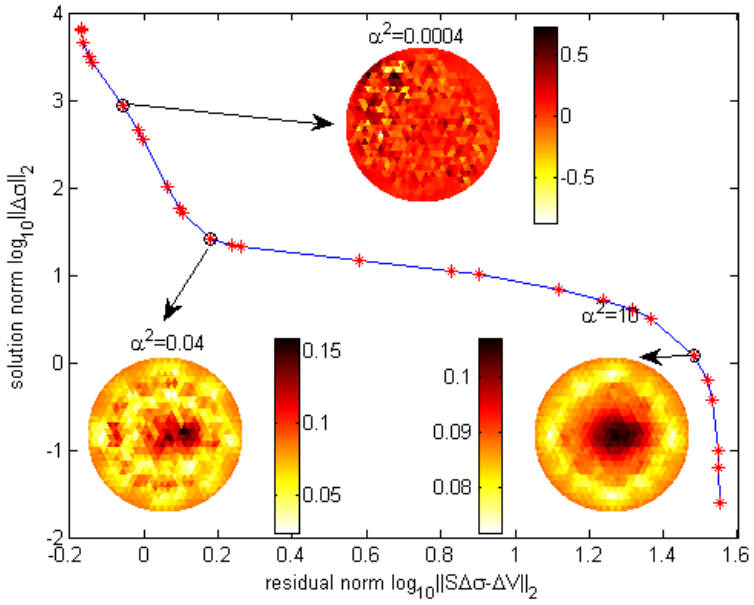

Figure 3. 20. The L-curve of the differential algorithm for the RPEA

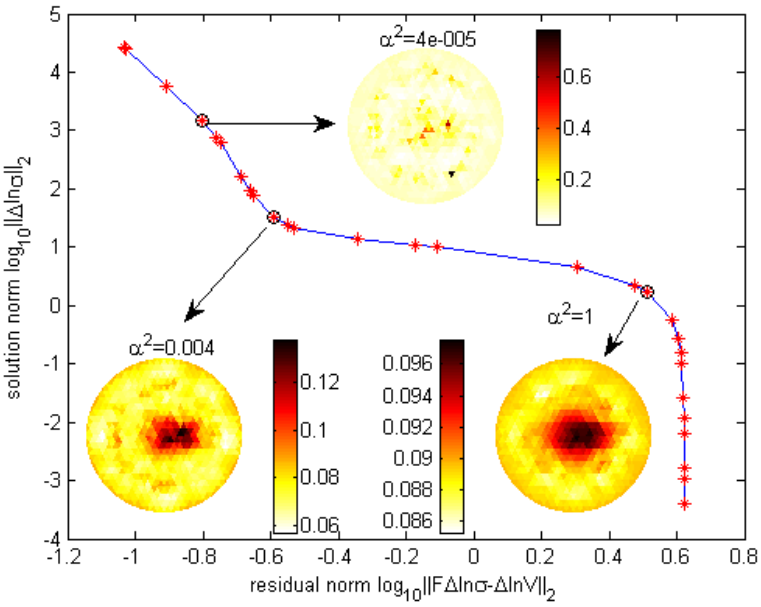

Figure 3. 21 The L-curve of the logarithm algorithm for the RPEA

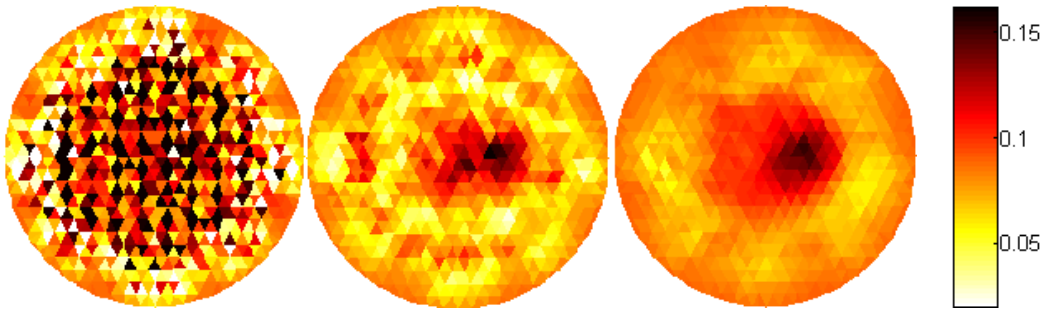

Figure 3. 22. The reconstructed result from the differential algorithm at the optimized α for the RPEA, $\alpha^2 = 0.04$. The images from left to right indicate the conductivity distribution in the bottom, middle, and top of the tank.

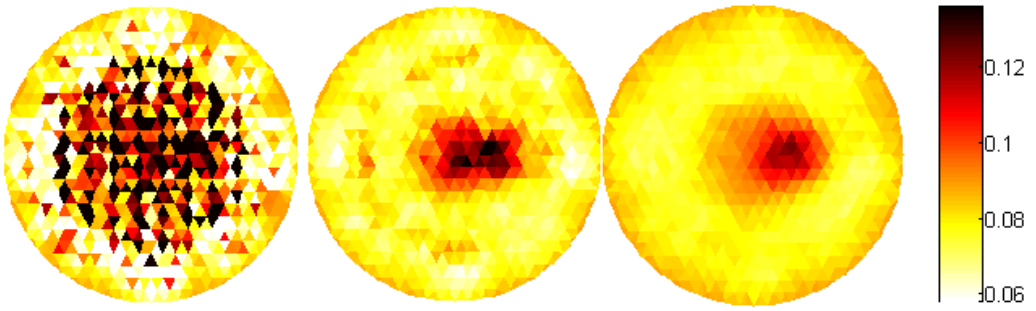

Figure 3. 23. The reconstructed result from the differential algorithm at the optimized α for the RPEA, $\alpha^2 = 0.04$. The images from left to right indicate the conductivity distribution in the bottom, middle, and top of the tank.

3.8 Conclusion

This chapter introduced the Sussex MK4 system and its image reconstruction algorithms. The MK4 system is a continuation of the research of the De Montfort MK system. It employs a tank and a bed for examination. The tank can confine the breast in a certain volume and provide accurate boundary conditions for the image reconstruction algorithms. The bed can make the examination more comfortable and help the patient to lie still for a relatively long time. The MK4 system is a relatively sophisticated EIM system made up with a saline pumping system, a saline warming system, an electrode adjustment system, a data acquisition system, a safety and emergency system, a cleaning system, and two power systems. The novel part of the MK4 system is the hexagonal electrode array and the hexagonal data acquisition method. The MK4 system has two

image reconstruction algorithms: one uses voltage differences to reconstruct the conductivity distribution in the tank, which is named as the differential algorithm; the other one uses the logarithm of the voltage ratios, which is named as the logarithm algorithm. Compared with the logarithm algorithm, the differential algorithm is more popular in EIT systems. However the logarithm algorithm is preferred for the MK4 system, as it can minimize the errors caused by the spacing of the electrodes, provides a positive constraint to the EIT inverse problem, and has a better noise tolerance than the differential algorithm (section 3.6). The MK4 system also has two planar electrode arrays: one of them has a rectangular pattern, which is named as the rectangular planar electrode array (RPEA); the other one has a hexagonal pattern, which is named as the hexagonal planar electrode array (HPEA). The HPEA is more efficient and can produce a better result than the RPEA, thus the HPEA is the one more frequently used. In the clinical trials of the MK4 system, the HPEA was used.

4. An Enhanced Image Reconstruction Algorithm and Clinical Results of the MK4 System

This chapter will introduce an enhanced image reconstruction algorithm which is more accurate and sensitive than the algorithm introduced in section 3.5. A comparison of the enhanced algorithm and the former algorithm will be made based on computer simulations, real experiments and clinical trials.

4.1 An enhanced image reconstruction algorithm

As mentioned in section 2.6, the regularization parameter α reduces the effects from the high order singular values, which limits noise in the reconstructed result. But meanwhile it also filters the high order information of the measurements, as a result, it achieves a blurred image with unclear edges and reduced image contrast. Even though the L-curve method has been proven to be a reliable method to determine an optimum value of α, achieving a trade-off between noise and image quality, a weakened image contrast is inevitable due to the omission of the high order singular values. To recover image contrast, a correction term is used, which is a novel modification of the former image reconstruction algorithm.

Assume $\boldsymbol{\sigma}$ is the real conductivity distribution, $\hat{\boldsymbol{\sigma}}_n$ is the *n*th iteration result from equation (3.5) and the conductivity error after the *n*th iteration is $\ln \boldsymbol{\sigma} - \ln \hat{\boldsymbol{\sigma}}_n$ (remembering: $\boldsymbol{\sigma}$ and $\hat{\boldsymbol{\sigma}}_n$ are the $K \times 1$ vectors indicating the conductivity values of the mesh elements). If we knew $\ln \boldsymbol{\sigma} - \ln \hat{\boldsymbol{\sigma}}_n$, we could use this error to correct the *n*th iteration conductivity $\hat{\boldsymbol{\sigma}}_n$ and make the final *n*th iteration result $\boldsymbol{\sigma}_n$ equal to the real conductivity $\boldsymbol{\sigma}$ (see (4.1))

$$\ln \boldsymbol{\sigma_n} = \ln \hat{\boldsymbol{\sigma}}_{\boldsymbol{n}} + (\ln \boldsymbol{\sigma} - \ln \hat{\boldsymbol{\sigma}}_{\boldsymbol{n}}) \quad (4.1)$$

However (4.1) is not available for there is no way to know the exact value of $\ln \boldsymbol{\sigma} - \ln \hat{\boldsymbol{\sigma}}_n$. But $\ln \boldsymbol{\sigma} - \ln \hat{\boldsymbol{\sigma}}_n$ can be approximated by the inverse algorithm. Assume $\Delta \ln \hat{\boldsymbol{\sigma}}_n$ is the approximation of $\ln \boldsymbol{\sigma} - \ln \hat{\boldsymbol{\sigma}}_n$, (4.1) becomes

$$\ln \boldsymbol{\sigma}_n = \ln \hat{\boldsymbol{\sigma}}_n + \beta \Delta \ln \hat{\boldsymbol{\sigma}}_n \quad (4.2)$$

where $\boldsymbol{\sigma}_n$ is the modified (or final) conductivity distribution of the *n*th iteration; $\hat{\boldsymbol{\sigma}}_n$ is the first conductivity distribution of the *n*th iteration from (3.5); β is a modifying factor (a scalar); $\Delta \ln \hat{\boldsymbol{\sigma}}_n$ is the approximation of $\ln \boldsymbol{\sigma} - \ln \hat{\boldsymbol{\sigma}}_n$. For Tikhonov regularization, if the change of conductivity is very small and the second constraint, which limits the change of conductivity is ignored, we can obtain the following equation：

$$\Delta \ln \hat{\boldsymbol{\sigma}}_n = (\boldsymbol{F}^T \boldsymbol{F} + \alpha^2 \boldsymbol{I})^{-1} \boldsymbol{F}^T \left(\ln \boldsymbol{V} - \ln \hat{\boldsymbol{V}}\right) = \boldsymbol{F}^+ \left(\ln \boldsymbol{V} - \ln \hat{\boldsymbol{V}}_n\right) \quad (4.3)$$

where $\hat{\boldsymbol{V}}_n$ is the $M \times 1$ vector indicating the simulated voltage measurements corresponding to the first reconstruction result $\hat{\boldsymbol{\sigma}}_n$, $\boldsymbol{F}^+ = (\boldsymbol{F}^T \boldsymbol{F} + \alpha^2 \boldsymbol{I})^{-1} \boldsymbol{F}^T$. Substituting (4.3) into (4.2), (4.2) becomes

$$\ln \boldsymbol{\sigma}_n = \ln \hat{\boldsymbol{\sigma}}_n + \beta \boldsymbol{F}^+ \left(\ln \boldsymbol{V} - \ln \hat{\boldsymbol{V}}_n\right) \quad (4.4)$$

If $\beta = 0$, $\boldsymbol{\sigma}_n = \hat{\boldsymbol{\sigma}}_n$, which is the former image reconstruction algorithm (3.5). If $\beta = 1$,

$$\ln \boldsymbol{\sigma}_n = \ln \hat{\boldsymbol{\sigma}}_n + \boldsymbol{F}^+ \left(\ln \boldsymbol{V} - \ln \hat{\boldsymbol{V}}_n\right) \quad (4.5)$$

where $\boldsymbol{F}^{+}\left(\ln\boldsymbol{V}-\ln\widehat{\boldsymbol{V}}_{n}\right)$, in fact, is the next iteration using the Tikhonov regularization without the second constraint. But actually the value of β is greater than 1, which is proven as follows. The solution of $\beta\Delta\ln\widehat{\boldsymbol{\sigma}}_{n}$ is

$$\beta\Delta\ln\widehat{\boldsymbol{\sigma}}_{n}=\sum_{i=1}^{r}\frac{\lambda_{i}^{2}}{\lambda_{i}^{2}+\alpha^{2}}\left(\beta\cdot\frac{\boldsymbol{u}_{i}^{T}\Delta\ln\widehat{\boldsymbol{V}}}{\lambda_{i}}\boldsymbol{w}_{i}\right) \qquad (4.6)$$

where $\Delta\ln\widehat{\boldsymbol{V}}=\ln\boldsymbol{V}-\ln\widehat{\boldsymbol{V}}_{n}$. As mentioned before, α filters the high order singular values leading to weakened image contrast. If $\beta>1$, it will amplify the change of the conductivity, which is helpful to increase the image contrast. However it doesn't mean that β can be arbitrarily large. An optimized β is calculated by the following method.

Equation (4.4) contributes the final nth conductivity $\boldsymbol{\sigma}_{n}$**.** The error between the real conductivity $\boldsymbol{\sigma}$ and $\boldsymbol{\sigma}_{n}$ is:

$$\Delta\ln\boldsymbol{\sigma}=\ln\boldsymbol{\sigma}-\ln\boldsymbol{\sigma}_{n}=\ln\boldsymbol{\sigma}-\ln\widehat{\boldsymbol{\sigma}}_{n}-\beta\boldsymbol{F}^{+}\left(\ln\boldsymbol{V}-\ln\widehat{\boldsymbol{V}}_{n}\right) \qquad (4.7)$$

Multiply (4.7) by $\boldsymbol{F}$, then we get the voltage error between real measurements and the *n*th simulated measurements $\Delta\ln\boldsymbol{V}$:

$$\Delta\ln\boldsymbol{V}=\boldsymbol{F}\Delta\ln\boldsymbol{\sigma}=\boldsymbol{F}(\ln\boldsymbol{\sigma}-\ln\widehat{\boldsymbol{\sigma}}_{n})-\beta\boldsymbol{F}\boldsymbol{F}^{+}\left(\ln\boldsymbol{V}-\ln\widehat{\boldsymbol{V}}_{n}\right) \qquad (4.8)$$

As known, $\boldsymbol{F}(\ln\boldsymbol{\sigma}-\ln\widehat{\boldsymbol{\sigma}}_{n})=\ln\boldsymbol{V}-\ln\widehat{\boldsymbol{V}}_{n}=\Delta\ln\widehat{\boldsymbol{V}}$, (4.8) can be rewritten as:

$$\Delta\ln\boldsymbol{V}=\Delta\ln\widehat{\boldsymbol{V}}-\beta\boldsymbol{F}\boldsymbol{F}^{+}\Delta\ln\widehat{\boldsymbol{V}} \qquad (4.9)$$

Establishing an auxiliary function $f(\beta)$,

$$f(\beta) = \|\Delta \ln \boldsymbol{V}\|^2 = \left\|\Delta \ln \widehat{\boldsymbol{V}} - \beta \boldsymbol{F}\boldsymbol{F}^{+}\Delta \ln \widehat{\boldsymbol{V}}\right\|^2 \quad (4.10)$$

To get the best β, minimising the difference between real measurements and simulated measurements, we need to make the derivative of $f(\beta)$ equal to 0.

$$\frac{df(\beta)}{d\beta} = 2\frac{d\left(\Delta \ln \widehat{\boldsymbol{V}} - \beta \boldsymbol{F}\boldsymbol{F}^{+}\Delta \ln \widehat{\boldsymbol{V}}\right)^T}{d\beta}\left(\Delta \ln \widehat{\boldsymbol{V}} - \beta \boldsymbol{F}\boldsymbol{F}^{+}\Delta \ln \widehat{\boldsymbol{V}}\right)$$

$$= -2\left(\boldsymbol{F}\boldsymbol{F}^{+}\Delta \ln \widehat{\boldsymbol{V}}\right)^T\left(\Delta \ln \widehat{\boldsymbol{V}} - \beta \boldsymbol{F}\boldsymbol{F}^{+}\Delta \ln \widehat{\boldsymbol{V}}\right) = 0 \quad (4.11)$$

Thus

$$\beta = \frac{\left(\boldsymbol{F}\boldsymbol{F}^{+}\Delta \ln \widehat{\boldsymbol{V}}\right)^T \Delta \ln \widehat{\boldsymbol{V}}}{\left\|\boldsymbol{F}\boldsymbol{F}^{+}\Delta \ln \widehat{\boldsymbol{V}}\right\|^2} \quad (4.12)$$

Therefore the enhanced image reconstruction algorithm is:

$$\ln \boldsymbol{\sigma}_n = \ln \widehat{\boldsymbol{\sigma}}_n + \frac{\left(\boldsymbol{F}\boldsymbol{F}^{+}\Delta \ln \widehat{\boldsymbol{V}}\right)^T \Delta \ln \widehat{\boldsymbol{V}}}{\left\|\boldsymbol{F}\boldsymbol{F}^{+}\Delta \ln \widehat{\boldsymbol{V}}\right\|^2}\boldsymbol{F}^{+}\left(\ln \boldsymbol{V} - \ln \widehat{\boldsymbol{V}}_n\right) \quad (4.13)$$

or

$$\boldsymbol{\sigma}_n = \widehat{\boldsymbol{\sigma}}_n \boldsymbol{e}^{\frac{\left(\boldsymbol{F}\boldsymbol{F}^{+}\Delta \ln \widehat{\boldsymbol{V}}\right)^T \Delta \ln \widehat{\boldsymbol{V}}}{\left\|\boldsymbol{F}\boldsymbol{F}^{+}\Delta \ln \widehat{\boldsymbol{V}}\right\|^2}\boldsymbol{F}^{+}\left(\ln \boldsymbol{V} - \ln \widehat{\boldsymbol{V}}_n\right)} \quad (4.14)$$

In summary, the process of the new algorithm is shown as Figure 4. 1. As the reconstructed conductivity $\widehat{\boldsymbol{\sigma}}_n$ could be obtained using equation (3.5), the corresponding voltage measurements $\widehat{\boldsymbol{V}}_n$ could be obtained using the forward algorithm. Compare the predicted voltage measurements $\widehat{\boldsymbol{V}}_n$ with the real voltage measurements $\boldsymbol{V}$, the change of the voltage measurements will be known; therefore the change of the conductivity $\Delta \ln \widehat{\boldsymbol{\sigma}}_n$ could be obtained using the inverse algorithm. $\beta \Delta \ln \widehat{\boldsymbol{\sigma}}_n$ is the correction item, where β is the parameter to be determined. The final result of the nth iteration $\ln \boldsymbol{\sigma}_n$ is equal to the sum of the logarithm of $\widehat{\boldsymbol{\sigma}}_n$ and the correction item. Provided the real

conductivity is $\boldsymbol{\sigma}$, the error of the final reconstructed result $\boldsymbol{\sigma}_n$ is expressed by $\Delta \ln \boldsymbol{\sigma} = \ln \boldsymbol{\sigma} - \ln \boldsymbol{\sigma}_n$. The dot arrow in Figure 4. 1 indicates that $\Delta \ln \boldsymbol{\sigma}$ is not directly obtained using $\ln \boldsymbol{\sigma} - \ln \boldsymbol{\sigma}_n$, but is a function of β and $\boldsymbol{\sigma}$. If we multiply the error of the reconstructed conductivity $\Delta \ln \boldsymbol{\sigma}$ by the sensitivity matrix $\boldsymbol{F}$, we will get the error of the voltage measurements $\Delta \ln \boldsymbol{V}$. By minimizing the 2-norm of the voltage measurements $\Delta \ln \boldsymbol{V}$, the parameter β could be obtained, hence the final nth reconstructed result $\boldsymbol{\sigma}_n$.

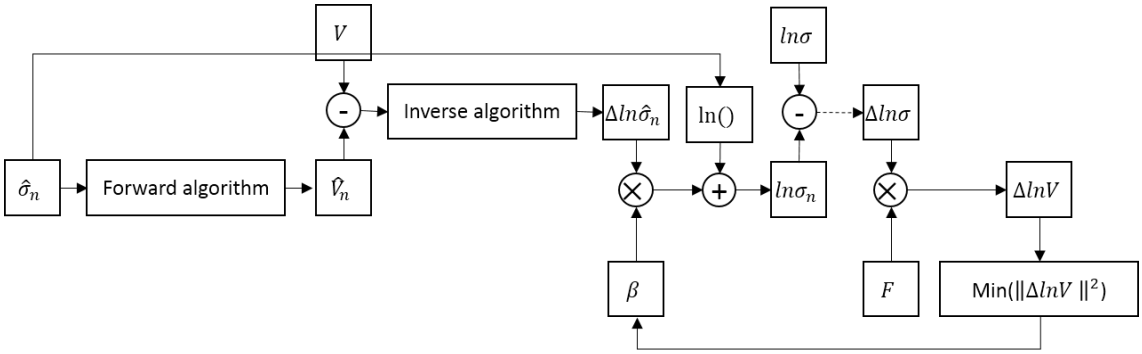

Figure 4. 1. The process of the new algorithm

In this enhanced iteration equation (4.14), it includes two reconstructions. The rough estimation of the *n*th conductivity $\hat{\boldsymbol{\sigma}}_n$ is the first reconstruction. This reconstruction includes two constraint terms ensuring a stable and smooth solution. In the second reconstruction, $\beta \Delta \ln \hat{\boldsymbol{\sigma}}_n$ is used to correct $\ln \hat{\boldsymbol{\sigma}}_n$. Given $\hat{\boldsymbol{\sigma}}_n$ from the first reconstruction, the corresponding voltage measurements $\hat{\boldsymbol{V}}_n$ become known, therefore the conductivity error between the real conductivity $\boldsymbol{\sigma}$ and $\hat{\boldsymbol{\sigma}}_n$ is appreciable and the estimation is $\Delta \ln \hat{\boldsymbol{\sigma}}_n$. When calculating $\Delta \ln \hat{\boldsymbol{\sigma}}_n$, we abandon the second constraint and multiply $\Delta \ln \hat{\boldsymbol{\sigma}}_n$ by a proper factor β to increase the image contrast. This approach brings the object conductivity closer to the real value, especially in the situation when the object is far from the electrodes. This is proven by the following results. The participation of the two reconstructions in the enhanced image reconstruction algorithm makes the result converge faster. The factor β in the new algorithm only properly amplifies the change of the conductivity. It doesn't change the filter effect of α; therefore it won't worsen the ill-posed problem or sharpen the edges in the image. So objectively this

enhanced image reconstruction algorithm has the ability to make the solution converge faster and improve the accuracy of the reconstructed conductivity image.

4.2 Trade-off of Speed and Accuracy

The relationship between the conductivity distribution and boundary voltage is a complex nonlinear function. To simplify the calculation, the real field is linearized, by subdividing the whole field into a number of elements. If the size of the element becomes smaller, the conductivity value of the element will approach the real value, which means the finer the mesh is, the closer to the truth the reconstructed image is. However, in practice, it is not affordable to use a very fine mesh, as the data volume and the computational time become too large. From this point of view, the trade-off between speed and accuracy in EIM is an optimization problem. To address this problem, this section presents a duo-mesh method.

The so-called duo-mesh method uses two meshes, one fine mesh and one coarse mesh, for image reconstruction. In the whole process of image reconstruction, the forward algorithm and inverse algorithm are both involved in each iteration, which means the inaccuracy in either of the algorithms will affect the quality of the results. Therefore, to get a better result, both of the algorithms need to be improved. Great efforts have been made to improve the image reconstruction algorithm (Choi et al., 2007, Mueller et al., 1999, Kim et al., 2001, Cao and Xu, 2013, Hamilton and Mueller, 2013, Zhang et al., 2012, Martins et al., 2012, Barber and Seagar, 1987, Barber et al., 1992). Our approach was introduced in the previous section. As the forward algorithm is relatively fast, a fine mesh can be used to get more accurate simulation measurements. When considering the computational time of the image reconstruction algorithm, a coarse mesh is used for the inverse problem. The two meshes are shown in Figure 4. 2.

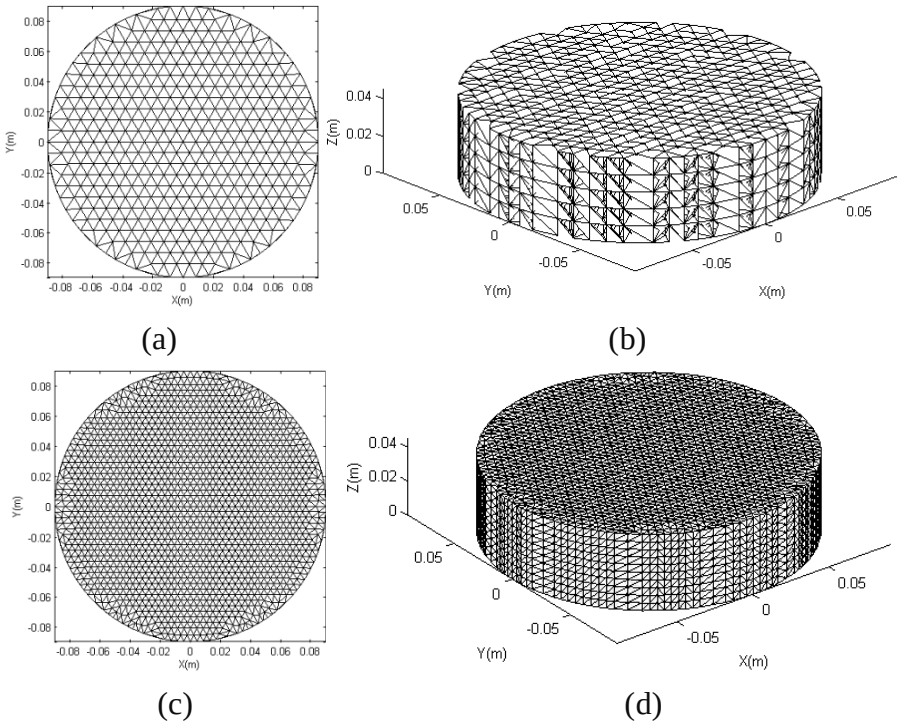

Figure 4. 2. Meshes in the image reconstruction algorithms. (a) and (b) are the 2D coarse mesh and the 3D coarse mesh for the EIT inverse problem. (c) and (d) are the 2D fine mesh and the 3D fine mesh for the EIT forward problem.

When designing the mesh, the electrode distribution is taken into consideration. Firstly, we need to ensure that the mesh nodes are located on the electrodes. Secondly, as the electrodes are evenly spaced, the mesh elements also need to be evenly distributed. The fine mesh is developed from the coarse mesh by dividing one triangle into 4 from the middle of each side, so that the electrodes can be located at the same nodes as the coarse mesh, furthermore, during each iteration, it is easy and accurate to map the conductivity distribution from the coarse mesh to the fine mesh. To build a 3D mesh, the triangles in the 2D mesh become triangular prisms and each triangular prism is divided into 3 tetrahedrons, therefore if there are N elements in the 2D mesh, there will be $3 \times N$ elements in each layer of the 3D mesh. There are 421 nodes and 780 elements in the coarse 2D mesh. If the model is divided into 5 layers, there will be $421 \times 6 = 2526$ nodes and $780 \times 3 \times 5 = 11700$ elements in total. For the fine mesh, there are 1621 nodes and 3120 elements in the 2D mesh and 17831 nodes and 93600 elements in the 3D mesh (10 layers). Compared with the coarse mesh, the fine mesh has a much greater data

volume, so the application of the fine mesh to the inverse problem would lead to a very considerable computational time. Moreover, due to the ill-posed nature of the inverse problem, if the number of elements is much greater than the number of independent measurements, a fine mesh will lead to a more unstable solution than a coarse mesh. Thus the duo-mesh method benefits both the accuracy, by enhancing the accuracy of the forward simulation, and the speed and stability of image reconstruction.

4.3 Results from computer simulations

This section presents some simulated results to demonstrate the improvements of the new algorithm. To make the simulations close to the real cases, noise is added to the simulated voltage measurements. There are two major kinds of noise in the MK4 system: the additive noise and the multiplicative noise. The additive noise (or background noise) can be minimised by increasing the sample number, so the impact of the additive noise on the image quality is very limited. The multiplicative noise from the amplifying circuit is the major factor, which affects the measurement accuracy. The error of the amplifying circuit is ±0.5%. The models of the simulations are shown in Figure 4. 3. The purpose of using these simple models is to test the performance of the former algorithm and the enhanced algorithm. The conductivity of the background is set to 0.05 S/m; the conductivity of the object is set to 0.08 S/m to simulate a higher-conductivity lesion. The tank height is set to 4.5cm (fitting breast cup size 38DD or 36E). In the 3D mesh, the tank is divided into 5 layers (each layer is 0.9 cm thick). The object is placed at the bottom (the first layer), the middle (the third layer) and the top (the fifth layer) respectively. In the simulations, the operating frequency is 500 kHz, the sampling frequency is 20MSa/s, the sample number is 100, both the additive noise (60dB white Gaussian noise) and the multiplicative noise (±0.5% random noise) are added, and the ADC quantization is also incorporated. The reconstructed results are shown in Table 4. 1, Table 4. 2 and Table 4. 3. The images in the first row are from the former algorithm with 6 iterations; the images in

the second row are from the enhanced algorithm with 2 iterations; the colour bars beneath the images indicate the conductivity value. For all three models, $\alpha^2 = 0.004$, which is an optimized value computed via the L-curve method. The following equation is used to evaluate the error of the reconstructed conductivity:

$$err = \|\boldsymbol{\sigma}_n - \boldsymbol{\sigma}\| \qquad (4.15)$$

where $\|\ \|$ indicates the Frobenious norm, $\boldsymbol{\sigma}_n$ is the $\mathrm{K} \times 1$ vector indicating the reconstructed conductivity of the *n*th iteration, $\boldsymbol{\sigma}$ is the $\mathrm{K} \times 1$ vector indicating the real conductivity, err is the error for evaluating the accuracy of the reconstructed conductivity. A smaller err indicates a more accurate result.

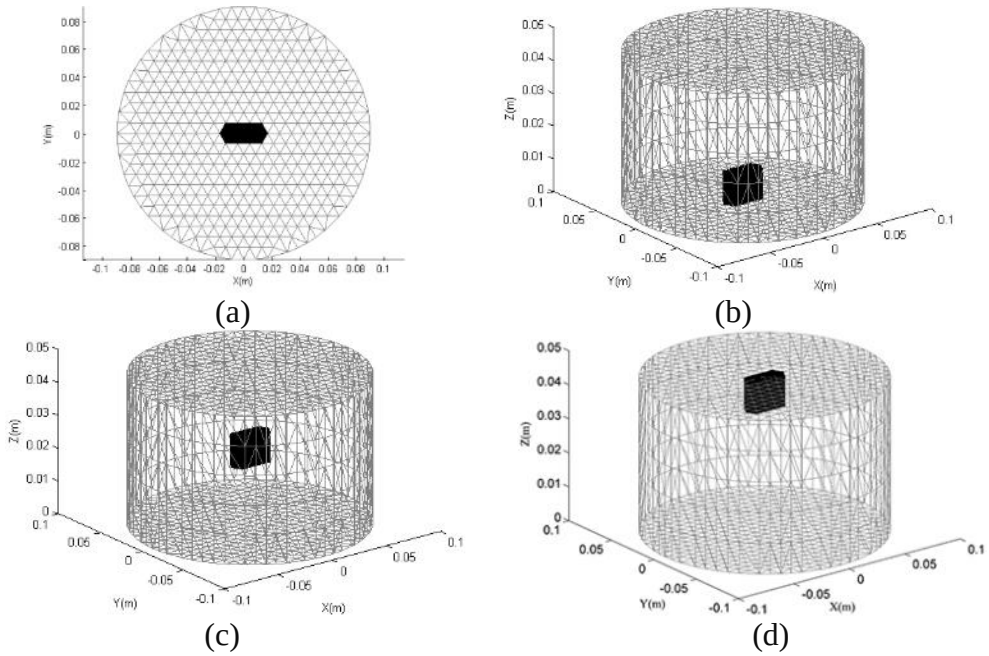

Figure 4. 3 Model 2. (a) The object in XY view. (b) the object in first layer. (c) the object in third layer. (d) the object in fifth layer.

Table 4. 1. Result of Model 2 for an object in the first layer

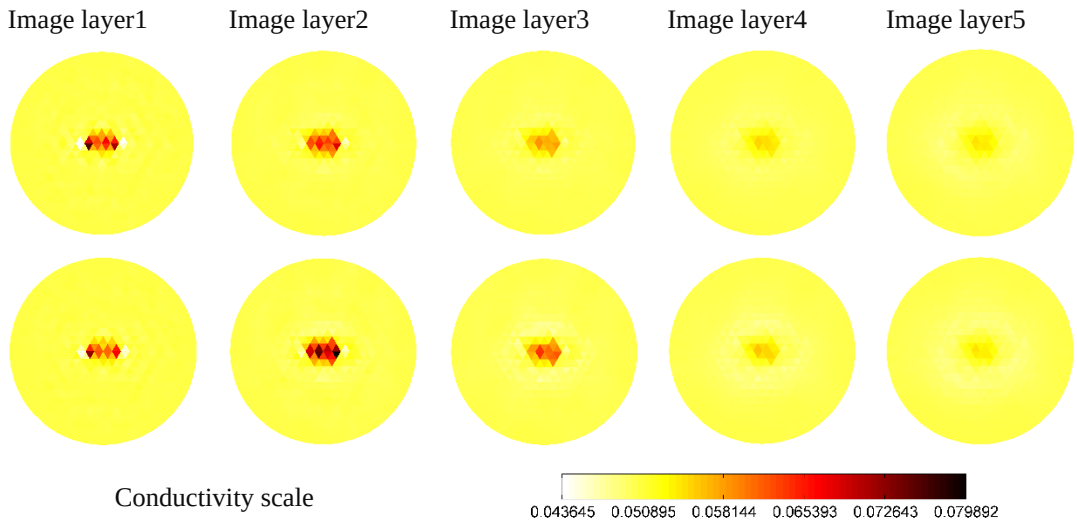

Table 4. 2. Result of Model 2 for an object in the third layer

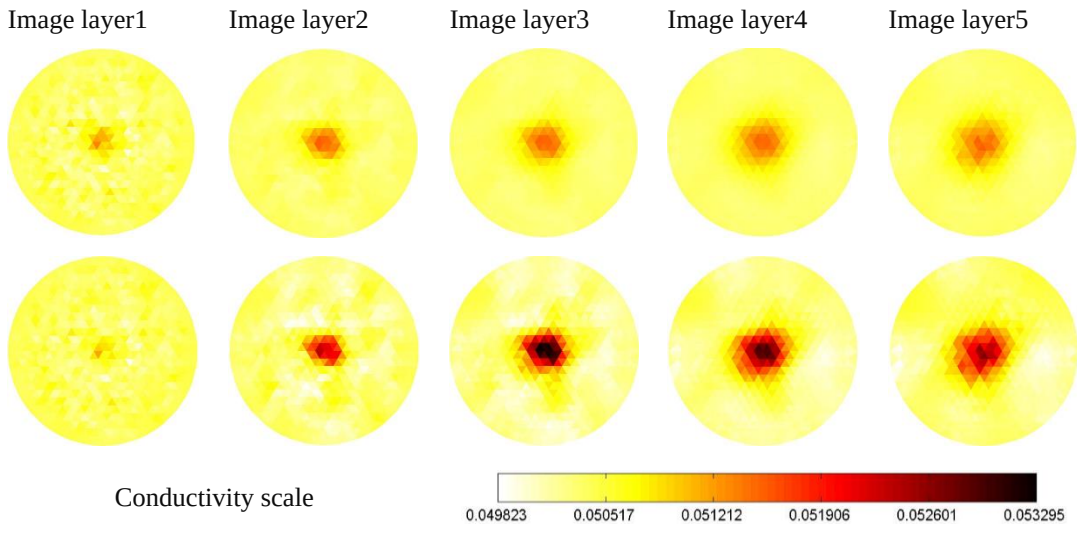

Table 4. 3 Result of Model 2 for an object in the fifth layer

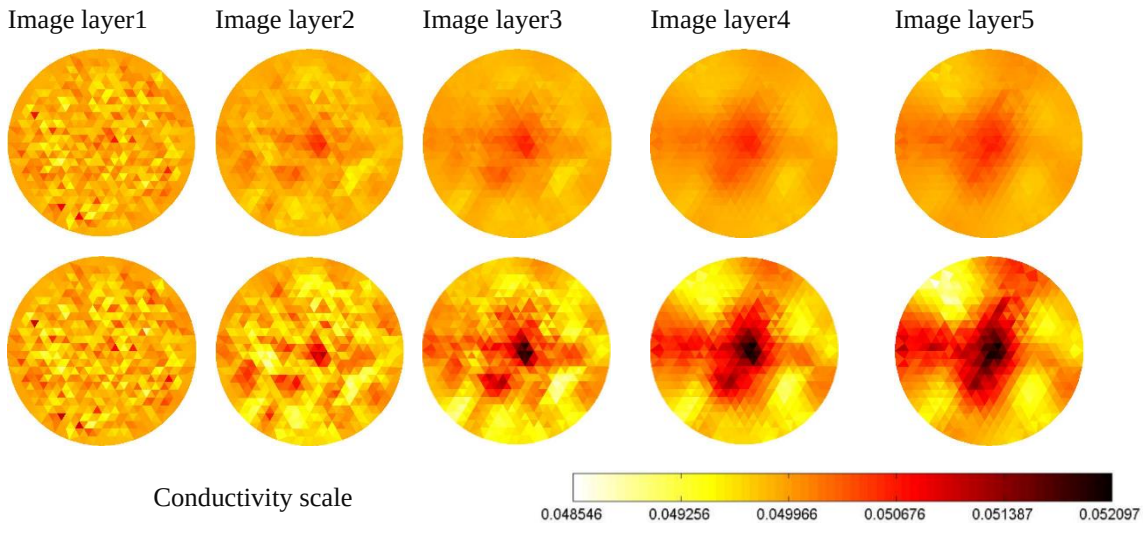

Table 4. 4. Comparison of the results

Model 2: an object in layer 1										
Algorithm	Former algorithm Equation					Enhanced algorithm Equation				
Conductivity scale	0.0436-0.0759 S/m					0.0446-0.0799 S/m				
Image Layer	1	2	3	4	5	1	2	3	4	5
Background conductivity (S/m)	0.05	0.05	0.05	0.05	0.05	0.05	0.05	0.05	0.05	0.05
Object conductivity (S/m)	0.08					0.08				
Image Contrast	1.4310	1.2970	1.2970	1.0884	1.0791	1.3392	1.4543	1.2245	1.0985	1.0508
Estimated object conductivity	0.0720	0.0651	0.0571	0.0542	0.0537	0.0674	0.0730	0.0610	0.0545	0.0532
Conductivity Error	0.0962					0.1222				

Model 2: an object in layer 3										
Algorithm	Former algorithm Equation					Enhanced algorithm Equation				
Conductivity scale	0.0494-0.0518 S/m					0.0493-0.0533 S/m				
Image Layer	1	2	3	4	5	1	2	3	4	5
Background conductivity (S/m)	0.05	0.05	0.05	0.05	0.05	0.05	0.05	0.05	0.05	0.05
Object conductivity (S/m)			0.08					0.08		
Image Contrast	1.0221	1.0285	1.0281	1.0270	1.0268	1.0136	1.0463	1.0708	1.0630	1.0508
Estimated object conductivity	0.0512	0.0515	0.0515	0.0514	0.0515	0.0503	0.0523	0.0538	0.0531	0.0526
Conductivity Error	0.1082					0.1046				

Model 2: an object in layer 5										
Algorithm	Former algorithm Equation					Enhanced algorithm Equation				
Conductivity scale	0.0495-0.0507 S/m					0.0491-0.0516 S/m				
Image Layer	1	2	3	4	5	1	2	3	4	5
Background conductivity (S/m)	0.05	0.05	0.05	0.05	0.05	0.05	0.05	0.05	0.05	0.05
Object conductivity (S/m)					0.08					0.08
Image Contrast			1.0104	1.0105	1.0103			1.0236	1.0259	1.0237
Estimated object conductivity			0.0504	0.0504	0.0504			0.0512	0.0514	0.0513
Conductivity Error	0.1103					0.1099				

Table 4. 1 to Table 4. 3 present the reconstructed conductivity of an object in different layers. According to Table 4. 1 to Table 4. 3, we can find that for the same level of noise, the image quality is affected by the object depth. If the object is close to the electrodes, the change of the electric field detected by the electrodes will be significant. The change of the electric field provided by the object is the useful information and if the object signal is much stronger than the noise, the impact of noise on the image quality will be very limited (Table 4. 1). However when the object is far from the electrodes, the change of the field detected by the electrodes will be very weak. Compared with the object signal, the noise becomes very significant, thus the image quality will deteriorate (Table 4. 3).

In Table 4. 1, both the former algorithm and the enhanced algorithm give clear images of the object. However in the result from the enhanced algorithm, there are 4 elements in image layer 2 that seem more conductive than image layer 1. This is due to

the ill-posed nature of the EIT inverse problem. For a planar electrode array, the measurement is a projection from the measurement volume. The boundary conditions only provide constraints in the plane of $Z=0$ (the plane of the electrodes) and there are no constraints in the Z direction. Therefore when performing image reconstruction, inevitably the change of the field in one particular layer will be projected into every layer. Different algorithms may result in differences in projections. In the case when the object is adjacent to the electrodes, the enhanced image reconstruction algorithm isn't superior to the former algorithm. However in practice, 1) the purpose is to detect the field change caused by a tumour and normally tumours are not adjacent to the electrodes; 2) the noise in the real measurements will be greater and more complicated than the simulated noise, which will worsen the image quality. For these conditions, the enhanced algorithm gives better performance. (This will be demonstrated by the results for the apple and agar phantom in Section 4.4.2.)

In Table 4. 2 and Table 4. 3, the images from the enhanced image reconstruction algorithm have a better 'conductivity contrast' (Seagar et al., 1987) or image contrast when the object is in layer 3 and 5. This point is quantitatively assessed in Table 4. 4. The conductivity scales of an object in layer 3 and 5 from the enhanced algorithm are 0.0493-0.0533 S/m and 0.0491-0.0516 S/m, compared with 0.0494-0.0518 S/m and 0.0495-0.0507 S/m from the former algorithm. The improvement of image contrast or conductivity contrast proves that the enhanced algorithm gives a much better performance or ability to distinguish the object from the background. In Table 4. 2, the result of the enhanced image reconstruction algorithm shows an obvious difference of conductivity contrast in each layer (the way to calculate the image contrast is introduced in Section 4.4.1.), which not only proves the improvement of algorithm accuracy but also provides the possibility to evaluate the vertical position of the object. For example, in the second row of Table 4. 2, the darkest area appears in the third layer, with an image contrast of 1.0708, which gives the biggest image contrast compared with the other layers in Table 4. 4. The estimated object conductivity in each layer, in Table 4. 4, is an average value of

all the conductivity values greater than a selected threshold. There is no obvious difference in the estimated conductivity value in each layer from the former algorithm when the object is in layer 3, however the enhanced image reconstruction algorithm gave the greatest values of the estimated object conductivity in the object layers in Table 4. 4. In Table 4. 3, when the object is far from the electrodes, the change of the field is not accurately detected under the influence of noise. In this case, the noise is very considerable and affects the detection of the object. The former image reconstruction algorithm hardly finds the object in the images; however using the enhanced image reconstruction algorithm, the object is detectable, although the shape and location of the object cannot be accurately determined.

Regarding the accuracy of the reconstructed conductivity image, because of the ill-posed nature, it is impossible to compute an accurate conductivity of the object. In fact the computed object conductivity will be much smaller than the real value. Referring to the models in Figure 4. 3, the volume of the object is small with a conductivity of 0.08S/cm; however in the reconstructed results, the image of the object spreads to a very large volume, especially in the vertical direction (Table 4. 1 to Table 4. 3). To make sure that the small volume and the large volume contribute to similar measurements, the large volume has to correspond to a much smaller conductivity than the small volume. The further the object is from the electrode plane, the larger is the spread in the reconstructed image volume; the larger the volume of the reconstructed object image spreads, the smaller the computed object conductivity is. This explains the reason that 1) the computed object conductivity is smaller than the real value for all cases in Figure 4. 3 and 2) the computed object conductivity decreases as the object moves further from the planar electrode array. Figure 4. 4 displays the error plots of the reconstructed conductivity. The error plot is a plot of the absolute values of $\boldsymbol{\sigma}_n - \boldsymbol{\sigma}$. The errors are from the object layer and along the direction of 9 o'clock to 3 o'clock. For example Figure 4. 4 (b) displays the error of the reconstructed conductivity on the x axis in layer 3 (refer to Figure 4. 3 for axis). When the object is in the first layer, the error plots of the two algorithms are very

close (Figure 4. 4 (a)). However when the object moves away from the planar electrode array, the errors from the enhanced image reconstruction algorithm become smaller than the errors from the former image reconstruction algorithm. Refer to Figure 4. 4 (b) and (c). The error plots of the reconstructed conductivity from the enhanced image reconstruction algorithm are generally beneath the error plots from the former algorithm. When the object is in Layer 3 and 5, the errors of the reconstructed conductivity from the enhanced algorithm are 0.1046 and 0.1099 compared with 0.1082 and 0.1103 from the former algorithm. Therefore in the cases when the object is not adjacent to the electrodes, the enhanced image reconstruction algorithm is more accurate.

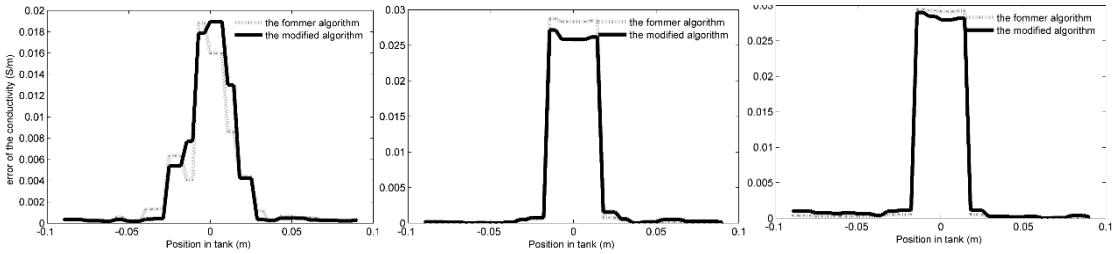

(a) (b) (c)

Figure 4. 4 The error of the reconstructed conductivity on the X axis in the object layer. (a) (b) and (c) correspond to the results from the object in Layer1, 3 and 5. The dashed lines indicate the error plots of the former algorithm. The full lines indicate the error plots of the enhanced algorithm.

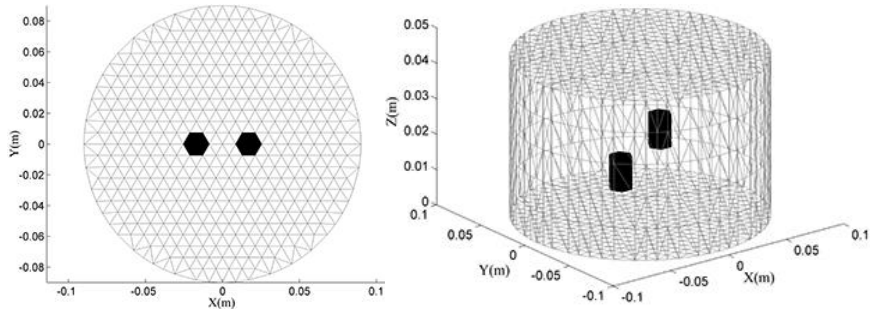

(a) (b)

Figure 4. 5 Model 3: two objects in different layers. (a) is the XY view. (b) is the XZ view. (c) is the 3D view

The conductivity scale in Table 4. 1, where the object is in layer 1, shows that the distribution of the conductivity values of the reconstructed result are very close to the model, but as the object moves away from the electrodes, as in Table 4. 2 and Table 4. 3, the range of the conductivity scale becomes smaller and the object conductivity gets

closer to the background conductivity. This illustrates the difficulty in using the planer array for deep lesion detection and also indicates that the lesions near the planar array strongly affect the electric field distribution, which may affect the detection of other remote lesions. To further validate the improvement of the enhanced algorithm, a model in Figure 4. 5 is used. The left object in Figure 4. 5 (a) is in the second layer; the same object is also positioned on the right-side in the third layer. In this simulation, the operating frequency is 500 kHz, the sampling frequency is 20MSa/s, the sample number is 100, SNR of 60dB white Gaussian additive noise and ±0.5% random multiplicative noise are added, and the ADC quantization is also incorporated. The imaging results are tabulated in Figure 4. 6. The enhanced algorithm gives a clear image of the left object and a relatively weak image of the right object; however the former algorithm doesn't visualize the right object even in its original third layer. These results prove that the enhanced algorithm is more accurate and sensitive than the former algorithm and it has some tolerance to the interference caused by objects near to the electrodes.

Table 4. 5 Results of two objects in tank

Image layer1	Image layer2	Image layer3	Image layer4	Image layer5
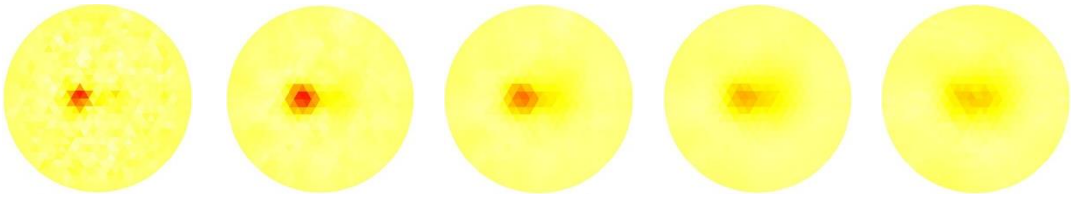				
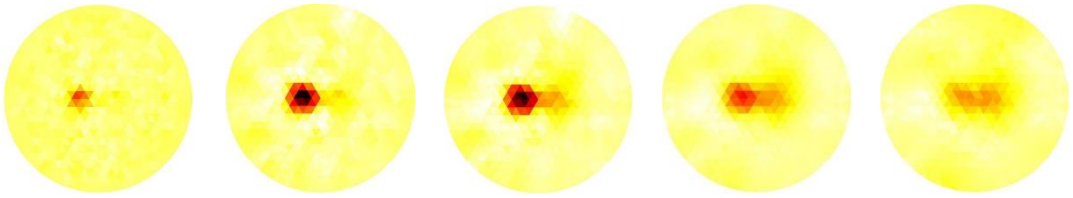				
Conductivity scale	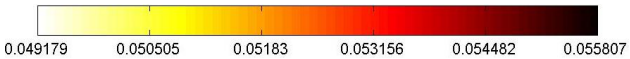			

Note: the result in the first row is from the former algorithm; the result in the second row is from the enhanced algorithm

4.4 Algorithm evaluation

4.4.1 Image processing based error analysis

To assess the new algorithm, a standard object is created, which is described by specified parameters. By comparing the parameters of the rebuilt image with the model, we can explore the shape and location accuracy of the object. Take an elliptic cylinder for example, which is described by the following equation:

$$\begin{cases} \dfrac{(x-x_0)^2}{a^2}+\dfrac{(y-y_0)^2}{b^2} \le 1 \\ |z-z_0| \le \dfrac{H}{2} \end{cases} \quad (4.16)$$

where a is the half length of the ellipse along the x axis, b is the half length of the ellipse along the y axis, $[x_0\ y_0\ z_0]$ is the center of the elliptic cylinder, H is the height of the elliptic cylinder. Assume that if we can get the relative parameters of the rebuilt image, we can quantitatively analyse the accuracy of the new algorithm in recovering the shape and the location of the object. Therefore the method to get the parameters of the rebuilt image is the key problem. In this section, an image processing based error analysis method is presented to solve this problem.

The image processing based error analysis method uses the following procedure. First of all, the conductivity map needs to be transformed into a picture; and then establish the conductivity value corresponding to the full width at half maximum (FWHM) of the conductivity distribution as a threshold; next, change the colour picture into a binary image according to the threshold value; then extract the edge of the binary image and finally evaluate the parameters of the rebuilt image. As an example, a model in Figure 4. 6 is used with its parameters given in Table 4. 6. The conductivity map of each layer is shown in Figure 4. 7. The conductivity map is then transformed into a picture with $201 \times$

201 pixels and then each layer is thresholded. A threshold T is defined as the conductivity value at FWHM. The results are shown in Figure 4. 8.

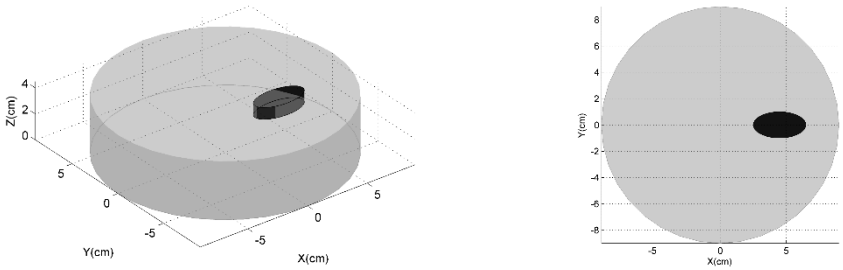

(a) (b)

Figure 4. 6. Model 4: Elliptic cylinder in layer 3 at 3 O'clock position; (a) is the 3D view; (b) is the XY view.

Table 4. 6. Model parameters

Tank Parameters	Shape	Cylinder	object	shape	elliptic cylinder
	Radius	9cm		Horizontal Center [x_0 y_0](cm)	[4.5 0]
				Vertical center	Layer 3
	Height	4.5cm		Half length and width [a b](cm)	[2 1]
Number of layers		5		Height (cm)	0.9
Background conductivity		0.5 mS/cm		Conductivity (mS/cm)	0.8

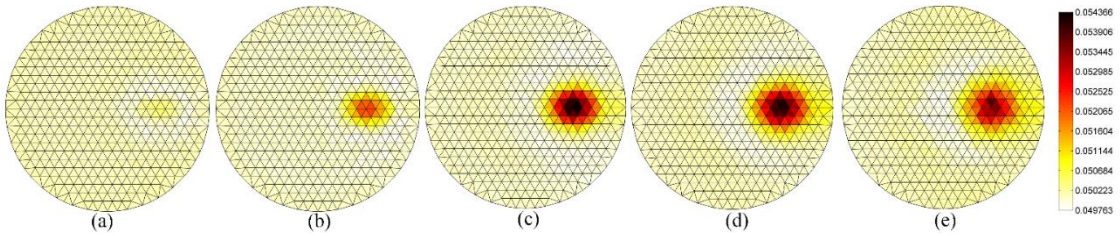

Figure 4. 7. Image of elliptic cylinder in layer 3 at 3 O'clock position. (a)~(e) indicates the image from layer 1~5

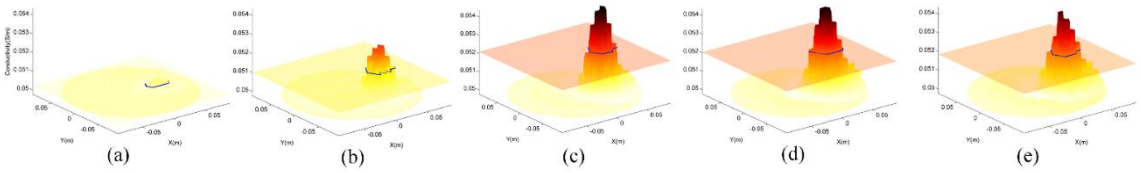

Figure 4. 8. Conductivity distribution and FWHM. (a)~(e) indicate the image from layer 1~5. The blue rings indicate the FWHM. The value of the circle is the threshold.

It is assumed that the vertical centre of the object is related to the image contrast of

each layer: the object is most likely to be located in the layer with the highest contrast. The expression for image contrast c is :

$$c = \frac{\bar{\sigma}_{Obj}}{\bar{\sigma}_{Bg}} \quad (4.17)$$

where $\bar{\sigma}_{Obj}$ is the average of σ greater than threshold T, $\bar{\sigma}_{Bg}$ is the average of σ smaller than threshold T. By comparing the contrast in each layer, the probability of the object centre being in a particular layer can be analysed using the following equation:

$$p_l = \frac{c_l}{\sum_{l=1}^{L} c_l} \quad (4.18)$$

where p_l is the probability of the object centre being in the *l*th layer; c_l is the normalized image contrast of the *l*th layer.

Table 4. 7. Probability analysis of the object centre in each layer

Image Layer	1	2	3	4	5
Conductivity threshold	0.0504	0.0513	0.0521	0.0521	0.0519
Image contrast	1.0110	1.0390	1.0597	1.0554	1.0504
Conductivity threshold normalization	0	0.5636	1.0000	0.9481	0.9272
Image contrast normalization	0	0.5748	1.0000	0.9117	0.8084
Probability of object centre in layer	0%	17.4%	30.3%	27.2%	24.5%

Table 4. 8. Parameter comparison

	x_0 (cm)	y_0(cm)	z_0(cm)	a(cm)	b(cm)	H(cm)
Model	4.5	0	Layer 3	2	1	0.9
Rebuilt image	4.34	1.06×10^{-2}	Layer 3	1.83	1.56	
Error	-0.16	1.06×10^{-2}	0	-0.17	0.56	

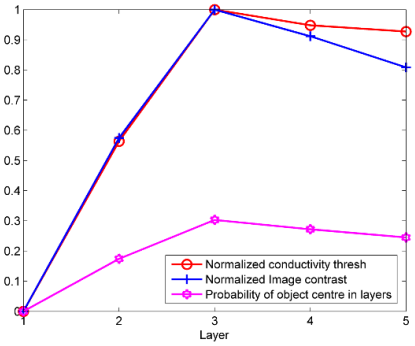

Figure 4. 9. Normalized conductivity threshold, image contrast and position probability

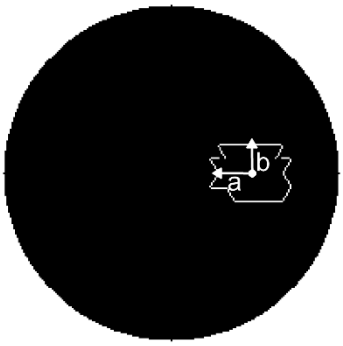

Figure 4. 10. Edge of the image in layer 3

Table 4. 7 and Figure 4. 9 show the contrast, conductivity threshold, and probability for the object centre for each layer. The highest image contrast is in layer 3 and the biggest probability for the object centre is located in layer 3, which is identical with the model. Assume that the object is located at the highest image contrast layer (the greatest probability layer for the object centre), other parameters can be found by edge extraction. See Figure 4. 10. The point within the edge outline is the centre $[x_0\ y_0]$ equal to $[4.34\ 1.06 \times 10^{-2}]$ (cm). The length and width $[a\ b]$ are equal to $[1.83\ 1.56]$ (cm). Please refer to Table 4. 8.

4.4.2 Result comparison based on phantoms

Figure 4. 11 shows an apple and agar phantom. The apple is placed in between 7 and 8 o'clock with an unknown conductivity. The agar is placed in between 4 and 5 o'clock with a conductivity of 0.2 S/m. Both objects are 3.7 cm in diameter. The height of the agar is 1.5 cm. The tank height is set to 4.5 cm. The apple is almost the same height as the tank. The conductivity of the saline is 0.05 S/m. The results from both of the algorithms are shown in Table 4. 9, which corresponds to an operating frequency of 50 kHz. There are 2 iterations for the former algorithm and 1 iteration for the enhanced algorithm. The dark area on the left hand side indicates the position of the apple; the bright area on the right hand side indicates the position of the agar. From the results, we can find

that 1) the conductivity of the apple at 50 kHz is smaller than 0.05 S/m; 2) the signal from the agar is stronger than that from the apple, which affects the detection of the apple.

Assume that the conductivity of the agar is constant at different frequencies; however the apple is a biological object whose conductivity is related to the frequency of the external excitation. Considering that the conductivity of the apple changes as the operating frequency changes, the ratio image of two reconstructed results at two different frequencies will show the conductivity changes of the apple with values greater or smaller than 1; however for the agar and the saline, there should be no obvious changes, with values approximately equal to 1. Using ratio images to visualize the objects of interests is an idea stemming from EIT multi-frequency imaging. The ratio images for the two algorithms are shown in Table 4. 10, which are evaluated by dividing the conductivity at 100 kHz by the conductivity at 10 kHz. By using the ratio images, for both algorithms, the apple is clearly presented and the influence from the agar is nearly excluded; the performance of the enhanced algorithm is better, as the image of the apple is clearer and the image of the agar is removed.

Figure 4. 11. The apple and agar phantom.

Table 4. 9. Result of the apple and agar phantom.

Image layer 1	Image layer 2
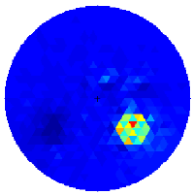	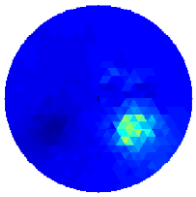
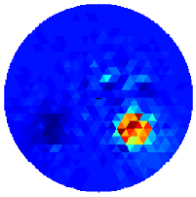	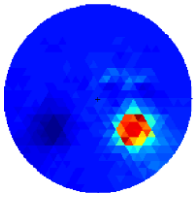
Conductivity scale 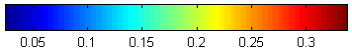	

Note: the result in the first row is from the former algorithm; the result in the second row is from the enhanced algorithm

Table 4. 10 Ratio images of the phantom of apple and agar

Image layer 1	Image layer 2	Ratio scale
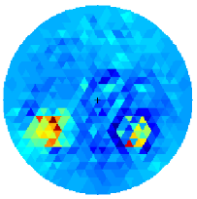	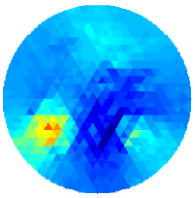	
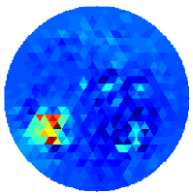	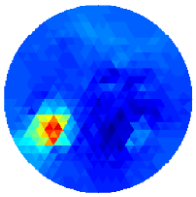	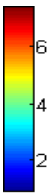

Note: the result in the first row is from the former algorithm; the result in the second row is from the enhanced algorithm.

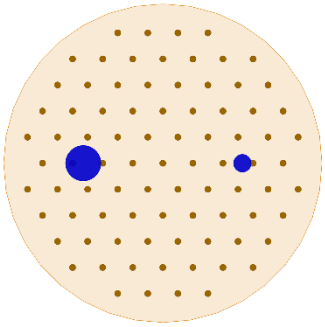

Figure 4. 12. Phantom with two agars

Table 4. 11. Results of the phantom with two agars

Image layer 1	Image layer 2	Image layer 3
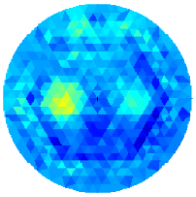	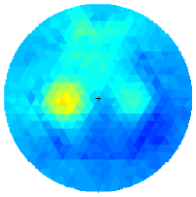	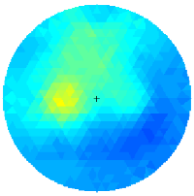
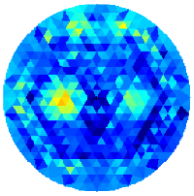	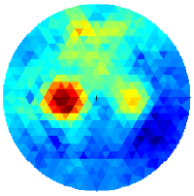	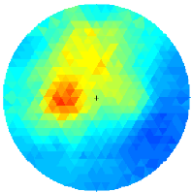
Conductivity scale	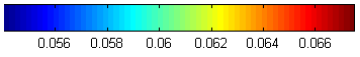	

Note: the result in the first row is from the former algorithm; the result in the second row is from the enhanced algorithm

Figure 4. 12 shows a phantom of a real experiment with two cylinders of agar placed at 9 o'clock and 3 o'clock. The two objects are placed approximately half-way along the radius of the tank and 1 cm away from the bottom. The heights of the agar phantoms are 2.5 cm. The diameters of the agars at 9 and 3 o'clock are 2 cm and 1 cm respectively. The conductivity of the two agars is 0.1 S/m. The height of the tank is 4.5 cm. There are 2 iterations for the former algorithm and 1 iteration for the enhanced algorithm. Table 4. 11

shows the reconstruction results at 500 kHz. From the results, the following conclusions are made: 1) the big object, which produces stronger signals, will affect the detection of the small object, which produces weaker signals; 2) the enhanced algorithm performs better in detecting the small object.

4.4.3 Result comparison based on patients

In a clinical trial, the situation is far more complex than simulations and phantoms, due to the noise from the EIT system and the complicated structure of a real breast; therefore the results are not as clear as those in the previous section. A clinical result for Patient 0703, whose left breast has a tumour, is given. The X-ray images are shown in Figure 4. 13. The cup size of the patient is C. In the clinical trial, the tank height is set to 1.8cm. In image reconstruction, there are 2 layers in the 3D mesh. The EIT cross-sectional images from the two algorithms are shown in Table 4. 12 using data produced at a current frequency of 1MHz. The result in the first row is from the former algorithm with 3 iterations. The result in the second row is from the enhanced algorithm with 1 iteration.

It seems that the red elements highlighted with a red circle in Table 4. 12 indicate that a tumour is present. However to make sure of this, we need to find the position of the breast and compare the EIT images with the X-ray images. Assume that the conductivity of the saline is constant with frequency, but the conductivity of the breast changes as the frequency changes. Therefore if dividing the reconstructed conductivity using an operating frequency ‘A’ by the reconstructed conductivity using a different frequency ‘B’, the values of the elements close to 1 will indicate the saline and the others will indicate breast. Figure 4. 14 shows the image ratio of the conductivities at 10 kHz and 200 kHz (dividing the 10 kHz image by the 200 kHz image). Since the conductivity of the adipose tissue increases as the frequency increases, the dark circle (where the value is smaller than 1) in Figure 4. 14 indicates the region where fat gathers. It should be emphasized that: the

dark ring is not the exact shape of the fat due to the non-local property of the EIT image and the size of the mesh elements; it indicates the region having the most fat. Figure 4. 15 is a combination of the outline of the dark rings and the cross-sectional conductivity image using the enhanced algorithm. It shows that the tumour is on the fat. Let's refer to the X-ray image, LCC in Figure 4. 13. The tumour is on the boundary of the fat. As we press the breast into the chest and observe the tumour in the chest-to-nipple direction, the tumour is exactly on the fat, thus the result from the MK4 system is consistent with the X-ray images.

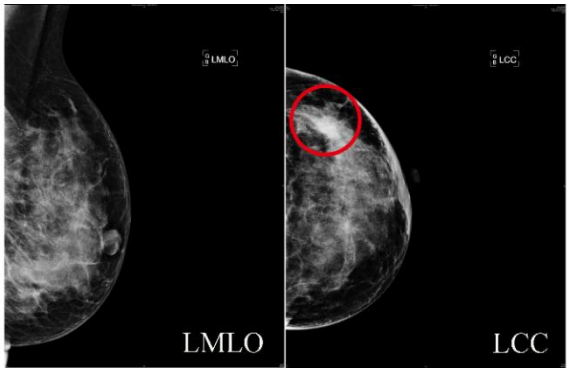

Figure 4. 13 X-ray images of Patient 0703, left breast.

Table 4. 12. Results of patient 0703

Image layer 1	Image layer 2
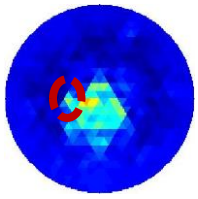	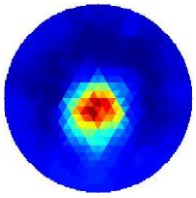
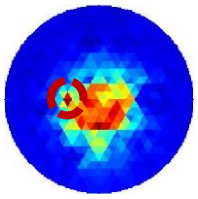	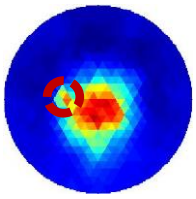
Conductivity scale	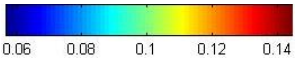

Note: the result in the first row is from the former algorithm; the result in the second row is from the enhanced algorithm

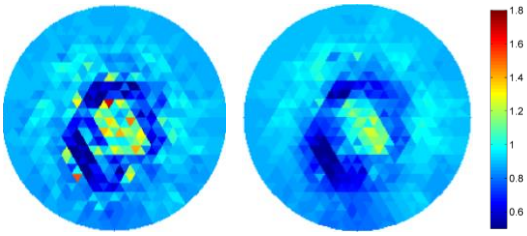

Figure 4. 14. Image of the conductivity ratio at 10KHz and 200KHz. The left cross-sectional image is for the first layer. The right cross-sectional image is for the second layer

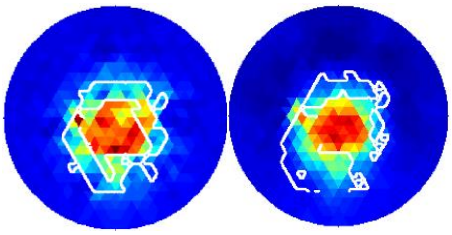

Figure 4. 15. The combined image of the dark ring and the conductivity image from the enhanced algorithm. The white lines are the outlines of the dark ring in Figure 4. 14.

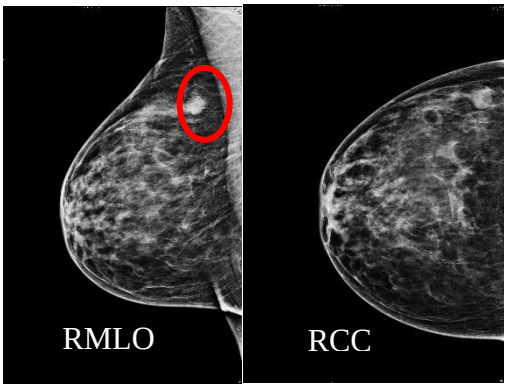

Figure 4. 16 X-ray images of Patient 0700, right breast.

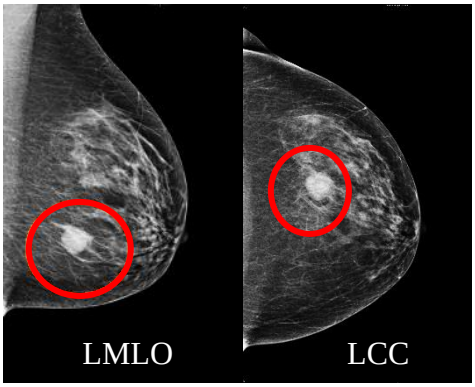

Figure 4. 17. X-ray images of Patient 0725, left breast

Table 4. 13. Results of Patient 0700

Image layer 1	Image layer 2	Image layer 3
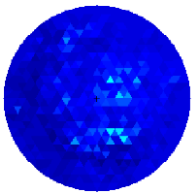	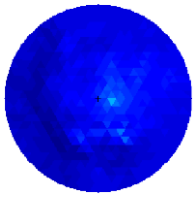	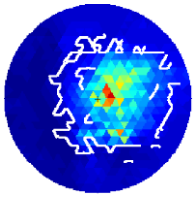
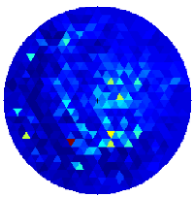	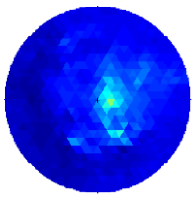	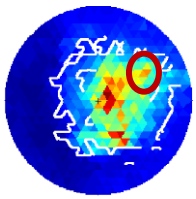
Conductivity scale	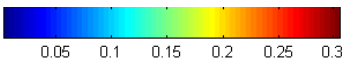	

Note: the result in the first row is from the former algorithm; the result in the second row is from the enhanced algorithm

Table 4. 14 Results of Patient 0725

Image layer 1	Image layer 2
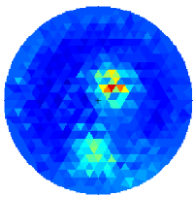	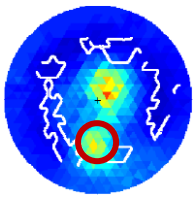
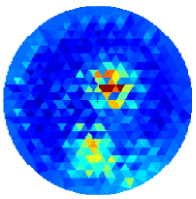	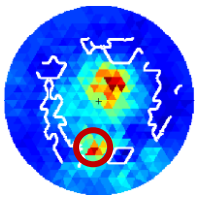
Conductivity scale	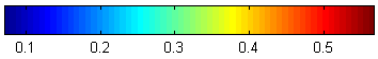

Note: the result in the first row is from the former algorithm; the result in the second row is from the enhanced algorithm

Using the same method, the reconstructed conductivity maps of Patient 0700 and 0725 are presented in Table 4. 13 and Table 4. 14. Patient 0700 has a tumour in her right breast. According to the X-ray images in Figure 4. 16, 1) the mammary gland is denser in the upper outside quadrant (UOQ) of the breast; 2) the tumour is close to the armpit. The cup size of Patient 0700 is D. In the clinical trial, the tank height is set to 2.6 cm. In image reconstruction, the whole tank is reconstructed in 3 layers. The reconstructed conductivity distributions of the two algorithms at 200 kHz are shown in Table 4. 13, where the white lines in the images indicate the estimated boundary of the adipose tissue. Compared with Patient 0703, it is more challenging to detect the tumour of Patient 0700, as the tumour is far from the electrode array and close to the dense gland area. Both the algorithms produce greater conductivities in the UOQ. This is consistent to the X-ray images, that gland is denser in the UOQ; however the enhanced algorithm performs better, as it clearly images the tumour in the third layer, which is highlighted by the red circle in Table 4. 13, while the tumour is missed by the former algorithm. The enhanced algorithm locates the tumour at 2 o'clock, which is the direction of the armpit and next to the boundary of the adipose tissue. This location is consistent with the X-ray images. Thus the following conclusions are made: 1) the enhanced algorithm performs better in detecting the remote tumour; 2)

by using the enhanced algorithm, the reconstructed conductivity distribution of Patient 0700 is consistent with the X-ray images.

Patient 0725 has a tumour in her left breast. According to the X-ray images in Figure 4. 17, 1) the mammary gland tissue is denser in the cranial breast (LMLO in Figure 4. 17); 2) the tumour is in the caudal breast (LMLO in Figure 4. 17); 3) if we were the patient and we observed the left breast, the convergence of the mammary gland to the nipple would be to the right side of the tumour (LCC Figure 4. 17).The cup size of Patient 0725 is C. In the clinical trial, the tank height is set to 1.8 cm. In image reconstruction, the tank is divided into 2 layers. Table 4. 14 shows the reconstructed results at 500 kHz. The bright area in the upper quadrants is caused by the dense normal gland tissue in the cranial breast. The red elements at about 6 o'clock highlighted with red circles in Table 4. 14 indicate the presence of the tumour. The white lines indicate the estimated boundary of the adipose tissue. The dense gland ducts in the cranial breast converge to the nipple and they are closer to the electrode array than the tumour, therefore they produce a strong signal and cause a red area at the upper, left side of the image of the tumour in the image layer 2 of the enhanced algorithm. Assuming that Patient 0725 lies in a prone position with the left breast pressed to the chest wall, the tumour will be to the south of the dense gland area and close to the boundary of the adipose tissue. By comparing the EIT images with the X-ray images, it shows that the results from MK4 are reliable. Also the enhanced algorithm performs better in distinguishing the tumour from the normal tissue.

4.5 Conclusion

In the simulations and the real case of phantoms and patients, the enhanced image reconstruction algorithm using the duo-mesh method has proven more accurate and sensitive than the former algorithm and effective in improving vertical resolution. Although this new algorithm is developed for the Sussex MK4 EIM system, the idea of using a correction strategy in the image reconstruction algorithm is relevant to any EIT

image reconstruction equipment - regardless of the hardware design. Despite the limitation in detection of the depth and height of the object, with the new algorithm the planar electrode array can generate a more accurate 3D image and roughly estimate the depth of the object. The image processing based error analysis method provides an intuitive and accurate method to evaluate the image reconstruction algorithm and outline the shape of the object of interest.

5. Digital Breast Phantom

5.1 introduction

Before entering clinical trials, the performance of the EIT systems were studied using various phantoms, which include agars, electric phantoms, and biological tissues (Gagnon et al., 2010, Holder et al., 1996, Sadleir et al., 2013); however these phantoms are not as complicated as a real breast, as a result, the experiments will be far from the real clinical trials.

This chapter will introduce a method to program a close-to-realistic digital breast phantom, which is composed of skin, fat, ducts, acini, a gland area, a nipple and a tumour (or tumours). This digital breast phantom is valuable in the mock clinical situation as it provides unlimited data for EIM system assessment and helps to set the tumour detection requirements for a particular EIM system (for example the detectable tumour size, depth, and the conductivity contrast between the tumour and the surrounding normal tissue). Although the data from the volunteers, diagnosed with breast cancer by x-ray or other methods, is very valuable, it cannot provide the real 3D information of the breast structure to precisely assess the EIM. For example, .mammography can only produce 2D projection images at particular angles; without an accurate 3D knowledge of the breast as a reference, it is very challenging to give an accurate analysis of the performance of EIM systems. Also, clinical trials are very expensive, and the available patient data is far from adequate to access EIM systems' performance. In this situation, close-to-realistic digital breast phantoms are more efficient and economical. However, it should be emphasised that digital breast phantoms are valuable in system assessment, but they are not replacements for clinical trials.

The method to set up a digital breast phantom is introduced in the following sections, in the order of the tank, breast envelope and nipple, ducts, acini, gland area and tumour.

5.2 Model

For the MK4 system, the breast is confined in the tank and pressed by the planar electrode array, therefore the shape of the breast is relevant with the tank. Figure 5. 1 presents a digital breast phantom in the tank of the MK4 system. The height of the tank is 3 cm. The pink structure indicates the skin envelope. The diameter of the contact area between the breast skin and the bottom of the tank is 9cm. The maximum diameter of the breast is 15cm. The thickness of the skin is 1.55 mm (Sutradhar and Miller, 2013). The space between the skin and the tank is filled with saline. The ducts are arranged in a tree shape. The acini are connected with the terminal ducts. A gland area wraps the ducts and the acini. The region between the gland area and the skin indicates fat. In the following sections, detailed methods to build this digital breast phantom will be introduced in the order of tank, skin envelope, ducts, acini, gland area and tumour.

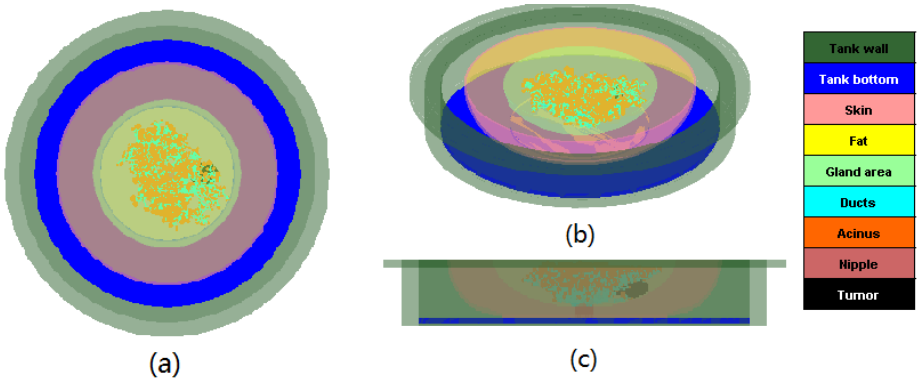

Figure 5. 1. A digital breast phantom in tank.

5.2.1 Modelling of the tank

The most important parameters of the tank are the depth and the diameter, which defines the boundary of the field under investigation. The tank is simulated by a hollow cylinder with an internal diameter of 18 cm and an external diameter of 20 cm. The depth of the tank is determined by the position of the planar electrode array. For the case in

Figure 5. 1, the depth is 3 cm. The reference plane is chosen on the surface of the planar electrode array as shown in Figure 5. 2 (c).

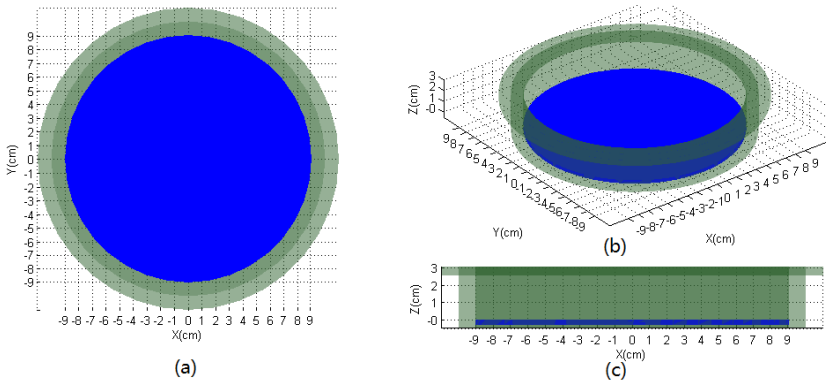

Figure 5. 2. The tank

5.2.2 Modelling of the breast envelope and nipple

The skin envelope, shown in Figure 5. 3, is defined by a portion of an ellipse, with the top at the maximum cross section and bottom at another cross section, which is h cm beneath the maximum one, where h is the height of the breast (or the depth of the tank). Assuming that the maximum diameter of the breast is d_1, the contact diameter is d_2, the skin envelope is defined by the following ellipsoid formula:

$$\begin{cases} \dfrac{x^2}{\left(\frac{d_1}{2}\right)^2} + \dfrac{y^2}{\left(\frac{d_1}{2}\right)^2} + \dfrac{(z-h)^2}{c^2} = 1 \\ 0 \le z \le h \end{cases} \quad (5.1)$$

where c is the semi-axis length along the Z axis,

$$c = \frac{h}{\sqrt{1 - \left(\frac{d_2}{d_1}\right)^2}} \quad (5.2)$$

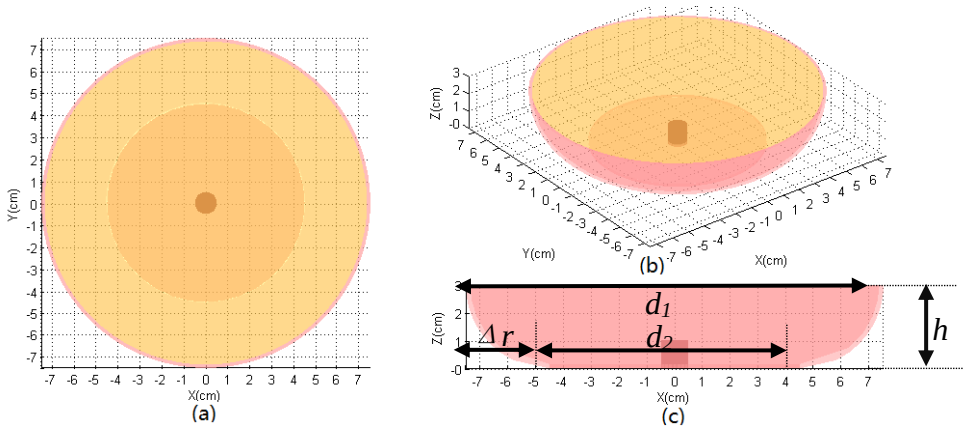

Figure 5. 3. The breast envelope and nipple

During examination, the breast is pressed flat in the tank, therefore we assume that the nipple is pushed into the breast. The nipple is simulated by a cylinder with a diameter of 10 mm and a projection of 10 mm (Hussain et al., 2003). The bottom of nipple is placed at [0, 0, 0], which is shown in Figure 5. 3.

5.2.3 Modelling of the ducts

Normally, there are 14 to 18 lactiferous lobes (mammary ducts) converging to the nipple in an adult breast. Each lactiferous lobe follows a tree branching pattern. Thus in the phantom, a network of cylinders, arranged in a tree shape, is used to simulate the ducts. The number of the major ducts, which are the first generation ducts developing from the nipple, is a random value between 14 and 18. The lengths of the major ducts have random values from 6mm to 8 mm; the diameters of the major ducts have random values between 2.0 mm and 4.5 mm. The major ducts are arranged as shown in Figure 5. 4 (a), with one duct vertically in the centre and the other ducts equally distributed around a circle and inclined to the XY plane at a certain angle. Figure 5. 4 shows a case of 16 major ducts, where the blue lines in (a) indicate directions and the lengths of the major ducts; (b) shows the real phantom. The start positions of the major ducts are at the surface of the nipple.

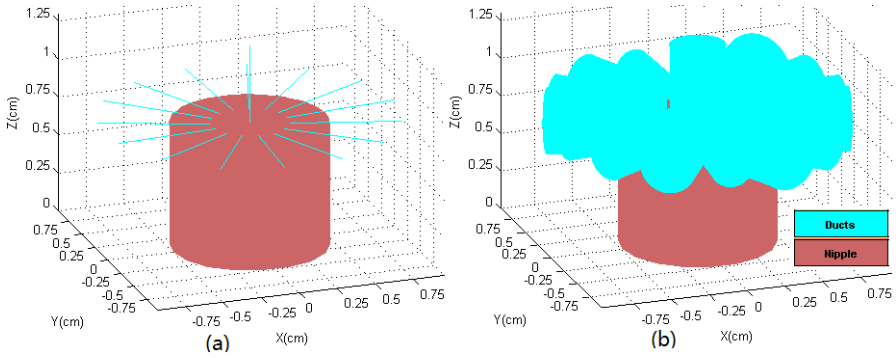

Figure 5. 4 The major ducts. (a) is a schematic diagram showing the direction and the length of the major ducts; (b) shows the real ducts in the digital phantom.

Table 5. 1 Parameters of the nipple and major ducts

Nipple	
Diameters of the nipple d_N	10 mm
Projection (height) of the nipple h_N	10 mm
Start Position	[0 0 0]
Major Ducts	
Number of the major ducts N_{MD}	14 ~ 18
Diameters of the major ducts d_{MD}	2.0 ~ 4.5 mm
Lengths of the major ducts l_{MD}	6 ~ 8 mm
Start position of the vertical major duct	[0, 0, h_N]
Start positions of the inclined major ducts	$\left[\frac{d_N}{4} * \cos\theta, \frac{d_N}{4} * \sin\theta, h_N\right]$ $\theta = \frac{2\pi}{N_{MD}-1} * (i-1), i\epsilon[1 \quad 2 \quad \cdots \quad N_{MD}-1]$

In the next generation, the number of the branches is a random value from 3 to 5; the lengths and the diameters of the ducts randomly decrease. Let l_{Gi} and d_{Gi} be the length and the diameter of the duct of *i*th generation, the length and diameter of its branches are:

$$l_{Gi+1} = r * l_{Gi} + (1-r) * l_{Gi} * rand \qquad (5.3)$$

$$d_{Gi+1} = d_{Gi} * \frac{l_{Gi+1}}{l_{Gi}} \qquad (5.4)$$

where $r \in (0,1)$, r controls the branch's length. Usually r is set to 0.5 in the program. $rand$ denotes a random value between 0 and 1. To make sure that the branches grow upward, 1) the direction of the branches should form an acute angle with the direction of

its parent (former) generation and 2) the branches' ends can't be lower than their origins. The direction of the branches are obtained by the following steps:

1) Assume that the start and end positions of the parent generation are $[x_{Gi0}, y_{Gi0}, z_{Gi0}]$ and $[x_{Gi1}, y_{Gi1}, z_{Gi1}]$, then we will obtain the direction of the parent generation $\boldsymbol{v0} = [x_{Gi1} - x_{Gi0}, y_{Gi1} - y_{Gi0}, z_{Gi1} - z_{Gi0}]$. Knowing the diameter and the length of the next generation branch, firstly, plot it along Z axis ([0, 0, 1]) as shown in Figure 5. 5 L1, therefore the state and end positions of L1 are $[x_{Gi1}, y_{Gi1}, z_{Gi1}]$ and $[x_{Gi1}, y_{Gi1}, z_{Gi1} + l_{Gi+1}]$.

2) Rotate L1 to L2 to make the branch in the same direction as its parent duct. The direction of the rotation axis is:

$$\boldsymbol{v1} = \boldsymbol{v0} \times [0,0,1] \tag{5.5}$$

The rotation degree is

$$\theta_1 = \frac{\boldsymbol{v0} \cdot [0,0,1]}{|\boldsymbol{v0}|} \tag{5.6}$$

where $\boldsymbol{v1} = [v_{1x}, v_{1y}, v_{1z}]$ is a vector perpendicular to the plane defined by Gi, L1 to L2. Given the rotation axis $\boldsymbol{v} = [v_x, v_y, v_z]$, the rotation degree θ and the rotation center $[x_0, y_0, z_0]$, the rotation equation is:

$$[x' \quad y' \quad z'] = [x - x_0 \quad y - y_0 \quad z - z_0]rot + [x_0 \quad y_0 \quad z_0] \tag{5.7}$$

where $[x_0 \quad y_0 \quad z_0]$ denotes the original coordinates, $[x' \quad y' \quad z']$ denotes the rotated coordinates, rot is the rotation matrix:

$$rot = \begin{bmatrix} C + {v_x}^2(1-C) & v_x v_y(1-C) - v_z S & v_x v_z(1-C) + v_y S \\ v_x v_y(1-C) + v_z S & C + {v_y}^2(1-C) & v_y v_z(1-C) - v_x S \\ v_x v_z(1-C) - v_y S & v_y v_z(1-C) + v_x S & C + {v_z}^2(1-C) \end{bmatrix} \quad (5.8)$$

where $C = \cos\theta$, $S = \sin\theta$, $v_x = v_x/|\boldsymbol{v}|$, $v_y = v_y/|\boldsymbol{v}|$, $v_z = v_z/|\boldsymbol{v}|$. Using (5.7), the end position of L2 $[x_2, y_2, z_2]$ can be computed

3) Let the direction and the start position of L2 be the rotation axis and rotation centre of $\boldsymbol{v1}$ and make $\boldsymbol{v1}$ rotate a random angle, then we can get $\boldsymbol{v2}$. $\boldsymbol{v1}$, $\boldsymbol{v2}$ and o define a plane, which is perpendicular to L2. Rotating L2 a random acute angle θ_2 toward the $v_1 o v_2$ plane will make sure that the new branches do not grow backward to their parent generation. The rotation axis is V2, the rotation centre is o. The end position of the branch $[x_{Gi1+1}, y_{Gi1+1}, z_{Gi1+1}]$ can be computed by (5.7). If θ_2 causes $z_{Gi1+1} < z_{Gi1}$, make $\theta_2 = -\theta_2$.

Figure 5. 6 shows the gland ducts, which are created using the above method, in which the red trace indicate one route of the ducts

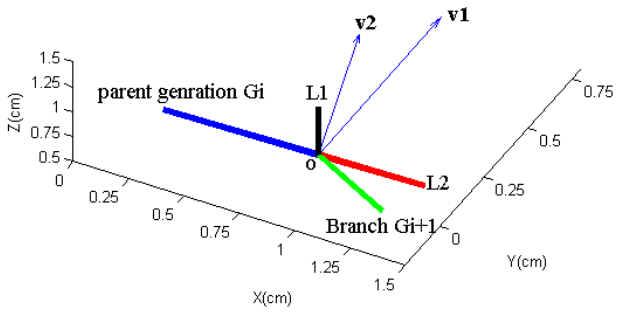

Figure 5. 5. Branch direction

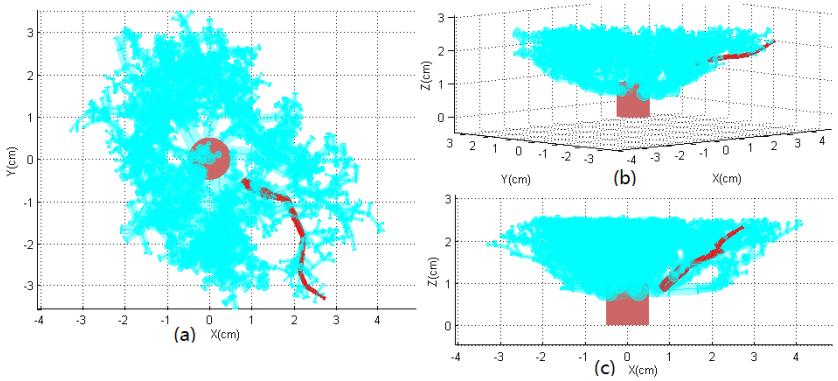

Figure 5. 6. The gland ducts. The red trace illustrates one route of the ducts

5.2.4 Modelling of the acini

Acini are simulated by spheres, which are connected with the terminal ducts, as shown in Figure 5. 7. The centres of the acini are in the extension of the central axis of the terminal ducts (the red dots in Figure 5. 7). The diameter of the acini d_A are defined by the following equation:

$$d_A = r_A d_{TD} \tag{5.9}$$

where r_A are ratios between the diameter of the acini and the diameter of the terminal ducts. In simulations, we usually make $r_A = 2$. The acinus distribution in the digital breast phantom is shown in Figure 5. 8.

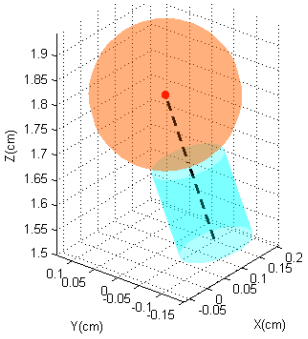

Figure 5. 7. Acinus and terminal duct

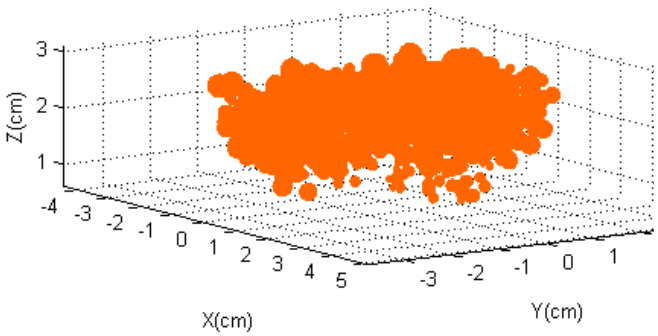

Figure 5. 8. Acini in the breast phantom

5.2.5 Modelling of the gland area

The gland area indicates the tissue that is more conductive than the adipose tissue but less conductive than the gland tissue (including ducts and acini). The gland area is simulated by a semi ellipsoid:

$$\begin{cases} \dfrac{x^2}{\left(\frac{d_{GA}}{2}\right)^2} + \dfrac{y^2}{\left(\frac{d_{GA}}{2}\right)^2} + \dfrac{(z-h)^2}{(h-h_N)^2} = 1 \\ z \le h \end{cases} \quad (5.10)$$

where d_{GA} is the diameter of the gland area, h is the height of the breast, h_N is the height of nipple. These parameters are shown in Figure 5. 9.

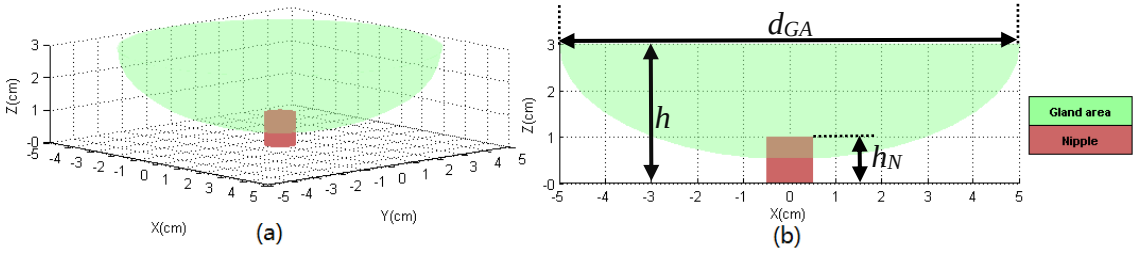

Figure 5. 9. Gland area

5.2.6 Modelling of the tumour

Tumour is simulated by an ellipsoid or a group of ellipsoids as shown in Figure 5. 10 (a) and (b). Figure 5. 10 (a) is defined by:

$$\frac{(x-x_0)^2}{a^2} + \frac{(y-y_0)^2}{b^2} + \frac{(z-z_0)^2}{c^2} = 1 \quad (5.11)$$

where $[x_0, y_0, z_0]$ denotes the centre of the tumour, a, b, and c denote the half lengths of the tumour along the X, Y, and Z axis. Figure 5. 10 (b) is defined by 9 ellipsoids with

an ellipsoids in the centre and the other ellipsoids surrounding around. The centres of the surrounding ellipsoids is on the surface of the centre ellipsoid.

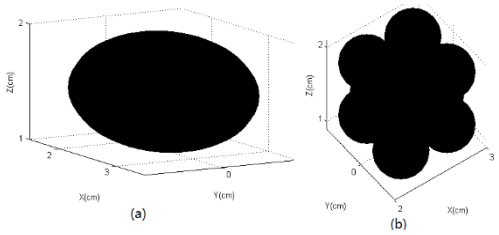

Figure 5. 10. Tumour

5.2.7 Discretization of the digital breast phantom

After setting up the digital breast phantom, we need to discretize it using the 3D mesh of the forward problem. The conductivity values of the mesh elements are equal to the conductivity at their centres. Firstly, we need to compute the coordinates of the centres of the mesh elements; and then we need to determine the structures that the centres of the elements belong to. When the value of the mesh elements are determined, the priority of the search sequence of the structures is: tumour, acini, nipple, ducts, gland area, skin, saline and fat. The discretized breast phantom is shown in Figure 5. 11.

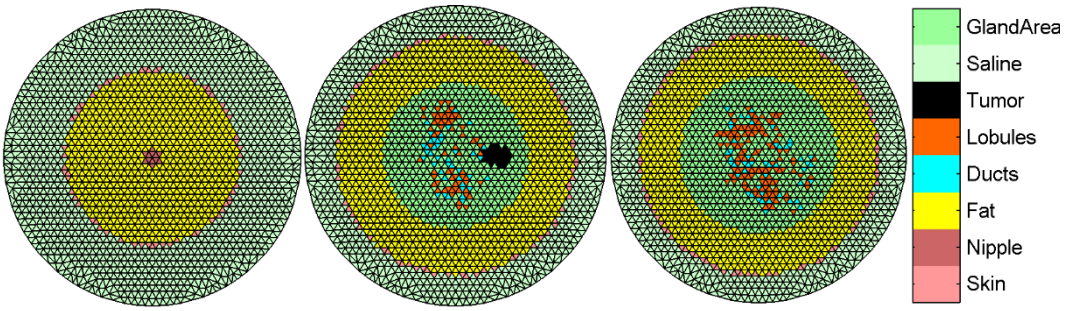

Figure 5. 11. The discretized breast phantom.

5.3 Conclusion

This chapter introduced the method to set up the digital breast phantom. The structures of the breast phantom are expressed using analytic geometry. To make the phantom available to the EIM system, it should be discretized using the mesh applied to the forward problem. The digital breast phantom is valuable in mock clinical trials and EIM system assessment. The digital breast phantoms will be used in the following chapters.

6. Feasibility study of a rotary planar electrode array EIM system

6.1 Summary

This chapter will introduce a novel rotary planar electrode array EIM (RPEIM) system. The RPEIM system is an evolution of the Sussex MK4 system, which is a prototype instrument for breast cancer detection. Comparing it with the other planar electrode EIM systems, the rotation feature enables a dramatic increase in the number of independent measurements. To assist impedance evaluation exploiting electrode array rotation, a synchronous mesh method is proposed. Using the synchronous mesh method, the RPEIM system is shown to have superior performance in image accuracy, spatial resolution and noise tolerance over the MK4 system.

6.2 Background of rotary EIT system

For the EIT inverse problem, the conductivity of the elements are chosen as the unknown (degree of freedom). For a chosen discretization of a breast, if ignoring the noise in the measurements, the number of degrees of freedom of this system is determined by the number of the independent measurements. More independent measurements provide more constraints to the field, which will decrease the number of degrees of freedom of the unknowns and hence is beneficial to the solution stability. Typically, increasing the number of electrodes is the most straightforward method to increase the number of independent measurements, however electrodes cannot be deployed in an unlimited manner due to their physical size; therefore flexible electrode arrays were studied aiming to increase independent measurements with a limited number of electrodes.

Frounchi and Bazzazi (2003) developed a novel rotary electrical capacitance

tomography (ECT) system with 4 electrodes evenly deployed in a ring (Frounchi and Bazzazi, 2003). The circular electrode array rotates through 90 degrees and for each rotation, 6 measurements are collected. According to their report, the rotation of the electrode array contributed to a dramatic increase in the number of independent measurements and thus achieved fairly high resolution images. Murphy and York (2006) proposed using non-stationary electrodes to monitor a mixing process, by fixing the electrodes onto the mixing impeller (Murphy and York, 2006). According to their simulations, the employment of the non-stationary electrodes, in an electrical impedance tomography (EIT) system, increases the number of the independent observations; as a result there are significant improvements in the resolution, the information content and the reliability of the reconstructed image. Huang, Yu and Chung (2007) reported a movable ring electrode array in their EIT system, named REIT (Yu et al., 2006, Huang et al., 2007). The REIT is equipped with 16 evenly distributed electrodes fixed on a ring rotational frame with a minimum and maximum rotation angle of 0.018 and 22.5 degrees respectively. This design allowed up to 1250 groups of measurements and produced a maximum of 130,000 independent measurements; however in practice, they only collected measurements from 5 positions due to the impractical length of time required for both data acquisition and image reconstruction. To support this rotating design, a finer mesh is required to make sure that every electrode is located at a mesh element.

Till now, only a few studies on rotary ring electrode arrays have been reported; the study of a movable planar electrode array is not available in the literature. The application of a moveable electrode array to EIT has not been widely studied as the following two problems are not solved: 1) a moveable electrode array is considered impractical for most cases, as the movements of the electrodes will bring agitations to the field under investigation. In most EIT systems, electrodes are directly attached to the surface of the objects being measured. The movement of the electrodes may affect the conductivity or/and permittivity distribution of the field, as a result, the boundary measurements from a movable electrode system may be sampled on several different fields, thus it will be

inappropriate to use all these measurements to reconstruct one field. For example, in mastopathy diagnosis, the movements of electrodes may twist or change the shape or position of the breast. Even though the changes are small, considering the ill-posed nature of the EIT inverse problem, the results will be extremely unreliable; 2) a moveable electrode array relies on a much finer discretization or subdivision, which not only increases computational time but also may worsen the ill-posed problem. In the image reconstruction algorithms of the EIT inverse problem, the electrodes are modelled by the mesh nodes or mesh elements at the corresponding positions. As the electrodes rotate, to record data from different positions, the measuring density (or the positions of the electrodes) will increase. To ensure that all the measuring electrodes are modelled by proper mesh nodes or mesh elements, the traditional method is to use a finer mesh, thus the more movements the electrode array makes, the finer the mesh is. However, studies suggest that a significantly finer mesh, whose elements are far smaller than the size that the system can distinguish, will result in greater ill-conditioning (Gisser et al., 1990, Tang et al., 2002). Thus, using a moveable electrode array in the EIT systems needs to: 1) prevent the disturbances from the moveable electrode array to the field under investigation; 2) avoid using an unreasonably fine mesh to support the movements of the electrode array in image reconstruction.

6.3 The RPEIM system

The achievement of the Sussex MK4 system based on phantoms and the real patients made us believe that using EIT to detect breast cancer is realistic (Zhang et al., 2014, SZE, 2012); however we are also aware of the limited ability of the MK4 system in image resolution and reliability. The RPEIM system is an upgraded version of the Sussex MK4 system, which aims to enhance the performance of our EIM system. The appearance of the RPEIM system the same with the MK4 system, which is a bed with a data acquisition tank in the appropriate position. The data acquisition tank is comprised of a support tank,

a breast container and an adjustable scanner head, which is shown in Figure 6. 1. The support tank is used to support and fasten the breast container to prevent its movement. The breast container is replaceable and has different sizes to accommodate different brassiere cups. The differently sized breast containers have the same diameter, which is 18cm but various depths, which are 1 cm, 1.5 cm, 2 cm, and up to 5 cm. The wall of the breast container is made from non-conducting material (Figure 6. 1. in green). The bottom of the breast container is 3mm thick and made from conducting material with a conductivity of approximately 0.05 S/m (Figure 6. 1. in blue). The scanner head is a planar electrode array. It is adjustable in the vertical direction and rotatable in the horizontal plane. The rotation range is from 0° to 60°. The RPEIM system retains the design of the hexagonal electrode arrangement and the data acquisition method of the MK4 system. The current excitations and voltage measurements are achieved in small hexagonal measurement areas. The total number of voltage measurements is 1416. The improvement of the RPEIM system is that the rotation of the planar electrode array will significantly increase the number of the independent measurements. The examination process is: 1) choose an appropriately sized breast container for the patient; 2) fill the breast container with the body-temperature saline with a conductivity of 0.05 S/m; 3) the patient lies on the bed with a breast in the container; 4) raise up the scanner head to engage the electrodes with the bottom of the container and acquire a group of measurements; 5) move the scanner head to the start position; 6) rotate one degree, and return the scanner head to the measurement position and collect another group of measurements, 7) repeat 5) and 6) till sampling is finished. The RPEIM system solves the contact problem by using the breast container, which avoids breast movements during examinations as the scanner head rotates, so that all the measurements correspond to the same conductivity distribution. The planar electrode array rotates within a 60° segment. Normally equal angular rotation is adopted; thus if N groups of measurements are required in the 60° segment, the electrode array will sample at $(p-1)*60/N$, $p=[1,2,\cdots,N]$. Returning the electrode array to the start position before the next measurement will avoid accumulation of the rotation errors. For example, if we want 3 measurement positions at 0°, 20° and 40°, for the last

measurement position, the electrode array goes from 0° to 40° rather than 20° to 40°. This will avoid the rotation error at 20°

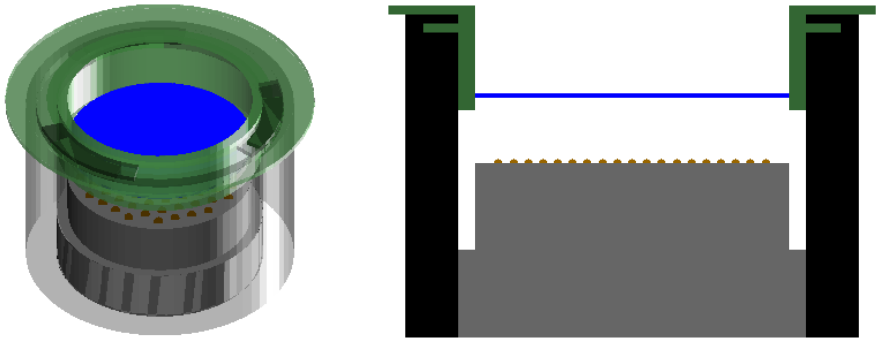

(a) (b)

Figure 6. 1 The data acquisition tank. (a) is a 3D view of the tank with the electrodes in the lowered position. (b) is the vertical cross-section of the tank.

6.4 The traditional method and the synchronous mesh method for the rotary-electrode EIT system.

In the former EIT system, the traditional method to support the rotation of the electrode array is subdividing the mesh in the area near the electrodes. This is an effective method for the rotary ring electrode array, as normally the number of the electrodes of the circular array is small and the mesh in use is 2D, so the number of mesh elements won't be too huge (for example Figure 6 in reference (Yu et al., 2006)). However the traditional method is not suitable for the RPEIM system for the following reasons:

(1) Using the traditional method will significantly increase the data volume and the computational time. Figure 6. 2 (a) shows the 2D mesh for the static detection, where the 85 red dots indicate the positions of the electrodes of the planar electrode array. Figure 6. 2 (b) shows the subdivided mesh to support the rotations of the planar electrode array, where the dots in different colour indicate different measurement positions of the planar electrode array. The 2D mesh in Figure 6. 2 (a) has 421 nodes

and 780 elements; for 3D imaging, the numbers of the 3D mesh nodes and elements are $421 \times (L+1)$ and $780 \times 3 \times L$, where L indicates the number of layers of the 3D mesh. The 2D mesh in Figure 6. 2 (b) has 673 nodes and 1284 elements; for 3D imaging, the numbers of the 3D mesh nodes and elements are $673 \times (L+1)$ and $1284 \times 3 \times L$. Obviously using the subdivided mesh will result in a significant increase in the data volume and hence the computational time.

(2) Using the traditional method will worsen the ill-posed problem. As we mentioned before, if the elements are far smaller than the size that the system can distinguish, it will lead to greater ill-conditioning. Obviously there are many small sized elements in Figure 6. 2 (b).

(3) Using the traditional method will increase the computational error. The ideal element for the finite element method (FEM) is the regular triangle (for the 3D problem, it is a regular tetrahedron). Conversely, if the elements are far from the regular triangle/ tetrahedron, it will cause great computational error; however there are many elements in Figure 6. 2 (b) which are far from the regular triangle.

(4) The sizes of the elements in Figure 6. 2 (b) vary over a large range. This will cause non-uniform resolution of the reconstructed conductivity maps.

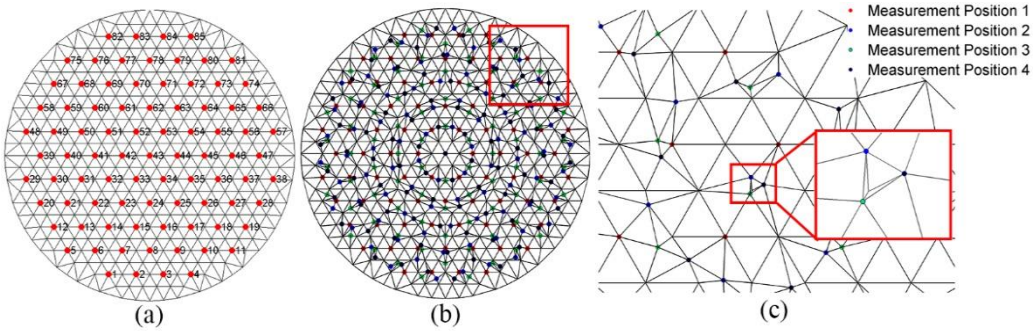

Figure 6. 2. The meshes for the RPEIM system using the traditional method. (a) is the mesh for 1 measurement position. (b) is the mesh for 4 measurement positions. (c) is the magnification of the area highlighted by the red frame in (b). The spots indicate the positions of the electrodes.

The problems above will become worse as the number of measurement positions increases; therefore the traditional method is not advisable for the rotary planar electrode array. We propose a synchronous mesh method, which is facilitated by rotating the mesh together with the electrodes, so that the electrodes can always locate at the same mesh nodes or mesh elements. In the RPEIM system, we still use the point electrode model (PEM), which was used in the MK4 system and proven to be reliable in clinical trials (Zhang et al., 2014). The synchronous mesh method for the RPEIM system is shown in Figure 6. 3. Figure 6. 3 (a) indicates that the mesh and the electrodes at the original position 0°; Figure 6. 3 (b) indicates that the electrodes have rotated 30° and the mesh rotates together with the electrodes 30°. The 19 highlighted dots in Figure 6. 3 (a) and (b) indicate the same electrodes but at a different measurement position. The 19 highlighted dots compose a hexagonal measurement area, in which the two big dots indicate the current excitation electrodes and the symbols '+' and '-' indicate the positive and negative poles. The 17 middle sized dots indicate the measuring electrodes, in which 12 voltage measurements are collected from the adjacent electrodes, parallel to the drive pair. The other small dots indicate the electrodes not participating in the data acquisition in this hexagonal measurement area. Figure 6. 3 only presents one excitation event and its corresponding measurements. By using the synchronous mesh method, the number of meshes in use is equal to the number of measurement positions.

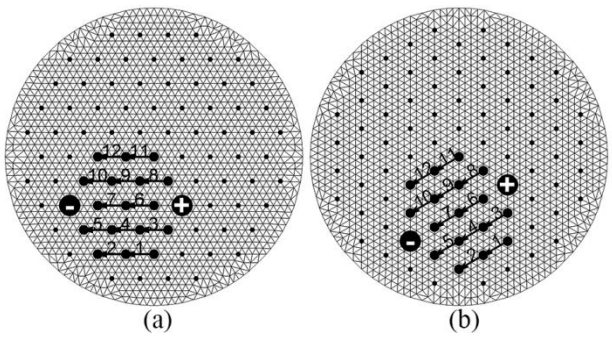

Figure 6. 3. Two positions of the fine mesh, the planar electrode array and a hexagonal measurement area. (a) is the display of the original position. (b) is the display of the rotated position at 30°.

6.5 The forward problem of the RPEIM system

The digital breast phantom in Figure 5. 1 is used to explain the forward problem of the RPEIM system. For the forward problem, we use a fine mesh to discretize the field in the breast container, which is shown in Figure 6. 4, having 7 layers, 65,520 elements and 12,968 nodes. The bottom layer of the mesh is 3mm in height indicating the discretized bottom of the breast container; therefore all the conductivity values of the 9,360 elements in the bottom layer are 0.05 S/m. The other 6 layers are 5mm in height and used to discretize the field within the breast container including the breast model and the background saline. There are 56,160 elements discretizing the field within the breast container.

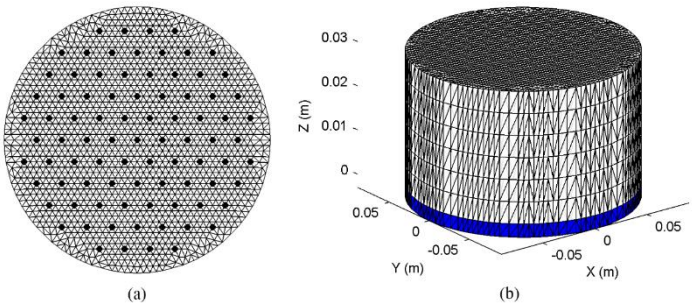

Figure 6. 4. The Mesh in the forward problem. (a) is the 2D fine mesh with the electrode arrangement. (b) is the 3D fine mesh applied to the forward problem.

If the conductivity distribution in the breast container is $\sigma(x, y, z)$, the conductivity values of the mesh elements are

$$\sigma_i^p = \sigma\left(x_{io}^p, y_{io}^p, z_{io}^p\right) \qquad (6.1)$$

where σ_i^p indicates the conductivity value of the *i*th element of the *p*th mesh for the *p*th measurement position, $\left(x_{i0}^p, y_{i0}^p, z_{i0}^p\right)$ indicate the coordinate of the center of the *i*th element of the *p*th mesh. The discretized breast phantom corresponding to the original

mesh and the 30°-rotation mesh are shown in Figure 6. 5. Parallel computation is used to find the conductivity value of each element, as the computational time is very large. The breast model in the phantom in Figure 5. 1 is a small model with only approximately 4000 structures. Every element is needed to determine the structure that it belongs to. It takes at least 2.5 hours to work out the values of the elements for 4 measurement positions (four meshes).

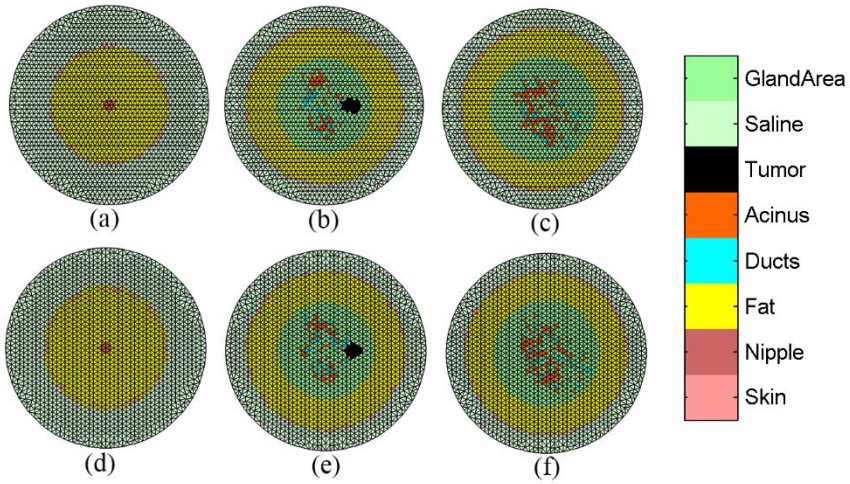

Figure 6. 5. The discretized breast phantom. (a) to (c) show the cross-sectional images of layer 1, 3, 5 in the mesh at the start position. (d) to (f) show the cross-sectional images of layer 1, 3, 5 in the mesh at the 30° position.

Knowing the conductivity values of the meshes, the voltage measurements can be computed using the equations in Section 2.2. According to the data acquisition method, in each measurement position, there are 1416 voltage measurements, which are: $V = [V_1 \quad V_2 \quad \cdots \quad V_{1416}]$. In this simulation, voltage measurements are obtained from 4 measurement positions. The operating frequency is 500 kHz, the sampling frequency is 20 MSa/s, the sample number is 1000, and the ADCs are 14 bit. Assume that the background noise is 60dB white Gaussian noise; the multiplicative noise, which is caused by the amplifying circuit, is $\pm 0.5\%$ random noise. The ADC quantization is considered. The noise is added as shown in Figure 6. 6, where Vi(tn) indicates the sample sequence of the *i*th measurement, Vi indicates the effective value of the sample sequence, which is the final measurement. For 1000 samples, the signal to noise ratio (SNR) of the whole

system will be greater than 70 dB. Finally four groups of measurements at 0°, 15°, 30° and 45° are obtained, which are denoted by V^1, V^2, V^3, and V^4.

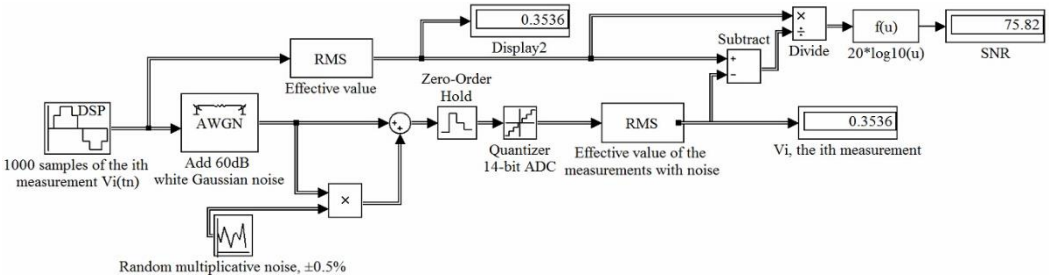

Figure 6. 6 The addition of noise to the simulated measurements

6.6 The inverse problem of the RPEIM system

In the inverse problem, we use a coarse mesh, which is shown in Figure 6. 7, so that it won't result in an excessive computational time and exacerbate the ill-conditioned problem. It has 4 layers, 14040 elements and 2947 nodes. The height of the bottom layer is 3 mm indicating the bottom of the breast container; the heights of the other 3 layers are 10 mm.

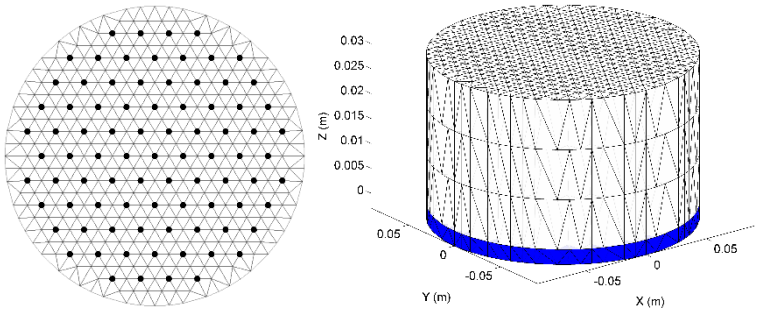

Figure 6. 7. Meshes in the inverse problem. (a) is the 2D coarse mesh with the electrode arrangement. (b) is the 3D coarse mesh applied to the inverse problem.

The enhanced image reconstruction algorithm is used to reconstruct the conductivity distribution of the field in the tank. The synchronous mesh requires different subdivisions of the field in the tank, which means if there are *N* groups of measurements; *N* 3D meshes

corresponding to the *N* positions of the planar electrode array will be needed. However one group of measurements can only contribute to one group of solutions of the corresponding mesh. For instance, the first group of measurements can only contribute to the value of the elements of the first mesh (the 3D coarse mesh at the original position). However in practice, we hope that all the groups of the measurements could interact with each other and finally achieve one 3D map, which is expected to be much better than any result from a single group of measurements. So the problem is: how do the other (*N-1*) groups of measurements influence the value of the elements of the *i*th mesh or how does the *i*th group of measurements contribute to the other (*N-1*) meshes. We propose the following steps to solve this problem: 1) make *N* 3D fine meshes for the forward problem and *N* 3D coarse meshes for the inverse problem; 2) solve the forward problems with some assumed conductivity and get *N* groups of predicted voltage measurements; 3) obtain the *N* groups of conductivity values (corresponding to coarse meshes) by using the image reconstruction algorithm; 4) map the conductivity values from the *N* 3D coarse meshes to the *N* 3D fine meshes (the mapping algorithm is shown in (7)); 5) if the conductivity distribution is satisfied, make the *N* groups of conductivity a 3D image or a group of cross-sectional images; however if the conductivity distribution is not satisfied, repeat 2) to 5).

To introduce the synchronous mesh method in the inverse problem, we still use the breast phantom in Figure 5. 1 as an example. Applying the four groups of measurements $\boldsymbol{V}^1$, $\boldsymbol{V}^2$, $\boldsymbol{V}^3$, and $\boldsymbol{V}^4$ to the enhanced image reconstruction algorithm (2.14), the corresponding conductivity values $\boldsymbol{\sigma}^1_{coare\_1}$, $\boldsymbol{\sigma}^2_{coare\_1}$, $\boldsymbol{\sigma}^3_{coare\_1}$, and $\boldsymbol{\sigma}^4_{coare\_1}$ are computed, where '*coarse*' indicates the coarse mesh, 1 in the subscript indicates the first iteration, 1-4 in the superscript indicate the indexes of the measurement positions. $\boldsymbol{\sigma}^1_{coare\_1}$ and $\boldsymbol{\sigma}^3_{coare\_1}$ are visualized in Figure 6. 8.

The four groups of conductivity values are the reconstructed results of the same field but from different measurement positions. The complementary information from the four different measurement positions will increase the reliability of the result. Merging the conductivity values

of the four coarse meshes into four fine meshes will strengthen the common knowledge and reduce the disagreements (for example the mesh and the noise). The mapping algorithm is (6.2):

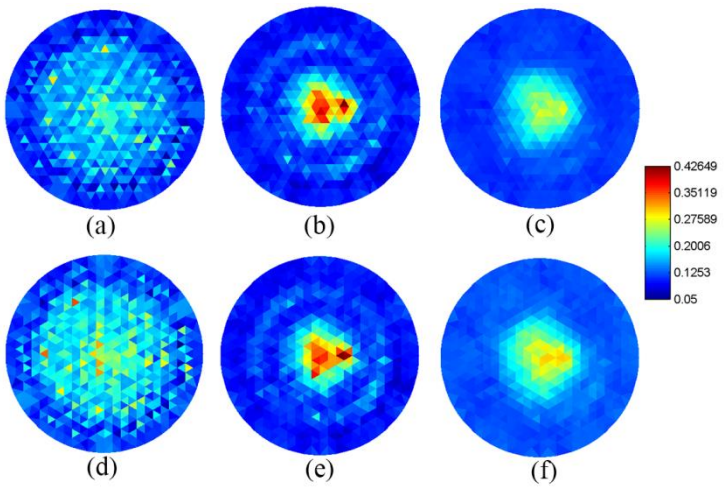

Figure 6. 8. The reconstructed conductivity of the first iteration. (a) to (c) show the reconstructed conductivity at the first measurement position (0°). (d) to (f) show the reconstructed conductivity at the third measurement position (30°). The colour bar indicates the conductivity scale.

$$\boldsymbol{\sigma}^{p}_{fine\_n}(i^{p}) = \sum_{p=1}^{P} \boldsymbol{\sigma}^{p}_{coarse\_n}(j^{p}) \Big/ P \qquad (6.2)$$

where P is the number of the measurement positions, i^{p} indicates the *i*th element of the *p*th 3D fine mesh, j^{p} indicates the *j*th element of the *p*th 3D coarse mesh, $\boldsymbol{\sigma}^{p}_{fine\_n}$ and $\boldsymbol{\sigma}^{p}_{coarse\_n}$ denote the conductivity values from the *n*th iteration, of the *p*th 3D fine and coarse mesh respectively. If $[x_i, y_i, z_i]$ indicates the coordinate of the center of i^{p}, $\mathrm{e}^{p}_{coarse}(k)$ indicates the space of the *k*th element of the *p*th coarse mesh,

$$j^{p} = k \quad if \quad [x_i, y_i, z_i] \in e^{p}_{coarse}(k) \qquad (6.3)$$

By using the mapping algorithm (6.2), the conductivity values of the four fine meshes are obtained. The cross-sectional images of the first fine mesh at 0° and the third fine mesh at 30° are shown in Figure 6. 9. Although there are 6 layers in the 3D fine

meshes, we only display 3 image layers by combining the two neighboring layers into one, corresponding to the layers of the coarse mesh. For iterations, knowing the reconstructed conductivity values of the fine meshes, four groups of the predicted voltage measurements $\boldsymbol{V}_1^1$, $\boldsymbol{V}_1^2$, $\boldsymbol{V}_1^3$, and $\boldsymbol{V}_1^4$ can be computed, where 1 in the subscript indicates the first iteration, 1-4 in the superscript indicate the indexes of the measurement positions. By comparing the real measurement with the updated reference measurements, we can update the conductivity values until they converge. Then we can make the conductivity values of the four 3D fine meshes into one 3D picture or several cross-sectional pictures. The value of each pixel is computed by (6.4).

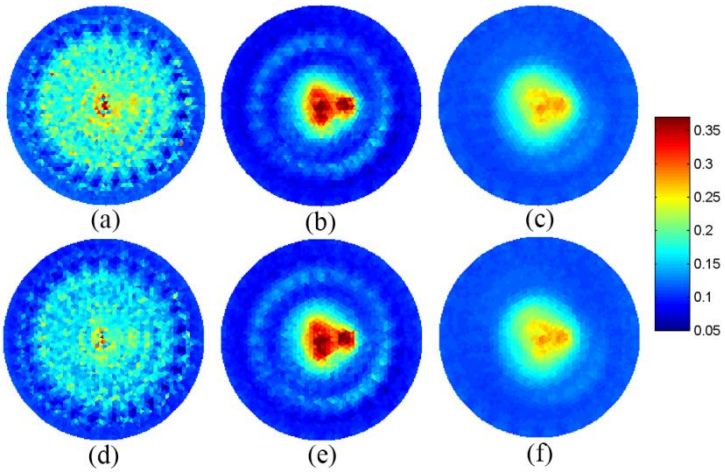

Figure 6. 9 The conductivity values of the fine meshes at measurement position 0° and 30°. (a) to (c) show the conductivity of the 3D fine mesh at 0. (d) to (f) show the conductivity of the 3D fine mesh at 30°. The color bar indicates the conductivity scale.

$$I_{img}(x,y,z) = \sum_{p=1}^{P} \boldsymbol{\sigma}_{fine\_n}^{p}(h^p) \Big/ P \qquad (6.4)$$

where $I_{img}(x,y,z)$ indicates the conductivity value of the 3D space in the breast container, P denotes the number of the measurement positions, h^p denotes the *h*th element of the *p*th 3D fine mesh, $\boldsymbol{\sigma}_{fine\_n}^{p}$ denotes the reconstructed conductivity value of the *p*th 3D fine mesh of the *n*th iteration. If $e_{fine}^{P}(K)$ denotes the space of the *K*th element of the *p*th fine mesh,

$$h^p = K \quad if \quad (x, y, z) \in e^P_{fine}(K) \tag{6.5}$$

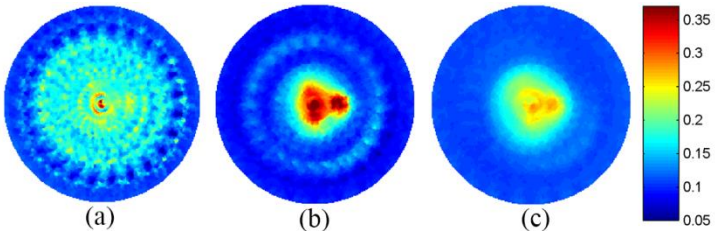

Figure 6. 10. The final reconstructed conductivity distribution of four measurement positions. (a) to (c) indicate the cross-sectional images at the bottom, middle and top of the tank.

Figure 6. 10 shows the final cross-sectional images, which is contributed by the conductivity values of the four 3D fine meshes of the second iteration. The number of the pixels is 201×201. The big bright circular area in the first cross-sectional image is caused by the highly conductive skin. The bright area in the center of the second cross-sectional image is the image of the gland area. Before analyzing the second cross-sectional image, let's refer to the breast phantom in Figure 5. 1 (a) and the discretized breast model in Figure 6. 5 (b) and (e) to get the features of the breast: the ducts and acini distribute similarly to an ellipse with two ends pointing to 11 and 6 O'clock. The red area in the center of Figure 6. 10 (b) is consistent with these features, which indicates the cluster of the ducts and acini. The darkest area in the center is caused by the nipple and the ducts, which converge to the nipple. The darkest area at 3 O'clock indicates that the tumor is present. The bright ring round the gland area is caused by the highly conductive skin. The dark area in between the gland area and the skin is the adipose tissue. In the third cross-sectional image, the gland area is clearly imaged in the center; the red area at 3 O'clock is a projection of the tumor, which is inevitable for a planar electrode array (Bouchette et al., 2014); the ducts and the acini are not well imaged, as they are far from the electrodes. The data volume of the EIT problem is determined by the meshes applied to the forward and inverse problem. To make this program work, it requires at least 16G RAM. The computational time of the EIT problem is affected by the meshes, the algorithms and the

number of measurements positions. The computational time is almost linear with the number of measurements positions. In this simulation, using an i7-4790 CPU @ 3.60 GHz, the computational time is about 93 seconds for one measurement position and about 374 seconds for 4 measurement positions.

6.7 Result

6.7.1 Evaluation method

The evaluation method of the RPEIM system is similar to that of the MK4 system, which was introduced in Section 4.4.1. It is required to find the edges of the objects of interest from the reconstructed image to evaluate the accuracy of the geometric parameters. In this digital breast phantom, the target object is the ellipsoid tumor, which is located at [2.5, 0, 1.5] (cm), with size of [2, 1.5, 1] along the X, Y, Z axis. Assume that $[x_E, y_E]$ are the coordinates on the edge of the target object, where $x_E = [x_{E1}, x_{E2}, \cdots, x_{EN}]$, $y_E = [y_{E1}, y_{E2}, \cdots, y_{EN}]$, N represents the number of the coordinates. The centre of the object $(\tilde{x}_0, \tilde{y}_0)$ can be estimated using (6.6).

$$\begin{cases} \tilde{x}_0 = \sum_{i=1}^{N} x_{Ei} \Big/ N \\ \tilde{y}_0 = \sum_{i=1}^{N} y_{Ei} \Big/ N \end{cases} \quad (6.6)$$

The size parameters can be computed by nonlinear least-squares curve fitting. For an elliptical object,

$$[\tilde{a}, \tilde{b}] = argmin_{\tilde{a},\tilde{b}} \left\| 1 - \frac{(x_E - \tilde{x}_0)^2}{\tilde{a}^2} - \frac{\left(y_E - \tilde{y}_0\right)^2}{\tilde{b}^2} \right\|_2^2 \quad (6.7)$$

where: $argmin_{\tilde{a},\tilde{b}}$.means the argument $\tilde{a}$ and $\tilde{b}$, which minimize what follows, $\| \ \|_2$ is the 2-norm, $\tilde{a}$ and $\tilde{b}$ indicate the computed semi-principal axes of the ellipse. We also define a parameter D to evaluate the whole distortion of the object.

$$D = \frac{\left\| 1 - \frac{(x_E - x_0)^2}{a^2} - \frac{\left(y_E - y_0\right)^2}{b^2} \right\|_2^2}{N} \qquad (6.8)$$

where: $x_0,\ y_0,\ a,\ b$ are the parameters of the real model. A small D value means a small difference between the image and the real object. If there is more than one object in the same layer, the total distortion is

$$D = \frac{\sum_{i=1}^{Num} \left\| 1 - \frac{\left(x_E^i - x_0^i\right)^2}{a^{i\,2}} - \frac{\left(y_E^i - y_0^i\right)^2}{b^{i\,2}} \right\|_2^2}{N} \qquad (6.9)$$

where: *Num* indicates the number of objects. x_E^i and y_E^i indicates the coordinates of the points on the edge of the *i*th object; (x_0^i, y_0^i) indicates the centre of the *i*th object, a^i and b^i indicate the size of the *i*th object; *N* is the total number of points on the edges of the *N* objects.

6.7.2 The accuracy of the RPEIM system

The increase of measurement positions will enhance the image accuracy; however this relationship is not linear; or in other words, there will be no obvious improvement of image accuracy, where the number of rotations is greater than an optimum value. Figure 6. 11 and Figure 6. 12 present the reconstructed conductivity distributions of the breast phantom detected by the MK4 system and the RPEIM system with 8 measurement positions. According to Figure 6. 10, Figure 6. 11 and Figure 6. 12, the RPEIM system

gives a significant improvement in image accuracy over the MK4 system; however for the RPEIM system, the result from eight measurement positions doesn't show obvious improvement over the result from four measurement positions. Therefore the number of measurement positions for the RPEIM system is a non-linear optimization problem, which trades off the image accuracy and the computational time. Figure 6. 13 shows the edges of the tumour corresponding to different numbers of measurement positions. By using the image processing based error analysis method, we get the position and shape parameters of the tumour, which are tabulated in

Table 6. 1 and plotted in Figure 6. 14, this explores the relationship between the number of rotations and the location and shape errors of the tumour.

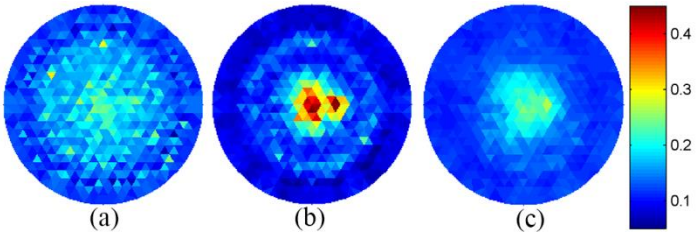

Figure 6. 11. The reconstructed conductivity maps of the digital breast phantom using the MK4

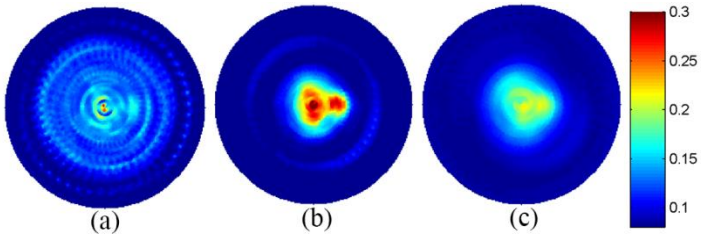

Figure 6. 12. The reconstructed conductivity maps of the digital breast phantom using the RPEIM system with 8 measurement positions

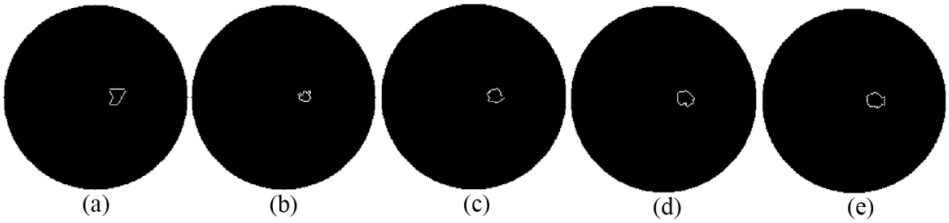

Figure 6. 13. The edge of the tumour corresponds to different numbers of measurement positions. (a) is from the MK4 system. (b) to (f) are from the RPEIM system using 2, 3, 4 and 8 measurement positions.

Table 6. 1. The critical parameters obtained from the images

Parameters	MK4	The RPEIM system		
Measurement positions	1	2	3	4
Horizontal center, (cm)	[2.06,0.11]	[2.13,0.11]	[2.07,0.08]	[2.10,0.10]
Vertical center in layer	Layer 2	Layer 2	Layer 2	Layer 2
Conductivity contrast in LOI	10.27	8.19	6.71	7.66
Half length and width, [a b](cm)	[0.78, 0.86]	[0.59, 0.50]	[0.81, 0.68]	[0.81, 0.70]
Object distortion, D	0.38	0.30	0.30	0.26
Parameters	The RPEIM system			
Measurement positions	5	6	7	8
Horizontal center, (cm)	[2.12, 0.11]	[2.10, 0.07]	[2.07, 0.09]	[2.10, 0.07]
Vertical center in layer	Layer 2	Layer 2	Layer 2	Layer 2
Conductivity contrast in LOI	5.85	5.69	5.67	6.42
Half length and width, [a b](cm)	[0.76, 0.71]	[0.82, 0.73]	[0.70, 0.63]	[0.9, 0.7]
Object distortion, D	0.26	0.27	0.25	0.29

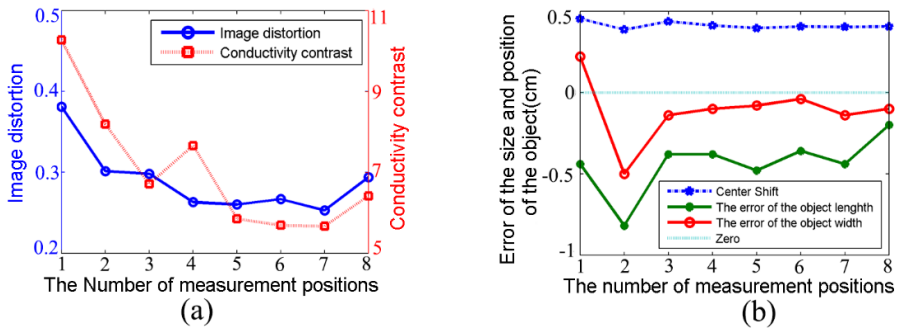

Figure 6. 14. Relationship between the image quality and the number of measurement positions. (a) shows the conductivity contrast and the object distortion versus the number of measurement positions. (b) presents the size and the position errors of the object versus the number of measurement positions. 1 on the X axis indicates the results from the MK4 system.

In Figure 6. 13, the shape of the tumour from the MK4 system is seriously affected by the triangular shape of the elements; however as the number of the measurement positions increases, the shape accuracy of the tumour is significantly improved. According to

Table 6. 1 and Figure 6. 14 (a), the image contrast drops from 10.27 for the MK4 system to 5.85 for the RPEIM system with 5 measurement positions and then becomes stable. In image reconstructions, because of the ill-posed nature and the influence of the noise, there will be some mesh elements having abnormally high or low conductivity values, which results in a big image contrast for the MK4 system; however when we have several measurement positions and use the merged value to denote the conductivity value at $[x, y, z]$, the abnormally high or low values will be averaged, resulting in a reduced

image contrast. The image contrast doesn't drop linearly with the number of measurement positions; it becomes stable when the number of measurement positions exceeding a threshold value, which is 5 in this case. The image distortion D gives a comprehensive evaluation of the image accuracy of the tumour, including the location and the shape of the tumour. In Figure 6. 14 (a), the curve of the image distortion (D) drops sharply from 1 to 4 measurement positions and becomes stable from 4 to 7 measurement positions and then slightly rises at 8 measurements positions. This indicates that there is a significant improvement of image accuracy as the number of measurement positions increases from 1 to 4, after which the improvement becomes very marginal. The centre shift is the distance between the centres of the real object and its image, which assesses the positional accuracy. According to Figure 6. 14 (b), the positional error doesn't get smaller as the number of measurement positions increases. The errors of the object length and width in Figure 6. 14 (b) are used to assess the size error of the tumour. As the number of measurement positions increases to 3, the size error stabilizes. By comprehensively analysing the reconstructed conductivity distributions, the outlines of the tumour in Figure 6. 13 and the critical parameters in

Table 6. 1 and Figure 6. 14, and also considering the computational time, we suggest three to five measurement positions for a real experiment. Three measurement positions is preferred to reduce computational time, whilst five measurement positions will give higher accuracy.

6.7.3 The spatial resolution of the RPEIM system

A breast phantom with two tumours in Figure 6. 15 is used to illustrate the advantage of the RPEIM system in spatial resolution. The two tumours are the same size with length of 2 cm, width of 1.5 cm, and height of 1 cm, but they are placed perpendicularly. Tumour 1 is placed at [2.5, 1.25, 1.5] (cm); Tumour 2 is placed at [2.5, -1.5, 1.5] (cm). The smallest boundary to boundary distance between the two tumours is 1 cm. The spatial resolution

of an EIT system is considered relative to the electrode density and the distance to the electrode array. According to the electrode arrangement of the MK4 and RPEIM system, it can at least distinguish the two objects at the electrode-contact plane with a separation distance of about 1.7 cm. In this case, we aim to show the improvement in spatial resolution using the RPEIM system, by separating the two objects with a distance smaller the adjacent electrode distance.

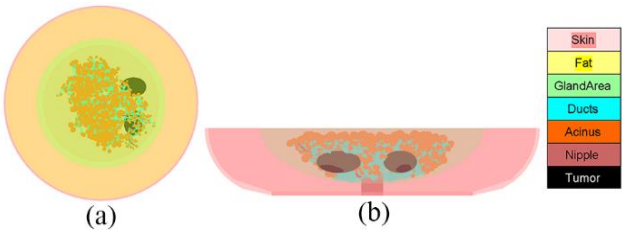

Figure 6. 15. The breast model with two tumors. (a) is the XY view. (b) is the YZ view

Figure 6. 16 and Figure 6. 17 present the reconstructed image from the MK4 system and the RPEIM system with five measurement positions respectively. Clearly Figure 6. 17 is much closer to the digital breast phantom than Figure 6. 16. For the case with two tumours, we use two steps to assess the image accuracy: general analysis which analyses the image as a whole and further analysis which analyses the region of interest (ROI). Step 1 roughly establishes the location and size parameters of the two tumours from Figure 6. 17 (b), using the image processing based error analysis method. When two (or more) tumours are close together in the breast, one will affect the reconstructed conductivity of the other one and its surrounding area, especially in the region in between them. In this situation, using the threshold at half maximum of the conductivity range may be inappropriate. The threshold in this case is 0.25 S/m, which is a minimal value that separates the images of the two tumours. The roughly analysed geometrical parameters of the two tumours are shown in Table 6. 2. The centres of Tumour 1 and Tumour 2 shift 0.65 cm and 0.48 cm respectively. The object distortions of Tumour 1 and Tumour 2 are 0.92 and 0.34 respectively. The image of Tumour 2 is more accurate than Tumour 1. This may be because Tumour 1 is closer to the region of the high density gland

than Tumour 2 and the signal from the high density gland is so strong that it affects the detection of the tumour nearby. Step 2 uses the location of Tumour 2 as a reference (as the location of Tumour 2 is more accurate) and plots the conductivity distributions in Figure 6. 18 (b) and (d), along the black lines in Figure 6. 18 (a) and (c), to provide further analysis to the ROI. Both Figure 6. 18 (b) and (d) have two peaks; however the curve in Figure 6. 18 (b) is too coarse to evaluate the locations and the sizes of the two tumours. While Figure 6. 18 (d) shows two clearly separated humps with a boundary-to-boundary distance of 0.99 cm, which is consistent with the breast model. Please note the difference from Step 1, in which we used one threshold to determine the sizes and locations of the tumours; in Step 2, we use two thresholds as the conductivity scales of the two tumours are different in Figure 6. 18 (d). If we take the inflection points at the ends of the two humps as the boundary of the two tumours, the sizes of the two tumours along y-axis are 1.22 cm and 1.04 cm. If we assume that the centres of the two tumours are at the middle of the two humps, the coordinates of the tumours' centres on the y-axis are 0.88 cm and -1.24 cm. By observing the cross-sectional images in Figure 6. 16 and the conductivity distribution of the ROI in Figure 6. 18 (b), we find that when the boundary-to-boundary distance of the two tumours are equal to 1cm, it is difficult for the MK4 system to separate the two tumours and get accurate positions for them. However by observing Figure 6. 17 and Figure 6. 18 (d), we conclude that 1) the RPEIM system can separate the two tumours with a boundary-to-boundary distance equal to 1 cm; 2) the RPEIM system can provide a better spatial resolution than the MK4 system.

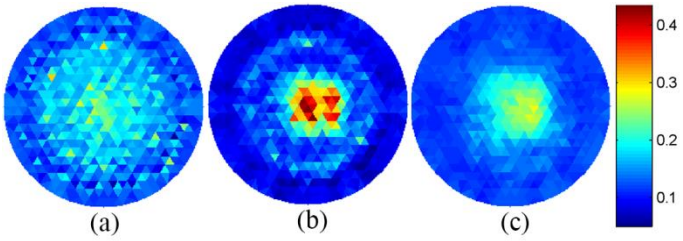

Figure 6. 16. The reconstructed result of the two-tumor breast phantom using the MK4 system. (a) to (c) indicate the cross-sectional images from the bottom to the top.

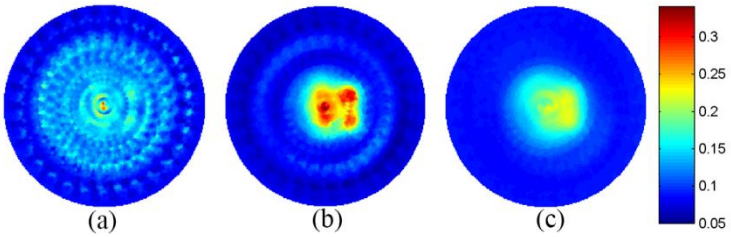

Figure 6. 17. The reconstructed result of the two-tumor breast phantom using the RPEIM system with 5 measurement positions. (a) to (c) indicate the cross-sectional images from the bottom to the top.

Table 6. 2. The roughly estimated parameters of the two tumours (Step 1)

Tumour 1			
Parameters	Real value	Estimated value	Error
Horizontal centre (cm)	[2.5,1.25]	[1.98,0.86]	[-0.52,-0.39]
Vertical centre	Layer 2	Layer 2	
Length and width (cm)	[2,1.5]	[1.80,1.38]	[-0.2,-0.12]
Centre shift (cm)	0.65		
Object distortion	0.92		
Tumour 2			
Parameters	Real Value	Estimated value	Error
Horizontal centre (cm)	[2.5,-1.5]	[2.18,-1.14]	[-0.32,0.36]
Vertical centre	Layer 2	Layer 2	
Length and width (cm)	[1.5,2]	[1.08,1.38]	[-0.42,-0.62]
Centre shift (cm)	0.48		
Object distortion	0.34		
Total distortion of the two tumours	0.64		

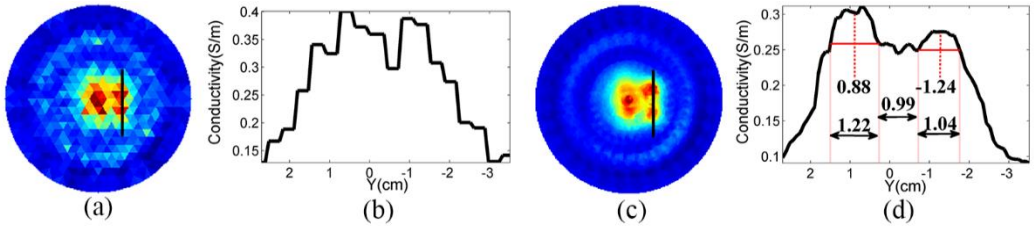

Figure 6. 18. The conductivity distribution of the ROI. (b) and (d) plot the conductivity distribution of the region on the black lines in (a) and (c). (a) and (c) are the images from Figure 6. 16 (b) and Figure 6. 17 (b) respectively. (d) shows the further analyzed parameters from Step 2.

6.7.4 The noise tolerance of the RPEIM system

The conductivity value, from the RPEIM system using the synchronous mesh method, is a merged value from multiple measurement positions; therefore it is supposed to have a better noise tolerance. To illustrate this point, we still use the breast model in Figure 5. 1. We add 30 dB white Gaussian noise and $\pm 1\%$ random multiplicative noise

to the simulated measurements at the 500 kHz operating frequency. For 1000 samples, the SNR of the whole system is approximately 45 dB. The reconstructed images corresponding to the MK4 system and the RPEIM system with four measurement positions are shown in Figure 6. 19 and Figure 6. 20. Comparing Figure 6. 19 with Figure 6. 11, which are all from the MK4 system but with different noise levels, the reconstructed result in Figure 6. 19 is seriously affected by the noise. The red elements at 12 o'clock to 6 o'clock indicate the presence of the cluster of the ducts and acini, but obviously the distribution is inconsistent with the breast phantom. The highly conductive elements at 3 o'clock indicate the presence of the tumour. By comparing Figure 6. 10 and Figure 6. 20, which are all from the RPEIM system with 4 measurement positions, we find that reducing the SNR from 70dB to 45 dB doesn't make a big change of the reconstructed result. The image of the tumour and the cluster of the ducts and acini in Figure 6. 20 is still clear and consistent with the breast phantom. Comparing Figure 6. 19 and Figure 6. 20, which are from different systems but with the same noise level, we find that the conductivity distribution in Figure 6. 20 from the RPEIM system is much closer to the breast phantom than that in Figure 6. 19. Thus, we conclude that 1) for the same system but with different noise levels, the reconstructed result from the RPEIM system is not affected as badly as that from the MK4 system; 2) for the same noise level but different systems, the RPEIM system performs better than the MK4 system in image accuracy. These two points prove that the RPEIM system has a better noise tolerance than the MK4 system.

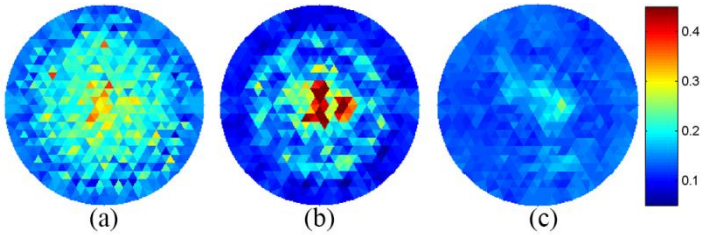

Figure 6. 19. The reconstructed result from the MK4 system, with SNR of 45 dB. (a) to (c) indicate the cross-sectional images from the bottom to the top.

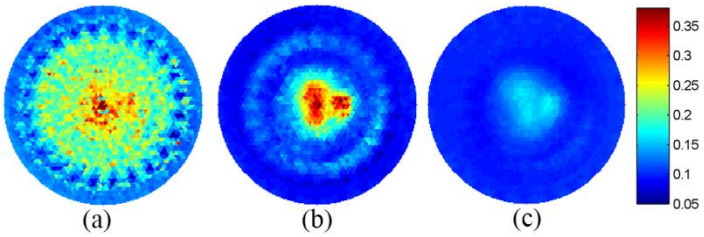

Figure 6. 20. The reconstructed result from the RPEIM system of four measurement positions, with SNR of 45 dB. (a) to (c) indicate the cross-sectional images from the bottom to the top.

6.7.5 The detectability of the RPEIM system

Before investigating the detectability of the RPEIM systems, let's review the statistics of tumour size and breast cancer survival in Table 1. 3. If the tumour can be detected when it is smaller than 2 cm, the patient will have at least a 90% survival rate. The target of our EIM systems is to find the tumour smaller than 2 cm.

Considering the hardware, the maximum volume of the MK4 and the RPEIM system is about 1,270 cc, with a maximum of 5cm depth and 18 cm diameter; this volume is adequate for approximately 90% of women. The spatial resolution of an EIT system with a planar electrode array is determined by the electrode density and the distance away from the electrode plane. The distance between the adjacent electrodes of the planar electrode array is 1.7cm; thus theoretically, both systems can detect an object of 1.7 cm at the electrode plane; the detectability reduces as the object moves away from the electrode plane.

Considering the mesh we used for image reconstruction (shown in Figure 6. 7), the length of the sides of the triangular elements is 0.85 cm. If the object is smaller than 0.85 cm, it is below the size that the mesh can present, so it is better that the object under detection is bigger than 0.85 cm

To analyse the detectability and the RPEIM system, a big volume digital breast phantom is used, which is shown in Figure 6. 21. The height of the breast is 4.5 cm. The

maximum diameter of the breast is 15 cm. The contact diameter between the breast and the electrode plane is 6 cm. Considering that invasive lobular carcinomas is a common cancer, which usually occurs in the region between nipple and armpit, we place the tumour in the upper outer quadrant at [-3.5 3] cm. Tumours of sizes of 1 cm, 2 cm are placed at the depths of 1.35 cm, 2.25 cm and 4.05 cm. The conductivity value of the breast phantom is shown in Table 6. 3. For image reconstruction, there are five image layers in the 3D mesh; the height of each layer is 0.9 cm.

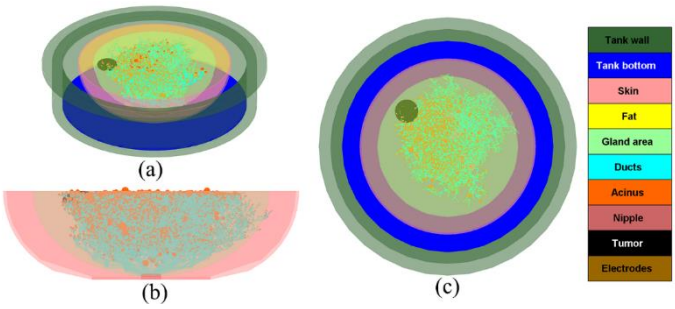

Figure 6. 21 Big volume breast phantom. (a) is the 3D view of the breast in the tank. (b) is the XZ view of the breast. (c) is the XY view of the breast in the tank

Table 6. 3. The conductivity values of the breast phantom (Unit: S/m)

skin	fat	ducts, acini, nipple	gland area	tumour	saline
0.465	0.05	0.2	0.08	0.6	0.05

Case 1: The tumour is located at [-3.5, 3, 1.35] (in the second image layer) with a size of 1cm. The reconstructed results of the MK4 system and the RPEIM system with 4 measurement positions are shown in Figure 6. 22 and Figure 6. 23 respectively.

Result for case 1: For both Figure 6. 22 and Figure 6. 23, in image layer 1, the red circular area in the centre is caused by the highly conductive skin. In image layer 2, the circular centre with relatively high conductivity values is caused by the mammary gland. The ring around the mammary gland is caused by skin. The dark area in between the highly conductive centre and ring indicates adipose tissue. The red area at 11 o'clock, indicated by the black arrow, shows the presence of the tumour. In Image layer 3 and 4,

the red area at 11 o'clock is the projection of the tumour. In image layer 5, the red area in the left upper quadrant is caused by the dense mammary gland. Both the MK4 system and the RPEIM system can detect the tumour of size equal to 1 cm when it is 1.35 cm away from the electrode plane. However the image in the object layer (image layer 2) from the MK4 system is noisy; the isolated highly conductive elements highlighted by the red circles are artifacts, which may result from the system noise or the ill-posed nature of the EIM inverse problem. These artifacts will affect judgment. The result from the RPEIM system is better, as the tumour is well imaged and no artifacts appear.

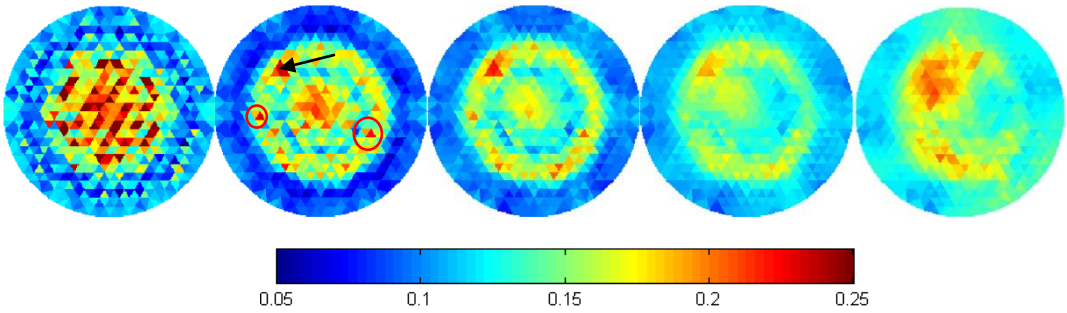

Figure 6. 22. The reconstructed result of case 1, using the MK4 system. The cross-sectional image from left to right indicates the conductivity distribution from the bottom to the top of the tank.

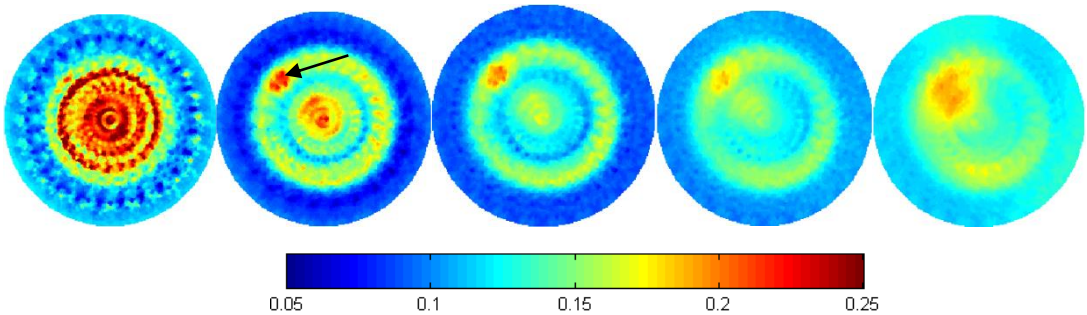

Figure 6. 23. The reconstructed result of case 1, using the RPEIM system with 4 measurement positions.

Case 2: The tumour is located at [-3.5, 3, 2.25] (in the third image layer) with a size of 1cm. The reconstructed results of the MK4 system and the RPEIM system are shown in Figure 6. 24 and Figure 6. 25 .

Result for case 2: When the tumour with size of 1cm moves to 2.25 cm away from

the planer electrode array, the signal from the tumour and the signal from the skin seem to become overlapped, as shown in the 3rd image of Figure 6. 24 and Figure 6. 25; thus for both systems, the tumour is not clearly imaged.

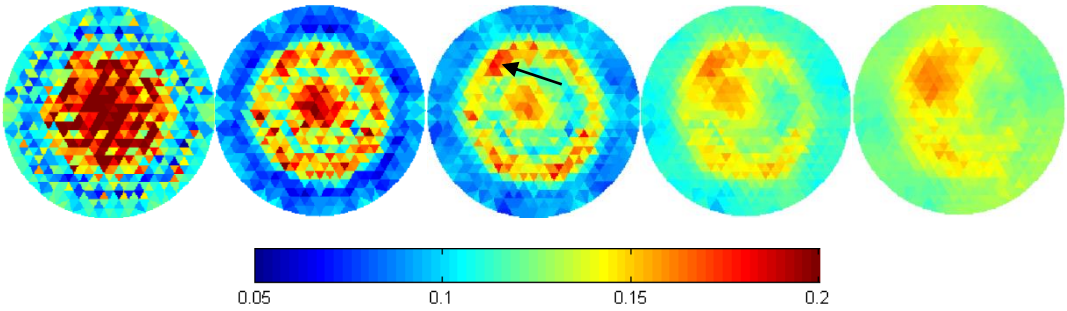

Figure 6. 24. The reconstructed result of case 2, using the MK4 system.

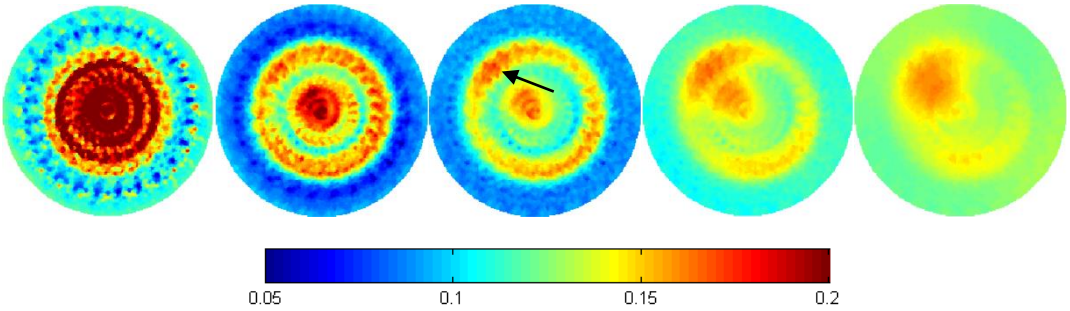

Figure 6. 25. The reconstructed result of case 2, using the RPEIM system with 4 measurement positions.

Case 3: The tumour is located at [-3.5, 3, 2.25] with a size of 2cm. The reconstructed results of the MK4 system and the RPEIM system are shown in Figure 6. 26 and Figure 6. 27.

Result for case 3: Based on Case 2, the size of the tumour is increased to 2 cm. In this situation, the signal from the tumour becomes stronger than that from the skin, thus the tumour becomes visible in both Figure 6. 26 and Figure 6. 27. So a tumour with size of 2 cm is detectable by the MK4 system and the RPEIM system, when it is 2.25 cm away from the planar electrode array.

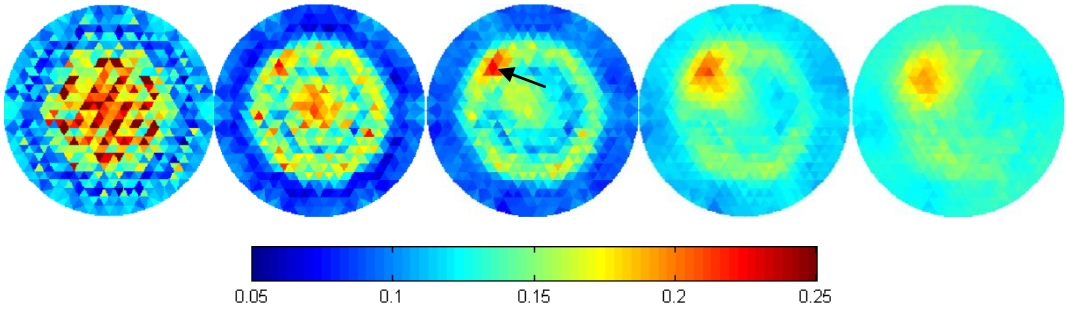

Figure 6. 26. The reconstructed result of case 3, using the MK4 system.

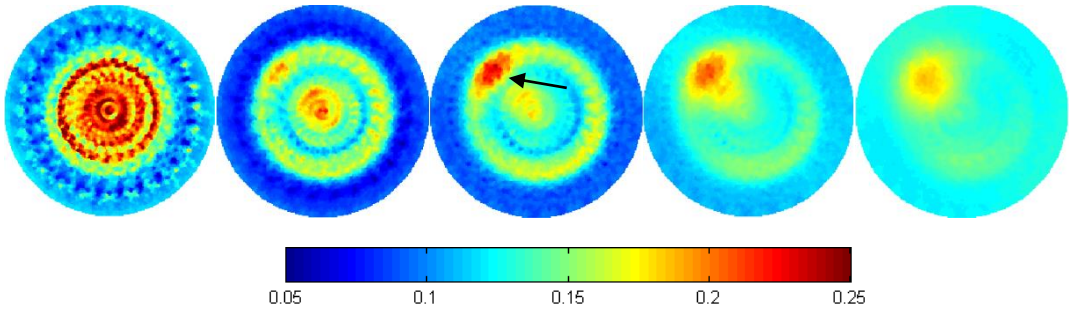

Figure 6. 27. The reconstructed result of case 3, using the RPEIM system with 4 measurement positions.

Case 4: The tumour is located at [-3.5, 3, 4.05] (in the fifth image layer) with a size of 2cm. The reconstructed results of the MK4 system and the RPEIM system are shown in Figure 6. 28 and Figure 6. 29.

Result for case 4: When the tumour with a size of 2 cm moves further to 4.05 cm away from the planar electrode array, the image of the tumour enlarges. The sensitivity in the region remote from the planar electrode array is poor, so the object in that region is not well imaged.

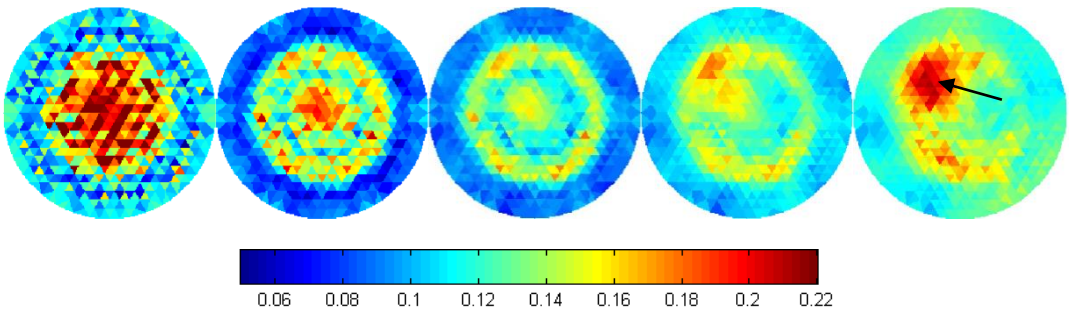

Figure 6. 28. The reconstructed result of case 4, using the MK4 system.

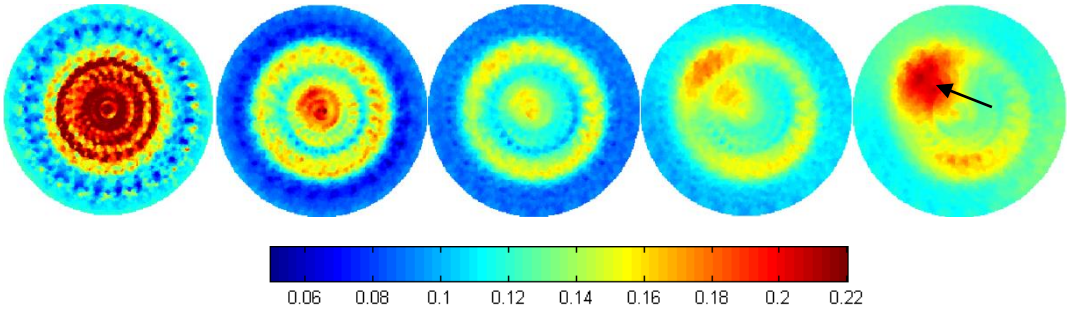

Figure 6. 29. The reconstructed result of case 4, using the RPEIM system with four measurement positions.

Table 6. 4. Summary of the detectability of the MK4 and the RPEIM system

	Tumour location (cm)	Tumour size (cm)	Detectable		Image accuracy	
Case 1	[-3.5, 3, 1.35]	1	MK4	Yes	MK4	Poor
			RPEIM	Yes	RPEIM	Good
Case 2	[-3.5, 3, 2.25]	1	MK4	No	MK4	
			RPEIM	No	RPEIM	
Case 3	[-3.5, 3, 2.25]	2	MK4	Yes	MK4	Poor
			RPEIM	Yes	RPEIM	Good
Case 4	[-3.5, 3, 4.05]	2	MK4	Yes	MK4	Poor
			RPEIM	Yes	RPEIM	Poor

Table 6. 4 gives a summary of the detectability of the MK4 system and the RPEIM system. The detectability of the MK4 system and the RPEIM system is similar, which can detect a 1 cm tumour within depth of 1.35 cm and 2 cm tumour in any depth of the tank. But as the tumour moves away from the planar electrode array, the image accuracy of both system gets worse. This shows the limitation of the MK4 and the RPEIM system in detecting the tumour in depth of the dig volume breasts.

6.7.6. Simulations based on a real patient

The conductivity map of Patient 0703 detected by the MK4 system is given in Section 4.4.3. In this section, a digital breast phantom of Patient 0703 is made and applied to both the MK4 system and the RPEIM system to achieve two comparisons: 1) comparing the conductivity maps of the real patient and the breast phantom, which will demonstrate that the digital breast phantom is a good replica of the breast of Patient 0703; 2) comparing the conductivity maps from the MK4 system and the RPEIM system based on the breast phantom, which will present the improvements of the RPEIM system.

Although this study is based on simulation, this approach will make sure that the mock clinical trial is very close to realistic.

Figure 6. 30 shows the X-ray images and the conductivity maps of Patient 0703's left breast, in which LMLO and LCC indicate the mediolateral-oblique (MLO) and craniocaudal (CC) view of the left breast (the first L indicates the left breast). The breast phantom of Patient 0703 is set up according to both the X-ray images and the conductivity maps. Before setting up the breast phantom, it should be emphasized that the breast phantom cannot be exactly the same as the real breast as the inner structure and the exact conductivity values of the breast tissues are unknown, but the breast phantom can be close to the real breast, if it is carefully defined according to the features of the real breast. The cup size of Patient 0703 is C. In examination, the thickness of the breast is pressed to 1.8cm by the MK4 system. The features of the breast of Patient 0703 are: 1) according to Figure 6. 30 (a), the mammary gland in the caudal breast is denser than the cranial breast, so for the breast phantom, there should be more ducts and acini in the caudal breast than the cranial breast (Figure 6. 31 (b)); 2) according to Figure 6. 30 (b), the mammary gland on the left hand side is dense and has a round profile; however the mammary gland on the right hand side is not dense and has an almost straight profile, so the breast phantom is built as Figure 6. 31 (c); 3) according to Figure 6. 30 (c) and (d), the tumour is at the upper outside quadrant; 4) according to Figure 6. 30 (c), the conductivity in the upper inner quadrant (UIQ) is relatively small, so there should be less ducts and acini in that area. With these features, we set up the breast phantom of Patient 0703 in Figure 6. 31. The size and location of the tumour is estimated according to the conductivity maps, which is located at [-2.98 1.47 0.9] (cm) and has a size of 0.7 cm in width, 1.3 cm in length and 0.5 cm in height. The conductivity values of the breast phantom are estimated according to the conductivity maps and shown in Table 6. 5. In simulations, the operating frequency is 500 kHz, the sampling frequency is 20 MSa/s, the sample number is 1000, the ADCs are 14 bit, the background noise is 60dB white Gaussian noise, and the multiplicative noise is $\pm 0.5\%$ random noise.

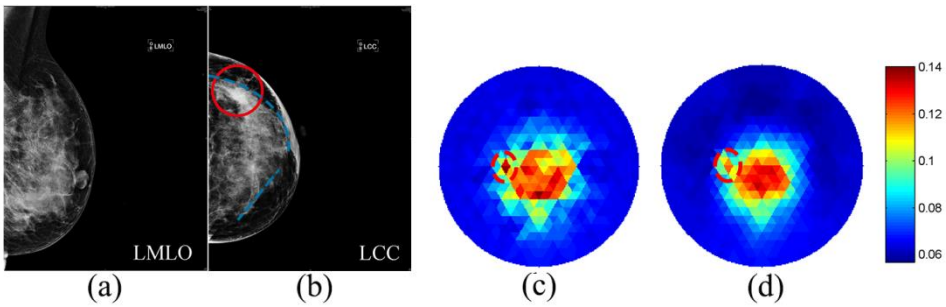

Figure 6. 30. X-ray images and conductivity maps of Patient 0703, tumor indicated by red circle. (a) and (b) are the LMLO and the LCC image. (c) and (d) are the conductivity maps of the bottom and the top layer.

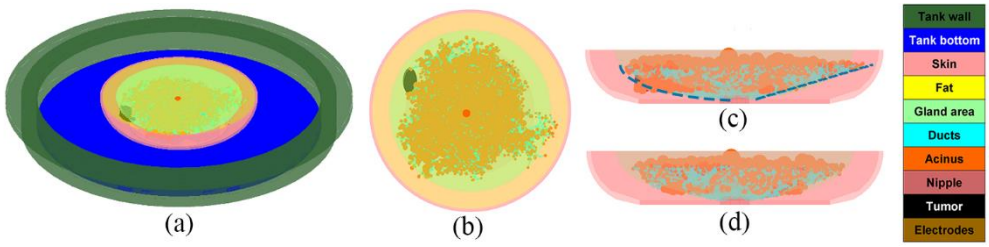

Figure 6. 31. The breast phantom of Patient 0703. (a) shows the compressed breast in the breast container. (b) is the XY view of the breast phantom. (c) is the XZ view of the breast phantom. (d) is the YZ view of the breast phantom.

Table 6. 5 The conductivity of the breast phantom

Breast	Saline	Skin	Fat	Gland area	Nipple, ducts, acinus	Tumor
Conductivity (S/m)	0.05	0.15	0.04	0.06	0.14	0.6

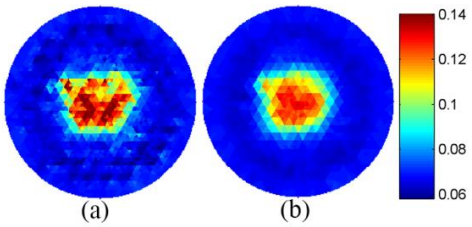

Figure 6. 32. The conductivity distribution of the breast phantom of Patient 0703 detected by the MK4 system.

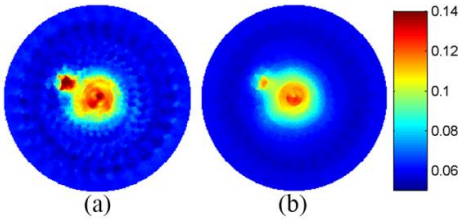

Figure 6. 33. The conductivity distribution of the breast phantom of Patient 0703 detected by the RPEIM system with 5 measurement positions, using two layers.

Figure 6. 32 presents the simulated result of the breast phantom detected by the MK4 system. The red elements highlighted by the circles indicate the presence of the tumour.

The red area in the centre is caused by the gland. By comparing Figure 6. 30 (c) (d) and Figure 6. 32, we find that 1) the size and the location of the tumour in Figure 6. 30 (c) (d) and Figure 6. 32 are similar; 2) the areas of the gland (the red area in the centre of the conductivity maps) in Figure 6. 30 (c) (d) and Figure 6. 32 are similar; 3) both Figure 6. 30 (c) and Figure 6. 32 (a) have a less conductive area in the UIQ and the shapes of the less conductive areas are similar; therefore we conclude that 1) the breast phantom could simulate the conductivity distribution of a real breast at the precision that the EIT systems can distinguish; 2) the digital breast phantom is valuable for the mock clinical trials of EIT. Knowing that the breast phantom of Patient 0703 could contribute to a similar conductivity map with the real examination, we apply the RPEIM system to this breast phantom for a mock clinical trial. Figure 6. 33 shows the reconstructed conductivity maps of the breast phantom, detected by the RPEIM system with five measurement positions. Comparing Figure 6. 32 and Figure 6. 33, we find that the result from the MK4 system is seriously affected by the noise and the size of the mesh elements; however by using the RPEIM system, the influences from the noise and the size of the mesh are significantly reduced, the image of the tumour is much clearer, and the spatial resolution of the conductivity maps is significantly improved.

6.8 Discussion

The advantages of the RPEIM system compared with the former MK4 system are: high accuracy, high spatial resolution and good tolerance to noise.

Regarding the accuracy, to make a reliable performance assessment of the RPEIM system, we define some critical parameters, which include: conductivity contrast, object centre, object size (length and width), errors of object centre and size, and object distortion. These parameters are plotted and tabulated in Figure 6. 14 and

Table 6. 1 to investigate the relationships between the image accuracy and the number of measurement positions. Generally the RPEIM system generates better results than the MK4 system. For the RPEIM system, we suggest three to five measurement

positions: three measurement positions is preferred for speed; five measurement positions is preferred for higher accuracy. Increasing the number of measurement positions beyond 5 is pointless, as it is time consuming and no further improvement can be obtained.

As for the spatial resolution, the RPEIM system exhibits a significant improvement over the MK4 system. To demonstrate this, a breast model with two tumours is employed and the results corresponding to the MK4 system and the RPEIM system with 5 measurement positions are shown in Figure 6. 16, Figure 6. 17 and Figure 6. 18. For the MK4 system, the image of the normal gland and the images of the two tumours are mixed together. If we didn't have the knowledge of the structures of the breast phantom, we could hardly determine the existence of the tumours. However for the RPEIM system, the images of the normal gland and the two tumours are clearly separated. By plotting the conductivity distribution across the centres of the two tumours in Figure 6. 18 (d), we estimated that the boundary to boundary distance is equal to 0.99 cm. This result is very close to the real distance of 1cm. Thus, we believe that the RPEIM system could deliver a better spatial resolution than the MK4 system.

Considering noise, the RPEIM system has a much better noise tolerance than the MK4 system as the errors of the reconstructed conductivity values are averaged by the algorithm of the synchronous mesh method. Figure 6. 11 and Figure 6. 19 present the reconstructed results of the breast model in Figure 5. 1, by using 70 dB and 45 dB measurements from the MK4 system. Comparing these two results, we can find that as the noise increases, the image quality deteriorates seriously. Figure 6. 10 and Figure 6. 20 present the reconstructed results of the same breast model, by using 70 dB and 45 dB measurements from the RPEIM system with four measurement positions. According to these results, we can find that although the noise increased to a high level, it didn't affect the detection of the tumour, which proves that the RPEIM system could achieve a good noise tolerance by increasing the number of the measurement positions. By comparing Figure 6. 19 and Figure 6. 20, we believe that the RPEIM system with the synchronous

mesh method not only reduces the errors caused by the noise from the system, but also reduces the errors caused by the size of the mesh elements.

The detectability of the MK4 and the RPEIM system is similar, which can detect 1 cm cancer at a depth of 1.35 cm and 2 cm cancer at any depth of the tank. However when the cancer is far from the electrode plane, the image quality is not very good.

To validate our study, we made simulations based on Patient 0703, whose tumour was detected by the MK4 system. To apply the RPEIM system to this patient, we firstly built a digital breast phantom in Figure 6. 31. By comparing the simulated result in Figure 6. 32 with the experimental result in Figure 6. 30, we conclude that 1) the digital breast phantom is a close replica of the real breast; 2) the digital breast phantom could be an alternative approach to clinical trials when the number of volunteers is limited. We then applied the RPEIM system to this digital breast phantom. By comparing the result in Figure 6. 33 with the results in Figure 6. 30 and Figure 6. 32, we conclude that the RPEIM system has better performances in image accuracy, spatial resolution and noise tolerance than the MK4 system.

6.9 Conclusion

The RPEIM system is superior to the MK4 system in image accuracy, spatial resolution and noise tolerance due to the increase in the number of independent measurements and the synchronous mesh method. The increase of the independent measurements provides more boundary conditions, which increases the solution constraints, hence ensuring a more accurate result. The synchronous mesh method avoids refining the mesh to support the electrode rotations; therefore it prevents greater ill-conditioning caused by the fine mesh. The rotations of the mesh, together with the electrode array, permit the conductivity maps to be reconstructed at different angles. The

mapping algorithm merges the conductivity values of the coarse meshes into the values of the fine meshes, and finally combines them into one 3D image or several cross-sectional images. This minimizes the influence of the mesh and makes the conductivity distribution smooth, not lumpy, hence giving better spatial resolution. The final image is reconstructed from several groups of measurements; therefore the random noise from one group of measurements will be ameliorated, hence delivering better noise tolerance. In general, the RPEIM system with the synchronous mesh benefits the image accuracy, spatial resolution and noise tolerance. However the improvement of the image quality is not linear with the number of measurement positions. There won't be an obvious improvement if the number of measurement positions exceeds five. Indeed, considering the computational time, three to five positions are reasonable in practice. The RPEIM system doesn't have an improvement in detectability over the MK4 system. For planar electrode arrays, it is very challenging to detect the cancer deep in the breast accurately.

7. Combined electrode array EIM system

As studied in Section 6.6.5, the planar electrode array is not sensitive to the tumour remote from the electrode plane. This chapter will introduce a novel 3D EIM system, which combines a ring electrode array with a planar electrode array that can operate independently or together. This combined electrode array EIM system is named the CEIM system. It has three operational modes. It provide enhanced detectability of a tumour deep within the tissue, as required for a large volume breast.

7.1 The data acquisition method of the CEIM system

The CEIM system is an evolution of the MK4 system, which keeps the planar electrode array of the MK4 system and adds a ring electrode array at the top of the tank (see Figure 7. 1 (a)). The planar electrode array is adjustable in the vertical directions to accommodate different breast volumes. There are 85 electrodes in the planar electrode which are deployed in a hexagonal manner (see Figure 7. 1 (b)). The ring electrode array has 18 electrodes, which are equally distributed in the upper inner wall of the tank. The ring electrode array and the planar electrode array can work separately and together.

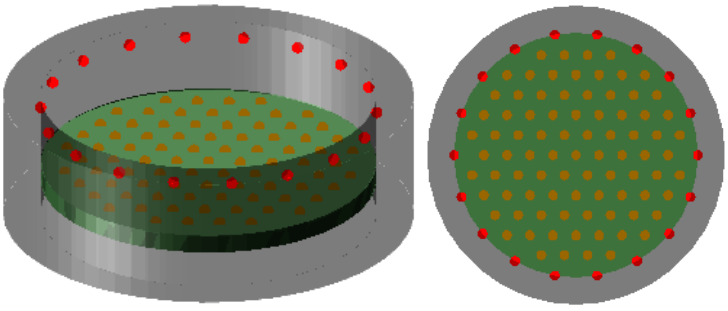

Figure 7. 1. The electrode arrangement of the CEIM system

In the CEIM system, current excitation and voltage measurement is adopted. The CEIM system has three operational modes. Mode 1 works in the same manner as the MK4

system, which has 123 current excitations and 1416 voltage measurements using the planar electrode array; Mode 2 provides current excitations from the ring electrode array and measures voltages using the planar electrode array; Mode 3 combines Mode 1 and Mode 2.

For Mode 2, current excitations are applied from 9 directions at 0°, 20°, 40°, 60°, 80°, 100°, 120°, 140°, and 160°. In each driving direction, there are 7 driving events, which are performed sequentially; thus the total number of the driving events is 63. Figure 7. 2 shows the driving events at 0° and 20°. The big dots connected by the arrows indicate the drive pairs, in which '+' and '-' indicate the positive and negative poles. The small dots indicate the electrodes of the ring electrode array, which do not participate in excitations in that direction.

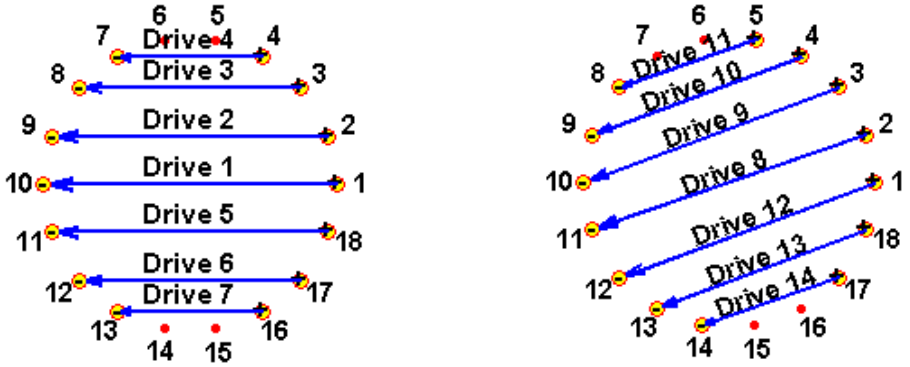

(a) (b)

Figure 7. 2. The driving method for the CEIM system. (a) shows the driving events at 0° (they don't happen simultaneously); (b) shows the 7 driving events at 20° (they don't happen simultaneously).

In Mode 2, an adaptive measuring method is adopted: for each excitation, only the strongest voltage measurements from the adjacent electrodes of the planar electrode array are collected. This is achieved by simulations base on a uniform field in the tank. Given the size of the tank and the conductivity of the saline in the tank, we can compute the voltage measurements of all the possible adjacent pairs, under current excitation from the *n*th drive. For the planar electrode array, which is denoted by the 85 small dots in Figure

7. 3, there are 222 adjacent electrode pairs in total; therefore the total number of voltage measurements, corresponding to 63 excitations, is 222×63=13986. A threshold is used to exclude the small amplitude measurements. This will make sure that all the measurements left are strong and have a small dynamic range. Figure 7. 3 shows the measurement pairs corresponding to Drive 1 and Drive 8, for the case when the tank depth is set to 4.5 cm and the conductivity of the saline in the tank is 0.05 S/m. The threshold chosen for this case is:

$$T = V_{min} + \frac{V_{max} + V_{min}}{2} \qquad (7.1)$$

where: T is the threshold, V_{min} and V_{max} denote the minimum and maximum measurement of the 13986 measurements. In Figure 7. 3, the dots numbered from 1 to 18 indicate the ring electrode array, where the big dots with '+' and '-' indicate the drive pairs; the other dots indicate the planar electrode array, where the dots connected by arrows indicate the measuring pairs corresponding to the highlighted drive pairs. According to this design, there are 2036 independent measurements.

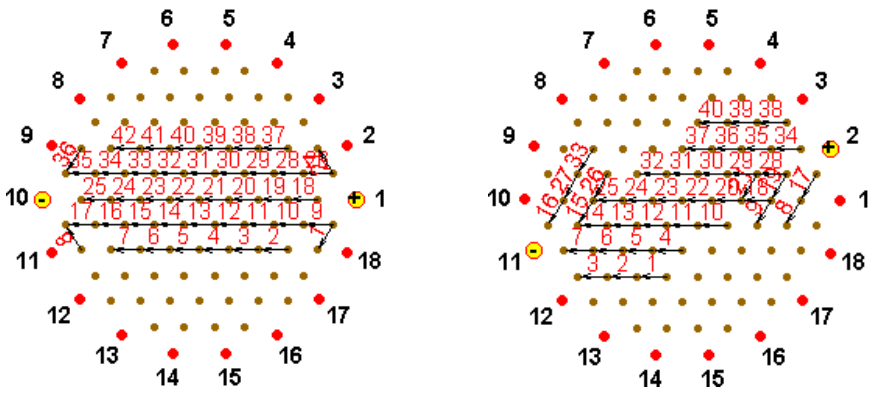

(a) (b)

Figure 7. 3. The measuring method of the CEIM system. (a) shows the voltage measurements corresponding to Drive 1. (b) shows the voltage measurements corresponding to Drive 8.

Mode 3 is a combination of Mode 1 and Mode 2. It produces 3452 voltage

measurements, in which 1416 measurements are from Mode 1 with current excitations and voltage measurements from the planar electrode array and 2036 measurements are from Mode 2 with current excitations from the ring electrode array and voltage measurements from the planar electrode array. The configuration of the CEIM system is tabulated in Table 7. 1.

Table 7. 1. The configuration of the CEIM system

	Mode 1 (MK4)	Mode 2	Mode 3
Working electrode	planar electrodes	planar and ring electrodes	planar and ring electrodes
Drive electrode	planar electrodes	ring electrodes	planar and ring electrodes
Measuring electrode	planar electrodes	planar electrodes	planar electrodes
Number of drives	123	63	186
Number of measurements	1416	2036	3452
Measurements of 4.5cm saline-filled tank (the conductivity of the saline is 0.05 S/m)			
Measurement scale	0.35~1.13	0.22~0.54	0.35~0.54
Dynamic range	3.2	2.4	5.1

Note: the number of the voltage measurements of the CEIM system depends on the height of the tank.

7.2 Simulation result of the CEIM system

Figure 7. 4 shows a digital breast phantom, which is composed of skin, fat, ducts, acini, gland area, tumour and nipple. Figure 7. 4 (a) shows the breast phantom in the tank; Figure 7. 4 (b) (c) and (d) are the XY, XZ and YZ views of the breast phantom. The conductivity values of the breast phantom are shown in Table 7. 2. This breast phantom is 4.5 cm thick. The maximum diameter of the breast is 15 cm. The contact diameter between the breast and the electrode plane is 6 cm. The tumour is placed at Cartesian coordinate position [4, 3.5, 4.05] cm with a length of 2 cm, a width of 1.5 cm and a height of 0.9 cm. The mesh for image reconstruction has 5 layers, 2526 nodes and 11700 elements. Figure 7. 5 to Figure 7. 7 show the reconstructed results of the breast phantom using the three operational modes. The results are raw data without image processing or interpolation. In Figure 7. 5, the left image shows the conductivity distribution in the bottom of the tank, where the red circular area in the centre indicates the highly conductive skin and the other area indicates the saline; the middle image shows the

conductivity distribution in the middle of the tank, where the red area in the centre is caused by the ducts and acini, the red ring is caused by the high conductivity skin, the green area in between the red ring and the red centre indicates the fat, the green area outside the red ring indicates the saline; the right image shows the conductivity distribution in the top of the tank, where the tumour is not imaged. In Figure 7. 6, as the ring electrode array excites the field at the top of the tank, the top region becomes more sensitive than the MK4 system (Mode 1); therefore we can observe that the image of the tumour in the top layer of Figure 7. 6 (right) is clearer than that of Figure 7. 5 (right). By using Mode 3, which combines all the measurements from Mode 1 and Mode 2, the tumour is very clearly imaged in the top layer of Figure 7. 7 (right).

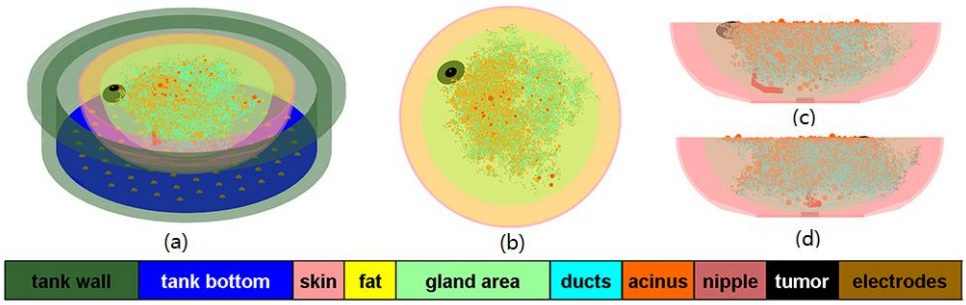

Figure 7. 4. Digital breast phantom

Table 7. 2. The conductivity values of the breast phantom (Unit: S/m)

skin	fat	ducts, acinus, nipple	gland area	tumor	saline
0.465	0.05	0.16	0.08	0.32	0.05

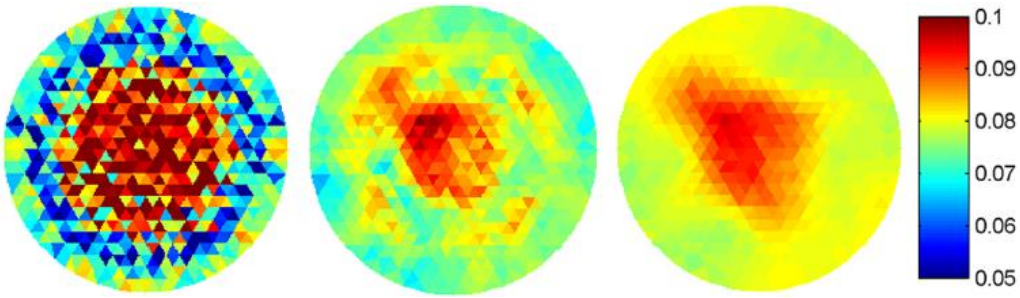

Figure 7. 5. The reconstructed conductivity maps of the bottom layer (left), the middle layer (middle) and the top layer using Mode 1 (the MK4 system)

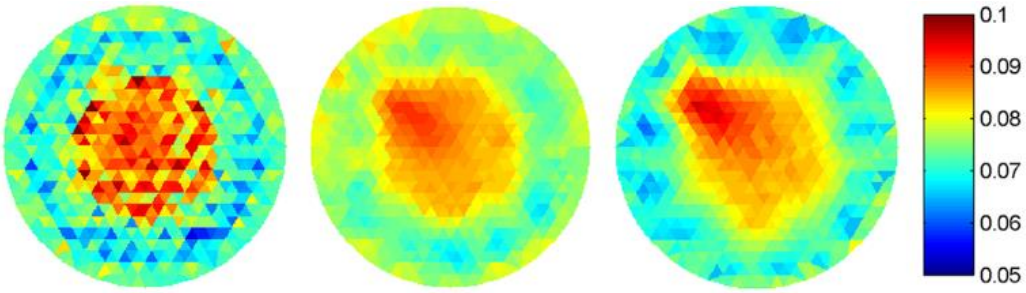

Figure 7. 6. The reconstructed conductivity maps of the bottom layer (left), the middle layer (middle) and the top layer using Mode 2

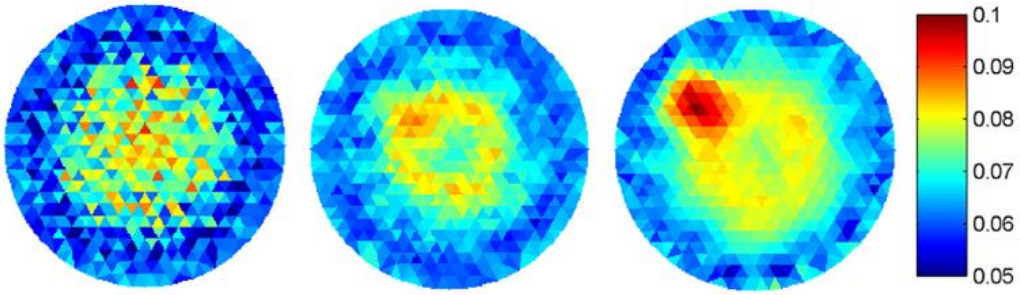

Figure 7. 7. The reconstructed conductivity maps of the bottom layer (left), the middle layer (middle) and the top layer using Mode 3

7.3 Conclusion

This chapter introduced the CEIM system which has a ring electrode array and a planar electrode array at the top and the bottom of the tank. The two electrode arrays can work independently or together. As an evolution of the MK4 system, the CEIM system has 3 operational modes. Mode 1 is the heritage of the MK4 system, which uses current excitations and voltage measurements from the planer electrode array at the bottom of the tank; therefore it is insensitive to a tumour deep in the breast. Mode 2 and Mode 3 utilise a ring electrode array at the top of the tank for current excitation, hence the CEIM system gives an improved performance in detecting a tumour deep in the breast. Mode 3 gives greatly enhanced performance.

8. Discussion and Conclusion

This chapter gives discussions of this thesis and concludes the contributions of this research.

8.1 Discussion

The breast, breast development, breast cancer and the risk factors of breast cancer are firstly introduced. This will help people understand where, when and how breast cancer develops. Breast cancer has already attracted great public attention in the developed western countries due to the high morbidity and mortality, however in developing countries, it is not widely concerned. For example, in China, females don't have regular breast examinations, especially in the outlying poverty-stricken areas, females even don't have basic breast knowledge. The author hopes that this section could help more women to understand their breasts and prevent breast diseases. This chapter also introduced the breast cancer detection methods and their advantages and limitations. EIM is a relatively new breast cancer detection method which is safe, painless, non-invasive, and non-ionizing. These features attract more and more researchers to study and develop EIM systems. The main groups working on EIM systems are introduced. Some EIM systems are under clinical trials but not commercialized, as there are still challenges with sensitivity, spatial resolution and detectability needing to be addressed. The work in the thesis focuses on these challenges.

The mathematical and physical basis of EIT are introduced, giving the definitions of the EIT forward problem and the EIT inverse problem. The finite element method is used to solve the EIT forward problem and the EIT inverse problem. All the relative mathematical formulas are given to help researchers to understand the EIT algorithms. If the change of the conductivity of the field under investigation is small, the EIT inverse problem can be approximated by a linear problem; however if the change of the

conductivity is significant, the EIT inverse problem can be solved by iteration. As the EIT inverse problem is very ill-posed, regularization is used to obtain the approximate solution of the EIT inverse problem. The regularization parameter, which trades off the fitting accuracy and the change of conductivity, can be determined using the L-curve method.

The Sussex MK4 system is introduced. This is a novel 3D EIM system, developed by the bio-medical group in the University of Sussex. It is a dedicated EIM system with functions of data acquisition, self-cleaning and safety. The most novel part of the MK4 system is the hexagonal electrode arrangement and the hexagonal data acquisition method. The image reconstruction algorithm used in the MK4 system is different from the generally used regularization method, which uses voltage differences (we name it differential algorithm). The MK4 system uses the logarithm of the voltage ratios to reconstruct the conductivity distribution (we name it logarithm algorithm), as the algorithm can minimize the spacing errors of the electrodes, has a positive constraint to the solution and has a better noise tolerance than the differential algorithm.

An enhanced image reconstruction algorithm is presented. The novel part of the new algorithm is the correction term. The enhanced image reconstruction algorithm using a duo-mesh method improves the vertical accuracy and sensitivity. To address the improvements of the new algorithm over the former algorithms, comparisons are made based on simulations, phantoms and real patents. To assess the accuracy of the reconstructed result, an image processing based error analysis method is proposed. This method not only provides image errors of the target object but also outlines the shape of the object of interest.

A method to program digital breast phantoms is presented. It includes a skin envelope, ducts, acini, a nipple, a gland area and tumours. Digital breast phantoms are very important in studying EIM systems. Before manufacturing a new EIM system,

sufficient studies and simulations are needed to determine if the new equipment is worth investing in. In this case, close-to-realistic breast phantoms are valuable to make the studies and simulations close to clinical trials. Even though the EIM system is already made, the digital breast phantoms can be used to determine the tumour detection requirements, such as the detectable tumour size, depth, and the conductivity contrast between the tumour and the surrounding normal tissue. When the number of volunteers, who have been diagnosed with breast cancers is limited, the digital breast phantoms can provide unlimited data for the researchers to study. A detailed method to model the breast envelope, gland ducts, gland acini, gland area and tumours has been created and the method to apply the digital breast phantoms to EIM systems is demonstrated.

A novel rotary planar electrode array EIM (RPEIM) system has been developed. It is an upgraded version of the MK4 system. It permits the planar electrode array to rotate in the horizontal plane, so that it can achieve a significant increase of independent measurements. To avoid the rotation of the planar electrode causing changes of the field under investigation, breast containers with different depths are employed. The bottoms of the breast containers are conducting with a conductivity of about 0.05 S/m; the wall of the breast container is non-conducting. To support the rotation of the planar electrode array, a synchronous mesh method is developed. This method avoids using a fine mesh for image reconstruction, therefore it can avoid the unreasonably long computational time, the huge data volume, the worsening ill-posed problem and the non-uniform spatial resolution. The feasibility studies of the RPEIM system has proven that it has a better image accuracy, spatial resolution and noise tolerance than the MK4 system. But the detectability of the RPEIM system and the MK4 system is similar.

A combined electrode array EIM (CEIM) system has been created and tested. It is also an evolution of the MK4 system. It adds a ring electrode array at the top of the tank based on the MK4 system. This system has 3 operational modes. Mode 1 uses the planar electrode array for current excitation and voltage measurement, which is an inheritance

of the MK4 system. Mode 2 uses the ring electrode array for current excitation and the planar electrode array for voltage measurement. Applying the current excitations from the top of the tank will increase the sensitivity in the top region; therefore it will be more sensitive to the tumour deep in the breast. Mode 3 is a combination of Mode 1 and Mode 2. The studies on the CEIM system have demonstrated that Mode 3 can achieve a much better result than the other operational modes.

8.2 Conclusion

The achievement of this thesis includes:

1. A comparison of two regularization methods: the differential algorithm and the logarithm algorithm.
2. A comparison of two planar electrode arrays: the rectangular planar electrode array and the hexagonal electrode array.
3. An enhanced image reconstruction algorithm. This algorithm can improve the vertical image accuracy and sensitivity for the planar electrode array.
4. A method to set up a close-to-realistic digital breast phantoms for EIM systems
5. A design of a rotary planar electrode array EIM (RPEIM) system and the supporting algorithm. The RPEIM system gives much better performance in image accuracy, spatial resolution and noise tolerance (reliability).
6. A design of a combined electrode array EIM (CEIM) system. The CEIM system has improved detectability of the tumour deep in the breast.

The comparison of the differential algorithm and the logarithm algorithm is based on simulations. The differential algorithm uses the voltage differences between the real measurements and the reference measurements to reconstruct the conductivity distribution; however the logarithm algorithm uses the logarithm of the voltage ratios to reconstruct the conductivity distribution. To make the comparison equal, the same noise

was added to the measurements and L-curve method is used to determine the optimised regularization parameter α. From the reconstructed results, we can find that the logarithm algorithm has a better noise tolerance than the differential algorithm.

The comparison of the rectangle electrode array and the hexagonal planar electrode array shows that the hexagonal planar electrode array uses less electrodes than the rectangular electrode array, but can achieve smaller dynamic range, better image accuracy and better spatial resolution.

In the simulations and the real case of phantoms and patients, the enhanced image reconstruction algorithm using the duo-mesh method has been proven more accurate and sensitive than the former algorithm and effective in improving vertical resolution. Although this new algorithm is developed for the Sussex MK4 EIM system, the idea of using a correction strategy in the image reconstruction algorithm is relevant to any EIT image reconstruction equipment - regardless of the hardware design. Despite the limitation in detection of the depth and height of the object, with the new algorithm the planar electrode array can generate a more accurate 3D image and roughly estimate the depth of the object.

Digital breast phantoms are valuable in mock clinical trials. Before manufacturing new EIM systems, sufficient simulations are necessary to investigate if the new system is worth investing in. The digital breast phantom proposed in this thesis could make simulations much closer to real cases. A digital breast phantom of patient 0703 was made. By comparing the conductivity maps of the digital breast phantom and patient 0703 from the MK4 system, we can find that the digital breast phantom is a good replica of the real breast.

The RPEIM system is superior to the MK4 system in image accuracy, spatial resolution and noise tolerance due to the increase in the number of independent

measurements and the synchronous mesh method. The increase of the independent measurements provides more boundary conditions, which increases the solution constraints, hence ensuring a more accurate result. The synchronous mesh method avoids refining the mesh to support the electrode rotations; therefore it prevents greater ill-conditioning caused by the fine mesh. The rotations of the mesh, together with the electrode array, permit the conductivity maps to be reconstructed at different angles. The mapping algorithm merges the conductivity values of the coarse meshes into the values of the fine meshes, and finally combines them into one 3D image or several cross-sectional images. This minimizes the influence of the mesh and makes the conductivity distribution smooth, not lumpy, hence giving better spatial resolution. The final image is reconstructed from several groups of measurements; therefore the random noise from one group of measurements will be ameliorated, hence delivering better noise tolerance. In general, the RPEIM system with the synchronous mesh benefits the image accuracy, spatial resolution and noise tolerance. However the improvement of the image quality is not linear with the number of measurement positions. There won't be an obvious improvement if the number of measurement positions exceeds five. Indeed, considering the computational time, three to five positions are reasonable in practice.

As an evolution of the MK4 system, the CEIM system has 3 operational modes. Mode 1 is the heritage of the MK4 system, which uses current excitations and voltage measurements from the planer electrode array at the bottom of the tank; therefore it is insensitive to a tumour deep in the breast. Mode 2 provides current excitations from the ring electrode array and measures voltages using the planar electrode array; Mode 3 combines Mode 1 and Mode 2. Mode 2 and Mode 3 utilise a ring electrode array at the top of the tank for current excitation, hence the CEIM system gives an improved performance in detecting a tumour deep in the breast. Especially for Mode 3, it gives greatly enhanced performance.

9. Future Work

Following the work in this thesis, there are some research gaps suggested that need to be further investigated:

1) efficient drive and measuring methods

The drive pairs of the CEIM are performed sequentially. New studies can make the drive pairs in the same direction perform simultaneously and make the electric field in the driving electrode plane close to a uniform field. For this case, the tumour in that plane can be easily detected. The ring electrode array is not necessarily placed at the top of the tank. It could be placed at any depth and of any layers. For example, the tank could have 2 layers of ring electrode arrays, placed at the middle and the top positions. Or the ring electrode array could be made adjustable in the vertical direction. In this case, designers should think about the leakage problems of the tank.

2) Rotary CEIM system

The rotary CEIM system is a combination and RPEIM system and the CEIM system, which means the system can permit the ring electrode array and the planar electrode array to rotate in the horizontal plane. The rotations of the electrode array could provide much more independent measurements than the CEIM system, thus it will benefit image accuracy, spatial resolution and reliability; however this design requires consideration that the movements of the electrode arrays may result in agitation of the field under investigation.

3) Image reconstruction algorithms

EIT Image reconstruction algorithms have great influence on image quality. More effort is needed to improve the current image reconstruction algorithms. When designing image reconstruction algorithms, besides the image accuracy, the data

volume and the computational time should be considered.

4) Combine EIT with the other imaging modality

There is some research, which combines EIM with ultrasound or magnetic resonance (Béqo et al., 2010, Sadleir et al., 2013). Using two or more imaging modalities to diagnose the breast cancer will increase the accuracy and reliability of the result. As we know that the reference conductivity is very important in image reconstruction. If the reference conductivity distribution is close to the real conductivity distribution under investigation, the reconstructed result will be close to the real situation; however if the reference conductivity distribution is far from the real one, the reconstructed result may not converge. With the aid of the other imaging modalities, such as ultra sound and magnetic resonance, the profile and the anatomic features of the breast can be obtained. This could be used as prior knowledge. The more prior knowledge we have, the more accurate the result will be.

5) Database of breast conductivity

As mentioned in the former paragraph, the reference conductivity is very important in image reconstruction. Only knowing the anatomic features of the breast but having no knowledge of the breast conductivity, the reference conductivity is unknown. For example, by using ultrasound or magnetic resonance, we can distinguish the adipose tissue and the gland tissue; however if we don’t know the conductivity values of the adipose tissue and the gland tissue, in this situation, we can’t distinguish the adipose tissue and the gland tissue using the conductivity, as a result, we have no way to obtain the reference conductivity distribution. Therefore a breast conductivity database is very important. It will be helpful to improve the prior knowledge, hence this will benefit image accuracy.

References

Medical engineering & physics, Oxford : Butterworth-Heinemann, 1994-.

ALLEN, N. E., BERAL, V., CASABONNE, D., KAN, S. W., REEVES, G. K., BROWN, A., GREEN, J. & MILLION WOMEN STUDY, C. 2009. Moderate alcohol intake and cancer incidence in women. *J Natl Cancer Inst,* 101**,** 296-305.

AMERICAN CANCER SOCIETY 2011. Breast Cancer Facts & Figures 2011-2012. American Cancer Society.

AMERICAN CANCER SOCIETY 2014a. Breast Cancer Facts & Figures 2013-2014. American Cancer Society.

AMERICAN CANCER SOCIETY. 2014b. *How is breast cancer staged?* [Online]. Available: http://www.cancer.org/cancer/breastcancer/detailedguide/breast-cancer-staging [Accessed 6 January 2015].

AMERICAN CANCER SOCIETY 2014c. Mammograms and Other Breast Imaging Tests.

AMERICAN MEDICAL NETWORK. 2008. *Breast Anatomy and Development* [Online]. Available: http://www.health.am/cr/more/breast-anatomy-and-development/ [Accessed 27 December 2014].

AMMARI, H., KWON, O., SEO, J. K. & WOO, E. J. 2004. T-Scan Electrical Impedance Imaging System for Anomaly Detection. *SIAM Journal of Applied Mathematics,* 65**,** 252-266.

AVIS, N. J. & BARBER, D. C. 1995. Incorporating a priori information into the Sheffield filtered backprojection algorithm. *Physiol Meas,* 16**,** A111-22.

B QO, N., SZE, G., TUNSTALL, B., QIAO, G., ZARAFSHANI, A. & WANG, W. 2010. A flexible and configurable hardware for the combined EIM and Ultrasound device. *Journal of Physics: Conference Series,* 224**,** 012165.

BARBER, D. C. 2005. EIT: The view from Sheffield. *In:* HOLDER, D. (ed.) *Electrical impedance tomography : methods, history and applications.* Bristol: Institute of Physics.

BARBER, D. C., BROWN, B. H. & AVIS, N. J. Image reconstruction in Electrical Impedance Tomography using filtered back-projection. Engineering in Medicine and Biology Society, 1992 14th Annual International Conference of the IEEE, Oct. 29 1992-Nov. 1 1992 1992. 1691-1692.

BARBER, D. C. & SEAGAR, A. D. 1987. Fast reconstruction of resistance images. *Clin Phys Physiol Meas,* 8 Suppl A**,** 47-54.

BERG, W. A., ZHANG, Z., LEHRER, D. & ET AL. 2012. DEtection of breast cancer with addition of annual screening ultrasound or a single screening mri to mammography in women with elevated breast cancer risk. *JAMA,* 307**,** 1394-1404.

BOICE, J. D., JR., PRESTON, D., DAVIS, F. G. & MONSON, R. R. 1991. Frequent chest X-ray fluoroscopy and breast cancer incidence among tuberculosis patients in Massachusetts. *Radiat Res,* 125**,** 214-22.

BOUCHETTE, G., CHURCH, P., MCFEE, J. E. & ADLER, A. 2014. Imaging of Compact Objects Buried in Underwater Sediments Using Electrical Impedance Tomography. *Geoscience and Remote Sensing, IEEE Transactions on,* 52**,** 1407-1417.

BOYD, N. F., GUO, H., MARTIN, L. J., SUN, L., STONE, J., FISHELL, E., JONG, R. A., HISLOP, G., CHIARELLI, A., MINKIN, S. & YAFFE, M. J. 2007. Mammographic density and the risk and detection of breast cancer. *N Engl J Med,* 356**,** 227-36.

BREAST CANCER FUND. 2015. *Ionizing Radiation* [Online]. Available: http://www.breastcancerfund.org/clear-science/radiation-chemicals-and-breast-cancer/ionizing-radiation.html [Accessed 26 January 2015].

BREASTCANCER.ORG. 2015a. *Family History* [Online]. Available: http://www.breastcancer.org/risk/factors/family_history [Accessed 9 January 2015].

BREASTCANCER.ORG. 2015b. *Stages of Breast Cancer* [Online]. Available: http://www.breastcancer.org/symptoms/diagnosis/staging [Accessed 6 January 2015].

BREASTCANCER.ORG. 2015c. *U.S. Breast Cancer Statistics* [Online]. Available: http://www.breastcancer.org/symptoms/understand_bc/statistics [Accessed 9 January 2015].

BRIEN, M. R. 2011. *Further Exploration of EIT in Cancer Detection.* Doctor of Philosophy, University of Leicester.

BRINTON, L. A., SCHAIRER, C., HOOVER, R. N. & FRAUMENI, J. F. 1988. Menstrual Factors and Risk of Breast Cancer. *Cancer Investigation,* 6**,** 245-254.

BROWN, B. H. 1999. *Medical physics and biomedical engineering,* Philadelphia ; Bristol, Institute of Physics Publishing.

BROWN, B. H., BROWN, B. H. M. P. & PHYSIOLOGICAL, M. 1999. *Medical physics and biomedical engineering,* Philadelphia ; Bristol, Institute of Physics Pub.

CANCER RESEARCH UK. 2013a. *How a cancer grows* [Online]. Available: http://www.cancerresearchuk.org/about-cancer/cancers-in-general/what-is-cancer/grow/how-a-cancer-grows [Accessed 8 January 2015].

CANCER RESEARCH UK. 2013b. *How a cancer spreads* [Online]. Available: http://www.cancerresearchuk.org/about-cancer/cancers-in-general/what-is-cancer/grow/how-a-cancer-spreads [Accessed 8 January 2015].

CANCER RESEARCH UK. 2014. *Definite breast cancer risks* [Online]. Available: http://www.cancerresearchuk.org/about-cancer/type/breast-cancer/about/risks/definite-breast-cancer-risks [Accessed 9 January 2015].

CANCERQUEST. 2014. *Spread of Cancer Through the Lymphatic System* [Online]. Available: http://www.cancerquest.org/lymphatic-metastasis.html [Accessed 26 December 2014].

CAO, Z. & XU, L. J. 2013. Direct Image Reconstruction for 3-D Electrical Resistance Tomography by Using the Factorization Method and Electrodes on a Single Plane. *Ieee Transactions on Instrumentation and Measurement,* 62**,** 999-1007.

CHEN, W. Y., ROSNER, B., HANKINSON, S. E., COLDITZ, G. A. & WILLETT, W. C. 2011. MOderate alcohol consumption during adult life, drinking patterns, and breast cancer risk. *JAMA,* 306**,** 1884-1890.

CHEREPENIN, V., KARPOV, A., KORJENEVSKY, A., KORNIENKO, V., MAZALETSKAYA, A., MAZOUROV, D. & MEISTER, D. 2001. A 3D electrical impedance tomography (EIT) system for breast cancer detection. *Physiol Meas,* 22**,** 9-18.

CHEREPENIN, V. A., KARPOV, A. Y., KORJENEVSKY, A. V., KORNIENKO, V. N., KULTIASOV, Y. S., OCHAPKIN, M. B., TROCHANOVA, O. V. & MEISTER, J. D. 2002. Three-dimensional EIT imaging of breast tissues: system design and clinical testing. *IEEE Trans Med Imaging,* 21**,** 662-7.

CHOI, M. H., KAO, T. J., ISAACSON, D., SAULNIER, G. J. & NEWELL, J. C. 2007. A reconstruction algorithm for breast cancer imaging with electrical impedance tomography in mammography geometry. *Ieee Transactions on Biomedical Engineering,* 54**,** 700-710.

CUMMINGS, S. R., TICE, J. A., BAUER, S., BROWNER, W. S., CUZICK, J., ZIV, E., VOGEL, V., SHEPHERD, J., VACHON, C., SMITH-BINDMAN, R. & KERLIKOWSKE, K. 2009. Prevention of breast cancer in postmenopausal women: approaches to estimating and reducing risk. *J Natl Cancer Inst,* 101**,** 384-98.

CUTULI, B., BOREL, C., DHERMAIN, F., MAGRINI, S. M., WASSERMAN, T. H., BOGART, J. A., PROVENCIO, M., DE LAFONTAN, B., DE LA ROCHEFORDIERE, A., CELLAI, E., GRAIC, Y., KERBRAT, P., ALZIEU, C., TEISSIER, E., DILHUYDY, J. M., MIGNOTTE, H. & VELTEN, M. 2001. Breast cancer occurred after treatment for Hodgkin's disease: analysis of 133 cases. *Radiother Oncol,* 59**,** 247-55.

DE LUCIA, M., PARKER, G. J., EMBLETON, K., NEWTON, J. M. & WALSH, V. 2007.

Diffusion tensor MRI-based estimation of the influence of brain tissue anisotropy on the effects of transcranial magnetic stimulation. *Neuroimage,* 36**,** 1159-70.

DEROO, L. A., CUMMINGS, P. & MUELLER, B. A. 2011. Smoking before the first pregnancy and the risk of breast cancer: a meta-analysis. *Am J Epidemiol,* 174**,** 390-402.

ELIASSEN, A. H., HANKINSON, S. E., ROSNER, B., HOLMES, M. D. & WILLETT, W. C. 2010. Physical activity and risk of breast cancer among postmenopausal women. *Arch Intern Med,* 170**,** 1758-64.

ELKIN, E. B., HUDIS, C., BEGG, C. B. & SCHRAG, D. 2005. The effect of changes in tumor size on breast carcinoma survival in the U.S.: 1975-1999. *Cancer,* 104**,** 1149-57.

FOOTE, F. W. & STEWART, F. W. 1941. Lobular carcinoma in situ: A rare form of mammary cancer. *Am J Pathol,* 17**,** 491-496 3.

FROUNCHI, J. & BAZZAZI, A. 2003. High resolution rotary capacitance tomography system. *3rd World Congress on IPT Banff.* Canada.

GAFFNEY, D. K., HEMMERSMEIER, J., HOLDEN, J., MARSHALL, J., SMITH, L. M., AVIZONIS, V., TRAN, T. & NEUHAUSEN, S. L. 2001. Breast cancer after mantle irradiation for Hodgkin's disease: correlation of clinical, pathologic, and molecular features including loss of heterozygosity at BRCA1 and BRCA2. *Int J Radiat Oncol Biol Phys,* 49**,** 539-46.

GAGNON, H., COUSINEAU, M., ADLER, A. & HARTINGER, A. E. 2010. A resistive mesh phantom for assessing the performance of EIT systems. *IEEE Trans Biomed Eng,* 57**,** 2257-66.

GANG, Y., KIM HWA, L., RHETT, T. G., JR., GARY, A. Y., WILLIAM, T. J. & QING HUO, L. 2008. 3D EIT for breast cancer imaging: System, measurements, and reconstruction. *Microw Opt Technol Lett,* 50**,** 3261-3271.

GANG, Y., LIM, K. H., GEORGE, R., YBARRA, G., JOINES, W. T. & LIU, Q. H. A 3D EIT system for breast cancer imaging. Biomedical Imaging: Nano to Macro, 2006. 3rd IEEE International Symposium on, 6-9 April 2006 2006. 1092-1095.

GAUDET, M. M., GAPSTUR, S. M., SUN, J., DIVER, W. R., HANNAN, L. M. & THUN, M. J. 2013. Active smoking and breast cancer risk: original cohort data and meta-analysis. *J Natl Cancer Inst,* 105**,** 515-25.

GISSER, D. G., ISAACSON, D. & NEWELL, J. C. 1990. Electric Current Computed Tomography and Eigenvalues. *SIAM Journal on Applied Mathematics,* 50**,** 1623-1634.

GOFMAN, J. W. 1999. *Radiation from Medical Procedures in the Pathogenesis of Cancer and Ischemic Heart Disease: Dose-responseSstudies with Physicians per 100,000 Population,* San

Francisco, C.N.R. Book Division

GRIMNES, S. 1983. Impedance measurement of individual skin surface electrodes. *Med Biol Eng Comput,* 21**,** 750-5.

GUOFENG, Q., WEI, W., WEI, D., FAN, Z., SINCLAIR, A. J. & CHATWIN, C. R. 2012. Bioimpedance analysis for the characterization of breast cancer cells in suspension. *IEEE Trans Biomed Eng,* 59**,** 2321-9.

HAJDU, S. I. & TANG, P. 2009. Lobular carcinoma in situ. *Ann Clin Lab Sci,* 39**,** 413-5.

HALTER, R. J., HARTOV, A. & PAULSEN, K. D. 2008. A broadband high-frequency electrical impedance tomography system for breast imaging. *IEEE Trans Biomed Eng,* 55**,** 650-9.

HAMAJIMA, N., HIROSE, K., TAJIMA, K., ROHAN, T., CALLE, E. E., HEATH, C. W., JR., COATES, R. J., LIFF, J. M., TALAMINI, R., CHANTARAKUL, N., KOETSAWANG, S., RACHAWAT, D., MORABIA, A., SCHUMAN, L., STEWART, W., SZKLO, M., BAIN, C., SCHOFIELD, F., SISKIND, V., BAND, P., COLDMAN, A. J., GALLAGHER, R. P., HISLOP, T. G., YANG, P., KOLONEL, L. M., NOMURA, A. M., HU, J., JOHNSON, K. C., MAO, Y., DE SANJOSE, S., LEE, N., MARCHBANKS, P., ORY, H. W., PETERSON, H. B., WILSON, H. G., WINGO, P. A., EBELING, K., KUNDE, D., NISHAN, P., HOPPER, J. L., COLDITZ, G., GAJALANSKI, V., MARTIN, N., PARDTHAISONG, T., SILPISORNKOSOL, S., THEETRANONT, C., BOOSIRI, B., CHUTIVONGSE, S., JIMAKORN, P., VIRUTAMASEN, P., WONGSRICHANALAI, C., EWERTZ, M., ADAMI, H. O., BERGKVIST, L., MAGNUSSON, C., PERSSON, I., CHANG-CLAUDE, J., PAUL, C., SKEGG, D. C., SPEARS, G. F., BOYLE, P., EVSTIFEEVA, T., DALING, J. R., HUTCHINSON, W. B., MALONE, K., NOONAN, E. A., STANFORD, J. L., THOMAS, D. B., WEISS, N. S., WHITE, E., ANDRIEU, N., BREMOND, A., CLAVEL, F., GAIRARD, B., LANSAC, J., PIANA, L., RENAUD, R., IZQUIERDO, A., VILADIU, P., CUEVAS, H. R., ONTIVEROS, P., PALET, A., SALAZAR, S. B., ARISTIZABEL, N., CUADROS, A., TRYGGVADOTTIR, L., TULINIUS, H., BACHELOT, A., LE, M. G., PETO, J., FRANCESCHI, S., LUBIN, F., MODAN, B., RON, E., WAX, Y., FRIEDMAN, G. D., HIATT, R. A., LEVI, F., BISHOP, T., KOSMELJ, K., et al. 2002. Alcohol, tobacco and breast cancer--collaborative reanalysis of individual data from 53 epidemiological studies, including 58,515 women with breast cancer and 95,067 women without the disease. *Br J Cancer,* 87**,** 1234-45.

HAMILTON, S. J. & MUELLER, J. L. 2013. Direct EIT Reconstructions of Complex Admittivities on a Chest-Shaped Domain in 2-D. *Ieee Transactions on Medical Imaging,* 32**,** 757-769.

HANCOCK, S. L., TUCKER, M. A. & HOPPE, R. T. 1993. Breast cancer after treatment of Hodgkin's disease. *J Natl Cancer Inst,* 85**,** 25-31.

HARTOV, A., MAZZARESE, R. A., REISS, F. R., KERNER, T. E., OSTERMAN, K. S., WILLIAMS, D. B. & PAULSEN, K. D. 2000. A multichannel continuously selectable multifrequency electrical impedance spectroscopy measurement system. *IEEE Trans Biomed Eng,* 47**,** 49-58.

HARTOV, A., SONI, N. & HALTER, R. 2005a. Breast cancer screening with electrocal impedance tomography. *In:* HOLDER, D. (ed.) *Electrical impedance tomography : methods, history and applications.* Bristol: Institute of Physics.

HARTOV, A., SONI, N. & HALTER, Y. 2005b. Beast cancer screening with electrical impedance tomography. *In:* HOLDER, D. S. (ed.) *Electrical impedance tomography : methods, history and applications.* Bristol: Institute of Physics.

HASHEMI, R. H., BRADLEY, W. G. & LISANTI, C. J. 2003. *MRI : the basics*, Philadelphia, Pa. ; London, Lippincott Williams & Wilkins.

HASSAN, A. M. & EL-SHENAWEE, M. 2011. Review of electromagnetic techniques for breast cancer detection. *IEEE Rev Biomed Eng,* 4**,** 103-18.

HENDRICK, R. E. 2008. *Breast MRI : fundamentals and technical aspects,* New York ; London, Springer.

HEYES, G. J., MILL, A. J. & CHARLES, M. W. 2009. Mammography-oncogenecity at low doses. *J Radiol Prot,* 29**,** A123-32.

HOLDER, D. S., HANQUAN, Y. & RAO, A. 1996. Some practical biological phantoms for calibrating multifrequency electrical impedance tomography. *Physiological Measurement,* 17**,** A167.

HSIEH, C.-C., TRICHOPOULOS, D., KATSOUYANNI, K. & YUASA, S. 1990. Age at menarche, age at menopause, height and obesity as risk factors for breast cancer: Associations and interactions in an international case-control study. *International Journal of Cancer,* 46**,** 796–800.

HUANG, C.-N., YU, F.-M. & CHUNG, H.-Y. 2007. Rotational electrical impedance tomography. *Measurement Science and Technology,* 18**,** 2958.

HUSSAIN, M., RYNN, L., RIORDAN, C. & REGAN, P. J. 2003. Nipple-areola reconstruction: outcome assessment. *European Journal of Plastic Surgery,* 26**,** 356-358.

IMPEDANCE MEDICAL TECHNOLOGIES COMPANY. 2011. *Impedance Medical Technologies* [Online]. Available: http://medimpedance.com/index.html [Accessed January 31 2015].

JANOV, A. J., TULECKE, M., O'NEILL, A., LESTER, S., MAUCH, P. M., HARRIS, J., SCHNITT, S. J. & SHAPIRO, C. L. 2001. Clinical and pathologic features of breast cancers in women treated for Hodgkin's disease: a case-control study. *Breast J,* 7**,** 46-52.

JOSSINET, J. 1996. Variability of impedivity in normal and pathological breast tissue. *Med Biol Eng Comput,* 34**,** 346-50.

JOSSINET, J. & SCHMITT, M. 1999. A review of parameters for the bioelectrical characterization of breast tissue. *Ann N Y Acad Sci,* 873**,** 30-41.

KAO, T. J., BOVERMAN, G., KIM, B. S., ISAACSON, D., SAULNIER, G. J., NEWELL, J. C., CHOI, M. H., MOORE, R. H. & KOPANS, D. B. 2008. Regional admittivity spectra with tomosynthesis images for breast cancer detection: preliminary patient study. *IEEE Trans Med Imaging,* 27**,** 1762-8.

KELSEY, J. L., GAMMON, M. D. & JOHN, E. M. 1993. Reproductive factors and breast cancer. *Epidemiol Rev,* 15**,** 36-47.

KERNER, T. E., PAULSEN, K. D., HARTOV, A., SOHO, S. K. & POPLACK, S. P. 2002. Electrical impedance spectroscopy of the breast: clinical imaging results in 26 subjects. *IEEE Trans Med Imaging,* 21**,** 638-45.

KIM, B. S., ISAACSON, D., XIA, H., KAO, T. J., NEWELL, J. C. & SAULNIER, G. J. 2007. A method for analyzing electrical impedance spectroscopy data from breast cancer patients. *Physiol Meas,* 28**,** S237-46.

KIM, H. C., KIM, K. Y., PARK, J. W. & LEE, H. J. 2001. Electrical impendance tomograhpy reconstruction algorithm using extended Kalman filter. *Isie 2001: Ieee International Symposium on Industrial Electronics Proceedings, Vols I-Iii***,** 1677-1681.

LUO, J., MARGOLIS, K. L., WACTAWSKI-WENDE, J., HORN, K., MESSINA, C., STEFANICK, M. L., TINDLE, H. A., TONG, E. & ROHAN, T. E. 2011. Association of active and passive smoking with risk of breast cancer among postmenopausal women: a prospective cohort study. *BMJ,* 342**,** d1016.

MA, H., HILL, C. K., BERNSTEIN, L. & URSIN, G. 2008. Low-dose medical radiation exposure and breast cancer risk in women under age 50 years overall and by estrogen and progesterone receptor status: results from a case-control and a case-case comparison. *Breast Cancer Res Treat,* 109**,** 77-90.

MACKAY LIFE SCIENCES. 2014. *MEIK* [Online]. Available: http://www.mackaylifesciences.ph/meiktheory.html [Accessed January 30 2015].

MACMAHON, B., COLE, P., LIN, T. M., LOWE, C. R., MIRRA, A. P., RAVNIHAR, B., SALBER, E. J., VALAORAS, V. G. & YUASA, S. 1970. Age at first birth and breast cancer risk. *Bull World Health Organ,* 43**,** 209-21.

MALICH, A., BOEHM, T., FACIUS, M., FREESMEYER, M. G., FLECK, M., ANDERSON, R. & KAISER, W. A. 2001a. Differentiation of mammographically suspicious lesions: evaluation of breast ultrasound, MRI mammography and electrical impedance scanning as adjunctive technologies in breast cancer detection. *Clin Radiol,* 56**,** 278-83.

MALICH, A., BOHM, T., FACIUS, M., FREESSMEYER, M., FLECK, M., ANDERSON, R. & KAISER, W. A. 2001b. Additional value of electrical impedance scanning: experience of 240

histologically-proven breast lesions. *Eur J Cancer,* 37**,** 2324-30.

MANDAL, A. 2013. *Breast Anatomy* [Online]. Available: http://www.news-medical.net/health/Breast-Anatomy.aspx [Accessed 12 December 2014].

MARTINS, T. D., DE CAMARGO, E. D. L. B., LIMA, R. G., AMATO, M. B. P. & TSUZUKI, M. D. G. 2012. Image Reconstruction Using Interval Simulated Annealing in Electrical Impedance Tomography. *Ieee Transactions on Biomedical Engineering,* 59**,** 1861-1870.

MAXWELL, G. P. & GABRIEL, A. 2009. Breast Reconstruction. *In:* ASTON, S. J., STEINBRECH, D. S. & WALDEN, J. L. (eds.) *Aesthetic plastic surgery.* Edinburgh: Saunders.

MCGREGOR, D. H., LAND, C. E., CHOI, K., TOKUOKA, S., LIU, P. I., WAKABAYASHI, T. & BEEBE, G. W. 1977. Breast Cancer Incidence Among Atomic Bomb Survivors, Hiroshima and Nagasaki, 1950–69. *Journal of the National Cancer Institute,* 59**,** 799-811.

MEDICALLOOK. 2015. *BREAST MRI DEFINITION* [Online]. Available: http://www.medicalook.com/tests/Breast_MRI.html [Accessed January 28 2015].

MEDLINEPLUS. 2015. *Breast PET scan* [Online]. Available: http://www.nlm.nih.gov/medlineplus/ency/article/007469.htm [Accessed January 29 2015].

MELLOUL, M., PAZ, A., OHANA, G., LAVER, O., MICHALEVICH, D., KOREN, R., WOLLOCH, Y. & GAL, R. 1999. Double-phase 99mTc-sestamibi scintimammography and trans-scan in diagnosing breast cancer. *J Nucl Med,* 40**,** 376-80.

MILLIKAN, R. C., PLAYER, J. S., DECOTRET, A. R., TSE, C. K. & KEKU, T. 2005. Polymorphisms in DNA repair genes, medical exposure to ionizing radiation, and breast cancer risk. *Cancer Epidemiol Biomarkers Prev,* 14**,** 2326-34.

MUELLER, J. L., ISAACSON, D. & NEWELL, J. C. 1999. A reconstruction algorithm for electrical impedance tomography data collected on rectangular electrode arrays. *Ieee Transactions on Biomedical Engineering,* 46**,** 1379-1386.

MURPHY, S. C. & YORK, T. A. 2006. Electrical impedance tomography with non-stationary electrodes. *Measurement Science and Technology,* 17**,** 3042.

NATIONAL BREAST CANCER FOUNDATION, I. 2012. *Breast Anatomy* [Online]. Available: http://www.nationalbreastcancer.org/breast-anatomy [Accessed 23 December 2014].

NATIONAL CANCER INSTITUTE. 2012. *http://training.seer.cancer.gov/breast/anatomy/* [Online]. Available: http://training.seer.cancer.gov/breast/anatomy/ [Accessed 16 December 2014].

NEILSON, H. K., FRIEDENREICH, C. M., BROCKTON, N. T. & MILLIKAN, R. C. 2009. Physical activity and postmenopausal breast cancer: proposed biologic mechanisms and areas for

future research. *Cancer Epidemiol Biomarkers Prev,* 18**,** 11-27.

NG, E. Y., SREE, S. V., NG, K. H. & KAW, G. 2008. The use of tissue electrical characteristics for breast cancer detection: a perspective review. *Technol Cancer Res Treat,* 7**,** 295-308.

OSTERMAN, K. S., KERNER, T. E., WILLIAMS, D. B., HARTOV, A., POPLACK, S. P. & PAULSEN, K. D. 2000. Multifrequency electrical impedance imaging: preliminary in vivo experience in breast. *Physiol Meas,* 21**,** 99-109.

PETERS, T. M., SCHATZKIN, A., GIERACH, G. L., MOORE, S. C., LACEY, J. V., JR., WAREHAM, N. J., EKELUND, U., HOLLENBECK, A. R. & LEITZMANN, M. F. 2009. Physical activity and postmenopausal breast cancer risk in the NIH-AARP diet and health study. *Cancer Epidemiol Biomarkers Prev,* 18**,** 289-96.

PIPERNO, G., FREI, E. H. & MOSHITZKY, M. 1990. Breast cancer screening by impedance measurements. *Front Med Biol Eng,* 2**,** 111-7.

PREIDT, R. 2013. *Breast-Density Changes May Be Tied to Cancer Risk* [Online]. Available: http://www.webmd.com/breast-cancer/news/20131203/breast-density-changes-may-be-tied-to-cancer-risk-study [Accessed 9 January 2015].

PRESTON, D. L., MATTSSON, A., HOLMBERG, E., SHORE, R., HILDRETH, N. G. & BOICE, J. D., JR. 2002. Radiation effects on breast cancer risk: a pooled analysis of eight cohorts. *Radiat Res,* 158**,** 220-35.

RADIOLOGICAL SOCIETY OF NORTH AMERICA INC. 2015. *Magnetic Resonance Imaging (MRI) - Breast* [Online]. Available: http://www.radiologyinfo.org/en/info.cfm?pg=breastmr [Accessed January 28 2015].

RAGHEB, T. & GEDDES, L. A. 1991. The polarization impedance of common electrode metals operated at low current density. *Annals of Biomedical Engineering,* 19**,** 151-163.

RAMSAY, D. T., KENT, J. C., HARTMANN, R. A. & HARTMANN, P. E. 2005. Anatomy of the lactating human breast redefined with ultrasound imaging. *J Anat,* 206**,** 525-34.

RATINI, M. 2014. *Lobular Carcinoma (Invasive and In Situ)* [Online]. Available: http://www.webmd.com/breast-cancer/lobular-carcinoma-invasive-and-in-situ [Accessed 4 January 2015].

RUSSO, J. & RUSSO, I. H. 2004. *Molecular basis of breast cancer : prevention and treatment,* Berlin ; New York, Springer.

SABEL, M. S. 2009. *Essentials of breast surgery,* St. Louis, Mo. ; London, Elsevier Mosby.

SADLEIR, R. J., SAJIB, S. Z., KIM, H. J., KWON, O. I. & WOO, E. J. 2013. Simulations and

phantom evaluations of magnetic resonance electrical impedance tomography (MREIT) for breast cancer detection. *J Magn Reson,* 230**,** 40-9.

SAULNIER, G. J., ROSS, A. S. & LIU, N. 2006. A high-precision voltage source for EIT. *Physiol Meas,* 27**,** S221-36.

SCHOLZ, B. & ANDERSON, R. 2000. On electrical impedance scanning –Principles and Simulations. Siemens AG, Medical Engineering Group.

SCHWARTZ, G. F., HUGHES, K. S., LYNCH, H. T., FABIAN, C. J., FENTIMAN, I. S., ROBSON, M. E., DOMCHEK, S. M., HARTMANN, L. C., HOLLAND, R., WINCHESTER, D. J. & CONSENSUS CONFERENCE COMMITTEE THE INTERNATIONAL CONSENSUS CONFERENCE, C. 2008. Proceedings of the international consensus conference on breast cancer risk, genetics, & risk management, April, 2007. *Cancer,* 113**,** 2627-37.

SEAGAR, A. D., BARBER, D. C. & BROWN, B. H. 1987. Theoretical limits to sensitivity and resolution in impedance imaging. *Clin Phys Physiol Meas,* 8 Suppl A**,** 13-31.

SIEDBAND, M. P. 2010. Medical imaging systems. *In:* WEBSTER, J. G. & CLARK, J. W. (eds.) *Medical instrumentation : application and design.* 4th ed. ed. Hoboken, N.J.: Wiley ; [Chichester : John Wiley distributor].

SPANGLER, J. G., MICHIELUTTE, R., BELL, R. A. & DIGNAN, M. B. 2001. Association between smokeless tobacco use and breast cancer among Native-American women in North Carolina. *Ethn Dis,* 11**,** 36-43.

SUROWIEC, A. J., STUCHLY, S. S., BARR, J. B. & SWARUP, A. 1988. Dielectric properties of breast carcinoma and the surrounding tissues. *IEEE Trans Biomed Eng,* 35**,** 257-63.

SUTRADHAR, A. & MILLER, M. J. 2013. In vivo measurement of breast skin elasticity and breast skin thickness. *Skin Res Technol,* 19**,** e191-9.

SZE, G. 2012. *Detection of breast cancer with electrical impedance mammography.* Doctor of phylosophy, University of Sussex.

TAMIMI, R. M., BYRNE, C., COLDITZ, G. A. & HANKINSON, S. E. 2007. Endogenous hormone levels, mammographic density, and subsequent risk of breast cancer in postmenopausal women. *J Natl Cancer Inst,* 99**,** 1178-87.

TANG, M., WANG, W., WHEELER, J., MCCORMICK, M. & DONG, X. 2002. The number of electrodes and basis functions in EIT image reconstruction. *Physiol Meas,* 23**,** 129-40.

TROKHANOVA, O. V., OKHAPKIN, M. B. & KORJENEVSKY, A. V. 2008. Dual-frequency electrical impedance mammography for the diagnosis of non-malignant breast disease. *Physiol Meas,*

29**,** S331-44.

TUNSTALL, B., WANG, W., M., M., WALKER, R. & REW, D. 1997. Preliminary in vitro studies of electrical impedancemammography (EIM): a future technique for non-invasive breast tissue imaging? *The 5th Nottingham International Breast Cancer Conference.*

TURNBULL, C. & RAHMAN, N. 2008. Genetic predisposition to breast cancer: past, present, and future. *Annu Rev Genomics Hum Genet,* 9**,** 321-45.

WANG, W., TUNSTALL, B., CHAUHAN, D. & MCCORMICK, M. The design of De Montfort MK2 electrical impedance mammography system. Engineering in Medicine and Biology Society, 1998. Proceedings of the 20th Annual International Conference of the IEEE, 29 Oct-1 Nov 1998 1998. 1042-1043 vol.2.

WEISHAUPT, D., KOCHLI, V. & MARINCEK, B. 2003. *How does MRI work? : an introduction to the physics and function of magnetic resonance imaging,* Berlin ; London, Springer.

WIKIPEDIA. 2014a. *Breast* [Online]. Available: http://en.wikipedia.org/wiki/Breast [Accessed 16 December 2014].

WIKIPEDIA. 2014b. *Cooper's ligaments* [Online]. Available: http://en.wikipedia.org/wiki/Cooper%27s_ligaments [Accessed 21 December 2014].

YAFFE, M. J. 2010. Basic Physics of Digital Mammography. *In:* BICK, U. & DIEKMANN, F. (eds.) *Digital Mammography.* Springer.

YU, F. M., HUANG, C. N., CHANG, F. W. & CHUNG, H. Y. 2006. A Rotative Electrical Impedance Tomography Reconstruction System. *4th International Symposium on Instrumentation Science and Technology (ISIST' 2006),* 48.

ZHANG, S., XU, G. Z., ZHANG, X. Y., ZHANG, B., WANG, H. B., XU, Y. Y., YIN, N., LI, Y. & YAN, W. L. 2012. Computation of a 3-D Model for Lung Imaging With Electrical Impedance Tomography. *Ieee Transactions on Magnetics,* 48**,** 651-654.

ZHANG, X., WANG, W., SZE, G., BARBER, D. & CHATWIN, C. 2014. An Image Reconstruction Algorithm for 3-D Electrical Impedance Mammography. *Medical Imaging, IEEE Transactions on,* 33**,** 2223-2241.

ZHAO, R. 2008. *Transfer and Proliferation of Breast Cancer* [Online]. Available: http://ezinearticles.com/?Transfer-and-Proliferation-of-Breast-Cancer&id=1301200 [Accessed 26 December 2014].

Appendix I

For a 3D tetrahedral element shown in Figure I. 1, the linear function of the potential $\emptyset$ is written as:

$$\widetilde{\emptyset}(x,y,z) = \tau_1 + \tau_2 x + \tau_3 y + \tau_4 z \qquad (\text{I. 1})$$

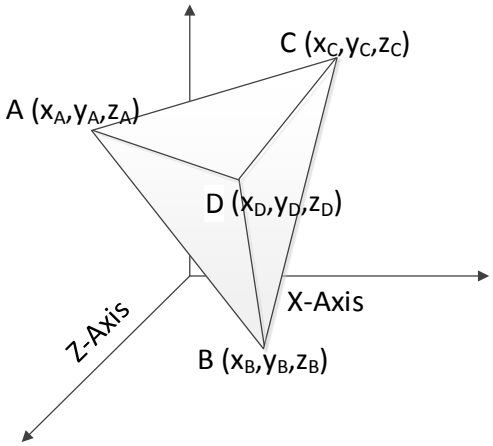

Figure I. 1. A tetrahedral element

If substituting the vertex coordinates of the tetrahedron (x_A, y_A, z_A), (x_B, y_B, z_B), (x_C, y_C, z_C), and (x_D, y_D, z_D) into (I. 1), we can get the following equations

$$\begin{cases} \widetilde{\emptyset}_A = \widetilde{\emptyset}(x_A, y_A, z_A) = \tau_1 + \tau_2 x_A + \tau_3 y_A + \tau_4 z_A \\ \widetilde{\emptyset}_B = \widetilde{\emptyset}(x_B, y_B, z_B) = \tau_1 + \tau_2 x_B + \tau_3 y_B + \tau_4 z_B \\ \widetilde{\emptyset}_C = \widetilde{\emptyset}(x_C, y_C, z_C) = \tau_1 + \tau_2 x_C + \tau_3 y_C + \tau_4 z_C \\ \widetilde{\emptyset}_D = \widetilde{\emptyset}(x_D, y_D, z_D) = \tau_1 + \tau_2 x_D + \tau_3 y_D + \tau_4 z_D \end{cases} \qquad (\text{I. 2})$$

where A, B, C, D denote the indexes of the mesh node. Writing (I. 2) in matrix form

$$\begin{bmatrix} \widetilde{\emptyset}_A \\ \widetilde{\emptyset}_B \\ \widetilde{\emptyset}_C \\ \widetilde{\emptyset}_D \end{bmatrix}^T = \begin{bmatrix} \tau_1 \\ \tau_2 \\ \tau_3 \\ \tau_4 \end{bmatrix}^T \begin{bmatrix} 1 & 1 & 1 & 1 \\ x_A & x_B & x_C & x_D \\ y_A & y_B & y_C & y_D \\ z_A & z_B & z_C & z_D \end{bmatrix} \qquad (\text{I. 3})$$

According to Clem's rule,

$$\tau_1 = \frac{\begin{vmatrix} \widetilde{\emptyset}_A & x_A & y_A & z_A \\ \widetilde{\emptyset}_B & x_B & y_B & z_B \\ \widetilde{\emptyset}_A & x_C & y_C & z_C \\ \widetilde{\emptyset}_B & x_D & y_D & z_D \end{vmatrix}}{\begin{vmatrix} 1 & x_A & y_A & z_A \\ 1 & x_B & y_B & z_B \\ 1 & x_C & y_C & z_C \\ 1 & x_D & y_D & z_D \end{vmatrix}} = \frac{a_A\widetilde{\emptyset}_A + a_B\widetilde{\emptyset}_B + a_C\widetilde{\emptyset}_C + a_D\widetilde{\emptyset}_D}{6V_e} \tag{I. 4}$$

where V_e is the volume of the tetrahedral element

$$a_A = \begin{vmatrix} x_B & y_B & z_B \\ x_C & y_C & z_C \\ x_D & y_D & z_D \end{vmatrix} \quad a_B = \begin{vmatrix} x_A & y_A & z_A \\ x_C & y_C & z_C \\ x_D & y_D & z_D \end{vmatrix} \quad a_C = \begin{vmatrix} x_A & y_A & z_A \\ x_B & y_B & z_B \\ x_D & y_D & z_D \end{vmatrix}$$

$$a_D = \begin{vmatrix} x_A & y_A & z_A \\ x_B & y_B & z_B \\ x_C & y_C & z_C \end{vmatrix} \qquad V_e = \frac{1}{6}\begin{vmatrix} 1 & x_A & y_A & z_A \\ 1 & x_B & y_B & z_B \\ 1 & x_C & y_C & z_C \\ 1 & x_D & y_D & z_D \end{vmatrix} \tag{I. 5}$$

Also we can get

$$\tau_2 = \frac{b_A\widetilde{\emptyset}_A + b_B\widetilde{\emptyset}_B + b_C\widetilde{\emptyset}_C + b_D\widetilde{\emptyset}_D}{6V_e}$$

$$\tau_3 = \frac{c_A\widetilde{\emptyset}_A + c_B\widetilde{\emptyset}_B + c_C\widetilde{\emptyset}_C + c_D\widetilde{\emptyset}_D}{6V_e}$$

$$\tau_4 = \frac{d_A\widetilde{\emptyset}_A + d_B\widetilde{\emptyset}_B + d_C\widetilde{\emptyset}_C + d_D\widetilde{\emptyset}_D}{6V_e} \tag{I. 6}$$

where

$$b_A = \begin{vmatrix} 1 & y_B & z_B \\ 1 & y_C & z_C \\ 1 & y_D & z_D \end{vmatrix} \quad b_B = -\begin{vmatrix} 1 & y_A & z_A \\ 1 & y_C & z_C \\ 1 & y_D & z_D \end{vmatrix} \quad b_C = \begin{vmatrix} 1 & y_A & z_A \\ 1 & y_B & z_B \\ 1 & y_D & z_D \end{vmatrix} \quad b_D = -\begin{vmatrix} 1 & y_A & z_A \\ 1 & y_B & z_B \\ 1 & y_C & z_C \end{vmatrix}$$

$$c_A = \begin{vmatrix} 1 & x_B & z_B \\ 1 & x_C & z_C \\ 1 & x_D & z_D \end{vmatrix} \quad c_B = -\begin{vmatrix} 1 & x_A & z_A \\ 1 & x_C & z_C \\ 1 & x_D & z_D \end{vmatrix} \quad c_C = \begin{vmatrix} 1 & x_A & z_A \\ 1 & x_B & z_B \\ 1 & x_D & z_D \end{vmatrix} \quad c_D = -\begin{vmatrix} 1 & x_A & z_A \\ 1 & x_B & z_B \\ 1 & x_C & z_C \end{vmatrix}$$

$$d_A = \begin{vmatrix} 1 & x_B & y_B \\ 1 & x_C & y_C \\ 1 & x_D & y_D \end{vmatrix} \quad d_B = -\begin{vmatrix} 1 & x_A & y_A \\ 1 & x_C & y_C \\ 1 & x_D & y_D \end{vmatrix} \quad d_C = \begin{vmatrix} 1 & x_A & y_A \\ 1 & x_B & y_B \\ 1 & x_D & y_D \end{vmatrix} \quad d_D = -\begin{vmatrix} 1 & x_A & y_A \\ 1 & x_B & y_B \\ 1 & x_C & y_C \end{vmatrix}$$

Submitting (I. 4) and (I. 6) to (I. 1), we get the following equation:

$$\begin{aligned} \widetilde{\emptyset}(x,y,z) = & \frac{\widetilde{\emptyset}_A}{6V_e}(a_A + b_A x + c_A y + d_A z) \\ & + \frac{\widetilde{\emptyset}_B}{6V_e}(a_B + b_B x + c_B y + d_B z) \\ & + \frac{\widetilde{\emptyset}_C}{6V_e}(a_C + b_C x + c_C y + d_C z) \\ & + \frac{\widetilde{\emptyset}_D}{6V_e}(a_D + b_D x + c_D y + d_D z) \\ & = \sum_{p=[A,B,C,D]} N_p^k(x,y,z)\widetilde{\emptyset}_p \end{aligned} \qquad (\text{I. } 7)$$

Equation (I. 7) shows the relationship between the potential at an arbitrary point in the *k*th tetrahedral element and the potentials at the vertexes. $\widetilde{\emptyset}$ can be written as the following equation:

$$\widetilde{\emptyset}(x,y,z) = [N_A^k \quad N_B^k \quad N_C^k \quad N_D^k] \begin{bmatrix} \widetilde{\emptyset}_A \\ \widetilde{\emptyset}_B \\ \widetilde{\emptyset}_C \\ \widetilde{\emptyset}_D \end{bmatrix} = [\boldsymbol{N}]_k [\emptyset]_k \qquad (\text{I. } 8)$$

where

$$\begin{cases} N_A^k = \dfrac{1}{6V_e}(a_A + b_A x + c_A y + d_A z) \\ N_B^k = \dfrac{1}{6V_e}(a_B + b_B x + c_B y + d_B z) \\ N_C^k = \dfrac{1}{6V_e}(a_C + b_C x + c_C y + d_C z) \\ N_D^k = \dfrac{1}{6V_e}(a_D + b_D x + c_D y + d_D z) \end{cases} \quad (\text{I. } 9)$$

Equation (I. 8) can be written as:

$$\begin{aligned} \widetilde{\emptyset}(x,y,z) = {} & N_A^k(x,y,z)\widetilde{\emptyset}_A + N_B^k(x,y,z)\widetilde{\emptyset}_B + N_C^k(x,y,z)\widetilde{\emptyset}_C \\ & + N_D^k(x,y,z)\widetilde{\emptyset}_D \end{aligned} \quad (\text{I. } 10)$$

For $p \in [A,B,C,D]$, we have the following equation:

$$\begin{aligned} \widetilde{\emptyset}(x_p,y_p,z_p) = {} & N_A^k(x_p,y_p,z_p)\widetilde{\emptyset}_A + N_B^k(x_p,y_p,z_p)\widetilde{\emptyset}_B \\ & + N_C^k(x_p,y_p,z_p)\widetilde{\emptyset}_C + N_D^k(x_p,y_p,z_p)\widetilde{\emptyset}_D \end{aligned} \quad (\text{I. } 11)$$

where (x_p,y_p,z_p) indicate the vertex coordinates. From (I. 11), we can find that

$$N_A^k(x_p,y_p,z_p) = \delta_{Ap} = \begin{cases} 1 & p = A \\ 0 & p \neq A \end{cases} \quad (\text{I. } 12)$$

According to (I. 8) and (I. 9), $[\boldsymbol{N}]_k$ is a function of (x,y,z), therefore we have the following equations:

$$\begin{cases} \dfrac{\partial \widetilde{\emptyset}}{\partial x} = \left[\dfrac{\partial N_A^k}{\partial x} \quad \dfrac{\partial N_B^k}{\partial x} \quad \dfrac{\partial N_C^k}{\partial x} \quad \dfrac{\partial N_D^k}{\partial x}\right]\begin{bmatrix}\widetilde{\emptyset}_A \\ \widetilde{\emptyset}_B \\ \widetilde{\emptyset}_C \\ \widetilde{\emptyset}_D\end{bmatrix} = \left[\dfrac{\partial \boldsymbol{N}}{\partial x}\right]_k [\emptyset]_k \\ \dfrac{\partial \widetilde{\emptyset}}{\partial y} = \left[\dfrac{\partial N_A^k}{\partial y} \quad \dfrac{\partial N_B^k}{\partial y} \quad \dfrac{\partial N_C^k}{\partial y} \quad \dfrac{\partial N_D^k}{\partial y}\right]\begin{bmatrix}\widetilde{\emptyset}_A \\ \widetilde{\emptyset}_B \\ \widetilde{\emptyset}_C \\ \widetilde{\emptyset}_D\end{bmatrix} = \left[\dfrac{\partial \boldsymbol{N}}{\partial y}\right]_k [\emptyset]_k \\ \dfrac{\partial \widetilde{\emptyset}}{\partial z} = \left[\dfrac{\partial N_A^k}{\partial z} \quad \dfrac{\partial N_B^k}{\partial z} \quad \dfrac{\partial N_C^k}{\partial z} \quad \dfrac{\partial N_D^k}{\partial z}\right]\begin{bmatrix}\widetilde{\emptyset}_A \\ \widetilde{\emptyset}_B \\ \widetilde{\emptyset}_C \\ \widetilde{\emptyset}_D\end{bmatrix} = \left[\dfrac{\partial \boldsymbol{N}}{\partial z}\right]_k [\emptyset]_k \end{cases} \quad (\text{I. } 13)$$

Submitting (I. 9) to (I. 13), we have the following equations

$$\begin{cases} \dfrac{\partial \widetilde{\emptyset}}{\partial x} = \dfrac{1}{6V_e}[b_A \quad b_B \quad b_C \quad b_D]\begin{bmatrix}\widetilde{\emptyset}_A \\ \widetilde{\emptyset}_B \\ \widetilde{\emptyset}_C \\ \widetilde{\emptyset}_D\end{bmatrix} \\ \dfrac{\partial \widetilde{\emptyset}}{\partial y} = \dfrac{1}{6V_e}[c_A \quad c_B \quad c_C \quad c_D]\begin{bmatrix}\widetilde{\emptyset}_A \\ \widetilde{\emptyset}_B \\ \widetilde{\emptyset}_C \\ \widetilde{\emptyset}_D\end{bmatrix} \\ \dfrac{\partial \widetilde{\emptyset}}{\partial z} = \dfrac{1}{6V_e}[d_A \quad d_B \quad d_C \quad d_D]\begin{bmatrix}\widetilde{\emptyset}_A \\ \widetilde{\emptyset}_B \\ \widetilde{\emptyset}_C \\ \widetilde{\emptyset}_D\end{bmatrix} \end{cases} \quad (\text{I. } 14)$$

Therefore

$$[\boldsymbol{\nabla}\emptyset] = [\boldsymbol{B}]_{\boldsymbol{k}}[\emptyset]_{\boldsymbol{k}} = \sum_{p=[A,B,C,D]} \boldsymbol{\nabla} \boldsymbol{N}_{\boldsymbol{p}}^{\boldsymbol{k}} \widetilde{\emptyset}_p \quad (\text{I. } 15)$$

where

$$[\boldsymbol{B}]_{\boldsymbol{k}} = \begin{bmatrix} \boldsymbol{\nabla N_A^k} & \boldsymbol{\nabla N_B^k} & \boldsymbol{\nabla N_C^k} & \boldsymbol{\nabla N_D^k} \end{bmatrix} = \frac{1}{6V_e} \begin{bmatrix} b_A & b_B & b_C & b_D \\ c_A & c_B & c_C & c_D \\ d_A & d_B & d_C & d_D \end{bmatrix} \quad \text{(I. 16)}$$

The energy of each element is:

$$\mathcal{F}^k(\emptyset) = \frac{1}{2}\int_{\Omega_k} \sigma^k \nabla\emptyset^2 d\Omega = \frac{1}{2}\int_{\Omega_k} \sigma^k \left(\sum_{p=[A,B,C,D]} \boldsymbol{\nabla N_p^k} \widetilde{\emptyset}_p \right)^2 d\Omega \quad \text{(I. 17)}$$

Equation (2.17) can be written as

$$\mathcal{F}(\emptyset) = \sum_{k=1}^{K} \frac{1}{2}\int_{\Omega_k} \sigma^k \left(\sum_{p=[A,B,C,D]} \boldsymbol{\nabla N_p^k} \widetilde{\emptyset}_p \right)^2 d\Omega + \int_{\partial\Omega} j\emptyset d\partial\Omega \quad \text{(I. 18)}$$

To minimize the energy equation in (I. 18), we need:

$$\frac{\partial \mathcal{F}(\emptyset)}{\partial \emptyset_i} = \sum_{k=1}^{K} \frac{\partial \mathcal{F}^k(\emptyset)}{\partial \emptyset_i} + \frac{\partial}{\partial \emptyset_i}\left(\int_{\partial\Omega} j\emptyset d\partial\Omega \right) = 0 \quad \text{(I. 19)}$$

therefore

$$\sum_{k=1}^{K} \frac{\partial \mathcal{F}^k(\emptyset)}{\partial \emptyset_i} = -\frac{\partial}{\partial \emptyset_i}\left(\int_{\partial\Omega} j\emptyset d\partial\Omega \right) \quad \text{(I. 20)}$$

The item on the left hand side of equation (I. 20) can be written as follows:

$$\sum_{k=1}^{K}\frac{\partial \mathcal{F}^k(\emptyset)}{\partial \emptyset_i}=\sum_{k=1}^{K}\frac{\partial}{\partial \emptyset_i}\left(\frac{1}{2}\int_{\Omega_k}\sigma^k\left(\sum_{p=[A,B,C,D]}\boldsymbol{\nabla N_p^k}\widetilde{\emptyset}_p\right)^2 d\Omega\right)$$

$$=\sum_{k=1}^{K}\sigma^k\int_{\Omega_k}\frac{1}{2}\frac{\partial}{\partial \emptyset_i}\left(\sum_{p=[A,B,C,D]}\boldsymbol{\nabla N_p^k}\widetilde{\emptyset}_p\right)^2 d\Omega$$

$$=\sum_{k=1}^{K}\sigma^k\left(\boldsymbol{\nabla N_i^k}\right)^T\sum_{p=[A,B,C,D]}\boldsymbol{\nabla N_p^k}\widetilde{\emptyset}_p\int_{\Omega_k}d\Omega$$

$$=\sum_{k=1}^{K}\sum_{p=[A,B,C,D]}\sigma^k\left(\boldsymbol{\nabla N_i^k}\right)^T\boldsymbol{\nabla N_p^k}\widetilde{\emptyset}_p V_e$$

$$=\sum_{k=1}^{K}\sum_{p=[A,B,C,D]}Y_{ip}^k\widetilde{\emptyset}_p \qquad (\text{I. 21})$$

where

$$Y_{ip}^k=\sigma^k\left(\boldsymbol{\nabla N_i^k}\right)^T\boldsymbol{\nabla N_p^k}=\frac{\sigma^k\left(b_ib_p+c_ic_p+d_id_p\right)}{36V_e} \qquad (\text{I. 22})$$

Equation (I. 21) can be written as

$$\sum_{k=1}^{K}\frac{\partial \mathcal{F}^k(\emptyset)}{\partial \emptyset_i}=Y_i\emptyset \qquad (\text{I. 23})$$

where $\emptyset$ is a $N\times 1$ vector indicating the unknown nodal potential, Y_i is a $1\times N$ vector, $Y_i=[Y_{i1},Y_{i2},\cdots Y_{iN}]$, $i\in[1,2,\dots N]$

$$Y_{ip}=\sum_{k=K_{ip}}Y_{ip}^k \qquad (\text{I. 24})$$

where K_{ip} indicate the elements, which have the common edge ip. For the item on the right hand side of equation (I. 20), on the boundary of the field, only if the coordinates are at the excitation electrodes, the current density is a nonzero value, therefore

$$-\frac{\partial}{\partial \emptyset_i}\left(\int_{\partial\Omega} j\emptyset d\partial\Omega\right)=\begin{cases}0 & (x_i,y_i,z_i)\notin e_{drive}\\ C_{inj} & (x_i,y_i,z_i)\in e_{drive}\end{cases} \qquad (\text{I. } 25)$$

where (x_i, y_i, z_i) denotes the coordinate of the *i*th mesh node, $\emptyset_i$ denotes the potential at *i*th mesh node, C_{inj} is a scalar equal to the current amplitude. If using Q_i to denote the item on the right hand side of equation (I. 20) and submitting (I. 23) to (I. 20), we can get the following equation:

$$Y_i\emptyset = Q_i \qquad (\text{I. } 26)$$

Equation (I. 26) is derived from $\partial\mathcal{F}(\emptyset)/\partial\emptyset_i = 0$. For the following equation

$$\begin{cases}\dfrac{\partial\mathcal{F}(\emptyset)}{\partial\emptyset_1}=0\\ \dfrac{\partial\mathcal{F}(\emptyset)}{\partial\emptyset_2}=0\\ \quad\vdots\\ \dfrac{\partial\mathcal{F}(\emptyset)}{\partial\emptyset_N}=0\end{cases} \qquad (\text{I. } 27)$$

We have：

$$\begin{cases}Y_1\emptyset = Q_1\\ Y_2\emptyset = Q_2\\ \quad\vdots\\ Y_N\emptyset = Q_N\end{cases} \qquad (\text{I. } 28)$$

Equation (I. 28) also can be written as

$$\boldsymbol{Y}\emptyset = \boldsymbol{Q} \quad or \quad \emptyset = \boldsymbol{Y^{-1}Q} \tag{I. 29}$$

where $\boldsymbol{Y}$ is a sparse $N \times N$ matrix, which is determined by the vertex coordinates of the mesh and the conductivity values of the elements. In each element, the conductivity is taken to be constant. $\emptyset$ is the $N \times 1$ vector of the unknown nodal scalar potentials, $\boldsymbol{Q}$ is the $N \times 1$ vector of the known nodal current.

Appendix II

According to the Gauss's theorem,

$$\int_{\partial\Omega} \emptyset_u \sigma \nabla\Psi_p d\partial\Omega = \int_{\Omega} \emptyset_u \nabla \cdot \left(\sigma \nabla\Psi_p\right) d\Omega + \int_{\Omega} \sigma \nabla\emptyset_u \cdot \nabla\Psi_p \, d\Omega \qquad (\text{II. } 1)$$

where $\int_{\Omega} \sigma \nabla\emptyset_u \cdot \nabla\Psi_p \, d\Omega$ is the item that needs to be determined. $\nabla \cdot \left(\sigma \nabla\Psi_p\right)$ in (II. 2) can be written as

$$\begin{aligned} \nabla \cdot \left(\sigma \nabla\Psi_p\right) &= \nabla\sigma \nabla\Psi_p + \sigma \nabla \cdot \nabla\Psi_p = \nabla\sigma \nabla\Psi_p + \sigma \nabla \cdot \nabla(\Psi - \Psi_u) \\ &= \nabla\sigma \nabla\Psi_p + \sigma \nabla \cdot \nabla\Psi - \sigma \nabla \cdot \nabla\Psi_u \end{aligned} \qquad (\text{II. } 2)$$

where $\nabla \cdot \nabla\Psi_u = 0$, $\sigma \nabla \cdot \nabla\Psi = \nabla(\sigma \cdot \nabla\Psi) - \nabla\sigma \nabla\Psi$. According to (2.12), $\nabla(\sigma \cdot \nabla\Psi) = 0$, therefore

$$\sigma \nabla \cdot \nabla\Psi = -\nabla\sigma \nabla\Psi = -\nabla\sigma \nabla\left(\Psi_u + \Psi_p\right) \qquad (\text{II. } 3)$$

Substituting (II. 3) to (II. 2), we have

$$\nabla \cdot \left(\sigma \nabla\Psi_p\right) = \nabla\sigma \nabla\Psi_p - \nabla\sigma \nabla\left(\Psi_u + \Psi_p\right) = -\nabla\sigma \nabla\Psi_u \qquad (\text{II. } 4)$$

Substituting (II. 4) to (II. 1), we have

$$\int_{\partial\Omega} \emptyset_u \sigma \nabla\Psi_p d\partial\Omega = -\int_{\Omega} \emptyset_u \nabla\sigma \nabla\Psi_u \, d\Omega + \int_{\Omega} \sigma \nabla\emptyset_u \cdot \nabla\Psi_p \, d\Omega \qquad (\text{II. } 5)$$

As $\nabla\sigma = \nabla\sigma_u + \nabla\sigma_p = \nabla\sigma_p$, equation (II. 5) can be written as

$$\int_{\partial\Omega} \emptyset_u \sigma \nabla\Psi_p d\partial\Omega = -\int_{\Omega} \emptyset_u \nabla\sigma_p \nabla\Psi_u \, d\Omega + \int_{\Omega} \sigma\nabla\emptyset_u \cdot \nabla\Psi_p \, d\Omega \qquad (\text{II. } 6)$$

According to Gauss divergence theorem

$$\int_{\partial\Omega} \emptyset_u \sigma_p \nabla\Psi_u d\partial\Omega = \int_{\Omega} \nabla \cdot \left(\emptyset_u \sigma_p \nabla\Psi_u\right) d\Omega$$

$$= \int_{\Omega} \emptyset_u \nabla\sigma_p \cdot \nabla\Psi_u d\Omega + \int_{\Omega} \sigma_p \nabla\emptyset_u \cdot \nabla\Psi_u d\Omega \qquad (\text{II. } 7)$$

Add equation (II. 6) and equation (II. 7):

$$\int_{\partial\Omega} \emptyset_u \sigma \nabla\Psi_p d\partial\Omega + \int_{\partial\Omega} \emptyset_u \sigma_p \nabla\Psi_u d\partial\Omega$$

$$= \int_{\Omega} \sigma\nabla\emptyset_u \cdot \nabla\Psi_p \, d\Omega + \int_{\Omega} \sigma_p \nabla\emptyset_u \cdot \nabla\Psi_u d\Omega \qquad (\text{II. } 8)$$

Obviously

$$\int_{\partial\Omega} \emptyset_u \sigma \nabla\Psi d\partial\Omega$$

$$= \int_{\partial\Omega} \emptyset_u \sigma_u \nabla\Psi_u d\partial\Omega + \int_{\partial\Omega} \emptyset_u \sigma_p \nabla\Psi_u d\partial\Omega$$

$$+ \int_{\partial\Omega} \emptyset_u \sigma \nabla\Psi_p d\partial\Omega \qquad (\text{II. } 9)$$

where $\sigma\nabla\Psi$ and $\sigma_u\nabla\Psi_u$ are current density. As the applied current is constant, we have $\sigma\nabla\Psi = \sigma_u\nabla\Psi_u$. Thus the left side of the equation (II. 8) is equal to 0, then we have:

$$\int_{\Omega} \sigma\nabla\emptyset_u \cdot \nabla\Psi_p \, d\Omega = -\int_{\Omega} \sigma_p\nabla\emptyset_u \cdot \nabla\Psi_u d\Omega \qquad \text{(II. 10)}$$

Similarly, we can get the following equation:

$$\int_{\Omega} \sigma\nabla\emptyset_p \cdot \nabla\Psi_u \, d\Omega = -\int_{\Omega} \sigma_p\nabla\emptyset_u \cdot \nabla\Psi_u d\Omega \qquad \text{(II. 11)}$$

$$\int_{\Omega} \sigma\nabla\emptyset_p \cdot \nabla\Psi_p \, d\Omega = -\int_{\Omega} \sigma_p\nabla\emptyset_u \cdot \nabla\Psi_p d\Omega \qquad \text{(II. 12)}$$